

ON THE STUDY AND DEVELOPMENT OF AQUEOUS INORGANIC HYDROXO-
AQUO TRIDECAMERS: STRUCTURAL OBSERVATIONS IN THE SOLID AND
SOLUTION PHASES

by

MAISHA KANYUA KAMUNDE-DEVONISH

A DISSERTATION

Presented to the Department of Chemistry and Biochemistry
and the Graduate School of the University of Oregon
in partial fulfillment of the requirements
for the degree of
Doctor of Philosophy

March 2015

DISSERTATION APPROVAL PAGE

Student: Maisha Kanyua Kamunde-Devonish

Title: On the Study and Development of Aqueous Inorganic Hydroxo-Aquo Tridecamers:
Structural Observations in the Solid and Solution Phases

This dissertation has been accepted and approved in partial fulfillment of the requirements for the Doctor of Philosophy degree in the Department of Chemistry and Biochemistry by:

| | |
|-------------------|------------------------------|
| David R. Tyler | Chairperson |
| Darren W. Johnson | Advisor |
| Catherine J. Page | Core Member |
| Mark H. Reed | Institutional Representative |

and

| | |
|--------------------|-----------------------------|
| J. Andrew Berglund | Dean of the Graduate School |
|--------------------|-----------------------------|

Original approval signatures are on file with the University of Oregon Graduate School.

Degree awarded March 2015

© 2015 Maisha Kanyua Kamunde-Devonish

DISSERTATION ABSTRACT

Maisha Kanyua Kamunde-Devonish

Doctor of Philosophy

Department of Chemistry and Biochemistry

March 2015

Title: On the Study and Development of Aqueous Inorganic Hydroxo-Aquo Tridecamers: Structural Observations in the Solid and Solution Phases

Group 13 metals play a pivotal role in many areas of research ranging from materials to environmental chemistry. An important facet of these disciplines is the design of discrete molecules that can serve as functional materials for electronics applications and modeling studies. A solution-based synthetic strategy for the preparation of discrete Group 13 hydroxo-aquo tridecamers with utility as single-source precursors for amorphous functional thin film oxides is introduced in this dissertation. Several techniques including ^1H -Nuclear Magnetic Resonance (NMR) spectroscopy, ^1H -Diffusion Ordered spectroscopy, Solid-state NMR, Dynamic Light Scattering, and Raman spectroscopy are used to acquire structural information necessary for understanding the nature of these precursors in both the solid and solution phases.

The dynamic behavior of these compounds has encouraged additional experiments that will pave the way for new studies with significant importance as the environmental ramifications of these compounds become relevant for future technologies.

This dissertation includes previously published and unpublished co-authored material.

CURRICULUM VITAE

NAME OF AUTHOR: Maisha Kanyua Kamunde-Devonish

GRADUATE AND UNDERGRADUATE SCHOOLS ATTENDED:

University of Oregon, Eugene, OR
California State University, Chico, Chico, CA

DEGREES AWARDED:

Doctor of Philosophy, Chemistry, 2015, University of Oregon
Master of Science, Chemistry, 2009, University of Oregon
Bachelor of Science, Chemistry, 2007, California State University, Chico

AREAS OF SPECIAL INTEREST:

Aqueous Inorganic Chemistry

PROFESSIONAL EXPERIENCE:

Graduate Research Assistant, Prof. Darren W. Johnson, University of Oregon,
June 2009 – February 2015

Graduate Teaching Assistant, Prof. Darren W. Johnson, University of Oregon,
June 2009 – July 2009

Graduate Teaching Fellow, University of Oregon, September 2014 – December
2014
and September 2008 – June 2009

Undergraduate Research Assistant, Prof. Randy C. Miller, California State
University, Chico, January 2006 – May 2007

Laboratory Technician, California State University, Chico, August 2005 – May
2007

Undergraduate Research Assistant, Prof. David C. Johnson, University of Oregon,
June 2005 - August 2005 and June 2004 – August 2004

GRANTS, AWARDS, AND HONORS:

National Science Foundation Integrative Graduate Education and Research
Traineeship Fellow (NSF-IGERT), University of Oregon, 2009-2010

PUBLICATIONS:

Kamunde-Devonish, M.K.; Jackson, Jr., M.N.; Zakharov, L.N.; Johnson, D.W.,
Synthesis and Structural Determination of a New Anionic $\{M(\mu\text{-OH})_2M\}$ Rhomb-
Centered Tetranuclear Copper (II) Sulfate Cluster That Forms a 1-D Hydrogen
Bonded Network in the Crystalline State, *manuscript accepted pending revisions*,
Acta Cryst C, 2015.

Kamunde-Devonish, M.K.; Mensinger, Z.L.; Fast, D.B.; Gatlin, J.T.; Dolgos, M.R.;
Johnson, D.W., Synthesis and Solid-State Structural Characterization of a Series of
Aqueous Heterometallic Tridecameric Group 13 Clusters, *manuscript accepted*
pending revisions, *Inorganic Chemistry*, 2015.

Kamunde-Devonish, M.K.; Jackson, Jr., M.N.; Mensinger, Z.L.; Zakharov, L.N.;
Johnson, D.W., Transmetalation of Aqueous Inorganic Clusters: A Useful Route to
the Synthesis of Heterometallic Aluminum and Indium Hydroxo-Aquo Clusters,
Inorganic Chemistry, 2014, 53, (14), 7101-7105. *ACS Editor's Choice*.

Ma, Z.L.; Wentz, K.M.; Hammann, B.A.; Chang, I-Y.; Kamunde-Devonish, M.K.;
Cheong, P.H-Y.; Johnson, D.W.; Terskikh, V.V.; Hayes, S.E., Solid-State ^{69}Ga and
 ^{71}Ga NMR Study of the Nanoscale Inorganic Cluster
 $[\text{Ga}_{13}(\mu_3\text{-OH})_6(\mu_2\text{-OH})_{18}(\text{H}_2\text{O})_{24}](\text{NO}_3)_{15}$, *Chemistry of Materials*, 2014, 26, (17),
4978-4983.

ACKNOWLEDGMENTS

None of this would have been possible without the endless love and support of my family. They are as much a part of my success as I could ever be. Almost as crucial to this process have been the friends I have made during this adventure. To my cohorts, I thank you for bringing sanity, dancing, and dinner parties to my life; and more importantly, for being the people I can still call my friends.

I would also like to give a special thank you to two things near and dear to me: my cat Howard - I could not ask for a better roommate; and my liver. I am grateful that you chose not to fail when the doctors expected otherwise. Thank you for giving me the motivation to finish what I started.

I wish to express my utmost appreciation to my boss Dr. Darren W. Johnson. Of all the specifics I could possibly point to, I am most thankful that he let me function in my bubble. Few would ever be so understanding.

Finally, a special thank you is owed to the entire Chemistry department as CSU Chico. Without all of them I would not be on this path.

My doctoral research was supported by funding from the National Science Foundation (NSF) IGERT (DGE-0549503) fellowship and the NSF Center for Sustainable Materials Chemistry (CHE-1102637) grant.

This dissertation is dedicated to my family, truly the best part of me.

TABLE OF CONTENTS

| Chapter | Page |
|--|------|
| I. FROM MINERALS TO MATERIALS: A SURVEY OF AQUEOUS GROUP 13 INORGANIC CHEMISTRY | 1 |
| I.1. Group 13 Elements in the Environment | 2 |
| I.2. Group 13 Elements as Functional Thin Film Precursors for Materials Applications | 6 |
| I.3. Group 13 Elements as Dynamic Oligomer Assemblies | 8 |
| I.4. Solution Dynamics of Group 13 Tridecamers | 11 |
| I.5. Characterization of Group 13 Tridecamers | 13 |
| I.5.1. 1-Dimensional Nuclear Magnetic Resonance Spectroscopy | 14 |
| I.5.2. Solid-state Nuclear Magnetic Resonance Spectroscopy | 15 |
| I.5.3. 2-Dimensional Nuclear Magnetic Resonance Spectroscopy | 16 |
| I.5.4. Dynamic Light Scattering | 18 |
| I.5.5. Raman Spectroscopy | 18 |
| I.5.6. Small-Angle X-Ray Scattering | 18 |
| I.6. Conclusions | 19 |
| I.7. Bridge to Chapter II | 20 |
| II. SYNTHESIS AND SOLID-STATE STRUCTURAL CHARACTERIZATION OF A SERIES OF AQUEOUS HETEROMETALLIC TRIDECAMERIC GROUP 13 CLUSTERS | 21 |
| II.1. Introduction | 22 |

| Chapter | Page |
|--|------|
| II.2. Synthetic Procedures for f-Ga_{13-x}In_x Clusters | 25 |
| II.3. Description of Characterization Methods | 25 |
| II.3.1. X-Ray Crystallography | 25 |
| II.3.2. Variable Temperature Powder X-Ray Diffraction | 27 |
| II.3.3. Bulk Sample Analysis | 28 |
| II.4. Determining Synthetic Parameters for Heterometallic Tridecamers | 28 |
| II.5. Single Crystal X-Ray Analysis for 1-6 | 30 |
| II.6. Conversion of Clusters to Oxides..... | 33 |
| II.7. Conclusions | 41 |
| II.8. Bridge to Chapter III | 41 |
| | |
| III. SOLID-STATE ⁶⁹ Ga AND ⁷¹ Ga NMR STUDY OF THE NANOSCALE INORGANIC CLUSTER [Ga ₁₃ (μ ₃ -OH) ₆ (μ ₂ -OH) ₁₈ (H ₂ O) ₂₄](NO ₃) ₁₅ | 43 |
| III.1. Introduction..... | 43 |
| III.2. f-Ga₁₃ Synthesis..... | 46 |
| III.3. Solid-State NMR Parameters..... | 47 |
| III.4. Theoretical Computations of NMR Parameters..... | 48 |
| III.5. NMR Spectral Fitting..... | 49 |
| III.6. Solid-State NMR Analysis..... | 49 |
| III.7. ⁷¹ Ga MAS Solid-State NMR at 21.1 T | 50 |
| III.8. ⁷¹ Ga MAS Solid-State NMR at 13.9 T | 53 |
| III.9. ⁶⁹ Ga MAS Solid-State NMR at 21.1 T and 13.9 T | 54 |

| Chapter | Page |
|--|------|
| III.10. Conclusions..... | 56 |
| III.11. Bridge to Chapter IV..... | 57 |
| | |
| IV. TRANSMETALATION OF AQUEOUS INORGANIC CLUSTERS - A USEFUL ROUTE TO THE SYNTHESIS OF HETEROMETALLIC ALUMINUM AND INDIUM HYDROXO-AQUO CLUSTERS..... | 58 |
| IV.1. Introduction..... | 59 |
| IV.2. Motivation for Precursor Design..... | 59 |
| IV.3. Metal Exchange..... | 61 |
| IV.3.1. Synthesis of f-Al₇In₆ | 63 |
| IV.3.2. Synthesis of f-Ga₇In₆ | 63 |
| IV.4. General Characterization Methods..... | 63 |
| IV.5. Summary of Crystallographic Data..... | 64 |
| IV.6. Solution-State Characterization of f-Al₇In₆ | 65 |
| IV.7. Solid-State Characterization of f-Al₇In₆ | 69 |
| IV.8. f-Al₇In₆ Thin Film Analysis..... | 70 |
| IV.9. Conclusions..... | 72 |
| IV.10. Bridge to Chapter V..... | 73 |
| | |
| V. INVESTIGATION OF THE PROTON EXCHANGE RATE KINETICS OF AQUEOUS [AL ₁₃ (μ ₃ -OH) ₆ (μ ₂ -OH) ₁₈ (H ₂ O) ₂₄] ¹⁵⁺ | 74 |
| V.1. Introduction..... | 74 |

| Chapter | Page |
|---|------|
| V.2. General Procedure for the Synthesis of $f\text{-Al}_{13}$ | 76 |
| V.3. $^1\text{H-NMR}$ Spectroscopy | 76 |
| V.4. Dynamic and Phase Analysis Light Scattering | 77 |
| V.5. Raman Spectroscopy | 78 |
| V.6. Rate Equations | 78 |
| V.7. $\text{H}_2\text{O}/\text{Acetone-}d_6$ | 80 |
| V.7.1. DLS Measurements at Different Acetone Concentrations | 82 |
| V.7.2. PALS Measurements at Different Acetone Concentrations | 84 |
| V.7.3. Infrared Spectroscopy Analysis of Hydrogen Bonding Interactions | 85 |
| V.8. $\text{H}_2\text{O}/\text{DMSO-}d_6$ | 86 |
| V.9. D_2O | 89 |
| V.10. Proton Exchange Rates for $f\text{-Al}_{13}$ | 90 |
| V.11. Conclusions | 92 |
| V.12. Bridge to Chapter VI | 92 |
| | |
| VI. AN ANIONIC $\{\text{Cu}(\mu\text{-OH})_2\text{Cu}\}$ RHOMB-CENTERED TETRANUCLEAR COPPER (II) SULFATE CLUSTER FORMS A 1-D HYDROGEN BONDED NETWORK IN THE CRYSTALLINE STATE | 93 |
| VI.1. Introduction | 93 |
| VI.2. Synthesis of $\{(\text{C}_5\text{H}_5\text{NH})_2[\text{Cu}_4(\text{OH})_2(\text{SO}_4)_4(\text{H}_2\text{O})_4]\}_n$ | 94 |
| VI.3. Crystal Structure Determination | 95 |
| VI.4. Crystallographic Structure Analysis | 96 |

| Chapter | Page |
|--|------|
| VI.5. Raman Spectroscopy Analysis | 100 |
| VI.6. Conclusions..... | 101 |
| VI.7. Bridge to Chapter VII | 102 |
| | |
| VII. CONCLUSIONS AND FUTURE OUTLOOKS | 103 |
| VII.1. Introduction | 103 |
| VII.2. Research Summary..... | 104 |
| VII.3. Future Outlooks..... | 105 |
| VII.3.1. Computational Peak Assignment for f-Al₁₃ | 105 |
| VII.3.2. Precursor Ecological Toxicology Studies | 106 |
| VII.3.3. DLS and SAXS Studies on f-Al₇In₆ | 107 |
| VII.3.3.1. Dynamic Light Scattering Experiments | 108 |
| VII.3.3.2. Small-Angle X-Ray Scattering Experiments | 109 |
| VII.3.4. Group 13 Cluster Speciation – Mass Spectrometry | 110 |
| VII.3.5. New Bridging Ligands | 111 |
| VII.3.6. Transition Metal Cluster Synthesis | 112 |
| VII.3.7. Main Group Cluster Synthesis | 114 |
| VII.4. Conclusions | 114 |
| | |
| APPENDICES | 115 |
| A. SOLUTION-STATE ANALYSIS OF THE f-AL₁₃ TRIDECAMER | 115 |
| B. SUPPLEMENTAL INFORMATION FOR CHAPTER II | 121 |

| Chapter | Page |
|--|------|
| C. SUPPLEMENTAL INFORMATION FOR CHAPTER III..... | 131 |
| D. SUPPLEMENTAL INFORMATION FOR CHAPTER IV | 141 |
| E. SUPPLEMENTAL INFORMATION FOR CHAPTER V | 159 |
| F. SUPPLEMENTAL INFORMATION FOR CHAPTER VI..... | 162 |
| G. SUPPLEMENTAL INFORMATION FOR CHAPTER VII..... | 173 |
| REFERENCES CITED..... | 176 |

LIST OF FIGURES

| Figure | Page |
|--|------|
| 1.1. Polyhedral representation of $(Al_{13}O_4(OH)_{24}(H_2O)_{12})^{7+}$ [κ - Al₁₃]. The structure contains one central $Al(O)_4$ tetrahedron surrounded by twelve edge-sharing AlO_6 octahedra | 5 |
| 1.2. The process for transforming f-Ga₇In₆ in to a thin film. A solution of f-Ga₇In₆ (0.3M) in either 18mΩ water or methanol is spin-cast on to a thermal oxide substrate and annealed at 600 °C to form a metal oxide film | 8 |
| 1.3. E-pH (Pourbaix) diagram for the equilibrium phases of aluminum in aqueous conditions. Predominant ion boundaries are shown with solid lines. Dotted lines demarcate the regions in which water oxidation and reduction occur at the anode and cathode, respectively. (Top) : In the upper region, water is oxidized to O ₂ . (Middle) : Water is stable and no decomposition occurs. (Bottom) : In the lower region water is reduced to H ₂ | 9 |
| 1.4. Brucite lattice diagramming growth of polynuclear species..... | 10 |
| 1.5. EXAFS data for the f-Ga₁₃ cluster in solution (blue), crystal form (red), and Ga(NO ₃) ₃ in solution (green) in R space..... | 13 |
| 1.6. Stokes-Einstein equation where k is the Boltzmann constant, T is temperature, η is solvent viscosity, and R_h is the hydrodynamic radius. The integer constant in the denominator, 6, is used under the assumption that the molecule is spherical..... | 17 |
| 2.1. The f-Ga_{13-x}In_x (x=1-6) heterometallic hydroxo-aquo clusters. Clockwise from the top right: Ga₁₂In₁ (1) , Ga₁₁In₂ (2) , Ga₁₀In₃ (3) , Ga₉In₄ (4) , Ga₈In₅ (5) , and Ga₇In₆ (6) . Gallium and indium metal ions are shown in blue and green, respectively. All six Ga/In positions in the outer shell are symmetrically equivalent. The x-ray structures show that only gallium atoms occupy the seven interior positions of each clusters, and gallium and indium atoms in the outer ring are disordered over all six positions rather than in specific locations..... | 24 |
| 2.2. Plot of the relationships between the equivalents of Ga(NO ₃) ₃ and In(NO ₃) ₃ required to form f-Ga_{13-x}In_x heterometallic clusters and the number of gallium and indium ions in the final structure. For example, to form f-Ga₁₀In₃ , 7 equivalents of Ga(NO ₃) ₃ must be used (value read for Ga = 10 on y-axis) while 6 equivalents of In(NO ₃) ₃ are required (value read for In = 3 on y-axis) | 29 |

| Figure | Page |
|--|------|
| 2.3. Side (left) and front (right) view of the three different coordination environments for the metal ion sites of 1-6 : M1 (core; yellow), M2 (middle; blue), and M3 (outer; bronze)..... | 30 |
| 2.4. Potential arrangements of indium atoms in the outer ring of f-Ga₁₀In₃ | 32 |
| 2.5. Powder XRD traces for a bulk sample of f-Ga₁₃ heated at specified temperatures..... | 34 |
| 2.6. Powder XRD traces for bulk samples of f-Ga₁₃ and 1-6 at 600 °C..... | 35 |
| 2.7. Powder XRD traces for a bulk sample of f-Ga₁₁In₂ heated at specified temperatures..... | 36 |
| 2.8. Powder XRD traces for a bulk sample of f-Ga₁₀In₃ heated at specified temperatures..... | 37 |
| 2.9. Powder XRD traces for a bulk sample of f-Ga₈In₅ heated at specified temperatures..... | 38 |
| 2.10. Pawley fits for f-Ga₁₂In₁ (1 , left) and f-Ga₈In₅ (5 , right). The observed trace (black), calculated trace (red) and the sum difference (green) shown. 1 transforms in to the β -Ga ₂ O ₃ structure with elevated temperatures. Phase separation occurs for 5 at elevated temperatures and results in a majority phase of β -Ga ₂ O ₃ and a minority phase of the In ₂ O ₃ bixbyite-type structure..... | 39 |
| 3.1. Representation of the [Ga ₁₃ (μ_3 -OH) ₆ (μ_2 -OH) ₁₈ (H ₂ O) ₂₄](NO ₃) ₁₅ cluster. a) Space-filling polyhedra show overhead and side views, according to prior single crystal results with NO ₃ ⁻ (omitted for clarity) to charge balance the metal-hydroxide cluster. b) Gallium sites are referred to as follows: (1) “core”, (2)-(7) “middle ring”, (8)-(13) “outer ring”. Oxygen atoms have been color-coded to indicate identical bonds and the colors are consistent with Figure 3.3..... | 45 |
| 3.2. ⁷¹ Ga NMR spectra of f-Ga₁₃ at 21.1 T and 62.5 kHz MAS. Top spectrum (black) is experimental data with 42,152 transients averaged. Middle spectrum (brown) is fit of experimental data using DMFit. Bottom spectra are models of the individual sites as defined in Figure 3.1. * indicates spinning sidebands and † denotes residual Ga(NO ₃) ₃ from the synthesis..... | 50 |

| Figure | Page |
|---|------|
| 3.3. Bond angles for a gallium monomer $[\text{Ga}(\text{H}_2\text{O})_6]^{3+}$ and the gallium sites in f-Ga₁₃ demonstrating the strained octahedra leading to large C_Q values. The core gallium is bonded to all μ_3 hydroxo-bridges, and the bonds are slightly distorted from a perfect octahedron yet yielding a small asymmetry parameter due to axial symmetry ($\eta_Q = 0$). In stark contrast, the middle ring gallium ions have four μ_2 and two μ_3 bonds ($\eta_Q \neq 0$) with bonding angles that are asymmetric and largely divergent from 90° . The outer ring ions are closer to octahedral symmetry but with a mixture of bridging -OH and H_2O ligands..... | 52 |
| 3.4. ^{71}Ga NMR spectrum of f-Ga₁₃ at 13.9 T and 33 kHz MAS with 51,200 transients averaged (top black). Middle spectrum (brown) is fit from experimental data using DMFit. Bottom spectra are models of the individual sites as defined in Figure 3.1. Parameters for modeling were used without modification from the 21.1 T data | 54 |
| 3.5. ^{69}Ga NMR spectra of f-Ga₁₃ at 21.1 T (a) and 13.9 T (b) with MAS at 62.5 kHz and 33 kHz, respectively. Spectra referenced to 1M $\text{Ga}(\text{NO}_3)_3$. Consistent with other figures, top spectrum (black) is experimental, the middle spectrum (brown) is the model, and the bottom (orange, blue, magenta) spectra are the individual gallium sites. Modeling was done by using the asymmetry parameter η_Q and δ_{iso} deduced from the 21.1 T ^{71}Ga results and varying the C_Q of each site until the model matched the experimental results at 21.1 T. The 21.1 T ^{69}Ga parameters were then applied to the 13.9 T data to confirm correct assignment of C_Q and η_Q | 56 |
| 4.1. Simple representation of the transformation from f-Al₁₃ to f-Al₇In₆ upon addition of $\text{In}(\text{NO}_3)_3$ to a solution of f-Al₁₃ (in either MeOH or H_2O). In^{3+} ions (green) displace Al^{3+} ions (purple) on the labile outer shell of the cluster. Images generated from crystals structures of f-Al₁₃ and f-Al₇In₆ | 60 |
| 4.2. ^1H -NMR of f-Al₁₃ (A), f-Al₇In₆ (B), and $\text{Al}(\text{NO}_3)_3$ (C). Crystals of f-Al₁₃ (confirmed using single-crystal XRD) were used for ^1H -NMR spectroscopy | 66 |
| 4.3. Top: (A) Autocorrelation function of 2 mM f-Al₁₃ (black) and 2 mM f-Al₇In₆ (grey) in d_6 -DMSO (traces stack on top of each other). Hydrodynamic radii of f-Al₁₃ (B) and f-Al₇In₆ (C) in d_6 -DMSO are displayed in the insets. Bottom: (A) Autocorrelation function of 0.2 M f-Al₁₃ (black) and 0.2 M f-Al₇In₆ (grey) in H_2O . Hydrodynamic radii of f-Al₁₃ (B) and f-Al₇In₆ (C) in H_2O are displayed in the insets | 68 |
| 4.4. Solid state Raman spectra of f-Al₇In₆ (A, grey) and f-Al₁₃ (B, black) between 100 cm^{-1} and 800 cm^{-1} | 69 |

| Figure | Page |
|---|------|
| 4.5. Top: EDX analysis of the solution processed f-Al₇In₆ precursor and cross-sectional TEM (top insert) of the Al _{13-x} In _x O _y thin film. The white circle represents the spot on which the EDX scan was performed. Bottom: AFM 3D side view of Al _{13-x} In _x O _y thin film (16 μm ²) | 71 |
| 5.1. ¹ H-NMR spectra (-5 °C to -20 °C) of f-Al₁₃ in a 2.5:1 (v/v) mix of H ₂ O/acetone-d ₆ . The peak centered at 5.2 ppm is associated with bulk water in the solution. The peak at 9.8 ppm represents the hexaaqua [Al(H ₂ O) ₆] ³⁺ complex seen in the spectrum for Al(NO ₃) ₃ . Peaks A, B, and C integrate to 1:1:2, respectively | 81 |
| 5.2. Diagram of f-Al₁₃ showing the different types of protons coordinated to the core (μ ₃ -OH, green), middle (μ ₂ -OH, purple), and outer (μ ₂ -OH', yellow) rings of aluminum metal ions. Water molecules are color-coded to reflect differences based upon symmetry, not coordination. Image was made using Crystalmaker | 82 |
| 5.3. Hydrodynamic radius of f-Al₁₃ as a function of mol % acetone..... | 83 |
| 5.4. Conductivity and zeta potential measurements for f-Al₁₃ | 85 |
| 5.5. Stacked ATR-IR spectra of (top) 1M f-Al₁₃ at 14 mol% acetone in H ₂ O, (middle) 14% acetone in an H ₂ O mixture, and (bottom) pure acetone | 86 |
| 5.6. ¹ H-NMR spectra of variable-temperature experiment for f-Al₁₃ in a 1:2 (v/v) solution of H ₂ O/DMSO- <i>d</i> ₆ | 87 |
| 5.7. Plot of the kinetics data for the μ ₂ -OH proton site (at 3.6 ppm) on f-Al₁₃ in a 1:2 (v/v) solution of H ₂ O/ DMSO- <i>d</i> ₆ | 89 |
| 5.8. ¹ H-NMR spectra of variable-temperature experiment for f-Al₁₃ in D ₂ O..... | 90 |
| 6.1. Ball and stick representation of the {(C ₅ H ₅ NH) ₂ [Cu ₄ (OH) ₂ (SO ₄) ₄ (H ₂ O) ₄]} _n tetramer. The pyridinium cation hydrogen bonds to the μ ₃ -sulfato ligand and water ligand of two adjacent Cu ₄ subunits. Oxygen and sulfur atoms neighboring Cu1 and Cu2 are labeled (hydrogen labels omitted for clarity)..... | 96 |
| 6.2. A fragment of {[Cu ₄ (OH) ₂ (SO ₄) ₄ (H ₂ O) ₄]} _n 1-D chain (a) and the view of the packing of {(C ₅ H ₅ NH) ₂ [Cu ₄ (OH) ₂ (SO ₄) ₄ (H ₂ O) ₄]} _n along the <i>a</i> axis. H-bonds are drawn by dash lines. Ellipsoids are presented at the 30% probability level | 98 |

| Figure | Page |
|--|------|
| 6.3. Selected bond lengths and angles for the rhomboid $\{M-(\mu-OH)_2-M\}$ core of $\{(C_5H_5NH)_2[Cu_4(OH)_2(SO_4)_4(H_2O)_4]\}_n$. Atoms are not to scale | 99 |
| 6.4. Bond lengths and angles for $\{(C_5H_5NH)_2[Cu_4(OH)_2(SO_4)_4(H_2O)_4]\}_n$ (left) and ranges observed for the rhomboid core in related $\{M-(\mu-O)_2-M\}$ sites (right). Image on the right from Que, <i>et. al.</i> Atoms are not shown to scale | 99 |
| 6.5. Stacked Raman spectra of pyridine (green), cupric sulfate (red), and $\{(C_5H_5NH)_2[Cu_4(OH)_2(SO_4)_4(H_2O)_4]\}_n$ (black). A) $100\text{ cm}^{-1} - 1700\text{ cm}^{-1}$ B) $2800\text{ cm}^{-1} - 3700\text{ cm}^{-1}$. C) inset of the copper cluster from 2800 cm^{-1} to 3700 cm^{-1} | 101 |
| 7.1. A comparison of Zebrafish mortality for $f-Al_{13}$ and organotin complexes. $f-Al_{13}$ has low mortality in comparison to Sn (formate) and Sn (phenylacetate) complexes for which significant mortality occurred at 50 mg/L and 250 mg/L, respectively | 106 |
| 7.2. A comparison of Zebrafish mortality for $f-Ga_7In_6$, $f-Ga_{10}In_3$, and CoM (M = Al and Ga) complexes. Higher toxicity (and higher variance in the amount of toxicity) was observed for the Co samples with CoGa being most toxic..... | 107 |
| 7.3. SAXS scatter curves for $f-Al_{13}$ and the expected $f-Al_7In_6$ tridecamers at 1M and 100mM concentrations | 110 |
| 7.4. Crystal structure of $[Fe(\mu_3-O)(H_2O)_3(CH_3-CO_2)_6(NO_3)(CH_3C(O)OH)](Fe_3)$ | 113 |

LIST OF TABLES

| Table | Page |
|---|------|
| 1.1. Common aluminum-containing minerals | 2 |
| 1.2. Common gallium-containing minerals | 4 |
| 1.3. Common indium-containing minerals | 4 |
| 1.4. Properties of various atomic nuclei for NMR spectroscopy. Relative frequency calculated at the 600 MHz | 16 |
| 2.1. Ratios of Ga(NO ₃) ₃ , In(NO ₃) ₃ , and DBNA for the heterometallic clusters 1-6 . The ratios of In(NO ₃) ₃ and DBNA are relative to the starting quantity of Ga(NO ₃) ₃ | 25 |
| 2.2. Crystal structure data for clusters 1-3 with fractional atom values | 26 |
| 2.3. Crystal structure data for clusters 4-6 with fractional atom values | 27 |
| 2.4. Single crystal XRD, (EA), and EPMA metal ratio results for 1, 3, 4, and 6 . Standard deviations from EA and EPMA are shown in parentheses..... | 30 |
| 2.5. Lattice parameters of oxides formed from f-Ga_{13-x}In_x clusters..... | 40 |
| 3.1. Experimental and computed ^{69/71} Ga NMR parameters for f-Ga₁₃ | 51 |
| 4.1. Ratio of f-Al₁₃ to In(NO ₃) ₃ for the synthesis of various f-Al_{13-x}In_x clusters | 62 |
| 4.2. Ratio of f-Ga₁₃ to In(NO ₃) ₃ for the synthesis of various f-Ga_{13-x}In_x clusters | 62 |
| 4.3. Reduction potentials for the synthesis of f-Al₁₃ | 67 |
| 5.1. Sample conditions for f-Al₁₃ in water/acetone light scattering experiments. 1 mL of each sample was prepared at an initial concentration of 0.10 M f-Al₁₃ in H ₂ O. The ratio of water to acetone (% mol/mol) was set so that the final concentration of f-Al₁₃ was 50 mM in 2 mL of total solution | 77 |
| 5.2. Full-width half-max (FWHM) values for the proton signal for f-Al₁₃ at 3.6 ppm in a 1:2 (v/v) solution of H ₂ O/ DMSO- <i>d</i> ₆ | 88 |

| Table | Page |
|--|------|
| 5.3. Exchange rates, residency times, and activation parameters for proton sites on f-Al₁₃ . Standard errors are in parentheses | 91 |
| 5.4. Exchange rates, residency times, and activation parameters for proton sites on κ-Al₁₃ . Available standard errors are in parentheses | 91 |
| 6.1. Selected bond lengths and angles for (1) | 95 |
| 7.1. Protic and aprotic solvents in which the f-Al₁₃ tridecamer is soluble..... | 105 |
| 7.2. Radius of gyration (R_g) of f-Al₁₃ and the transmetalation product from the addition of In(NO ₃) ₃ to f-Al₁₃ , expected to be f-Al₇In₆ . Both experiments were performed in H ₂ O at two different concentrations, 1M and 100mM..... | 109 |
| 7.3. Results of selected metal exchange experiments. Transmetalation occurred only in the instance where In(NO ₃) ₃ was mixed in solution with f-Ga₁₃ | 112 |

LIST OF SCHEMES

| Scheme | Page |
|--|------|
| 1.1. Reaction sequence for the synthesis of <i>f</i>-Ga₁₃ . <i>f</i>-Al₁₃ can be produced in the same manner with the addition of base in order to aid the hydrolysis of Al(NO ₃) ₃ | 11 |
| 1.2. Mixed-metal synthesis of <i>f</i>-M_{13-x}In_x tridecamers from a solution containing In(NO ₃) ₃ and <i>f</i>-M₁₃ , where M = Al of Ga..... | 12 |

CHAPTER I

FROM MINERALS TO MATERIALS: A SURVEY OF AQUEOUS GROUP 13 INORGANIC CHEMISTRY

Many of the scientific inquiries about the aqueous chemical dynamics of the Group 13 elements aluminum, gallium, and indium have transitioned into investigations of complex reactivity with environmental and technological implications. An important aspect of these disciplines is a unifying path towards the design of discrete compounds that can function as models and precursors viable for geological studies and in functional materials, respectively. This chapter provides a survey of Group 13 elements as found in both the environment and electronic materials. In addition, several of the Group 13 compounds derived in recent decades are mentioned; particular attention is paid to the hydroxo-aquo cationic tridecamers $[\text{M}_{13-x}\text{In}_x(\mu_3\text{-OH})_6(\mu_2\text{-OH})_{18}(\text{H}_2\text{O})_{24}]^{15+}$ ($\text{M} = \text{Al}$ or Ga ; $x = 0\text{-}6$), referred to by their respective $f\text{-M}_{13-x}\text{In}_x$ composition, which are the focal point of this thesis. A description of the techniques used to characterize these tridecamers follows.

I.1. Group 13 elements in the environment

Aluminum is the most abundant metal and third most abundant element (8.2×10^4 ppm, 8.3% by weight) in the Earth's crust behind oxygen and silicon.² It is not commonly found in its elemental form owing to a strong affinity for oxygen. Instead, most aluminum exists in several hydroxo- and oxo-phases, largely in bauxite ($\text{Al}_2\text{O}_3 \cdot x\text{H}_2\text{O}$) but also in bayerite ($\alpha\text{-Al}(\text{OH})_3$) as well as other minerals (Table 1.1). Alumina (Al_2O_3) is also found naturally in its crystalline form corundum ($\alpha\text{-Al}_2\text{O}_3$); impurities within this structure (i.e., chromium, and iron or titanium) result in precious gemstones such as rubies and sapphires, respectively. Alumina exists in two phases that differ in the arrangement of the Al^{3+} cations: α and γ . In the α -phase Al^{3+} are organized in hexagonal close packed forms and occupy octahedral sites; the γ -phase adopts a MgAl_2O_4 spinel-type structure in which Al^{3+} cations are arranged in a cubic close packed array and occupy both octahedral and tetrahedral sites.

Table 1.1. Common aluminum-containing minerals.*

| Mineral | Chemical formula |
|---------------------------|--|
| Feldspar | $\text{KAlSi}_3\text{O}_8\text{-NaAlSi}_3\text{O}_8\text{-CaAl}_2\text{Si}_2\text{O}_8$ |
| Turquoise | $\text{CuAl}_6(\text{PO}_4)_4(\text{OH})_8 \cdot 4\text{H}_2\text{O}$ |
| Spinel | MgAl_2O_4 |
| Cryolite | $(\text{Zn,Fe})\text{S}$ |
| Beryl | $\text{Be}_3\text{Al}_2(\text{SiO}_3)_6$ |
| Pyralspite garnets | |
| Almandine | $\text{Fe}_3\text{Al}_2(\text{SiO}_3)_3$ |
| Boehmite | $\text{Mg}_3\text{Al}_2(\text{SiO}_3)_4 [(\gamma\text{-Al}(\text{O})\text{OH})]$ |
| Diaspore | $\text{Mn}_3\text{Al}_2(\text{SiO}_3)_5 [(\alpha\text{-Al}(\text{OH})_3 \text{ or } \alpha\text{-Al}(\text{O})\text{OH})]$ |

* Beryl, $\text{Be}_3\text{Al}_2(\text{SiO}_3)_6$ is more commonly referred to as the emerald. Aluminum phases within the mineral types are bracketed next to the chemical formulas.

The low solubility of aluminum dictates that its environmental effect is minimal. As bioavailability increases under acidic conditions and in the presence of complexing ligands, concerns arise since aluminium is non-essential to living organisms and the effects of bioaccumulation are not well known. Aluminum leads to phytotoxicity and several studies have suggested a link between the absorption of soluble aluminum ions and Alzheimer's disease although the effects of exposure are still a topic of heated debate.³⁻⁵

Gallium is not as much of an environmental concern in comparison owing to its scarcity in the earth's crust (16.9 ppm). Gallium is found primarily in jarosite (Table 1.2); the ionic radius of Ga^{3+} (0.620 Å) is similar to that of both Al^{3+} and Fe^{3+} (0.535 Å and 0.600 Å, respectively), therefore Ga^{3+} can easily substitute into this structure.⁶ Other gallium-based minerals such as gallite and söhngeite are uncommon, and Ga^{3+} is trace in bauxite and sphalerite (Table 1.2).⁷ The amount of Ga^{3+} in other minerals such as germanite is negligible. Gallium oxide (Ga_2O_3) has five phases: α , β , δ , ϵ , and γ . α - Ga_2O_3 has a corundum-like structure identical to α - Ga_2O_3 , γ - Ga_2O_3 is similar to γ - Al_2O_3 , and β - Ga_2O_3 features a distorted cubic close packed form with Ga^{3+} ions occupying octahedral and tetrahedral sites.

Table 1.2. Common gallium-containing minerals.[†]

| Mineral | Chemical formula |
|----------------|--|
| Gallite | CuGaS ₂ |
| Söhngelite | Ga(OH) ₃ |
| Sphalerite | (Zn,Fe)S |
| Jarosite | KFe ³⁺ ₃ (OH) ₆ (SO ₄) ₂ |
| Germanite | Cu ₂₆ Fe ₄ Ge ₄ S ₃₂ |
| Bauxite | |
| Gibbsite | Al(OH) ₃ |
| Boehmite | γ-Al(O)OH |
| Diaspore | α-Al(O)OH |

[†] Gallium is a by-product of bauxite ore mining.

Indium is more rare in the Earth's crust than either aluminum or gallium (0.16 ppm). It is naturally occurring in sulfur-rich minerals such as stannite (Cu₂FeSnS₄) and chalcopyrite (CuFeS₂) in addition to others (Table 1.3).⁷ The crystalline phase of In₂O₃ exists in either the cubic (bixbyite, (Mn,Fe)₂O₃) or rhombohedral (corundum) forms.⁸

Table 1.3. Common indium-containing minerals.[‡]

| Mineral | Chemical formula |
|-----------------------------|---|
| Cadomoinite | CdIn ₂ S ₄ |
| Dzhalindite | In(OH) ₃ |
| Indite | FeIn ₂ S ₄ |
| Roquesite | CuInS ₂ |
| Laforetite | AgInS ₂ |
| unnamed ³ | (Zn,Fe) ₂ Cu ₃ In ₃ S ₈ |
| Yanomamite | InAsO ₄ · 2H ₂ O |
| Cassiterite | SnO ₂ |

[‡] Indium is a by-product of the mining of cassiterite ore. References for (Zn,Fe)₂Cu₃In₃S₈: a) Smith, D.G.W.; Nickel, E.H.; *A System of Codification for Unnamed Minerals: Report of the Subcommittee for Unnamed Minerals of the IMA Commission on New Minerals, Nomenclature and Classification*, Canadian Mineralogist, **2007**, 45, 983-1055b) Bull. Minéral. 108, 245 ; c) Am. Mineral. 71, 846.

The behavior of elements in the environment is of interest, particularly when mapping phenomena such as erosion and pollutant transportation/remediation. Aluminum ions have been studied in relation to heavy-metal contamination of various water systems.⁹ The combination of acidic run-off from mining areas and water at near neutral pH results in the precipitation of aluminum oxo-hydroxo flocculants - the predominant species observed in these flocs being the Keggin structure ($\text{Al}_{13}\text{O}_4(\text{OH})_{24}(\text{H}_2\text{O})_{12}$)⁷⁺ ($\kappa\text{-Al}_{13}$, Figure 1.1).^{10,11}

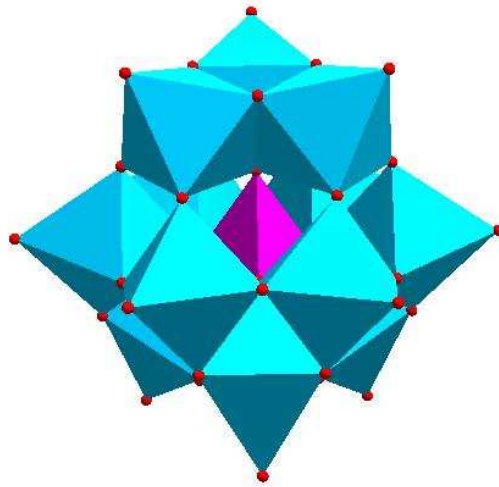


Figure 1.1. Polyhedral representation of ($\text{Al}_{13}\text{O}_4(\text{OH})_{24}(\text{H}_2\text{O})_{12}$)⁷⁺ [$\kappa\text{-Al}_{13}$]. The structure contains one central $\text{Al}(\text{O})_4$ tetrahedron surrounded by twelve edge-sharing AlO_6 octahedra.

The resulting suspension transports adsorbed heavy metals downstream leading to aquatic poisoning and phytotoxicity. However, industry is capitalizing on this adsorption process for waste-water remediation as shown recently with alumina nanoparticle-carboxylic acid adducts.¹² Geochemists have used oxide complexes to

simulate water-oxide interactions on mineral surfaces that are normally difficult to analyze because of extended geological time-scales and the limited availability of spectroscopic probes.¹³ Although these models are not currently as prevalent for gallium and indium as they are for Al^{3+} , Fe^{3+} , or Mn^{4+} metal ions, molecular-scaled structures do exist that can help visualize and predict potential environmental interactions that are currently difficult to analyze due to small data sets. The crystal structures of Group 13 minerals such as $\text{Al}(\text{OH})_3$ and Group 13 tridecamers are similar. This again suggests that they can act as models for exploring the solution behavior of minerals due to erosion and other natural occurrences. At the same time, these minerals can help to inform the development of new compounds with varying sizes and compositions. Thus, this knowledge can set the stage for new functional compounds inspired by nature.¹⁴

I.2. Group 13 elements as functional thin film precursors for materials applications

In the field of materials science Group 13 metals are utilized in semiconducting devices for transparent thin film transistors (TTFTs) with a multitude of electrical and optical applications.¹⁵ Gallium and indium are incorporated into multi-junction photovoltaic cells (InGaAs and InGaP).¹⁶⁻¹⁹ Other materials such as GaAs,²⁰ GaN,²¹⁻²⁵ and InGaN^{21,22} are used in a similar capacity as diodes.²⁶ Aluminum structures (e.g., AlGaAs) are featured in high-powered laser diodes, but overall aluminium is used to a lesser extent than gallium and indium which have band gap,

mobility, and on-off properties more favorable for high-performance semiconductors.²⁷⁻³¹

Thin films are traditionally fabricated using methods such as atomic layer deposition (ALD), chemical vapor deposition (CVD), and sputtering.³² Metals are deposited in their elemental form and as a result these techniques are highly effective for manufacturing dense materials. Solution processing is a production alternative that offers several advantages that include: 1) lower energy inputs compared to the high temperature and pressure requirements of deposition processes, 2) simple bench-top chemistry techniques, and 3) scalable manufacturing that is cost-effective and can lead to higher performance devices. Functional thin films are prepared by spin casting sol-gels of metal-organic precursors that are then pyrolyzed to their corresponding metal oxides. Unfortunately, thin films derived from these precursors often suffer from inhomogeneity and residual contamination by organics that, upon high-temperature processing, result in density and defect irregularities that negatively impact the performance of devices. Inorganic aqueous derivatives eliminate the need for organics and result in smooth, pinhole free films. The efficacy of this process was demonstrated by the fabrication of metal oxide TFTs from **f-Ga₁₃** and **f-Ga₇In₆** molecular precursors (Figure 1.2).³³ These compounds contain structural variabilities that can be used to study properties crucial for understanding and improving functional materials. As dynamic structures they also add diversity to the field of precursor chemistry, presenting new opportunities and unforeseen compositions for a wide variety of applications.

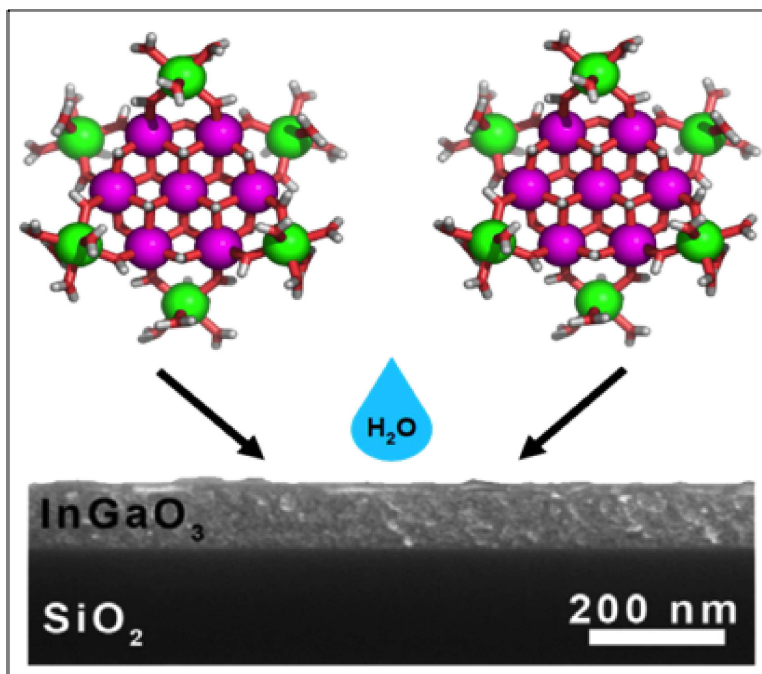


Figure 1.2. The process for transforming *f*-Ga₇In₆ in to a thin film. A solution of *f*-Ga₇In₆ (0.3M) in either 18mΩ water or methanol is spin-cast on to a thermal oxide substrate and annealed at 600 °C to form a metal oxide film.³³

I.3. Group 13 elements as dynamic oligomer assemblies

Synthesis of Group 13 compounds has advanced from serendipitous discovery to directed design.³⁴ Although these structures have been studied for over 50 years, the reported number of structures is limited.³⁵ Several methods have been implemented to drive this process under both organic and aqueous conditions. Exposure of reactions in organic solvents (i.e., sol-gels) to water promotes cluster formation via hydrolysis and in the absence of an organic solvent, solvothermal techniques lead to gels and polymers. The simplest reaction to consider is the hydrolysis of [Al(H₂O)₆]³⁺. Under basic aqueous conditions several hydroxo and

oxo-bridged species with varying solubility can form at OH/metal ion ratios between 1 to 2.5.³⁶ Below 1 only $[\text{Al}(\text{H}_2\text{O})_6]^{3+}$ is present and above 2.5 precipitation of polymeric hydroxides occurs. The complexity of this speciation is difficult to determine, especially in the context of traditional phase identification (Figure 1.3.).

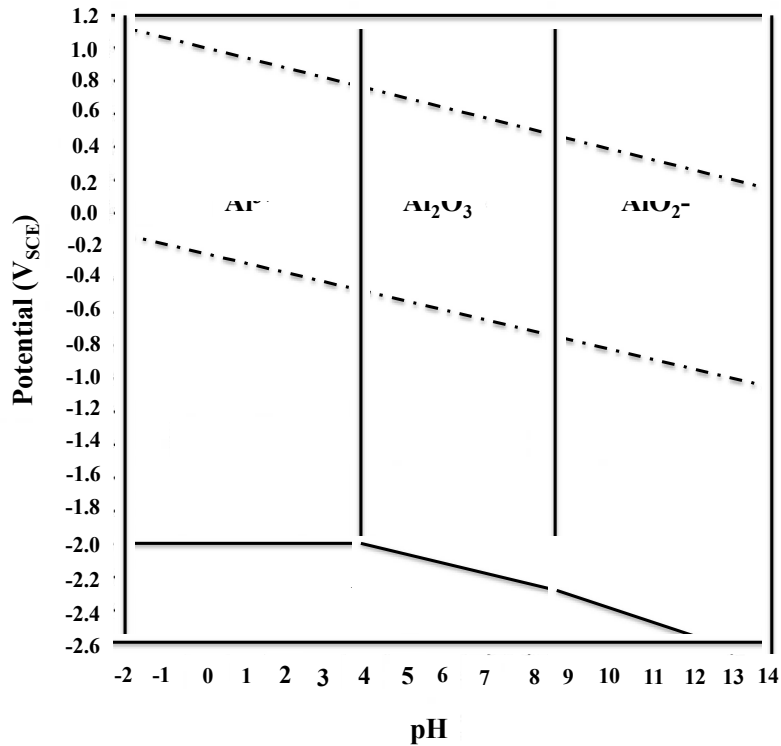


Figure 1.3. E-pH (Pourbaix) diagram for the equilibrium phases of aluminum in aqueous conditions. Predominant ion boundaries are shown with solid lines. Dotted lines demarcate the regions in which water oxidation and reduction occur at the anode and cathode, respectively. (**Top**): In the upper region, water is oxidized to O₂. (**Middle**): Water is stable and no decomposition occurs. (**Bottom**): In the lower region water is reduced to H₂.

E-pH (i.e., Pourbaix) diagrams map the equilibrium states in an electrochemical aqueous system. Aluminum has four distinct phases, however it is clear from

experiments that within these phases there are species that exist at the edges of ion boundaries not yet accounted for. The breadth of hydroxyl-bridged compounds has grown to include both ligand supported (*ligand* is defined as an organic molecule bound to metal and oxygen atoms within a structure) and non-ligand supported (termed *inorganic* with metal atoms bridged by H₂O, OH, and/or O linking moieties) species of varying composition, structure and size. For octahedral-coordinated metal ions, structures grow in a routine pattern similar to brucite lattices (Figure 1.4).³⁷ The first isolable inorganic structure of this kind was the dimer [Al₂(OH)₂(H₂O)₈](SO₄)₂·2H₂O (**Al**₂) species (also isolated with (SeO₄)₂ counteranion).^{38,39} Other inorganic species include (**Al**₄),⁴⁰ (**Al**₈),⁴¹ (*f*-**Al**₁₃),^{42,43} (**Al**₃₀),^{44,45} (*f*-**Ga**₁₃),¹ (**Ga**₃₂),⁴⁶ and *f*-**M**_{13-x}**In**_x (M = Al or Ga) heterometallic tridecamers.^{47,48} Organic ligand-supported compounds include (**Al**₂),^{39,49} (**Al**₁₂),⁴⁹ (*f*-**Al**₁₅),⁵⁰ (**Al**₃₀),⁴⁹ (**Ga**₂),³⁷ (**Ga**₁₀),⁵¹ and (*f*-**Ga**₁₃).³⁷

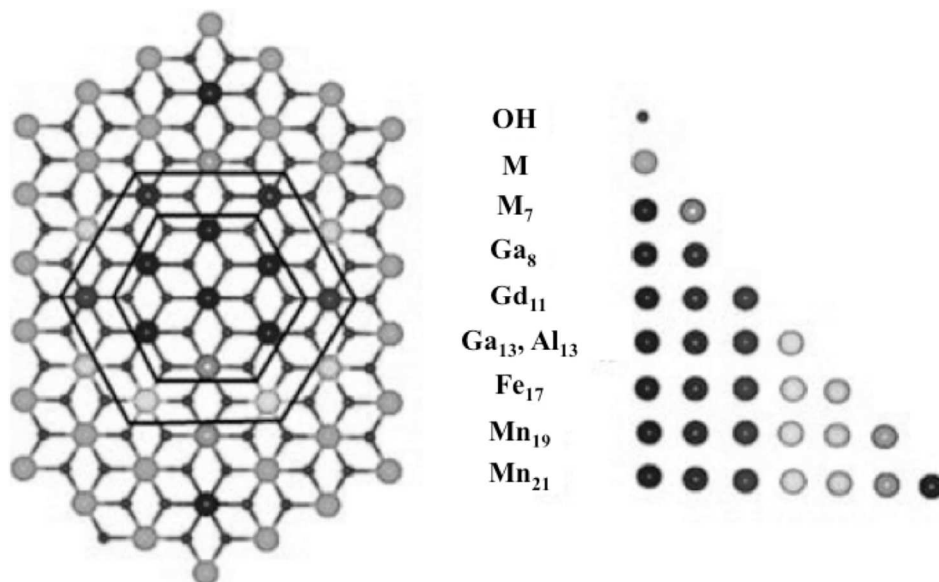
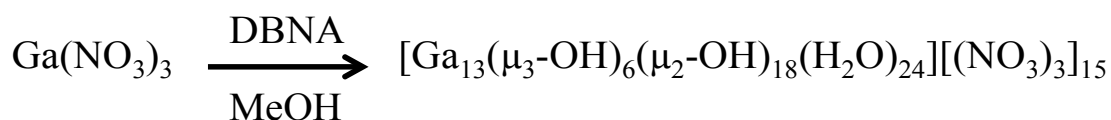


Figure 1.4. Brucite lattice diagramming growth of polynuclear species.³⁴

Particular attention has been paid to the $f\text{-M}_{13-x}\text{In}_x$ tridecamers (Scheme 1.1) for which the synthesis has improved as more sustainable and higher yielding procedures have been developed.^{52,53} Discovery of the dynamic nature of these compounds has prompted interest in understanding their reactivity and association behavior. A grasp of this fundamental information can help in predicting and accessing new structures with new elements from the periodic table.

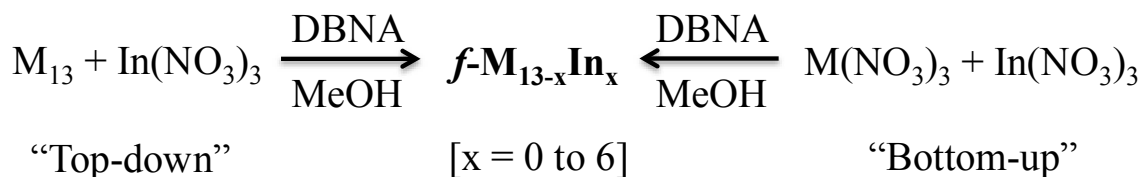


Scheme 1.1. Reaction sequence for the synthesis of $f\text{-Ga}_{13}$. $f\text{-Al}_{13}$ can be produced in the same manner with the addition of base in order to aid the hydrolysis of $\text{Al}(\text{NO}_3)_3$.

I.4. Solution dynamics of Group 13 tridecamers

Honing in on the dynamics of M_{13} tridecamers in solution - in particular the growth mechanism and stability of these discrete species in various chemical environments - has directed research in recent years. Much of the structural and compositional characteristics of these Group 13 compounds as crystalline solids and thin film metal oxides have been determined, but there is a gap in knowledge regarding their solution speciation, i.e. whether the tridecamers remain intact in solution or dissociate; and if so, to what extent. Understanding the possible degrees of speciation can provide insight into how these compounds form. For the specific example of heterometallic tridecamers, In^{3+} can be added to a solution of M_{13} and substitute into the exterior ring of the cluster through exchange routes (Scheme

1.2, and the subject of Chapter II). This “top-down” approach facilitates the same results as the standard “bottom-up” method.⁴⁸ Simultaneously this leads to several questions regarding the dynamic nature of these tridecamers.



Scheme 1.2. Mixed-metal synthesis of $f\text{-M}_{13-x}\text{In}_x$ tridecamers from a solution containing $\text{In}(\text{NO}_3)_3$ and $f\text{-M}_{13}$, where $\text{M} = \text{Al}$ or Ga .

Site-specific substitutions suggest an inherent stability of the M_7 core in solution. Extended X-ray absorption fine structure (EXAFS) analysis has been used to determine several solid and solution parameters with respect to the central metal atom of the tridecamer: the distances between neighboring atoms, the number of neighboring atoms, and changes in atom coordination.⁵⁴ Preliminary R space data (Figure 1.5) shows short-range similarities between the Ga_{13} structure in the crystal (red trace) and solution (blue trace) phases at 2.5Å and 3.3Å. In this range there is no similarity between either trace and $\text{Ga}(\text{NO}_3)_3$ in water (green trace) lending support to an inherent stability. Although EXAFS analysis has yet to be pursued further, these initial findings help to corroborate newfound knowledge regarding the dynamic behavior of these tridecamers.

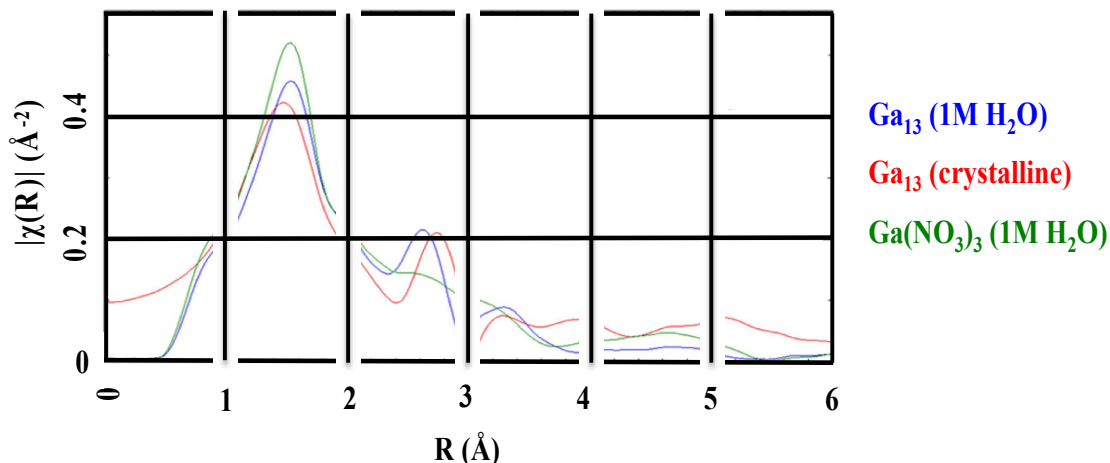


Figure 1.5. EXAFS data for the $f\text{-Ga}_{13}$ cluster in solution (blue), crystal form (red), and $\text{Ga}(\text{NO}_3)_3$ in solution (green) in R space.

I.5. Characterization of Group 13 tridecamers

An array of techniques including Nuclear Magnetic Resonance spectroscopy (NMR), Diffusion Ordered Spectroscopy (DOSY), Dynamic Light Scattering (DLS), Raman Spectroscopy, and Small Angle X-ray Spectroscopy (SAXS) provide complementary information about the structure and size of Group 13 tridecamers.⁵⁵ These characterization methods will be especially valuable for future exploration of the effect various conditions (e.g., pH, ion concentration, etc.) have on oligomer stability, reactivity, and subsequently, film properties. Each technique is described as it pertains to the characterization of $[\text{M}_{13-x}\text{In}_x(\mu_3\text{-OH})_6(\mu_2\text{-OH})_{18}(\text{H}_2\text{O})_{24}]^{15+}$ compounds.

1.5.1. 1-Dimensional Nuclear Magnetic Resonance spectroscopy

Nuclear Magnetic Resonance (NMR) utilizes the magnetic properties of atomic nuclei resonating at characteristic frequencies to ascertain how atoms within a molecule are bonded to one another, thus making it a powerful tool for structural analysis that is on par with X-ray diffraction (XRD). The chemical shifts of the nuclei resonances are influenced by properties including molecular geometry and the electronegativity of nearby atoms. This analytical information is proving valuable in inorganic chemistry and can be used to determine more detailed structural features of molecules.⁵⁶⁻⁶³

The important function of NMR spectroscopy in the study of aqueous hydroxo-aquo cations is the identification of the different local environments associated with each atom in the structure. Solution ¹H-NMR is a valuable technique that can be used in tandem with χ nuclei NMR for an additional level of analysis, particularly as the nuances of these molecules can be understood with solution NMR spectroscopy. There is a complexity due to ¹H exchange, ligand exchange, solvent exchange, and speciation in solution that arises. However, the ability to distinguish between local environments can help in assigning the resonances observed in the ¹H spectrum to protons on the tridecamer.

1.5.2. Solid-State Nuclear Magnetic Resonance spectroscopy

Solid state NMR has been used to map the local environments of the metal atoms within Group 13 clusters and identify specific crystallite species within the solid material that are more difficult to identify in solution. Previous work has employed ^{27}Al , $^{69/71}\text{Ga}$, and ^{17}O -NMR spectroscopy to investigate the structural features of Keggin- Al_{13} and Ga_{13} oxo-hydroxo cations as well as other ionic moieties both in the solid and solution states.^{64–66} The quadrupolar nature of Al and Ga nuclei (Table 1.4) leads to line broadening and has previously limited the assignments of gallium metal sites to simply monomeric vs. polymeric speciation and more specifically the coordination geometry of aluminum metal sites.^{67–69} The commercial availability of more sensitive spectrometers makes line broadening less of an issue. Recently more advanced solid-state NMR methods have been used to study Al_{13} and Ga_{13} hydroxo-aquo cations.⁷⁰ This study combined the coordination geometry analysis of Raman with ^{27}Al and $^{69/71}\text{Ga}$ nuclei NMR observations, crystal structure determination, and computational analysis to provide an all-encompassing understanding of the $f\text{-Al}_{13}$ structure. From this we have gained information about the M^{3+} sites within these tridecamers and are now interested in information regarding the coordinating hydroxide and aquo groups.

Table 1.4. Properties of various atomic nuclei for NMR spectroscopy. Relative frequency calculated at the 600 MHz.

| Nuclei | Abundance (%) | Spin | Rel. Freq. (MHz) | Rel. Sensitivity (vs. ^1H) | Magnetogyric ratio, γ ($10^7 \text{ rad T}^{-1} \text{ s}^{-1}$) |
|-------------------|---------------|------|------------------|--------------------------------------|---|
| ^1H | 99.99 | 1/2 | 600.0 | 1.00 | 26.75 |
| ^{17}O | 0.037 | 5/2 | 75.3 | 1.1×10^{-5} | -3.63 |
| ^{27}Al | 100 | 5/2 | 156.6 | 0.21 | 6.97 |
| ^{69}Ga | 60.4 | 3/2 | 144.0 | 0.004 | 6.70 |
| ^{71}Ga | 39.6 | 3/2 | 183.6 | 0.057 | 8.18 |
| ^{115}In | 95.7 | 9/2 | 132.0 | 0.33 | 5.90 |
| ^{113}In | 4.3 | 9/2 | 132.0 | 0.0015 | 5.89 |

1.5.3. 2-Dimensional Nuclear Magnetic Resonance spectroscopy

Two-dimensional NMR introduces a second frequency measurement in to experiments and is invaluable for mapping multiple structural relationships simultaneously. Pulse Field Gradient (PFG) Nuclear Magnetic Resonance (NMR) spectroscopy is one such technique that is used to determine the size of molecules in solution. The process, known as Diffusion Ordered Spectroscopy (DOSY), can be used to measure several physical parameters related to a specific molecule

including size, shape, host/guest encapsulation, and hydrogen bonding. DOSY can also be used for characterizing individual species found in synthetic mixtures. The diffusion coefficient (D) is determined experimentally using the Stokes-Einstein equation (Figure 1.6).⁷¹

$$D = \frac{kT}{6\pi\eta R_h}$$

Figure 1.6. Stokes-Einstein equation where k is the Boltzmann constant, T is temperature, η is solvent viscosity, and R_h is the hydrodynamic radius. The integer constant in the denominator, 6, is used under the assumption that the molecule is spherical.

DOSY maps chemical shift on the horizontal axis against diffusion coefficient on the vertical axis. Peaks with equivalent diffusion coefficients are related to species with similar hydrodynamic radii. This technique has become important in our quest to understand the solution behavior of these tridecameric species. In fact, 2D NMR spectroscopy now opens the door to more elaborate experiments (e.g., NOESY, ROESY, EXSY) that can yield additional information about bonding and exchange motifs within the tridecamers using cross and through-space coupling data.

1.5.4. Dynamic light scattering

DLS can be used to determine the size distribution profile of small particles, polymers, and proteins in solution. Since DLS measures fluctuations in scattered light intensity due to diffusing particles, the diffusion coefficient of the particles can be determined making this a corroborative technique with DOSY. DLS measurements are not impacted by solvent exchange phenomena the way NMR is, therefore it is easier to perform aqueous studies.

1.5.5. Raman spectroscopy

Raman spectroscopy is commonly used to acquire vibrational information that is specific to the chemical bonds and symmetry of molecules. Some vibrational modes are Raman active as opposed to IR active and this is particularly useful for observing M-O modes that are at the lower limits of IR detection.⁷² Vibrational bending and stretching modes are unique for each atom and are fingerprints by which tridecamers can be identified.

1.5.6. Small-angle X-ray scattering

The elastic scattering of X-rays at very low angles ($0.1 - 10^\circ$) provides information about the shape and size of molecules, polydispersity, pore sizes, and other properties. SAXS has been used to examine **K-Ga₁₃**,⁵⁴ the *in-situ* formation of Al species,⁷³ and recently SAXS has been used to monitor the formation of heterometallic tridecamers in solution.

I.6. Conclusions

This thesis presents the full scope of the synthesis and characterization of Group 13 tridecamers beginning with the full synthetic and structural information for $f\text{-Ga}_{13-x}\text{In}_x$ ($x = 0-6$) heterometallic compounds detailed in Chapter II, which was submitted to *Inorg. Chem.* (co-authors: Z.L. Mensinger, D.B. Fast, J.T. Gatlin, M.R. Dolgos, L.N. Zakharov, and D.W. Johnson). Additional solid-state characterization is presented in Chapter III as solid state NMR (SSMNR) is used to identify differences in the metal atom environments for $f\text{-Ga}_{13}$ (published in *Chem. Mater.*, co-authors: Z.L. Ma, B.A. Hammann, K.M. Wentz, I-Y. Chang, P.H-Y. Cheong, D.W. Johnson, V.V. Terskikh, and S.E. Hayes). The dynamics of Group 13 tridecamers is presented briefly in Chapter IV with the synthesis of $f\text{-Al}_{13-x}\text{In}_x$, which was published in *Inorg. Chem.* (co-authors: M.N. Jackson, Jr., Z.L. Mensinger, L.N. Zakharov, and D.W. Johnson). The exchange kinetics for $f\text{-Al}_{13}$ protons is summarized in Chapter V for comparison to the Keggin- Al_{13} (co-authors: M.N. Jackson, Jr., D.W. Zheng, C.A. Colla, W.H. Casey, and D.W. Johnson), which has significant environmental relevance. The first steps towards transition metal precursors are described in Chapter VI (submitted To *Acta. Cryst. C.*, co-authors: M.N. Jackson, Jr., L.N. Zakharov, and D.W. Johnson) and continued on in to Chapter VII along with future work for the characterization of more familiar precursors.

I.7. Bridge to Chapter II

Characterization of Group 13 tridecamers begins with the complete collection of single-crystal data for the ***f*-Ga_{13-x}In_x** structures. The synthesis of these compounds is detailed and variations between each structure are explored in a discussion of the transformation of these compounds to metal oxides.

CHAPTER II

SYNTHESIS AND SOLID-STATE STRUCTURAL CHARACTERIZATION OF A SERIES OF AQUEOUS HETEROMETALLIC TRIDECAMERIC GROUP 13 CLUSTERS

Drs. Jason T. Gatlin and Zachary L. Mensinger (previously of University of Oregon) developed the synthetic procedures outlined in this chapter. Dr. Mensinger was also responsible for drafting the original version of the manuscript, from which this chapter is adapted, prior to new data collection and concept restructuring. Dylan B. Fast (Oregon State University) performed the variable temperature powder XRD experiments, analyzed the data with Pawley fits and Reitveld refinement, and contributed to writing the corresponding sections of the manuscript. Dr. Lev N. Zakharov (University of Oregon) collected all single-crystal X-ray data and wrote the corresponding sections of the manuscript. Professors Dr. Darren W. Johnson and Dr. Michelle R. Dolgos (Oregon State University) were the principle investigators who oversaw this work and were integrally involved in both manuscript editing and concept. I synthesized the f - Ga_{13} and f - $\text{Ga}_{13-x}\text{In}_x$ tridecamers used for the single-crystal and variable

temperature powder XRD experiments. I also drafted the final version of the manuscript that was recently submitted to the journal Inorganic Chemistry. This chapter has been expanded from the submitted manuscript to include additional variable temperature powder XRD results which are available as supplemental information to the manuscript.

II.1. Introduction

The Group 13 metals, specifically aluminium, gallium, and indium, exhibit unique hydrolytic and condensation behavior in solution as a dynamic, pH-dependent series of structures that range from hydrated monomers to bridged hydroxide oligomers to oxides.^{33,37,39,41,43,46,53,63,74–78} For decades cationic aluminum species have received attention because of their environmental importance as flocculants and coagulants for the transport of heavy metals as well as their toxicity to plants and aquatic organisms.^{9,42,79–83} Corresponding gallium nanoclusters have received less attention, although several discrete Group 13 metal hydroxo/aquo structures have been successfully isolated and structurally characterized.^{1,33,37,46} The hydrolysis products of three different starting metal salts that produce ***f*-Ga₁₃**,¹ ***f*-Al₁₃**,^{43,53} and the heterometallic ***f*-Ga₇In₆**³³ were previously reported and are designated by the symbol “***f***”, (aka, flat) to differentiate them from the more widely studied Al₁₃ Keggin structures (***κ*-Al₁₃**).^{10,11,63,65,84,85} For the remainder of this chapter a specific “flat” cluster will be identified by its metal content, i.e., Ga₁₃(μ₃-OH)₆(μ-OH)₁₈(H₂O)₂₄(NO₃)₁₅ will be referred to as ***f*-Ga₁₃**.³⁵

Most preparations of Group 13 hydroxide structures have utilized organic supporting ligands to form stable clusters through charge balance and controlled hydrolysis.^{35,37,49,50,86,87} For example, aminocarboxylate ligands such as *N*-(2-hydroxyethyl)iminodiacetic acid (H₃heidi) have been used to synthesize ligand-supported versions of ***f*-Al₁₃** and ***f*-Ga₁₃**, as well as **Ga₂** and **Ga₈** intermediates.^{35,76,88,89} While many procedures exist to prepare such compounds, they do not enable large structural diversity owing to the aforementioned interplay of pH and charge balance; the isolation of only a few different structure types has occurred. As a result, a general synthetic strategy with variable outputs is highly desirable. Furthermore, organic supporting ligands can lead to defects and impurities when these clusters are used as materials precursors (inks), thus limiting their utility for bulk and thin-film oxides.

Until recently Group 13 heterometallic (**M,M'**)₁₃ clusters have been notably absent in the families of ligand-supported and purely inorganic **M₁₃** structures. The ***f*-Ga₇In₆** cluster, which was the first example of such an inorganic structure type, proved to be an effective single-source precursor for the preparation of a high-quality dense, smooth, and amorphous IGO thin film with a reported In_{0.92}Ga_{1.08}O₃ composition.⁹⁰ ***f*-Ga₇In₆** (in similar fashion to the previously reported ***f*-Ga₁₃** cluster) was synthesized by dissolving metal nitrate salts in methanol with an organic nitroso compound as an additive. Partial evaporation of these solutions at room temperature and open to air produced crystals within two weeks. Under slightly basic conditions (requiring the addition of NaOH, NH₄OH, or Al(OH)₃),

hydrated $\text{Al}(\text{NO}_3)_3$ forms the related $f\text{-Al}_{13}$ cluster with co-precipitation of other products.^{43,53}

As an extension to this previous work, a series of heterometallic $f\text{-Ga}_{13-x}\text{In}_x$ ($x = 1-6$) hydroxide structures (**1-6**) is presented (Figure 2.1).^{1,33} Published synthetic and structural details for $f\text{-Ga}_7\text{In}_6$ are included for comparison with the new heterometallic Ga/In clusters. This synthesis strategy provides facile tuning of the Ga:In ratio at the molecular level, providing a means by which to alter the properties of metal oxide thin films fabricated from these precursors.

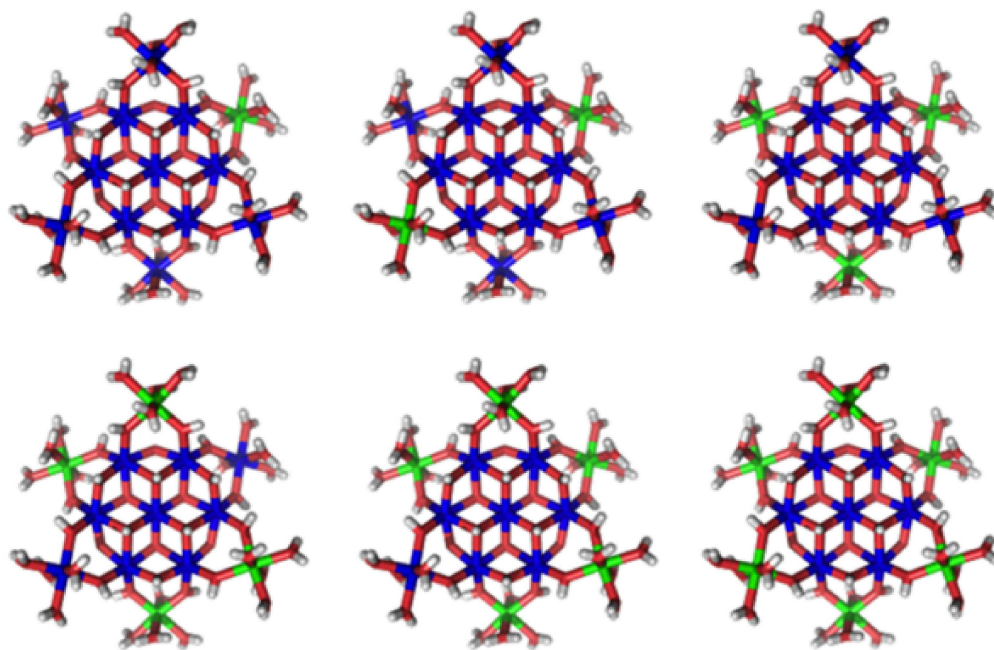


Figure 2.1. The $f\text{-Ga}_{13-x}\text{In}_x$ ($x=1-6$) heterometallic hydroxo-aquo clusters. Clockwise from the top right: $\text{Ga}_{12}\text{In}_1$ (**1**), $\text{Ga}_{11}\text{In}_2$ (**2**), $\text{Ga}_{10}\text{In}_3$ (**3**), Ga_9In_4 (**4**), Ga_8In_5 (**5**), and Ga_7In_6 (**6**). Gallium and indium metal ions are shown in blue and green, respectively. All six Ga/In positions in the outer ring are symmetrically equivalent. The x-ray structures show that only gallium atoms occupy the seven interior positions of each cluster, and gallium and indium atoms in the outer ring are disordered over all six positions rather than in specific locations.

II.2. Synthetic procedures for $f\text{-Ga}_{13-x}\text{In}_x$ clusters

$\text{Ga}(\text{NO}_3)_3$ and $\text{In}(\text{NO}_3)_3$ salt hydrates were dissolved in MeOH (10 mL). DBNA was added to this solution with a syringe; the solution was stirred uncapped and left undisturbed in air at room temperature. Within two weeks, most of the solvent evaporated and colorless, block-shaped single crystals of **1-6** formed at the bottom of the vial. DBNA was removed with a syringe and the product crystals were washed with acetone (yields range from 20-63%). The reagent ratios for clusters **1-6** are summarized in Table 2.1.

Table 2.1. Ratios of $\text{Ga}(\text{NO}_3)_3$, $\text{In}(\text{NO}_3)_3$, and DBNA for the heterometallic clusters **1-6**. The ratios of $\text{In}(\text{NO}_3)_3$ and DBNA are relative to the starting quantity of $\text{Ga}(\text{NO}_3)_3$.

| Structure | $\text{Ga}(\text{NO}_3)_3$ (g) | $\text{In}(\text{NO}_3)_3$ (g) | DBNA (mL) | Yield |
|--|--------------------------------|--------------------------------|-----------|------------------|
| $\text{Ga}_{12}\text{In}_1$ (1) | 0.250 | 0.059 | 0.8 | 20% |
| $\text{Ga}_{11}\text{In}_2$ (2) | 0.072 | 0.042 | 0.6 | 33% |
| $\text{Ga}_{10}\text{In}_3$ (3) | 0.250 | 0.252 | 0.6 | 62% |
| Ga_9In_4 (4) | 0.050 | 0.118 | 0.2 | 63% |
| Ga_8In_5 (5) | 0.050 | 0.323 | 0.4 | 35% |
| Ga_7In_6 (6) | 0.050 | 0.588 | 0.7 | 23% [§] |

[§] This synthesis also yields $f\text{-Al}_8\text{In}_5$ and $f\text{-Al}_9\text{In}_4$. NaOH is added to the solution of metal salts and DBNA (in MeOH).

II.3. Description of characterization methods

II.3.1. X-ray crystallography

Single crystal X-ray diffraction experiments were performed on a Bruker Smart Apex diffractometer at 153K and 173K using Mo $K\alpha$ radiation ($\lambda = 0.71073 \text{ \AA}$).

Absorption corrections were applied by SADABS.⁹¹ Data collection and structure refinement details are shown in Tables 2.2 and 2.3. Disordered NO₃⁻ anions and solvent molecules (H₂O and CH₃OH) were treated by SQUEEZE.⁹² Corrections provide a 601-679 electrons/cell range, which bracket the value (621) for the 36 disordered species in the full unit cell. Non-hydrogen atoms were refined with anisotropic thermal parameters (H atoms were not taken into consideration). All calculations were performed using the Bruker SHELXTL package.⁹³

Table 2.2. Crystal structure data for clusters **1-3** with fractional atom values.

| | 1 | 2 | 3 |
|---|---|---|---|
| empirical formula | C ₆ H ₉₆ Ga _{11.8} In _{1.2} N ₁₅ O ₉₉ | C ₆ H ₉₆ Ga _{10.4} In _{2.6} N ₁₅ O ₉₉ | C ₆ H ₉₆ Ga _{10.3} In _{2.7} N ₁₅ O ₉₉ |
| formula weight | 2923.38 | 2985.16 | 2990.57 |
| crystal system | Hexagonal | Hexagonal | Hexagonal |
| space group | R-3 | R-3 | R-3 |
| temp, K | 173 (2) | 173 (2) | 173 (2) |
| wavelength, Å | 0.71073 | 0.71073 | 0.71073 |
| a, Å | 20.1387(14) | 20.2946 (12) | 20.2925 (7) |
| b, Å | 20.1387(14) | 20.2946 (12) | 20.2925 (7) |
| c, Å | 18.490(3) | 18.456(2) | 18.4437 (12) |
| α, deg | 90 | 90 | 90 |
| β, deg | 90 | 90 | 90 |
| γ, deg | 120 | 120 | 120 |
| V, Å ³ | 6494.3(11) | 6583.2(9) | 6577.3(5) |
| Z | 3 | 3 | 3 |
| calcd density, g cm ⁻³ | 2.242 | 2.259 | 2.265 |
| abs coeff, mm ⁻¹ | 4.08 | 3.96 | 3.96 |
| F(000) | 4361 | 4435 | 4441 |
| θ range, deg | 2.5-28.2 | 2.5-28.2 | 2.5-28.2 |
| refls collected/unique | 13623/3412 [0.0317] | 13757/3460 [0.0217] | 13724/3464[0.0217] |
| refinement method | full matrix least squares on F ² | full matrix least squares on F ² | full matrix least squares on F ² |
| data/restraints/params | 3412/0/166 | 3460/0/166 | 3464/0/166 |
| GOF on F ² | 1.055 | 1.055 | 1.055 |
| final R indices [I > 2σ(I)] | R1 = 0.0328, wR2 = 0.0916 | R1 = 0.0337, wR2 = 0.0998 | R1 = 0.0249, wR2 = 0.0709 |
| R indices (all data) | R1 = 0.0372, wR2 = 0.0913 | R1 = 0.0371, wR2 = 0.1020 | R1 = 0.0273, wR2 = 0.0719 |
| largest diff peak and hole, e Å ⁻³ | 1.064 and -0.373 | 2.676 and -0.416 | 0.845 and -0.353 |

Table 2.3. Crystal structure data for clusters **4-6** with fractional atom values.

| | 4 | 5 | 6 |
|---|--|--|--|
| empirical formula | C ₆ H ₉₆ Ga _{9.1} In _{3.9} N ₁₅ O ₉₉ | C ₆ H ₉₆ Ga _{7.7} In _{5.3} N ₁₅ O ₉₉ | C ₆ H ₉₆ Ga ₇ In ₆ N ₁₅ O ₉₉ |
| formula weight | 3045.14 | 3106.47 | 3139.94 |
| crystal system | Hexagonal | Hexagonal | Hexagonal |
| space group | R-3 | R-3 | R-3 |
| temp, K | 173 (2) | 173 (2) | 173 (2) |
| wavelength, Å | 0.71073 | 0.71073 | 0.71073 |
| a, Å | 20.4329(10) | 20.6585 (9) | 20.6974 (14) |
| b, Å | 20.4329(10) | 20.6585 (9) | 20.6974 (14) |
| c, Å | 18.4080(18) | 18.2996(8) | 18.256 (3) |
| α, deg | 90 | 90 | 90 |
| β, deg | 90 | 90 | 90 |
| γ, deg | 120 | 120 | 120 |
| V, Å ³ | 6655.8(8) | 6763.5(5) | 6773(1) |
| Z | 3 | 3 | 3 |
| calcd density, g cm ⁻³ | 2.279 | 2.288 | 2.310 |
| abs coeff, mm ⁻¹ | 3.86 | 3.74 | 3.704 |
| F(000) | 4507 | 4580 | 4620 |
| θ range, deg | 2.5-28.2 | 2.5-28.0 | 2.5-27.0 |
| refls collected/unique | 14035/3500 [0.0176] | 15922/3642 [0.0560] | 16375/3290[0.0187] |
| refinement method | full matrix least squares on F ² | full matrix least squares on F ² | full matrix least squares on F ² |
| data/restraints/params | 3500/0/166 | 3642/0/166 | 3290/0/166 |
| GOF on F ² | 1.034 | 1.082 | 1.102 |
| final R indices [I > 2σ(I)] | R1 = 0.0237, wR2 = 0.0698 | R1 = 0.0370, wR2 = 0.0961 | R1 = 0.0246, wR2 = 0.0721 |
| R indices (all data) | R1 = 0.0253, wR2 = 0.0715 | R1 = 0.0444, wR2 = 0.0997 | R1 = 0.0256, wR2 = 0.0727 |
| largest diff peak and hole, e Å ⁻³ | 0.864 and -0.352 | 0.990 and -0.989 | 1.034 and -0.406 |

II.3.2. Variable temperature powder X-ray diffraction

Powder XRD data were collected for all cluster compositions (**f-Ga13** and **1-6**) on a Rigaku Ultima with a Cu Kα source (1.54 Å); 2θ = 5-60° at 0.5 °/min. Ex-situ heating was used to study the transformation from cluster to metal oxide. **f-Ga13** was measured after heating to set temperatures of 250 °C, 600 °C, 800 °C, 900 °C, 1000 °C and 1100 °C for 4 hours at a 10 °C /min ramp rate. Clusters **1-6** were

heated to the same temperatures as well as 1200 °C under the same conditions.⁹⁴ Topas Academic was used to perform Pawley fits to monitor changes to the phase and lattice parameters, and Reitveld refinements to monitor the indium occupancy in octahedral and tetrahedral sites.

II.3.3. Bulk sample analysis

Electron probe microanalysis (EPMA) measurements were carried out on a CAMECA SX50 Electron Microprobe. Desert Analytics conducted elemental analysis (EA) of bulk samples.

II.4. Determining synthetic parameters for heterometallic tridecamers

In early efforts to synthesize the series of ***f*-Ga_{13-x}In_x** heterometallic clusters, the ratio of metal atoms in the target compound was used to inform the starting ratio of Ga(NO₃)₃ to In(NO₃)₃. Single crystal XRD data of the initial attempt to form ***f*-Ga₇In₆** using a 7:6 ratio of Ga(NO₃)₃:In(NO₃)₃ resulted in ***f*-Ga₁₀In₃** forming instead. Subsequently, ***f*-Ga₇In₆** was successfully prepared by using a 1:12 ratio of Ga(NO₃)₃:In(NO₃)₃ (or a 1:10 ratio as shown in Table 2.1).³³ The excess of In(NO₃)₃ required to produce the desired product suggested a solubility of In(NO₃)₃ greater than that of Ga(NO₃)₃ in DBNA. A graph of the total gallium and indium content in these two Ga/In heterometallic clusters and ***f*-Ga₁₃** versus the equivalents of Ga(NO₃)₃ and In(NO₃)₃ used, provides a linear relationship that was then used as a guide to predict the ratio of starting materials required for the remaining Ga/In structures (Figure 2.2).

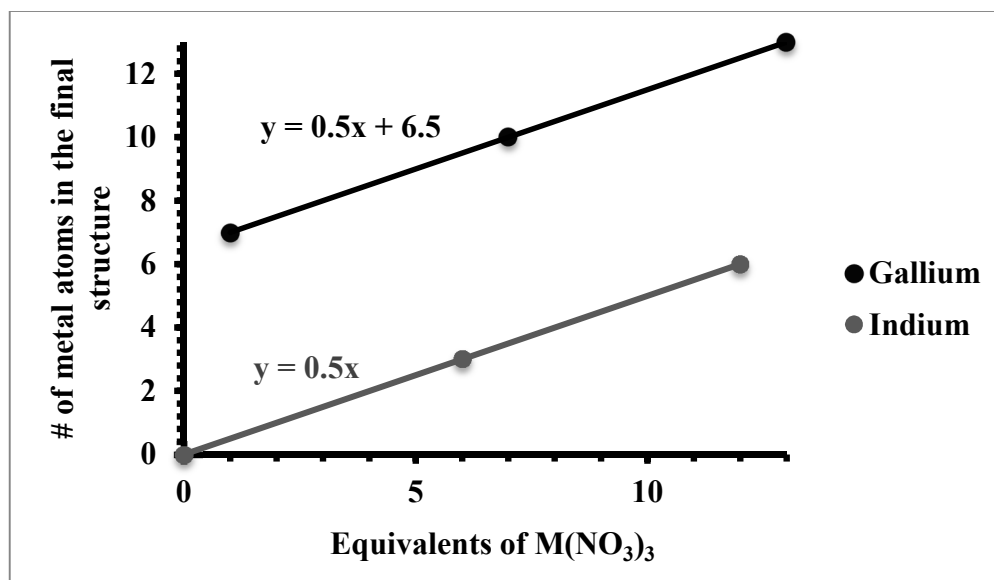


Figure 2.2. Plot of the relationships between the equivalents of $Ga(NO_3)_3$ and $In(NO_3)_3$ required to form $f-Ga_{13-x}In_x$ heterometallic clusters and the number of gallium and indium ions in the final structure. For example, to form $f-Ga_{10}In_3$, 7 equivalents of $Ga(NO_3)_3$ must be used (value read for Ga = 10 on y-axis) while 6 equivalents of $In(NO_3)_3$ are required (value read for In = 3 on y-axis).

This simple approach worked well and the resulting starting ratios of $Ga(NO_3)_3$ and $In(NO_3)_3$ required to form $f-Ga_{12}In_1$, $f-Ga_{11}In_2$, $f-Ga_9In_4$, and $f-Ga_8In_5$ were found to be 5:1, 2:1, 1:2, and 2:11, respectively. The final Ga/In ratio for each cluster was determined by a single crystal X-ray structure and refinement model with the gallium and indium atoms sharing the same position. EA and EPMA were used to confirm the metal ratios for bulk samples of several clusters with different indium substitutions (Table 2.4). The combination of both techniques resulted in metal atom ratios within error of those obtained from single crystal XRD. A high degree of control over composition within heterometallic clusters has seldom been

observed; thus these clusters represent a simple way to control product ratios using the starting salt stoichiometry as the primary variable.⁹⁵

Table 2.4. Single crystal XRD, EA, and EPMA metal ratio results for **1**, **3**, **4**, and **6**. Standard deviations from EA and EPMA are shown in parentheses.

| | Starting ratio | XRD | EA | EPMA |
|--------------------------------------|----------------|-------|-------------------------|--------------------|
| | Ga:In | Ga:In | Ga:In | Ga:In |
| Ga₁₂In₁ | 5:1 | 12:1 | 11.75(0.02):1.3(0.3) | 11.8(0.1):1.2(0.1) |
| Ga₁₀In₃ | 7:6 | 10:3 | 10.41(0.04):2.6(0.1) | 11.0(0.1):2.0(0.1) |
| Ga₉In₄ | 2:1 | 9:4 | 8.921(0.009):4.08(0.02) | 9.5(0.1):3.5(0.1) |
| Ga₇In₆ | 1:12 | 7:6 | 6.31(0.05):6.69(0.04) | 6.5(0.9):6.5(0.9) |

II.5. Single crystal X-ray structures analysis for 1-6

Characterization of **1-6** by single-crystal XRD reveals structures similar to that of the previously reported *f*-Ga₁₃.¹ Three different distorted octahedral metal coordination environments (**M1**: core, **M2**: middle ring, **M3**: outer ring; Figure 2.3) are observed in these compounds.

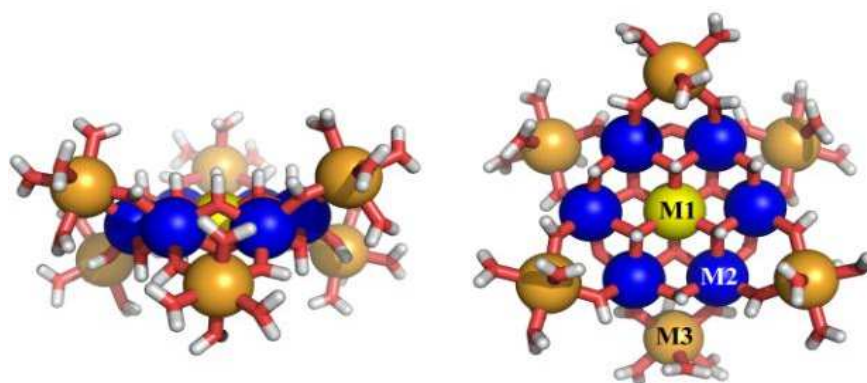


Figure 2.3. Side (left) and front (right) view of the three different coordination environments for the metal ion sites of **1-6**: **M1** (core; yellow), **M2** (middle; blue), and **M3** (outer; bronze).

All structures feature a rigid planar core of seven gallium atoms (**M1** and **M2**).¹ The six outer ring metal ions (**M3**) are bound to the planar core by μ -OH bridges and alternate above and below the plane of said core; each metal ion fills its remaining coordination sites with four water molecules. All compounds are isostructural and have a space group of symmetry *R*-3. All crystal structures are comprised of a $[(\text{Ga}_7)\text{In}_x\text{Ga}_{6-x}(\text{OH})_{24}(\text{H}_2\text{O})_{24}]^{15+}$ ($x = 0-6$) cation located on a $\bar{3}$ axis. Three nitrate (NO_3^-) anions are in general positions; two form H-bonds with the *f*-**M13** cation while the third is disordered and shares six other possible positions around the cation with solvent molecules. Thus the *f*-**M13** cation in the crystal structure is surrounded by fifteen NO_3^- anions and nine solvent molecules (six methanol and three water molecules) forming H-bonds with $-\text{OH}$ groups and terminal water molecules bound to the metal ions in the outer ring. Solvent molecules sharing positions with the NO_3^- anion are disordered as well. All structures contain two nearby positions occupied by disordered solvent molecules (water or methanol) in a 1:1 ratio. In all clusters observed so far refinements of occupation factors of the metal ions in the planar M_7 core are close to 1, meaning there is no disorder; therefore, only gallium ions occupy these positions. The observed Ga-O (1.926 - 1.963 Å) distances are typical for these bonds also indicating that gallium occupies all seven positions. The refined occupation factor of the metal ions in the outer ring of **1-6** is intermediate between that corresponding to gallium and indium ions. The M-OH and M-OH₂ distances found in these structures are in the range between the shorter Ga -O and longer In-O distances and depend on the Ga/In ratio for the metal ions in the outer ring. The

unit cell volumes that increase from 6494 \AA^3 ($f\text{-Ga}_{13}$) to 6773 \AA^3 ($f\text{-Ga}_7\text{In}_6$) help to approximate the level of substitution as more indium atoms are incorporated into the outer ring of each structure.

The number of indium ions in the **M3** ring is determined by refinement of occupation factors for the gallium and indium atoms sharing these positions. The refinement of occupation factors provides partial atom values for gallium and indium stoichiometries (for example $f\text{-Ga}_{10.3}\text{In}_{2.7}$ vs. $f\text{-Ga}_{10}\text{In}_3$). All six Ga/In positions in the **M3** ring are symmetrically equivalent. The gallium and indium ions appear to be randomly distributed over the six positions and their precise location in the clusters cannot be determined. For example, there are three potential arrangements for **M3** indium ions in $f\text{-Ga}_{10}\text{In}_3$ (Figure 2.4).

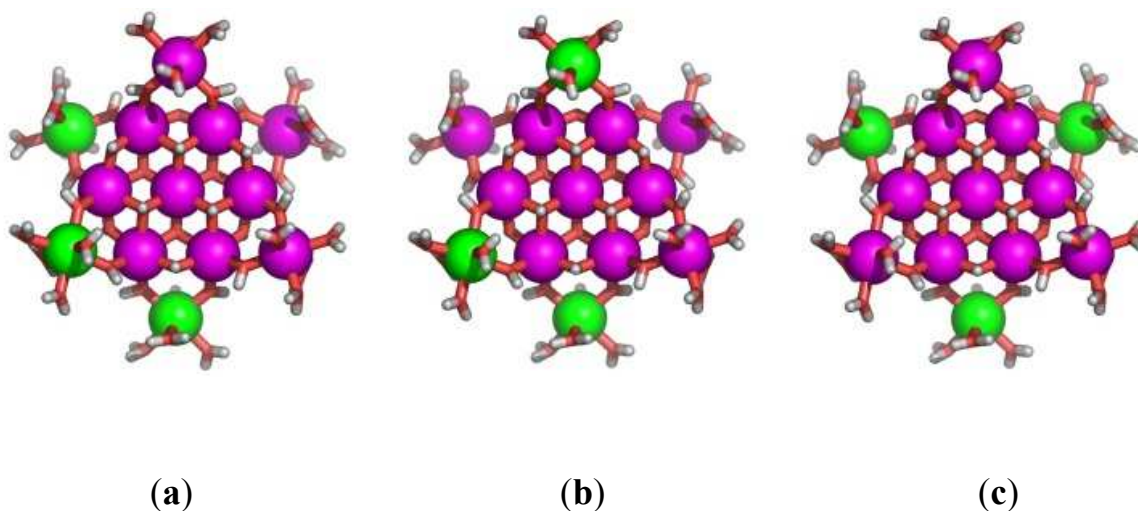


Figure 2.4. Potential arrangements of indium atoms in the outer ring of $f\text{-Ga}_{10}\text{In}_3$.

Structure (c) in Figure 2.4 is the most reasonable arrangement; it is the most symmetric structure, and it affords the most space between indium ions (ionic radius (r): Ga = 62 pm, In = 80 pm).⁹⁶ In this case, the cluster would be rotationally disordered and result in a structure with partial value stoichiometries. It cannot be ruled out from single crystal XRD that the observed single crystal structures are mixtures of clusters with different stoichiometries (e.g., **f-Ga₁₀In₃** = 50% **f-Ga₇In₆** + 50% **f-Ga₁₃**) rather than a mixture of disordered heterometallic cluster isomers. It is important to note, however that regardless of the make-up of the crystals according to crystallographic analysis, the atomic makeup of the final product can be tuned and confirmed by other methods. However, powder XRD data reported below suggest that all six heterometallic clusters are distinct species, and a recent complete structural solution of these clusters by ¹H NMR spectroscopy confirms that each cluster is a distinct species in wet DMSO.⁹⁷

II.6. Conversion of clusters to oxides

One of the primary applications for these clusters is as precursors/inks for metal oxide thin films. Experiments were carried out to determine the types of oxides formed from the decomposition of these clusters with heating. Products were identified and compared to known gallium/indium oxides.^{8,98} The dehydration of **f-Ga₁₃** produces a white amorphous solid that persists up to just above 600 °C (Figure 2.5) at which point a reflection for monoclinic gallium oxide (β -Ga₂O₃) emerges. Above 600 °C additional Bragg peaks appear and continue to sharpen up to 1100 °C.

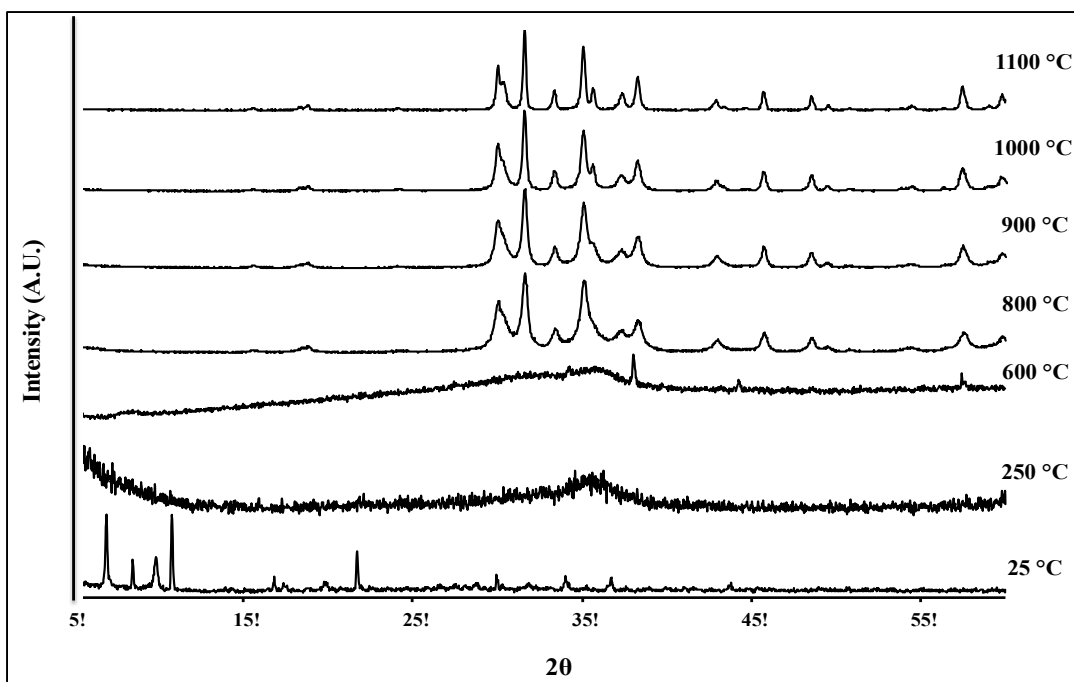


Figure 2.5. Powder XRD traces for a bulk sample of *f*-Ga₁₃ heated at specified temperatures.

In general the decomposition behaviors of **1-6** differ from what is observed for *f*-Ga₁₃ (Figure 2.6). Peaks for **2-5** are also visible at 600 °C while *f*-Ga₁₃ and **1** are predominantly amorphous at this temperature. In fact the mixed-metal clusters show reflections arising at lower temperatures than for *f*-Ga₁₃. By 900 °C reflections for the β-Ga₂O₃ structure type begin to appear for all clusters shift to smaller 2θ values for the mixed-metal structures relative to the standard β-Ga₂O₃ pattern due to expansion of the lattice by larger indium ions.

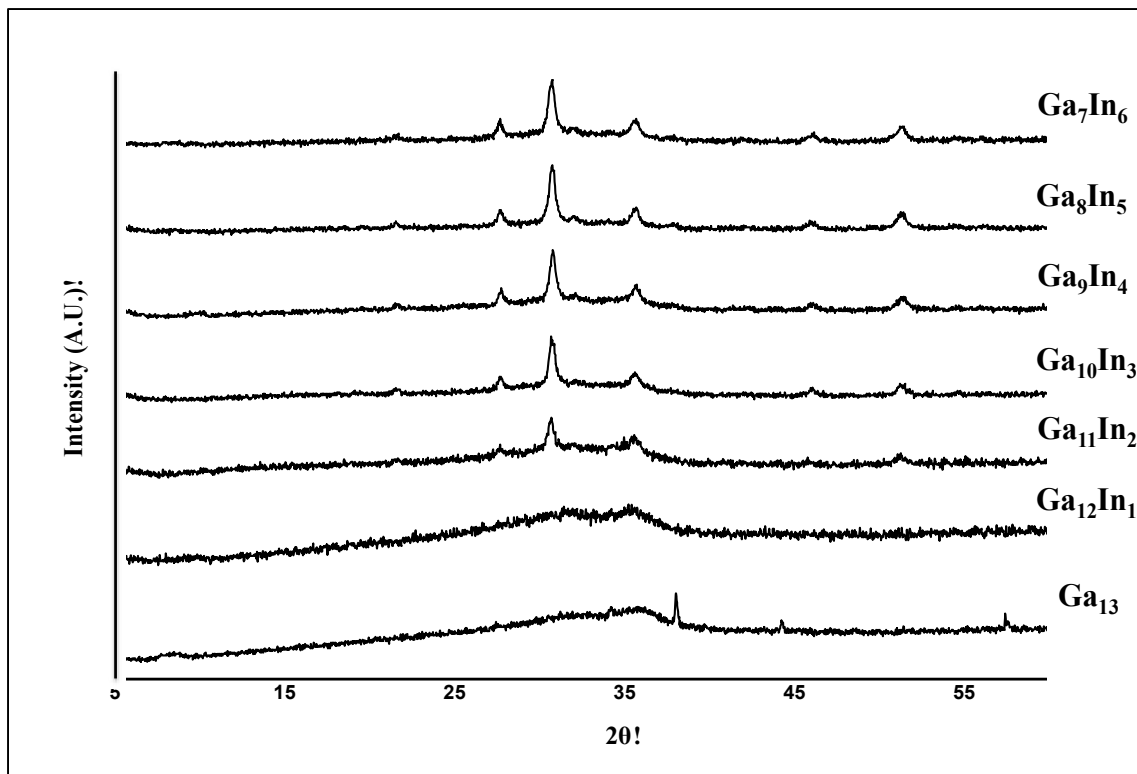


Figure 2.6. Powder XRD traces for bulk samples of *f*-Ga₁₃ and 1-6 at 600 °C.

f-Ga₁₁In₂ (Figure 2.7) most closely resembles *f*-Ga₁₂In₁ although it follows a decomposition path of its own. At 250 °C two peaks associated with β-Ga₂O₃ are visible although the product is primarily amorphous. These peaks become more prominent with increasing temperatures up to 900 °C at which point more β-Ga₂O₃ reflections appear. At 1000 °C this crystalline oxide is fully realized with a shift to lower 2θ values because of the presence of indium in the structure.

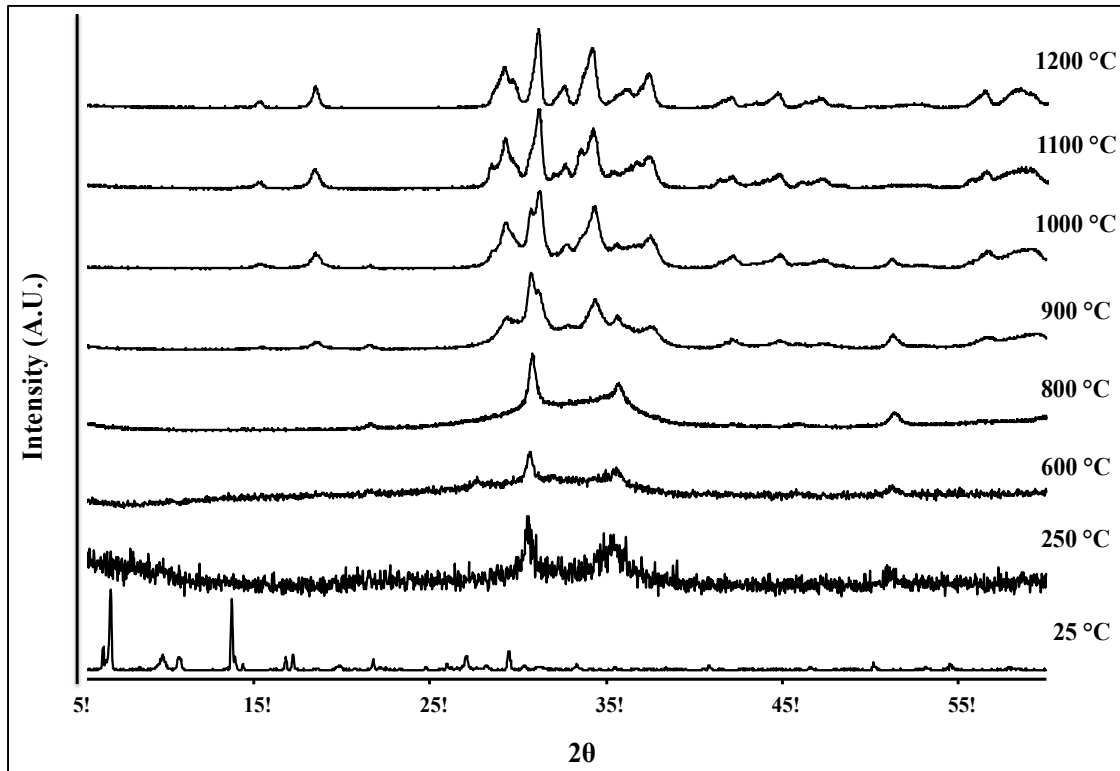


Figure 2.7. Powder XRD traces for a bulk sample of $f\text{-Ga}_{11}\text{In}_2$ heated at specified temperatures.

$f\text{-Ga}_{10}\text{In}_3$ (Figure 2.8) and $f\text{-Ga}_9\text{In}_4$ experience similar thermal transformations upon heating. For both compounds Bragg peaks for $\beta\text{-Ga}_2\text{O}_3$ are visible at temperatures as low as 250 °C. At 1100 °C the remaining Bragg peaks for $\beta\text{-Ga}_2\text{O}_3$ sharpen and the powders become completely crystalline at 1200 °C.

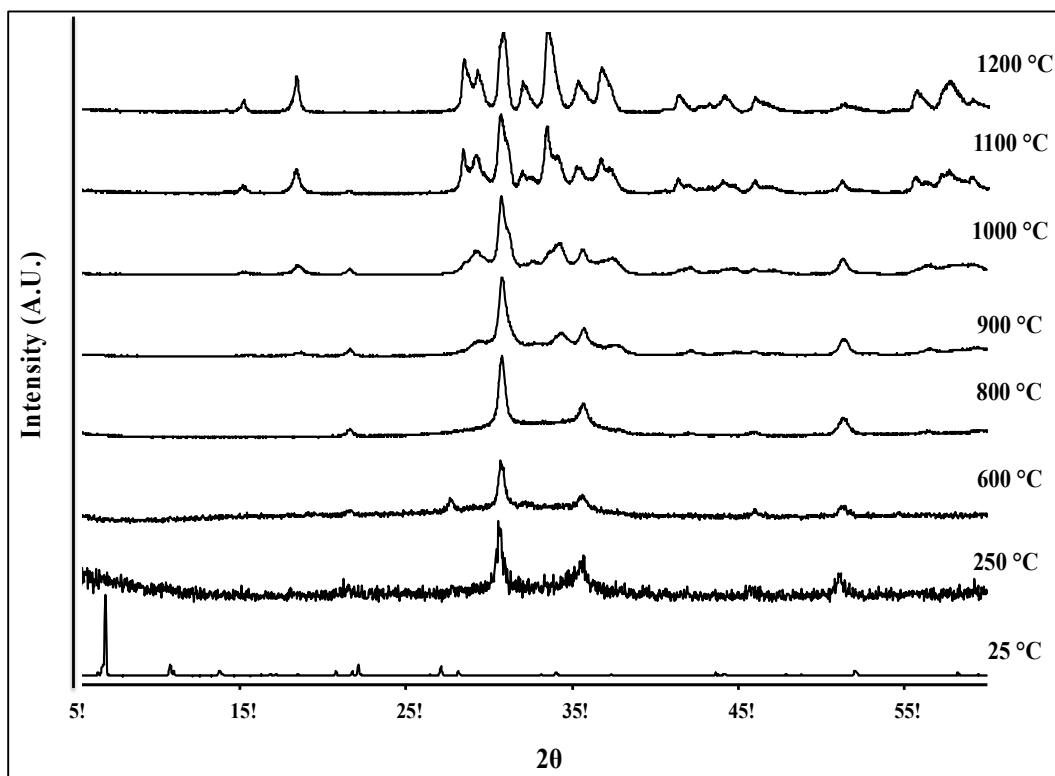


Figure 2.8. Powder XRD traces for a bulk sample of $f\text{-Ga}_{10}\text{In}_3$ heated at specified temperatures.

The dehydration of $f\text{-Ga}_8\text{In}_5$ (Figure 2.9) and $f\text{-Ga}_7\text{In}_6$ results in a primarily amorphous solid at temperatures below 600 °C, although reflections begin to emerge at temperatures as low as 250 °C. As with $f\text{-Ga}_{13}$ more of these peaks appear above 600 °C and sharpen up to 1200 °C.

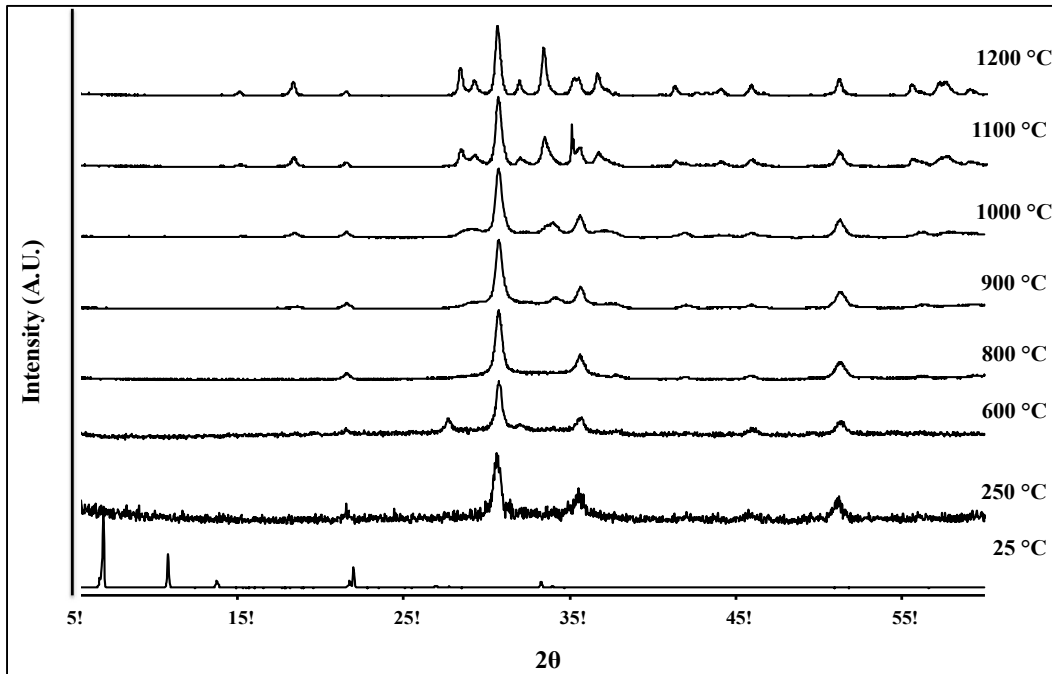


Figure 2.9. Powder XRD traces for a bulk sample of $f\text{-Ga}_8\text{In}_5$ heated at specified temperatures.

Upon heating all compositions first transform into a thermally robust amorphous oxide. At higher temperatures, **1-4** crystallize directly into a distorted $\beta\text{-Ga}_2\text{O}_3$ structure while **5** and **6** phase separate upon crystallization into a majority phase of $\beta\text{-Ga}_2\text{O}_3$ and a minority phase of the bixbyite In_2O_3 structure as demonstrated in the Pawley fits for $f\text{-Ga}_{12}\text{In}_1$ and $f\text{-Ga}_8\text{In}_5$ (Figure 2.10).⁸ It can be noted that this mixed phase composition arises once the $\beta\text{-Ga}_2\text{O}_3$ lattice stops expanding with increasing indium substitution (Table 2.5) and can therefore be thought of as occurring only after the gallium oxide lattice is completely saturated with indium.

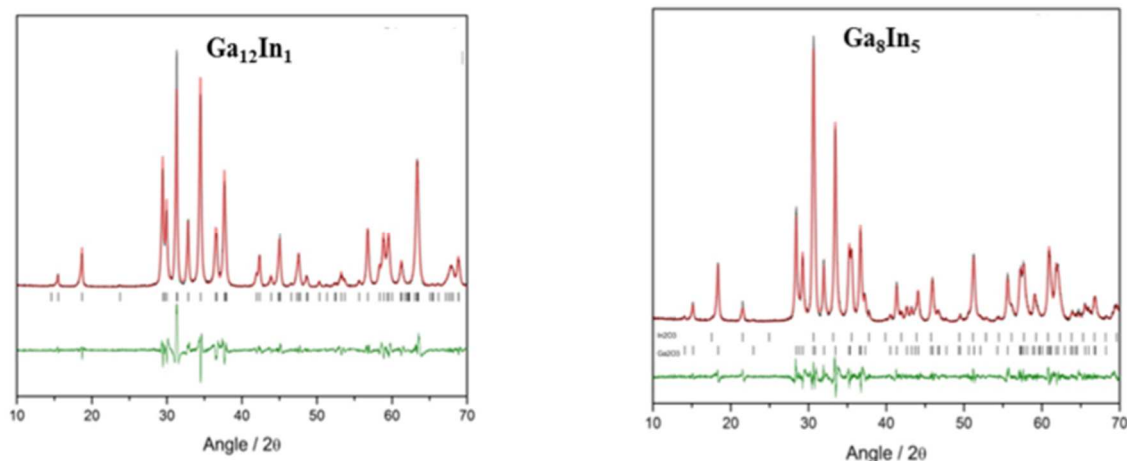


Figure 2.10. Pawley fits for ***f*-Ga₁₂In₁** (**1**, left) and ***f*-Ga₈In₅** (**5**, right). The observed trace (black), calculated trace (red) and the sum difference (green) are shown. **1** transforms in to the β -Ga₂O₃ structure with elevated temperatures. Phase separation occurs for **5** at elevated temperatures and results in a majority phase of β -Ga₂O₃ and a minority phase of the In₂O₃ bixbyite-type structure.

These studies show that substitution of the larger indium ion results in an increase in the unit cell volume as well as the a , b , and c lattice parameters (confirmed by powder XRD data) and a decrease in the β angles (Table 2.5). These changes produce a shift of β -Ga₂O₃ reflections as a function of indium content due to the substitution of indium for gallium into the lattice. As the In₂O₃ bixbyite structure emerges in the oxides formed from ***f*-Ga₈In₅** and ***f*-Ga₇In₆**, no significant peak shifts are observed in the β -Ga₂O₃ phase above $x = 0.62$ (32 mol%) and $x = 0.77$ (38 mol%). This value is lower than that reported by Edwards et al. (42 mol%),⁹⁹ but falls within the range reported by Shannon and Prewitt (33-50 mol%).¹⁰⁰ Indium incorporation into the β -Ga₂O₃ structure has been previously studied showing preferential substitution of indium into octahedral gallium sites to form

the β -GaInO₃ structure.^{99,100} This result was confirmed through Rietveld refinements for f -Ga₁₃ and 1-6, with a variable occupancy parameter assigning 100% of the indium ions to octahedral vacancies.

Table 2.5. Lattice parameters of oxides formed from f -Ga_{13-x}In_x clusters.

Ga₂O₃ Parameters - Monoclinic

| | a (Å) | b (Å) | c (Å) | β (°) |
|--------------------------------------|-----------------|----------------|----------------|----------------|
| Ga₁₃ | 12.222(0.003) | 3.042(0.001) | 5.808(0.001) | 103.88(0.01) |
| Ga₁₂In₁ | 12.455(0.001) | 3.1012(0.0003) | 5.8662(0.0005) | 103.444(0.006) |
| Ga₁₁In₂ | 12.581(0.003) | 3.1207(0.0008) | 5.916(0.002) | 103.00(0.02) |
| Ga₁₀In₃ | 12.782(0.004) | 3.1691(0.0007) | 5.962(0.002) | 102.48(0.02) |
| Ga₉In₄ | 12.803(0.002) | 3.1805(0.0004) | 5.9615(0.0009) | 102.485(0.009) |
| Ga₈In₅ | 12.844(0.001) | 3.1920(0.0001) | 5.9757(0.0005) | 102.401(0.008) |
| Ga₇In₆ | 12.8395(0.0007) | 3.1928(0.0002) | 5.9732(0.0007) | 102.350(0.007) |

In₂O₃ Parameters – Cubic

| | a (Å) |
|-------------------------------------|-----------------|
| Ga₈In₅ | 10.096(0.005) |
| Ga₇In₆ | 10.0783(0.0004) |

II.7. Conclusions

Synthetic control over the metal ratios in a series of heterometallic Group 13 tridecameric hydroxo-aquo clusters (from $f\text{-Ga}_{12}\text{In}_1$ to $f\text{-Ga}_7\text{In}_6$) has been demonstrated. The variability of this synthesis enables highly specific molecular control over the composition of metal oxides. Powder XRD studies show that heat treatment of $f\text{-Ga}_{13}$ and **1-6** leads to different metal oxide structures depending on the fraction of indium within the cluster. Studies also show a saturation limit for incorporation of indium into the final $\beta\text{-Ga}_2\text{O}_3$ phase.

These heterometallic clusters represent a new set of compounds with implications in the development of single-source precursors for the fabrication of metal oxide thin films. The preparation of these clusters could enable the isolation of more heterometallic clusters that incorporate non-Group 13 metals. The stability of the planar M_7 core suggests the outer ring ions are components amenable to transmetalation.⁴⁷ These compounds lead to a promising pathway for a new sub-set of mixed-metal materials.

II.8. Bridge to Chapter III

The synthesis and solid-state characterization of the complete series of aqueous heterometallic $f\text{-Ga}_{13-x}\text{In}_x$ tridecamers was presented. Preliminary solid-state analysis encouraged further investigations of the local environments of each metal ion site within these compounds. The efficacy of additional characterization

techniques is demonstrated in Chapter III in which Solid-State NMR (SSNMR) is used to analyze the local coordination environments of ***f*-Ga₁₃**.

CHAPTER III

SOLID-STATE ^{69}Ga AND ^{71}Ga NMR STUDY OF THE NANOSCALE INORGANIC CLUSTER $[\text{Ga}_{13}(\mu_3\text{-OH})_6(\mu_2\text{-OH})_{18}(\text{H}_2\text{O})_{24}](\text{NO}_3)_{15}$

Dr. Zayd L Ma, Katherine M. Wentz and Blake A. Hammann (Washington University in St. Louis), and Dr. Victor V. Terskikh (University of Ottawa) performed solid-state NMR spectra, modeling, and data interpretation. Drs. I-Ya Chang and Paul Ha-Yeon Cheong (Oregon State University) performed DFT computations of NMR parameters. I prepared all of the $f\text{-Ga}_{13}$ that was used for solid-state NMR analysis. The results presented in this chapter were published in 2014 in *Chemistry of Materials*, a publication of the American Chemical Society, volume 26 pages 4978-4983.

III.1. Introduction

Nanoscale Group 13 metal hydroxo-aquo complexes have garnered significant interest for potential applications such as single-source precursors for metal oxide thin films. A number of these species have yielded thin films with minimal defects from water-based solutions through straightforward condensation processes such as spin-coating and other solution-based methods (including spray coating).^{33,47,101,102} The high density of these metal oxide films makes them suitable candidates for the next generation

of high-k dielectrics in semiconductor devices such as the closely related IGO (indium gallium oxide) films.

A variety of methods for preparing Group 13 clusters in gram-scale quantities have been published.^{1,43,55,72,103} These clusters serve as excellent precursors for the metal oxide films described above, and a study their speciation in solution is underway.^{55,103} Aside from X-ray diffraction studies on single crystals of Group 13 samples, the inorganic clusters are not readily characterized in the solid state owing to their lack of long-range periodicity. The clusters are known to form a wide array of oligomers in the solid state under a variety of conditions, further complicating their analysis.³⁵ While single-crystal structures have been determined, the presence of impurities and amorphous domains still are difficult to characterize by diffraction methods. In order to eventually determine the thin film products of these clusters, a thorough knowledge of the predominant structures present in the nanoscale clusters is critical, and solid-state NMR (SSNMR) is an ideal spectral tool to identify cluster isomers and to characterize mixtures that contain multiple species, amorphous materials, and molecular crystals such as these. Several methods for solid-state ^{69}Ga and ^{71}Ga NMR characterization of $[\text{Ga}_{13}(\mu_3\text{-OH})_6(\mu_2\text{-OH})_{18}(\text{H}_2\text{O})_{24}](\text{NO}_3)_{15}$ are discussed in order to identify the characteristics of the different gallium sites within the cluster, which we refer to hereafter as “*f*- Ga_{13} ” (Figure 3.1).

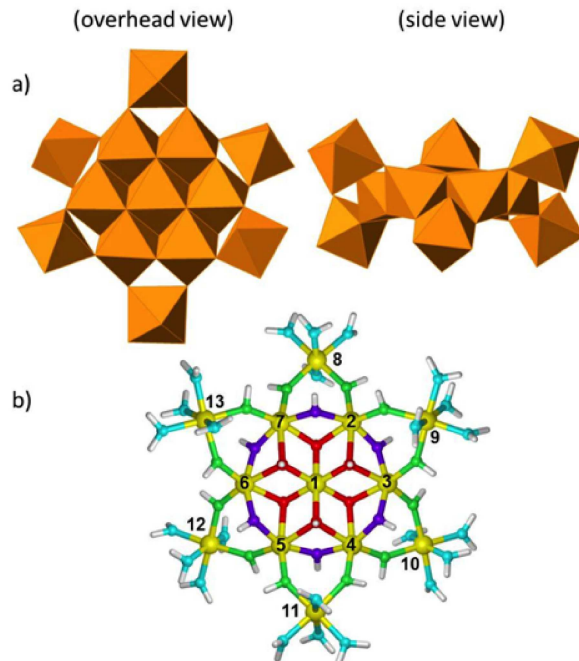


Figure 3.1. Representation of the $[\text{Ga}_{13}(\mu_3\text{-OH})_6(\mu_2\text{-OH})_{18}(\text{H}_2\text{O})_{24}](\text{NO}_3)_{15}$ cluster. a) Space-filling polyhedra show overhead and side views, according to prior single crystal results⁴⁵ with NO_3^- (omitted for clarity) to charge balance the metal-hydroxide cluster. b) Gallium sites are referred to as follows: (1) “core”, (2)-(7) “middle ring”, and (8)-(13) “outer ring”. Oxygen atoms have been color-coded to indicate identical bonds and the colors are consistent with Figure 3.3.

The $f\text{-Ga}_{13}$ cluster is comprised of three types of six-coordinate gallium metal ions. Six “outer” ring sites, each possessing two $\mu_2\text{-OH}$ bridges and four H_2O ligands; six “middle” ring sites coordinated by two $\mu_3\text{-OH}$ and four $\mu_2\text{-OH}$ bridges; and one “core” site with only $\mu_3\text{-OH}$ bridges surrounding it. The core and middle ring gallium atoms are in a flat plane of edge-sharing octahedra with the outer ring atoms in corner-sharing sites above and below the plane (Figure 3.1). This unique structure offers the opportunity for NMR analysis to yield details about the variation in spectra for the multiple sites. Future studies on both clusters and the thin films that are condensed from these clusters will rely

heavily on the detailed information regarding site-to-site variation afforded by solid-state $^{69/71}\text{Ga}$ NMR and the parameters determined here.

Gallium NMR has been used to analyze semiconductors since 1959; however, it is much less commonly used than other NMR active nuclei (i.e., ^1H , ^{13}C).¹⁰⁴ Both NMR-active isotopes of gallium (^{69}Ga and ^{71}Ga) are spin-3/2 ($I=3/2$) species, and as a consequence they have a non-zero quadrupole moment that can interact with an electric field gradient (EFG) at the site of the nucleus. The quadrupole-EFG interaction often significantly broadens the Zeeman resonances probed with NMR and gives structural information regarding the coordination environment, the symmetry, and notably for this study, any distortion to the local bonding environment (such as distortion from perfect octahedral geometry). With recent advances in both ultra-high magnetic fields and fast magic-angle-spinning (MAS) technology, the ability to resolve and interpret quadrupolar-broadened NMR spectra has expanded greatly.

Herein, we present a solid-state gallium NMR study of ***f*-Ga₁₃** with complementary computational analysis showing three distinct gallium sites with near-octahedral coordination. This spectroscopic information will be invaluable in tracking gallium coordination and structural changes during the formation of thin films from these precursors as well as in other related materials.

III.2. *f*-Ga₁₃ synthesis

***f*-Ga₁₃** was synthesized using modification of a known procedure.¹ $\text{Ga}(\text{NO}_3)_3$ (250 mg, 0.978 mmol) was dissolved in MeOH (10 mL) and N-Nitrosodibutylamine (DBNA)

was added to this solution (286 mg, 1.809 mmol). Slow evaporation of the resultant mixture in air and at room temperature yielded colorless, block-like crystals of **f-Ga₁₃**. The crystals were isolated by removing DBNA with a syringe and several washes with acetone. These samples were fully characterized by a variety of tools including single/powder X-ray diffraction and FTIR.^{1,33,35,43,47,55,72,103}

III.3. Solid-state NMR parameters

Gallium NMR spectra were acquired using a variety of experimental conditions at magnetic field strengths of 13.9 T (¹H at 589.85 MHz, ⁷¹Ga at 179.89 MHz, ⁶⁹Ga at 141.59 MHz) and 21.1 T (¹H at 899.82 MHz, ⁷¹Ga at 274.42 MHz, ⁶⁹Ga at 215.99 MHz). All 1D spectra were obtained under MAS conditions (33.0 or 62.5 kHz) with a central transition selective $\pi/2$ - τ - π rotor synchronized echo,¹⁰⁵ then left shifted to the top of the echo, zero-filled, Fourier transformed, and phased to result in an absorptive peak. All recycle delays were 200ms, which was found sufficient for complete relaxation to acquire quantitative spectra. 13.9 T data were acquired with a 2.5mm HX MAS probe (Bruker) and a Redstone NMR spectrometer (TecMag) with a radio-frequency (rf) field strength of 89.3 kHz for ⁷¹Ga and 69.4 kHz for ⁶⁹Ga, corresponding to nonselective $\pi/2$ pulses of 2.8 and 3.6 μ s, respectively. 21.1 T data were acquired with a 1.3mm HX MAS probe (Bruker) and Bruker Avance II console with an rf field strength of 125 kHz for both ⁶⁹Ga and ⁷¹Ga. High-power proton decoupling was found experimentally to have no additional narrowing effect, and no spectra presented were acquired with proton decoupling. Spectra were referenced to a 1.0 M Ga(NO₃)₃ solution at 0 ppm. ⁷¹Ga 3QMAS was attempted with **f-Ga₁₃**; however, due to the large quadrupole coupling, the conversion efficiency

between higher quantum coherences¹⁰⁶ was not sufficient to observe all three sites. All NMR spectra were acquired without any variable temperature control; however, data were consistent between different rotor sizes and no change in the spectra was detected at different spinning speeds (40kHz, 50kHz, and 62.5kHz).

III.4. Theoretical computations of NMR parameters

Quadrupolar NMR parameters such as the quadrupole coupling constant (C_Q) and asymmetry (η_Q), and parameters such as chemical shift are difficult to calculate. While some programs offer excellent opportunities to do so, in the absence of such software one can still use the predictive tools of density functional theory (DFT) calculations, such as Gaussian, to help interpret spectra. For example, “ballpark” numbers (and the appropriate trend) in C_Q can be computed using the widely available program.

EFG tensors of **f-Ga₁₃** were computed by DFT using the program, Gaussian, to acquire NMR parameters C_Q and η_Q .^{107,108} Both the approximate values and the trend in C_Q can be computed using this widely available program. An isolated **f-Ga₁₃** was fully optimized in the rijB3LYP/def2-SVP level of theory.^{109–112} The vibrational-frequency computation confirmed that this optimized **f-Ga₁₃** structure is the ground-state geometry. The EFG tensors were obtained in B3LYP/def2-TZVP level of theory.¹¹³ Both the geometry optimization and EFG tensors were computed under vacuum condition without a balancing electrostatic potential or dielectric medium. Calculations predict a negative C_Q for the middle ring of gallium atoms, and we report an absolute value from fitting since only $|C_Q|$ can be determined experimentally from NMR data.¹¹⁴

III.5. NMR spectral fitting

NMR spectra were fit using DMFit¹¹⁵ with consideration for the sample spinning rate, chemical shift, η_Q , C_Q , and all quadrupolar interactions up to second order. Initially, three sites were assumed, and the intensity, η_Q , C_Q , and isotropic shift in ppm were allowed to float individually in an iterative fashion until the fit converged on a model of NMR line shapes that matched the data. The broadening factors in the fitted spectra are approximately 500 Hz for ⁷¹Ga and approximately 3000 Hz for ⁶⁹Ga.

III.6. Solid-state NMR analysis

Gallium can have very large quadrupole coupling, 3 to 18 MHz in gallium oxides based upon prior work;^{104,115,116} therefore, it was necessary to first acquire NMR spectra at high field and high MAS rates to minimize the contribution from second-order quadrupolar effects. For powder samples under rapid MAS conditions, the line broadening due to the chemical shift anisotropy and dipole-dipole coupling is efficiently averaged out and only need consider the contributions from first- and second-order quadrupole interactions with the EFG need to be considered. Under these conditions, the quantities of significance are the asymmetry parameter $\eta_Q = (V_{XX} - V_{YY})/V_{ZZ}$, which can vary from 0 to 1, and the quadrupole coupling constant $C_Q = (V_{ZZ} \cdot eQ)/h$,¹¹⁷ where V_{ii} is a diagonal element of the diagonalized EFG tensor with X, Y, and Z defining the Cartesian directions (eQ is the nuclear quadrupole moment, and h is Planck's constant). η_Q dictates the shape of a quadrupolar-broadened NMR resonance and, by convention, is set by the distribution of charge in directions transverse to the largest component of the EFG tensor.

C_Q defines the width of the resonance and is controlled by the magnitude of the EFG. Solution-state ^{71}Ga NMR spectra obtained for $f\text{-Ga}_{13}$ in aqueous solutions were much less informative with a single broad and featureless resonance centered at about 0 ppm (not shown). These results are in agreement with earlier solution-state ^{71}Ga NMR spectra reported for solutions of related Ga_{13} polyoxometalates, i.e., the Keggin-type structure $\kappa\text{-Ga}_{13}$.^{36,54,118}

III.7. ^{71}Ga MAS solid-state NMR at 21.1 T

A ^{71}Ga MAS NMR spectrum acquired for solid $f\text{-Ga}_{13}$ at 21.1 T is shown (Figure 3.2). The 21.1 T data were modeled using DMFit software in conjunction with DFT-computed EFG parameters as initial trial values. The resulting fit parameters from DMFit for ^{71}Ga are listed in Table 3.1

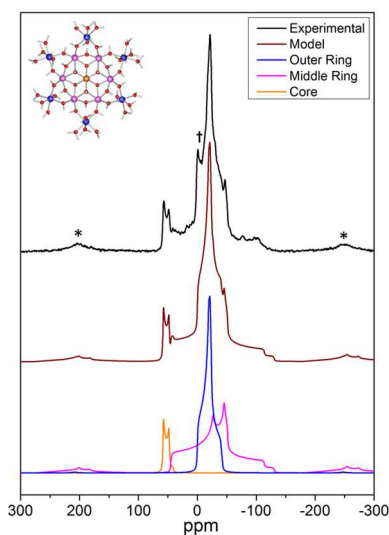


Figure 3.2. ^{71}Ga NMR spectra of $f\text{-Ga}_{13}$ at 21.1 T and 62.5 kHz MAS. Top spectrum (black) is experimental data with 42,152 transients averaged. Middle spectrum (brown) is a fit of experimental data using DMFit. Bottom spectra are models of the individual sites as defined in Figure 3.1. * indicates spinning sidebands and † denotes residual $\text{Ga}(\text{NO}_3)_3$ from the synthesis.

Table 3.1. Experimental and computed $^{69/71}\text{Ga}$ NMR parameters for $f\text{-Ga}_{13}$.

| | Core | | Middle ring | | Outer ring | |
|--|---------------|----------|-----------------------|---------------------|-----------------------|---------------------|
| | Exp. Fit** | Comput†† | Exp. Fit ⁵ | Comput ⁶ | Exp. Fit ⁵ | Comput ⁶ |
| $\delta_{\text{iso}}(^{69,71}\text{Ga}),^{\ddagger\ddagger}$ ppm | 60.7 | | 45.6 | | -0.6 | |
| $C_Q(^{71}\text{Ga}),^{\S\S}$ MHz | 5.0 | 6.36 | 13.9 | -12.28 | 6.7 | 4.73 |
| $C_Q(^{69}\text{Ga}),^8$ MHz | 9.0 | 10.16 | 21.5 | -19.63 | 11.1 | 7.57 |
| CQ ratio ($^{69}\text{Ga}/^{71}\text{Ga}$) | 1.80 | 1.60 | 1.54 | 1.60 | 1.65 | 1.60 |
| η_Q | 0.0 | 0.018 | 0.8 | 0.262 | 0.9 | 0.260 |
| Integrated area ($^{71}\text{Ga}@$ 13.9T) | 10 % | | 40 % | | 50 % | |

** “Exp. Fit” are the values to produce the line shapes shown in Figure 3.2 (^{71}Ga) and Figure 3.5 (^{69}Ga).

†† “Comput” are the values from Gaussian Computations.

$\ddagger\ddagger$ δ_{iso} is the isotropic chemical shift in ppm.

$\S\S$ Absolute experimental values $|C_Q(\text{Ga})|$ are reported.

The sites were assigned with a combination of NMR spectral-fitted and DFT-computed EFG parameters, integrated peak intensities, and consideration of local bonding structure around each gallium nucleus. The core gallium site (orange) is the narrowest feature, as expected, given its high-symmetry coordination environment. The outer ring gallium sites (blue) are also relatively narrow, while the middle ring gallium sites (magenta) are the most broad. The ^{71}Ga spectra have a narrow Gaussian peak near 0 ppm marked by † that does not fit with the models. This peak is consistent with $\text{Ga}(\text{NO}_3)_3 \cdot x\text{H}_2\text{O}$ and is an impurity remaining from the synthesis. Figure 3.3 depicts the 6-coordinate GaO_6 structures that make up these sites.

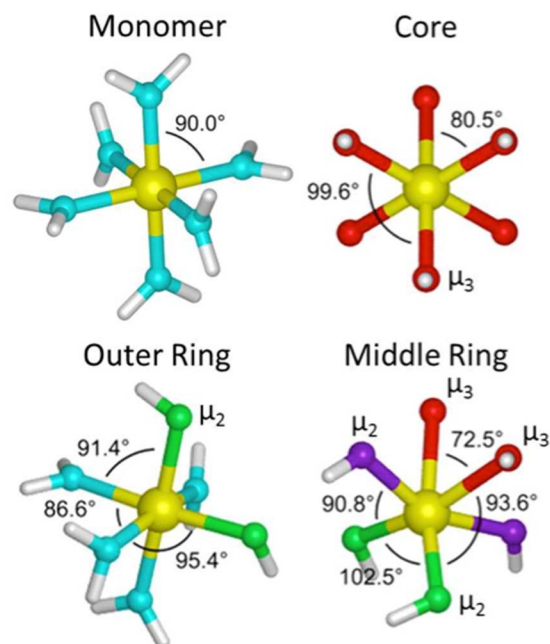


Figure 3.3. Bond angles for a gallium monomer $[\text{Ga}(\text{H}_2\text{O})_6]^{3+}$ and the gallium sites in *f*-**Ga**₁₃ demonstrating the strained octahedra leading to large C_Q values. The core gallium is bonded to all μ_3 hydroxo-bridges, and the bonds are slightly distorted from a perfect octahedron, yet yielding a small asymmetry parameter due to axial symmetry ($\eta_Q = 0$). In stark contrast, the middle ring gallium ions have four μ_2 and two μ_3 bonds ($\eta_Q \neq 0$) with bonding angles that are asymmetric and largely divergent from 90° . The outer ring ions are closer to octahedral symmetry but with a mixture of bridging -OH and H_2O ligands.

As expected, the highest symmetry core site, a trigonal antiprismatic C_{3v} structure, is bonded to six μ_3 -OH bridges with axial symmetry $\eta_Q = 0$ and also has the smallest $C_Q(^{71}\text{Ga}) = 5.0$ MHz. Each Ga in the outer ring is coordinated to four H_2O molecules and two μ_2 -OH bridges with a large asymmetry parameter ($\eta_Q = 0.90$) and a slightly larger $C_Q(^{71}\text{Ga}) = 6\text{--}7$ MHz. The middle ring with Ga bonded to four μ_2 -OH and two μ_3 -OH bridges has $\eta_Q = 0.78$. However, the middle ring is substantially distorted from ideal octahedral symmetry with the bonds bent significantly towards the middle of the cluster

resulting in a C_Q value approximately twice as large as that of the core and outer ring gallium sites. The distortion from ideal octahedral symmetry of the middle ring Ga sites is evident when considering the bond angles from the X-ray determined crystal structure¹ and geometry optimized calculations with values that range from 76.2° to 103.8°.

^{69,71}Ga NMR isotropic chemical shifts in solid gallium oxide compounds are known to depend on Ga coordination in GaO_x polyhedral.^{104,119} While 4-coordinate GaO₄ species are typically found in the chemical shift range from about +100 to +200 ppm, 6-coordinate GaO₆ species generally fall in the range from -50 to +50 ppm. The ^{69,71}Ga NMR isotropic chemical shifts measured for three Ga sites in **f-Ga₁₃** are consistent with all three sites being 6-coordinate. ⁷¹Ga MAS NMR spectra were reported previously for the related Ga₁₃ polyoxometalate of the Keggin-type.¹¹⁹ In agreement with the Keggin structure, the ⁷¹Ga MAS NMR signal for the central tetrahedral gallium site was found at approximately 175 ppm, while the octahedrally coordinated gallium sites were seen as a broad featureless resonance at about 30 ppm (the spectra were recorded at 9.4 T). No four-coordinate Ga was observed for **f-Ga₁₃** studied in this work, thus confirming the crystal structure composed of only six-coordinate Ga sites as illustrated in Figure 3.1.

III.8. ⁷¹Ga MAS solid-state NMR at 13.9 T

Two independent tests were used to check the model parameters of the assigned peaks. First, the ⁷¹Ga EFG parameters from the 21.1 T model (Figure 3.2) were used to predict the ⁷¹Ga MAS NMR spectrum recorded at 13.9 T (Figure 3.4) without modification. At lower field, the broadening from second order quadrupole interactions will be much more pronounced¹¹⁴ while the splitting, in Hz, between the isotropic

chemical shifts will diminish. The results of both experimental measurement and modeling are shown in Figure 3.4.

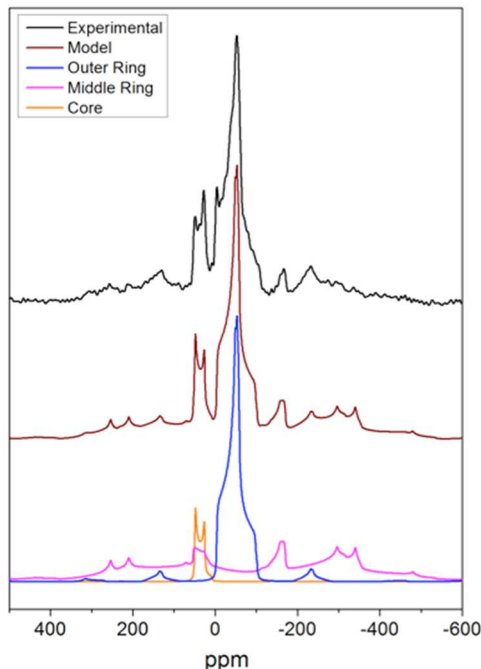


Figure 3.4. ^{71}Ga NMR spectrum of *f*- Ga_{13} at 13.9 T and 33 kHz MAS with 51,200 transients averaged (top, black). Middle spectrum (brown) is fit from experimental data using DMFit. Bottom spectra are models of the individual sites as defined in Figure 3.1. Parameters for modeling were used without modification from the 21.1 T data.

The middle ring gallium resonances broaden almost completely into the baseline (magenta), but the DMFit model still accurately represents features seen in the experimental MAS spectra.

III.9. ^{69}Ga MAS solid-state NMR at 21.1 T and 13.9 T

NMR experiments were executed on ^{69}Ga at both 21.1 T and 13.9 T (Figure 3.5). The asymmetry parameter (η_Q) should be identical for ^{71}Ga and ^{69}Ga as the charge

distribution around each gallium site will be the same for ^{69}Ga as ^{71}Ga . Using η_Q and δ_{iso} values from the ^{71}Ga DMFit modeling and iterating the C_Q value, a ^{69}Ga model was generated that fit the 21.1 T data. Then, with the same procedure, the ^{69}Ga model was also fit to 13.9 T NMR data without modification of the EFG parameters. ^{69}Ga results are also listed in Table 3.1. Further confirmation of the correctly-modeled C_Q values is seen in that the ^{71}Ga to ^{69}Ga C_Q ratio is similar to the ratio of their quadrupole moments ($Q_{69}/Q_{71} = 1.60$)¹²⁰ for each site (Table 3.1).

^{71}Ga 3QMAS NMR experiments were attempted at 21.1 T to resolve the three Ga sites, yet these attempts were not very successful. The Ga resonance from the middle ring ($C_Q(^{71}\text{Ga}) = 13.9\text{MHz}$) was impossible to detect in ^{71}Ga 3QMAS and ^{71}Ga 3QMAS-SPAM spectra; this was not surprising given the large C_Q value, even after three days of averaging. Efficiency of MQMAS experiments depends to a large extent on the ratio of the quadrupolar frequency, ν_Q , to the power level of excitation on conversion pulses.¹⁰⁶ For spin 3/2 nuclei like ^{71}Ga , the quadrupolar coupling constant of 5 MHz corresponds to a quadrupolar frequency of $\nu_Q = 3C_Q/2I(2I-1) = 2.5$ MHz, which makes 140 kHz of rf power of excitation and conversion pulses employed in this work sufficient to observe ^{71}Ga 3QMAS signals for the core and the outer ring gallium sites in reasonable time. To achieve the same 3Q efficiency for the middle ring gallium sites with $C_Q(^{71}\text{Ga}) = 13.9$ MHz would require about 400 kHz of rf power for the 3Q excitation, which is not practical using most NMR probes. The inherent inability of MQMAS to observe NMR signals with very large C_Q values is known and was reported previously.¹²¹

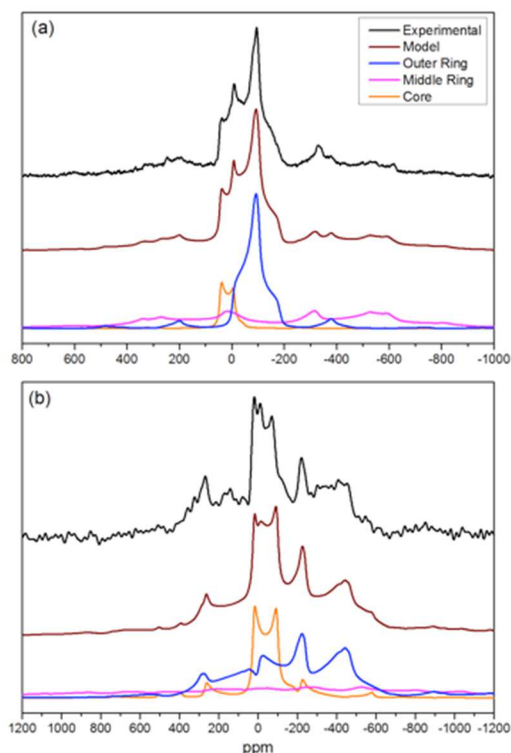


Figure 3.5. ^{69}Ga NMR spectra of $f\text{-Ga}_{13}$ at 21.1 T (a) and 13.9 T (b) with MAS at 62.5 kHz and 33 kHz, respectively. Spectra referenced to 1M $\text{Ga}(\text{NO}_3)_3$. Consistent with other figures, top spectrum (black) is experimental, the middle spectrum (brown) is the model, and the bottom spectra (orange, blue, magenta) are for the individual gallium sites. Modeling was done by using the asymmetry parameter η_Q and δ_{iso} deduced from the 21.1 T ^{71}Ga results and varying the C_Q of each site until the model matched the experimental results at 21.1 T. The 21.1 T ^{69}Ga parameters were then applied to the 13.9 T data to confirm correct assignment of C_Q and η_Q .

III.10. Conclusions

Solid-state ^{69}Ga and ^{71}Ga NMR at two field strengths has successfully elucidated line shapes for the distorted octahedra present in metal hydroxo-aquo $f\text{-Ga}_{13}$ clusters. Insights into the local chemical environments of gallium ions within the $f\text{-Ga}_{13}$ cluster will ultimately be critical when examining thin films made from these precursors.

Computational analysis supports the finding of three distinct gallium sites related to the core, middle, and outer ring of gallium ions within the clusters. Knowledge of NMR parameters such as η_Q and C_Q provides information about the local environment surrounding each gallium nucleus, especially those arising from the EFG. This research also lays the groundwork for studying systems with more complexity, such as mixed metal clusters of $f\text{-M}_{13-x}\text{In}_x$ (M = Ga or Al; x=1-6) compounds, and thin films made from these precursors.

III.11. Bridge to Chapter IV

Solid-state ^{69}Ga and ^{71}Ga NMR were used to investigate the structure of $f\text{-Ga}_{13}$. This data provides information fundamental to understanding the nature and behavior of these tridecamers. This will especially be useful for studies of new structures such as $f\text{-Al}_7\text{In}_6$, which is discussed in the next chapter. Chapter IV presents a return to synthesis by introducing a new route that opens the door to additional Group 13 tridecameric structures.

CHAPTER IV

TRANSMETALATION OF AQUEOUS INORGANIC CLUSTERS – A USEFUL ROUTE TO THE SYNTHESIS OF HETEROMETALLIC ALUMINUM AND INDIUM HYDROXO-AQUO CLUSTERS

Milton N. Jackson, Jr. (University of Oregon) performed Raman spectroscopy on the solid $f\text{-Al}_7\text{In}_6$ tridecamer and Dynamic Light Scattering (DLS) experiments on the $f\text{-Al}_7\text{In}_6$ and $f\text{-Al}_{13}$ solutions. He also produced the thin film from $f\text{-Al}_7\text{In}_6$ on which transmission electron microscopy (TEM), energy dispersive X-ray spectroscopy (EDX), and atomic force microscopy (AFM) were used, with assistance from Joshua Razink (University of Oregon, CAMCOR) to determine film composition and roughness. Dr. Lev N. Zakharov collected all single-crystal X-ray data. My contributions to this work were in developing the synthesis for $f\text{-Al}_7\text{In}_6$, synthesizing $f\text{-Al}_{13}$ (synthesis developed by Dr. Jason T. Gatlin) for comparison studies, and performing $^1\text{H-NMR}$ and $^1\text{H-DOSY}$ experiments with $f\text{-Al}_7\text{In}_6$ and $f\text{-Al}_{13}$. Professor Dr. Darren W. Johnson was the principle investigator for this work and was involved in manuscript editing. The results presented in this chapter were published in 2014 in *Inorganic Chemistry*, a publication of the American Chemical Society, volume 53 pages 7101-7105.

IV.1. Introduction

Transparent electronics and devices have emerged as one of the most promising developments for next generation technologies. Solution-processed multi-component materials such as indium gallium oxide (IGO) and aluminum indium oxide (AIO) offer routes to enable new or enhanced performance levels in large area electronics and energy devices such as flat-panel displays, solar cells, and LEDs.^{27,101,102,122–125}

A general synthetic route for an array of nanoscale Group 13 tridecameric hydroxo-aquo clusters composed of gallium and indium is known in the literature.^{1,33} The utility of these clusters as precursors/inks for metal oxide semiconductors was previously demonstrated in an IGO thin film device formed from **f-Ga₇In₆**.³³ The resulting dense, uniform, and pinhole-free film represents an emergent example of the low-temperature solution processing of thin film transistors (TFTs) in which a completely inorganic cluster is used as a precursor material. This process provides a low temperature alternative for producing thin films as compared to the deposition and sputtering techniques traditionally used to create similar devices.^{27,125} As a result, we have begun to explore the use of other inorganic aqueous precursor solutions for materials applications.

IV.2. Motivation for precursor design

Aluminum-oxide based materials show promise as precursor candidates in several applications including dielectric layers and capacitors.^{126–130} The current

number of soluble precursors for low temperature aqueous processing is limited to $f\text{-Al}_{13}$,^{43,53,75} Al_8 ,⁴¹ and Al_4 .^{35,40} The synthesis of $f\text{-Al}_{13}$ originally required the addition of a base (NaOH or NH_4OH) and the carcinogenic additive N-dibutylnitrosoamine (DBNA).⁴³ For heterometallic Al/In clusters, the product was difficult to reproduce under the same conditions. A transmetalation process yields the new hydroxo-aquo cluster $[\text{Al}_7\text{In}_6(\mu_3\text{-OH})_6(\mu\text{-OH})_{18}(\text{H}_2\text{O})_{24}](\text{NO}_3)_{15}$ ($f\text{-Al}_7\text{In}_6$) (Figure 4.1) by direct treatment of the related $f\text{-Al}_{13}$ cluster with indium nitrate.

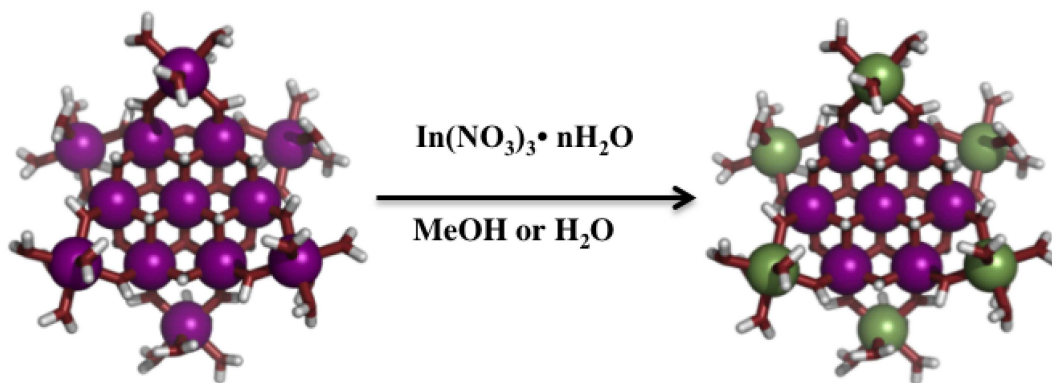


Figure 4.1. Simple representation of the transformation from $f\text{-Al}_{13}$ to $f\text{-Al}_7\text{In}_6$ upon addition of $\text{In}(\text{NO}_3)_3$ to a solution of $f\text{-Al}_{13}$ (in either MeOH or H_2O). In^{3+} ions (green) displace Al^{3+} ions (purple) on the labile outer shell of the cluster. Images generated from crystals structures of $f\text{-Al}_{13}$ and $f\text{-Al}_7\text{In}_6$.

This is the first instance of direct transmetalation of metal ions into the exterior ring of such hydroxo-aquo cluster species and currently the most reliable route to form Al/In congeners. Transmetalation eliminates the need for base and organic reagents as well as provides a reliable synthesis for preparing otherwise inaccessible heterometallic clusters. Furthermore, the resulting clusters can be

used as precursors for smooth, amorphous aluminum indium oxide (AlO) thin films that are comparable to films of similar content produced by atomic layer deposition or sputter deposition.^{126,127,131} In addition, transmetalation is an unusual reaction for aqueous coordination clusters.

IV.3. Metal exchange

The metal exchange phenomenon for has been exhibited in several examples of polyoxometalate structures.^{132–135} Electrospray Ionization Mass Spectroscopy (ESI-MS) characterization was used to identify mixed-metal phosphate-centered Keggin ions in aqueous tungsten and phosphodocemetalate solutions.^{132,133} Similar experiments for niobate/tantalate¹³⁴ and Mo/V-Selenite¹³⁵ systems showed additional mixed-metal species. Altering the pH conditions of monomeric salt solutions has led to the substitution of the central metal ion of $\kappa\text{-Al}_{13}$ by gallium, iron, or germanium as well as a variety of di- and trivalent metal ions in to the Anderson cluster $[\text{Mo}_7\text{O}_{24}]^{6-}$.^{65,84,136–139} In the process of metal exchange for tridecameric clusters, mixing $f\text{-Al}_{13}$ with $\text{In}(\text{NO}_3)_3$ allows indium ions to substitute in to the exterior metal sites of the cluster and produce $f\text{-Al}_7\text{In}_6$. The ability of $f\text{-Al}_{13}$ to easily convert into $f\text{-Al}_7\text{In}_6$ hints at dynamic metal and ligand exchange that occurs in solution and could influence speciation of $f\text{-Al}_{13}$ and related Al clusters (Table 4.1).

Table 4.1. Ratio of $f\text{-Al}_{13}$ to $\text{In}(\text{NO}_3)_3$ for the synthesis of various $f\text{-Al}_{13-x}\text{In}_x$ clusters.

| $f\text{-Al}_{13}$ (equiv.) | $\text{In}(\text{NO}_3)_3$ (equiv.) | Cluster structure |
|-----------------------------|-------------------------------------|-------------------------------|
| 1 | 19 | $f\text{-Al}_7\text{In}_6$ |
| 1 | 17 | $f\text{-Al}_8\text{In}_5$ |
| 1 | 14 | $f\text{-Al}_{10}\text{In}_3$ |

Here the focus is on $f\text{-Al}_7\text{In}_6$, however related studies reveal that the previously described $f\text{-Ga}_7\text{In}_6$ cluster³³ as well as other Ga/In clusters have also been synthesized via transmetalation (Table 4.2). For example, a 1:12 ratio of $f\text{-Ga}_{13}:\text{In}(\text{NO}_3)_3$ produces $f\text{-Ga}_7\text{In}_6$. The reverse reaction is also possible: when excess $\text{Ga}(\text{NO}_3)_3$ is added to $f\text{-Ga}_7\text{In}_6$, $f\text{-Ga}_{13}$ forms. This provides further evidence of a dynamic equilibrium between the $f\text{-M}_{13}$ (M = Al or Ga) cluster and $\text{M}(\text{NO}_3)_3$ monomer. Nuclear Magnetic Resonance (NMR) spectroscopy, Diffusion Ordered Spectroscopy (DOSY), Dynamic Light Scattering (DLS) and Raman spectroscopy have been used to provide valuable information in the characterization of these inorganic cluster species.^{55,72,103} These techniques were used in tandem to identify size and structural differences between $f\text{-Al}_{13}$ and $f\text{-Al}_7\text{In}_6$ in solution.

Table 4.2. Ratio of $f\text{-Ga}_{13}$ to $\text{In}(\text{NO}_3)_3$ for the synthesis of various $f\text{-Ga}_{13-x}\text{In}_x$ clusters.

| $f\text{-Ga}_{13}$ (equiv.) | $\text{In}(\text{NO}_3)_3$ (equiv.) | Cluster structure |
|-----------------------------|-------------------------------------|-------------------------------|
| 1 | 24 | $f\text{-Ga}_7\text{In}_6$ |
| 1 | 12 | $f\text{-Ga}_8\text{In}_5$ |
| 1 | 9 | $f\text{-Ga}_{10}\text{In}_3$ |
| 1 | 2 | $f\text{-Ga}_{12}\text{In}_1$ |

IV.3.1. *Synthesis of f-Al₇In₆*

A solution of **f-Al₁₃** (0.078 g, 0.037 mmol)⁵³ and In(NO₃)₃ (0.27 g, 0.90 mmol) in MeOH (10 mL) was left to evaporate open to air. After several days crystals of **Al₇In₆** formed (10% product yield with respect to starting amount of **f-Al₁₃**). Single crystal XRD reveals a structure identical in geometry to the previously reported heterometallic clusters.³³

IV.3.2. *Synthesis of f-Ga₇In₆*

f-Ga₇In₆ was synthesized following the same method as for **f-Al₇In₆**. A solution of **f-Ga₁₃** (0.100 g, 0.037 mmol) and In(NO₃)₃ (0.27 g, 0.90 mmol) in MeOH (10 mL) was left to evaporate open to air. **f-Ga₇In₆** crystals formed after several days (20% yield with respect to the amount of **f-Ga₁₃**). Both **f-Al₁₃** and **f-Ga₁₃** were used as is, following a wash with acetone.

IV.4. General characterization methods

Single crystal XRD experiments were carried out on a Bruker Smart Apex diffractometer at 153 and 173 K using Mo K α radiation ($\lambda = 0.71073 \text{ \AA}$). Absorption corrections were applied by SADABS. ¹H-NMR and ¹H-DOSY spectra were obtained on a Varian INOVA-500 MHz NMR Spectrometer. The Bipolar Pulse Pair Stimulated Echo (Dbppste) pulse sequence was used to acquire diffusion data with a 50 ms diffusion delay, 200 ms gradient length, 20 gradient levels, and nt = 16 scans. The Varian DOSY package was used for processing and measuring the diffusion coefficient (D_t). The hydrodynamic radius (R_h) was

calculated using the Einstein-Stokes equation ($R_h = \frac{K_b T}{6\pi\eta D_t}$) where K_b = Boltzmann's constant, T = temperature in kelvin, η = viscosity, and D_t = translational diffusion coefficient.¹⁰³ Percent error was calculated using measured values for ferrocene in DMSO.^{140,141} DLS measurements were taken using the Mobius from Wyatt technologies. The samples were filtered using a 0.1 μm PTFE syringe tip to remove any particulate matter followed by immediate analysis ($t < 1$ minute). Dynamics software was used and averaged over 20 measurements with a 5 second integration time per acquisition. Raman spectra of the **f-Al₇In₆** single crystals were collected using an Alpha 300S SNOM confocal Raman microscope. The spectra from each sample were averaged over 2000 accumulations at 0.5 s exposure time per scan. Thin films were fabricated via spin coating (3000 rpm for 30 seconds) a 0.2 M aqueous solution of **f-Al₇In₆** onto a p-type Si wafer pre-treated with a piranha solution (7:3 v/v ratio of concentrated H₂SO₄ and 35% H₂O₂). Prior to spin coating, the solutions were filtered through a 0.1 μm PTFE syringe tip to remove any particulate matter and/or potential agglomerates. The subsequent films were then annealed at 300 °C for 30 minutes prior to analysis.

IV.5. Summary of crystallographic data

Refinements of all crystal structures were performed in the same way. Disordered NO₃⁻ anions and solvent molecules were treated by SQUEEZE. Corrections of the X-ray data by SQUEEZE provide a range of 594 - 644 electrons/cell, which bracket the required value of 621 electrons/cell for nine NO₃⁻ anions, eighteen water molecules and nine methanol molecules in the full unit cell.

All non-hydrogen atoms were refined with anisotropic thermal parameters. H atoms were not taken into consideration. Calculations were performed using the Bruker SHELXTL package. ***f*-Al₇In₆** has a space group of symmetry *R*-3 located on a $\bar{3}$ axis. Three nitrate (NO₃⁻) anions are in general positions; two form H-bonds with the ***f*-M₁₃** cation while the third is disordered and shares six other possible positions around the cation with solvent molecules. Thus the ***f*-M₁₃** cation in the crystal structure is surrounded by fifteen NO₃⁻ anions and nine solvent molecules (three methanol and six water molecules) forming H-bonds with –OH groups and terminal water molecules bound to the metal atoms of the outer ring. Solvent molecules sharing positions with the NO₃⁻ anion are disordered as well. All structures contain two nearby positions occupied by disordered solvent molecules (water or methanol) in a 1:1 ratio.

IV.6. Solution-state characterization of *f*-Al₇In₆

The ¹H-NMR spectra of ***f*-Al₁₃** and ***f*-Al₇In₆** reveal several differences between the compounds (Figure 4.2). The peaks between 9.10 ppm and 9.32 ppm in ***f*-Al₁₃** (**A**) that are observed in the spectra of Al(NO₃)₃ (inset, **C**) are mostly absent from **B**. It appears that this species is a remnant of the co-crystallization of Al(NO₃)₃ and ***f*-Al₁₃**. Subsequent recrystallization to produce ***f*-Al₇In₆** eliminates this species. Another set of peaks is observed between 7.04 ppm and 7.21 ppm. The observed 1:1:1 triplet is associated with a spin ½ nucleus (such as ¹H) coupling to an S = 1 nucleus (such as ¹⁴N).

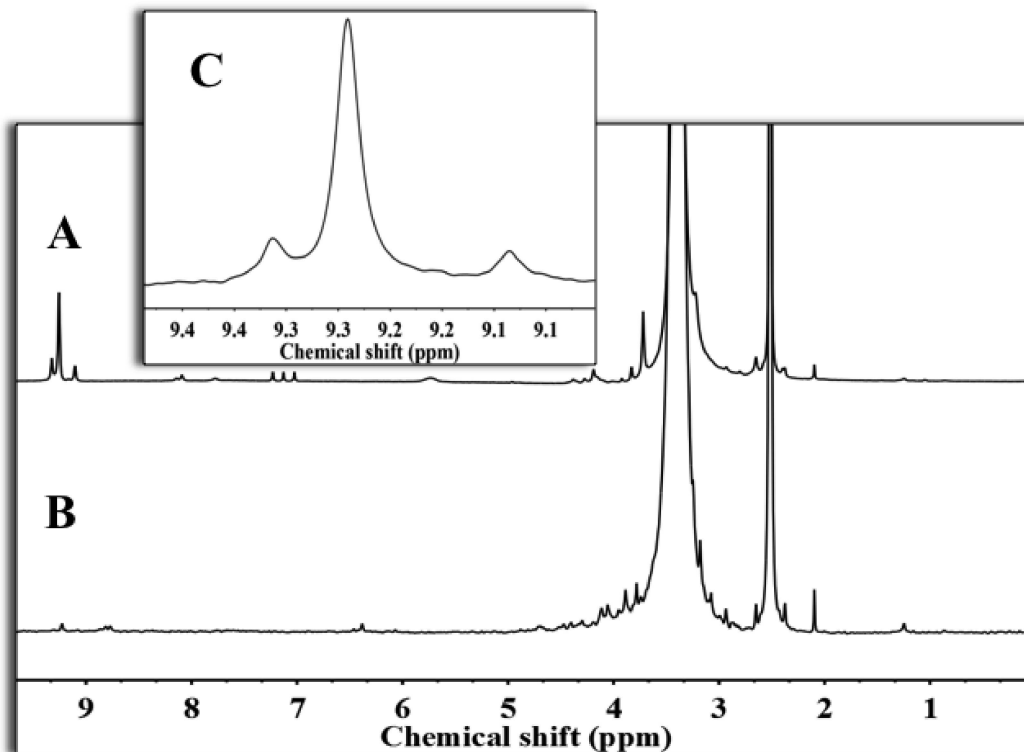
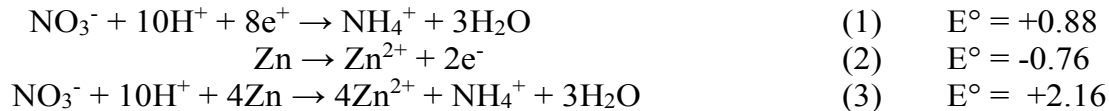


Figure 4.2. $^1\text{H-NMR}$ of $f\text{-Al}_{13}$ (A), $f\text{-Al}_7\text{In}_6$ (B), and $\text{Al}(\text{NO}_3)_3$ (C). Crystals of $f\text{-Al}_{13}$ (confirmed using single-crystal XRD) were used for $^1\text{H-NMR}$ spectroscopy.

$f\text{-Al}_{13}$ is produced by the reduction of $\text{Al}(\text{NO}_3)_3$ by zinc powder.⁵³ The reduction of nitrate ions with zinc metal is thermodynamically feasible (Table 4.3), particularly in acidic environments.¹⁴² Therefore, it is plausible that the triplet is a result of reducing nitrate to ammonium at an acidic pH. Those peaks disappear when $f\text{-Al}_7\text{In}_6$ is formed and isolated owing to the volatility of ammonium.

Table 4.3. Reduction potentials for the synthesis of **f-Al₁₃**.



¹H-DOSY was performed to compare the sizes of **f-Al₁₃** and **f-Al₇In₆** in solution. The hydrodynamic radii (R_h) of **f-Al₁₃** and **f-Al₇In₆** are within error of each other ($R_h = 1.1 \text{ nm} \pm 0.3 \text{ nm}$ and $1.0 \text{ nm} \pm 0.3 \text{ nm}$, respectively) in d_6 -DMSO although we expected the R_h for **f-Al₇In₆** to be slightly larger than that of **f-Al₁₃** based upon the size of the ionic radii for Al (0.535 Å) and In (0.800 Å),⁶ and the average calculated Al-O (1.839 Å) and In-O (2.086 Å) bond lengths.

Utilizing dynamic light scattering (DLS) as a corroborative technique to DOSY, the size of both the **f-Al₁₃** and **f-Al₇In₆** clusters are known in d_6 -DMSO as well as in aqueous solutions. In a direct solvent comparison with the DOSY experiment, the R_h of **f-Al₁₃** and **f-Al₇In₆** in d_6 -DMSO are very close to those measured with DOSY at $1.0 \text{ nm} \pm 0.3 \text{ nm}$ and $0.9 \text{ nm} \pm 0.4 \text{ nm}$, respectively (Figure 4.3). In water, DLS confirms that the R_h of **f-Al₁₃** is $1.0 \text{ nm} \pm 0.1 \text{ nm}$. By comparison, the measured R_h for **f-Al₇In₆** is $12.0 \text{ nm} \pm 1.5 \text{ nm}$, roughly an order of magnitude larger in water than its homometallic counterpart, suggesting that **f-Al₇In₆** may not be a discrete and stable species in water, but rather favors the formation of stable nanoparticles.

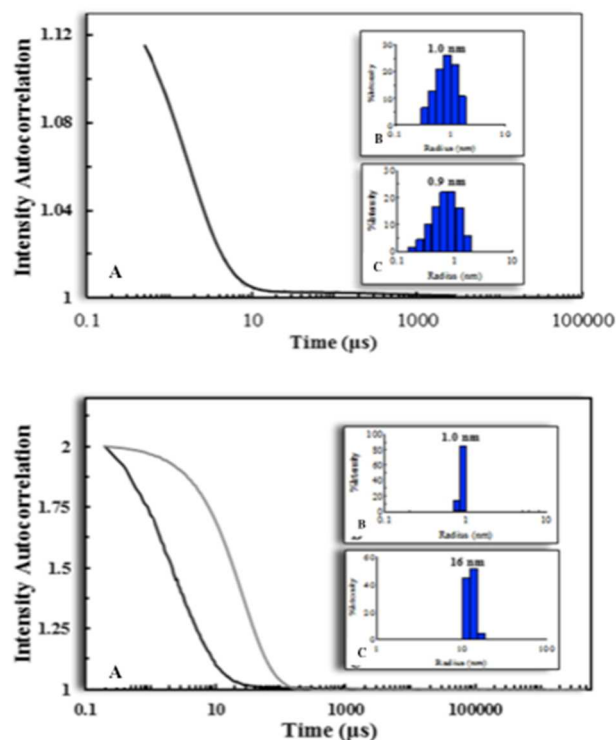


Figure 4.3. *Top:* (A) Autocorrelation function of 2 mM $f\text{-Al}_{13}$ (black) and 2 mM $f\text{-Al}_7\text{In}_6$ (grey) in $d_6\text{-DMSO}$ (traces stack on top of each other). Hydrodynamic radii of $f\text{-Al}_{13}$ (B) and $f\text{-Al}_7\text{In}_6$ (C) in $d_6\text{-DMSO}$ are displayed in the insets. *Bottom:* (A) Autocorrelation function of 0.2 M $f\text{-Al}_{13}$ (black) and 0.2 M $f\text{-Al}_7\text{In}_6$ (grey) in H_2O . Hydrodynamic radii of $f\text{-Al}_{13}$ (B) and $f\text{-Al}_7\text{In}_6$ (C) in H_2O are displayed in the insets.

Although the R_h of $f\text{-Al}_{13}$ in water is the same as in $d_6\text{-DMSO}$, the autocorrelation function suggests greater polydispersity for the cluster in $d_6\text{-DMSO}$ than in H_2O . This difference is likely due to the viscosity effects of $d_6\text{-DMSO}$ (2.0 cP and 0.89 cP for DMSO and H_2O , respectively, at 25 °C) that would cause fluctuations in the diffusion rates for $f\text{-Al}_{13}$ in solution. Solution studies are currently in progress to fully understand the solution speciation and other dynamic characteristics of these clusters in various solvents. Nevertheless, it is clear that $f\text{-}$

Al_{13} and $f\text{-Al}_7\text{In}_6$ behave differently in aqueous solution and that these characterization techniques provide a routine platform for understanding the solution chemistry of hydroxo-aquo clusters in general.

IV.7. Solid-state characterization of $f\text{-Al}_7\text{In}_6$

Solid state Raman spectroscopy is a valuable technique for characterizing single crystals of this structure type. In previous work, quantum mechanical computations were used to identify the various vibrational modes associated with $f\text{-Al}_{13}$.⁷² Incorporation of indium into the cluster results in new vibrational features; therefore each cluster has its own unique Raman signature (Figure 4.4).

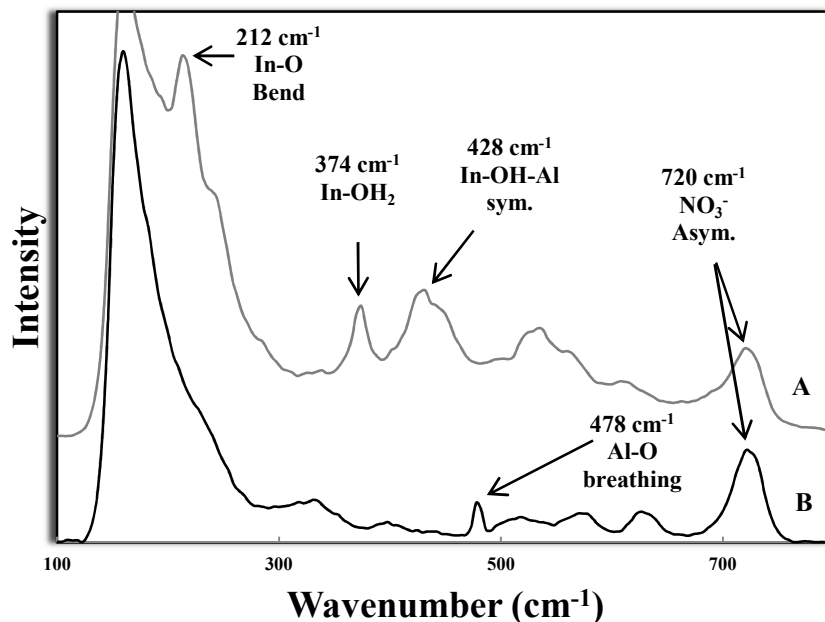


Figure 4.4. Solid state Raman spectra of $f\text{-Al}_7\text{In}_6$ (A, grey) and $f\text{-Al}_{13}$ (B, black) between 100 cm^{-1} and 800 cm^{-1} .

The spectrum of ***f*-Al₇In₆** contains several new modes that distinguish it from ***f*-Al₁₃**. The most significant difference between the two clusters is the disappearance of the breathing mode at 478 cm⁻¹ for ***f*-Al₁₃** in the spectrum for ***f*-Al₇In₆**. The broad peak with medium relative intensity at 428 cm⁻¹ can be attributed to Al-OH-In stretching vibrations. A narrower band with slightly less intensity at 374 cm⁻¹ corresponds to the vibrations of indium ions and their coordinated water ligands (In-OH₂) in the outer ring of the cluster. The lower wavenumber peak at 212 cm⁻¹ can be also be assigned as an In-O bending mode due to the lack of spectral evidence for a bound nitrate to the cluster.¹⁴³ More specifically, there are no signs of peak splitting in the anti-symmetric and symmetric NO₃⁻ peaks (720 cm⁻¹ and 1048 cm⁻¹, respectively) that denote the existence of an indium nitrato species (In(NO₃)(H₂O)₅²⁺).¹⁴³ The vibrational modes associated with the free NO₃⁻ ions in ***f*-Al₇In₆** are consistent with those observed in ***f*-Al₁₃** (721 cm⁻¹, 1048 cm⁻¹, 1350 cm⁻¹, and 1411 cm⁻¹) suggesting that the nitrates behave similarly in both clusters. There are also several weaker modes present between 450-650 cm⁻¹ attributed to the Al-O vibrations that are similar to what has been previously reported for ***f*-Al₁₃**.⁷²

IV.8. *f*-Al₇In₆ thin film analysis

A single layer thin film of ***f*-Al₇In₆** was prepared from an aqueous solution at a 0.2 M total metal concentration. Both transmission electron microscopy (TEM) and X-ray reflectivity (XRR) measurements indicate a film thickness of close to 6 nm (5.7 nm for SEM and 5.5 nm ± 0.2 nm for XRR). TEM and atomic force

microscopy (AFM) images reveal that *f*-Al₇In₆ produces uniform and atomically smooth thin films from spin coating when used as a solution precursor (Figure 4.5).

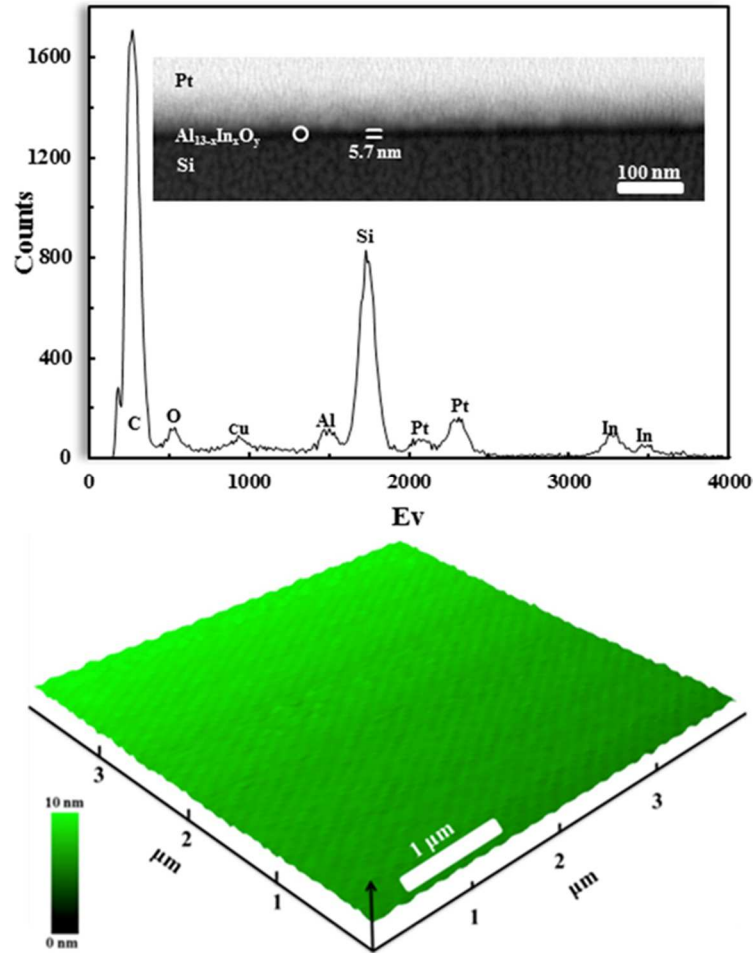


Figure 4.5. Top: EDX analysis of the solution processed *f*-Al₇In₆ precursor and cross-sectional TEM (top insert) of the Al_{13-x}In_xO_y thin film. The white circle represents the spot on which the EDX scan was performed. **Bottom:** AFM 3D side view of Al_{13-x}In_xO_y thin film (16 μm²).

In comparison to the indium gallium oxide (IGO) solution-processed film formed from *f*-Ga₇In₆, the AIO film surface morphology is also dense and

pinhole-free with minimal signs of inhomogeneity.³³ The 16 μm^2 AFM image shows that the ***f*-Al₇In₆** film is very smooth across the surface (RMS roughness = 0.145 nm), despite film thinness. Energy dispersive x-ray spectroscopy (EDX) analysis confirms the existence of an oxide composed of aluminum and indium in the film (aluminum indium oxide, AIO). The relative composition measurements give a ratio of Al_{1.02}In_{0.98}O_{2.95}, close in comparison to the aforementioned IGO thin film device.³³ Electrical measurements and device fabrication are on the horizon for future studies.

IV.9. Conclusions

In summary the heterometallic ***f*-Al₇In₆** hydroxo-aquo cluster has been synthesized via a transmetalation reaction. ¹H-NMR and Raman spectroscopies reveal that in the solution and solid states, respectively, ***f*-Al₇In₆** has distinct spectral features in relation to the ***f*-Al₁₃**. ¹H-DOSY and DLS show that these clusters persist in solution as multiple discrete species. In addition a dense, smooth, uniform, thin film of AIO was fabricated using ***f*-Al₇In₆**. By utilizing these techniques to identify ***f*-Al₇In₆** in the solid and solution phases, we are better equipped to explore and understand the complex solution dynamics and exchange reactions of these clusters. They also serve as potential precursors for solution deposition of metal oxide thin films. Heterometallic clusters have the additional advantage of tuning the metal ratios at the molecular level in spin-coating applications.

IV.10. Bridge to Chapter V

Transmetalation was used to synthesize the new $f\text{-Al}_7\text{In}_6$ heterometallic tridecamer and in a similar manner to the $f\text{-Ga}_{13}$ SSNMR results, solution NMR can show that different chemical environments exist for atoms in $f\text{-Al}_{13}$ and $f\text{-Al}_7\text{In}_6$. In Chapter VI variable temperature ^1H -NMR is used to determine the as proton lifetime kinetics and energy parameters for protons on the $f\text{-Al}_{13}$ structure. These studies are used to explore new avenues of the solution dynamics associated with Group 13 tridecamers and build on information currently available for these compounds.

CHAPTER V

INVESTIGATION OF THE PROTON EXCHANGE RATE KINETICS OF AQUEOUS $[\text{Al}_{13}(\mu_3\text{-OH})_6(\mu_2\text{-OH})_{18}(\text{H}_2\text{O})_{24}]^{15+}$

Christopher A. Colla (University of California, Davis) computed all proton rate exchange and energy parameters. Milton Jackson, Jr. performed dynamic light scattering, phase analysis light scattering, and AT-IR spectroscopy for $f\text{-Al}_{13}$. He also helped to write the corresponding portions of the manuscript from which this work was based. I performed all variable temperature ^1H -NMR experiments in addition to ^1H and ^{27}Al NMR titrations. I also drafted the manuscript based upon these studies. Dr. William H. Casey (UC Davis) helped to write the sections dedicated to calculations for determining proton lifetimes and energy parameters. He also helped to edit the manuscript along with Dr. Darren W. Johnson who was the principle investigator for this project.

V.1. Introduction

Aluminum is the most abundant metal and third most abundant element in the earth's crust behind oxygen and silicon.² Its ubiquitous nature has lead to an encyclopedic catalogue of the hydrolytic behaviour of aluminum ions: in mineral

surface-water reactions, in coordination complexes, in organic media, etc.^{144–148} There has been particular attention paid to specific hydrolysis products such as the Keggin structure $[\text{AlO}_4\text{Al}_{12}(\text{OH})_{24}(\text{H}_2\text{O})_{12}]^{7+}$ ($\kappa\text{-Al}_{13}$), which was first structurally characterized in 1960.^{10,11} This molecule was identified as the major component of flocculants found in several streams where the combination of acidic mining runoff and neutral water resulted in hydrolysis and precipitation.⁹ The strong heavy metal affinity of these flocculants leads to environmental ramifications that include water contamination and phytotoxicity. Since then $\kappa\text{-Al}_{13}$ has been adopted as a molecular-scale model to study the formation of polymeric flocculants as well as the surface chemistry reactivity of metal-oxide minerals with structural similarities.⁶³ Recently, another tridecameric aluminium species $[\text{Al}_{13}(\mu_3\text{-OH})_6(\mu_2\text{-OH})_{18}(\text{H}_2\text{O})_{24}]^{15+}$ (referred to herein as “ $f\text{-Al}_{13}$ ”) has been synthesized and crystallographically confirmed.^{43,52,53} Early synthetic methods utilized base (i.e. NaOH, NH_4OH and $\text{Al}(\text{OH})_3$) hydrolysis to form the polynuclear species, which caused a pH gradient and subsequently lead to co-crystallization of $f\text{-Al}_{13}$ and other aluminium moieties including $\kappa\text{-Al}_{13}$. After several washes with acetone, $f\text{-Al}_{13}$ is isolated in its pure form. Nevertheless this implies that $f\text{-Al}_{13}$ and $\kappa\text{-Al}_{13}$ can readily condense under the same conditions, within the same pH regime. Furthermore, evidence of a penta-coordinated aluminum complex in the aforementioned flocculant suggested that more polycations might be present as either solid intermediates or soluble species. Thus, piecing together the composition of aqueous aluminum formations in the environment is a complex task; and it becomes important to investigate how different molecular species can

serve as new models for environmental phenomena. The exchange rates of protons bound to the hydroxo-aquo ligands of $f\text{-Al}_{13}$ have been calculated from variable temperature (VT) $^1\text{H-NMR}$ experiments. These studies serve as a preliminary comparison between $f\text{-Al}_{13}$ and $\kappa\text{-Al}_{13}$ that could help to inform how structural variability is related to reactivity.¹⁴⁹

V.2. General procedure for the synthesis of $f\text{-Al}_{13}$

$f\text{-Al}_{13}$ was prepared using a previously published synthesis.⁵³ Zn powder (87 mg, 1 mmol) was added to a scintillation vial containing $\text{Al}(\text{NO}_3)_3$ (100 mg, 2 mmol) dissolved in MeOH (10 mL). The vial was capped loosely and the resulting mixture was left to stir overnight until Zn dissolved completely. Once the final solution was transparent and particulate-free the vial was uncapped and the solution was left to evaporate. Within five days colorless, block crystals formed (35% yield).

V.3. $^1\text{H-NMR}$ spectroscopy

Variable-temperature NMR experiments were conducted using a Bruker Avance III-HD 600 NMR spectrometer. Three different experiments: 1) $\text{H}_2\text{O}/d_6\text{-Acetone}$, 2.5:1 (v/v); 2) $\text{H}_2\text{O}/d_6\text{-DMSO}$, 2:1 (v/v); and 3) D_2O were performed in order to span a temperature range of $-20\text{ }^\circ\text{C}$ to $75\text{ }^\circ\text{C}$. 16 scans were recorded over a sweep width of 20.0 KHz. Sample temperature was determined using low-temperature (4% MeOH in $d_4\text{-CD}_3\text{OD}$) and high-temperature (80% Ethylene glycol in 20%

DMSO-*d*₆) standards. VT NMR experiments were also performed on Al(NO₃)₃ as controls.

V.4. Dynamic and phase analysis light scattering

2 mL solutions of 50 mM *f*-Al₁₃ were prepared with different mol% ratios of H₂O:acetone solution mixtures (Table 5.1). Each sample was filtered through a 0.1 PTFE μm syringe filter into a cuvette to remove any particulate matter prior to analysis.

Table 5.1. Sample conditions for *f*-Al₁₃ in water/acetone light scattering experiments. 1 mL of each sample was prepared at an initial concentration of 0.10 M *f*-Al₁₃ in H₂O. The ratio of water to acetone (% mol/mol) was set so that the final concentration of *f*-Al₁₃ was 50 mM in 2 mL of total solution.

| % acetone | <i>f</i> -Al ₁₃ | H ₂ O | Acetone |
|-----------|----------------------------|------------------|---------|
| (V/V) | (mL) | (mL) | (mL) |
| 0 | 1.0 | 1.0 | 0.0 |
| 5 | 1.0 | 0.9 | 0.1 |
| 10 | 1.0 | 0.8 | 0.2 |
| 15 | 1.0 | 0.7 | 0.3 |
| 20 | 1.0 | 0.6 | 0.4 |
| 25 | 1.0 | 0.5 | 0.5 |
| 30 | 1.0 | 0.4 | 0.6 |
| 35 | 1.0 | 0.3 | 0.7 |
| 40 | 1.0 | 0.2 | 0.8 |
| 50 | 1.0 | 0.0 | 1.0 |

DLS was used to measure changes in the hydrodynamic radius (R_h) of the alumina species in solution. The Dynamics software uses the Einstein-Stokes equation ($R_h = K_b T / 6\pi\eta D_t$) where K_b = the Boltzmann constant, T = temperature in

kelvin, η = viscosity, and D_t = translational diffusion coefficient to solve for the R_h value. Viscosity measurements of **f-Al₁₃** in the H₂O : acetone mixtures were consistent with previously measured results.¹⁵⁰ Phase analysis light scattering (PALS) was then run subsequently to measure the change in conductivity and zeta potential as a function of mol% acetone. The samples were measured under an electric field frequency of 10 Hz, a voltage amplitude of 3.0 V and the values were averaged over a collection period of 20 seconds. Both measurements were taken using the Mobiuż instrument from Wyatt technologies.

V.5. Raman spectroscopy

Infrared spectra for both clusters were collected with a Nicolet 6700 ATR-IR spectrometer. Spectra spanning the range of 650 cm⁻¹ - 4000 cm⁻¹ were obtained with 64 scans at a resolution of 4 cm⁻¹.

V.6. Rate equations

Although there are several proton sites on **f-Al₁₃** that can exchange in solution, it is reasonable to assume that exchange between these sites is via the reservoir of bulk water and not intramolecular exchange. Thus the system can be treated with a two-site exchange model. The NMR line shape for the exchanging two-site system is calculable from the Bloch-McConnell equations, but here a more useful approximation is possible because the mole fraction of protons in water is much larger than the mole fraction of protons in the exchange sites on **f-Al₁₃**, and because exchange in the regime where two peaks can be resolved is slow. Under

these conditions the lifetime of a particular proton and activation parameters can be gauged from the variation of the line width with temperature (Equation 5.1):

$$\frac{1}{\tau} = \pi \cdot (FWHM_i - FWHM_o) \quad (5.1)$$

In this equation, the $FWHM_i$ corresponds to the measured line width and the $FWHM_o$ is the line width in the absence of exchange. The $FWHM_o$ is probably on the order of 2-3 Hz by analogy to the $^1\text{H-NMR}$ signals assigned to methyl groups in similar solutions. The experimental peaks show evidence of exchange broadening over a hundred Hz in line width; therefore the widths are negligible.

To test the accuracy of the approximation, six sets of data ($0.02 \leq \tau \leq 0.0008$ s) were generated by solving the Bloch-McConnell equations for two-site exchange and for two cases where $|v_w - v_{Al}|^{***} = 2000$ and 5000 Hz. In the simulations, the intensity of the $f\text{-Al}_{13}$ signal was set to 0.0005 that of the solvent proton signal to approximate our case where the concentrations of protons in exchanging sites differ by a large amount. The synthetic data were then treated as experimental results. In each case, the approximation was found to be appropriate and leads to estimates of residency times (τ) that are accurate to within a factor of two. This variation is within the uncertainties given by errors in the activation parameters that are exponentiated.

*** $|v_w - v_{Al}|$ is the difference in Hertz of the resonance of the $^1\text{H-NMR}$ signals from water and sites on the $f\text{-Al}_{13}$, respectively.

The temperature dependence of $k_{ex}^{(298)}$ (s^{-1}), the first-order rate coefficient for exchange of water molecules from the inner-coordination sphere to the bulk solution, takes the form of the Eyring equation (Equation 5.2):

$$\frac{1}{\tau} = k_{ex} = \frac{k_b \cdot T}{h} e^{\frac{\Delta S^\ddagger}{R}} e^{\frac{-\Delta H^\ddagger}{RT}} \quad (5.2)$$

where k_b is Boltzmann's constant and the exponential terms include the activation entropy $[\Delta S^\ddagger]$ and activation enthalpy $[\Delta H^\ddagger]$ for chemical exchange. The parameters T , R , and h are absolute temperature, the gas constant, and Planck's constant, respectively.

The increasing line widths with temperature were fit to a version of the Eyring equation. Implicit in this fitting is the assumption of a two-site exchange. Uncertainties are normally distributed for $\log(k_{ex}^{(298)})$, not $k_{ex}^{(298)}$, and were estimated by Monte Carlo propagation from uncertainties in the activation enthalpies derived from the Eyring equation.

V.7. H₂O/ Acetone-*d*₆

At -20°C and below, four resonances at 9.8 ppm (D), 7.8 ppm (C), 4.5 ppm (B), and 3.8 ppm (A) are observed in the spectra for **f-Al₁₃** (Figure 5.1). The peak at 9.8 ppm is also present in the spectrum for Al(NO₃)₃ and is assigned to the aluminum hexaaqua complex [Al(H₂O)₆]³⁺. The exchanges rates for two of the peaks are $\log(k_{ex}^{(298)}) = 4 \pm 1 s^{-1}$ and $3.0 \pm 0.2 s^{-1}$. $\log(k_{ex}^{(298)})$ for the η -OH₂ protons of **κ-**

\mathbf{Al}_{13} (observed at 8 ppm) was determined to be 3.7 s^{-1} (all values are listed in section V.10.). We hypothesize that these rates correspond to signals B and C because the FWHM does not change with temperature for peak A, and peak D is not related to $f\text{-Al}_{13}$. The assignment of peaks B and C to specific proton sites is explained in further detail in section V.8 and tandem computational analysis is introduced in Chapter VII, section 3.1.

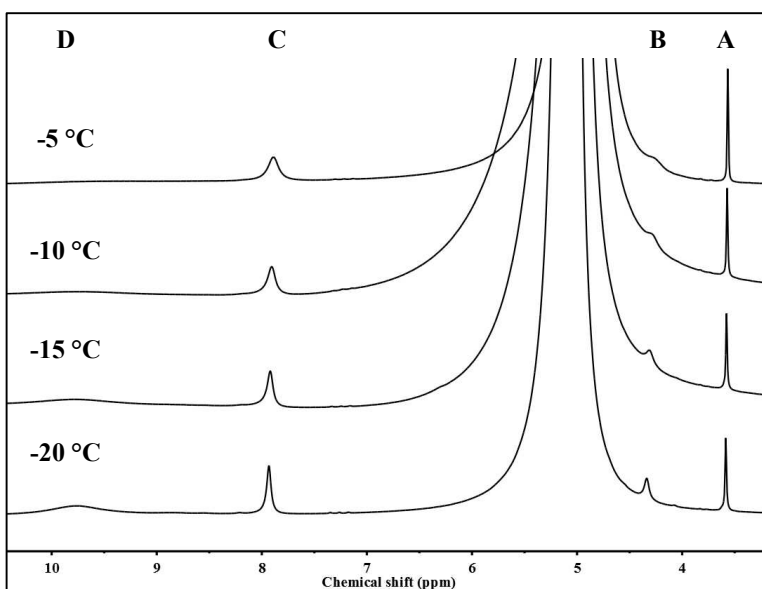


Figure 5.1. ^1H -NMR spectra ($-5 \text{ }^\circ\text{C}$ to $-20 \text{ }^\circ\text{C}$) of $f\text{-Al}_{13}$ in a 2.5:1 (v/v) mix of $\text{H}_2\text{O}/\text{acetone-}d_6$. The peak centered at 5.2 ppm is associated with bulk water in the solution. The peak at 9.8 ppm represents the hexaaqua $[\text{Al}(\text{H}_2\text{O})_6]^{3+}$ complex seen in the spectrum for $\text{Al}(\text{NO}_3)_3$. Peaks A, B, and C integrate to 1:1:2, respectively.

Over the entire temperature range the chemical shifts and integration values for $f\text{-Al}_{13}$ and $\kappa\text{-Al}_{13}$ signals are very similar.¹⁴⁹ Three proton resonances exist for $\kappa\text{-Al}_{13}$: $\mu_2\text{-OH}$, $\mu_2\text{-OH}'$, and H_2O . $f\text{-Al}_{13}$ contains three types of hydroxide protons in addition to the protons associated with water (Figure 5.2). The first set of

hydroxide protons ($\mu_3\text{-OH}$, green) connects the core aluminium ion to the middle ring of aluminium ions. The second set of protons ($\mu_2\text{-OH}$, purple) act as bridging ligands for the middle ring of aluminium ions. The third set ($\mu_2\text{-OH}'$, yellow) links the middle and outer rings of aluminium ions. Four water molecules fill the remaining coordination sites for each outer ring metal ion.

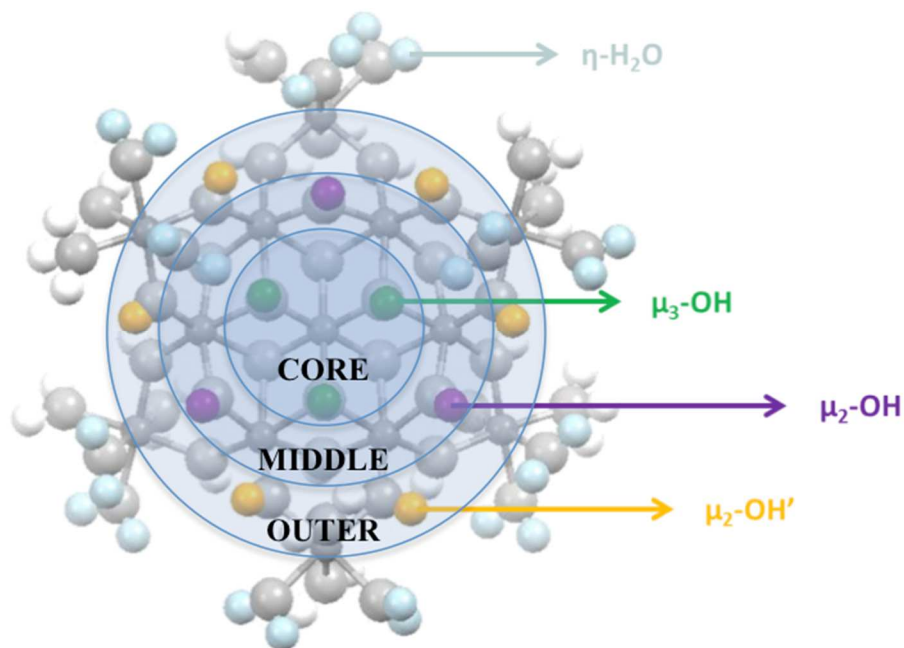


Figure 5.2. Diagram of $f\text{-Al}_{13}$ showing the different types of protons coordinated to the core ($\mu_3\text{-OH}$, green), middle ($\mu_2\text{-OH}$, purple), and outer ($\mu_2\text{-OH}'$, yellow) rings of aluminium metal ions. Water molecules are color-coded to reflect differences based upon symmetry, not coordination. Image was made using CrystalMaker.

V.7.1. DLS measurements at different acetone concentrations

If all proton resonances for $f\text{-Al}_{13}$ are accounted for, the integrations based upon chemical shifts equate to 1(A):1(B):2(C):4(D) respectively. However, the data does not reflect this. Therefore two possibilities exist: 1) the chemical shifts for

H₂O ligands on *f*-Al₁₃ are not visible due to rapid exchange on the NMR timescale, or 2) *f*-Al₁₃ is rearranging to form *κ*-Al₁₃. Dynamic and phase analysis light scattering (DLS and PALS, respectively) and infrared spectroscopy were used to investigate this potential rearrangement further.

DLS results show that the hydrodynamic radius (R_h) of *f*-Al₁₃ decreases from 1.00 nm ± 0.05 nm to approximately half its original size at 0.55 nm ± 0.09 nm with increasing mol % of acetone (Figure 5.3). ¹H-DOSY experiments, where R_h = 0.6 nm ± 0.4 nm and 1.2 nm ± 0.3 nm for *κ*-Al₁₃ and *f*-Al₁₃, respectively, corroborated these DLS values.¹⁵ Since R_h is influenced by the overall charge of a molecule, it is easy to speculate that the resultant species is *κ*-Al₁₃ based upon the decreased charge of *κ*-Al₁₃ (+7) compared to *f*-Al₁₃ (+15). Viscosity effects can be ruled out due to the fact that the measured diffusion coefficients readily increase even though the viscosities at lower mol % of acetone (< 5% acetone) are higher relative to water (η = 1.019 cP at 20 °C).

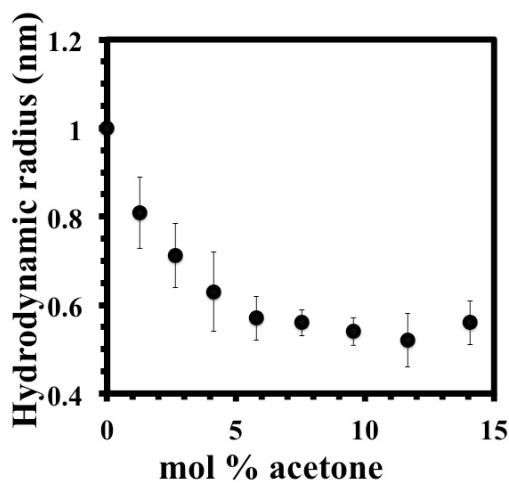


Figure 5.3. Hydrodynamic radius of *f*-Al₁₃ as a function of mol % acetone.

V.7.2. PALS measurements at different acetone concentrations

A similar trend is also observed with conductivity (σ) and zeta potential (ζ) measurements. The conductivity drops to half of its original value from 5.0 mS/cm to 2.5 mS/cm as acetone is added to the solution (Figure 5.4). The zeta potential decreases sharply from +54 mV to +0.5 mV at 10 mol % acetone before leveling out. A drop in potential and conductivity at constant concentration is indicative of cation aggregation that will eventually lead to precipitation.^{151,152} However, since there is no observable increase in size or precipitation over time, ion association is not occurring. The most probable scenario is that acetone begins to hydrogen bond with **f-Al₁₃**, effectively displacing nitrate ions in the coordination sphere. The analogous $[\text{Ga}_{13}(\mu_3\text{-OH})_6(\mu_2\text{-OH})_{18}(\text{H}_2\text{O})_{24}]^{15+}$ (**f-Ga₁₃**) has a radius of gyration (R_g) (core size without the influence of counterions) of $0.6 \text{ nm} \pm 0.2 \text{ nm}$ and an R_h of $0.90 \text{ nm} \pm 0.08 \text{ nm}$.¹⁰³ Assuming **f-Al₁₃** has a similar core size to that of **f-Ga₁₃**, what is observed via DLS at higher mol % of acetone is closer to the core size of the cluster. This is possible because the hydrogen bonding interactions between the acetone carbonyl group and **f-Al₁₃** water ligands of the clusters are greater than the $\text{NO}_3^- : \text{H}_2\text{O}$ interactions. The overall size of the ionic sphere surrounding the cluster shrinks as the acetone is continuously added, resulting in a smaller R_h .

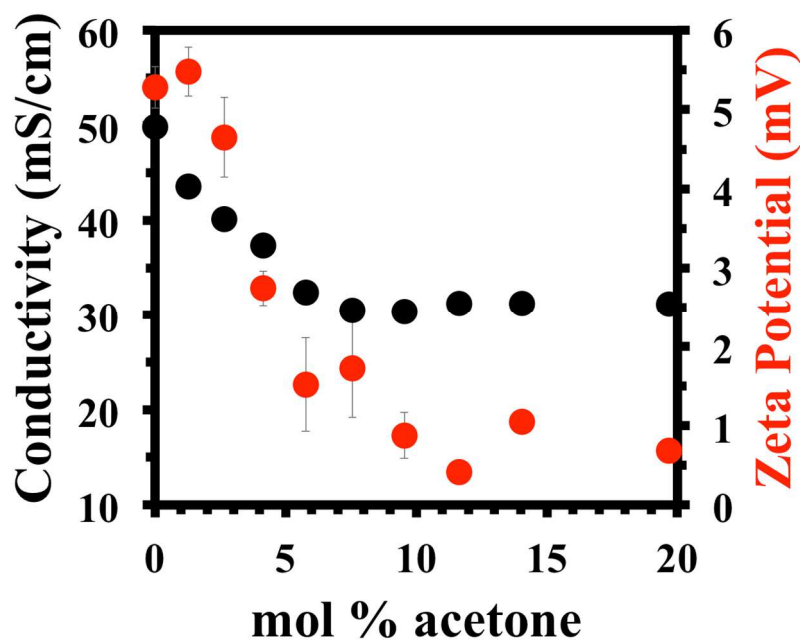


Figure 5.4. Conductivity and zeta potential measurements for *f*-Al₁₃.

V.7.3. Infrared spectroscopy analysis of hydrogen bonding interactions

ATR-IR spectra of a 1 M *f*-Al₁₃ solution (14 mol % acetone) were compared to spectra of 14 mol % acetone in water and pure acetone (Figure 5.5). The spectra reveal that the C=O stretching vibration at 1711 cm⁻¹ for acetone red shifts to 1698 cm⁻¹ while the C—H deformation mode (1355 cm⁻¹) and C—C (1219 cm⁻¹) blue shift to 1362 cm⁻¹ and 1234 cm⁻¹ respectively. These observed spectral shifts are common and well-studied for C=O•••H—OH bonding interactions. The red shift of the C=O bond is due the elongation of this bond while the blue shifts are caused by the shortening of the C—H and C—C bonds.¹⁵³ These interactions are pronounced at lower acetone quantities (mol % ≤ 15) and likely occurring between water molecules on *f*-Al₁₃ and acetone in solution.

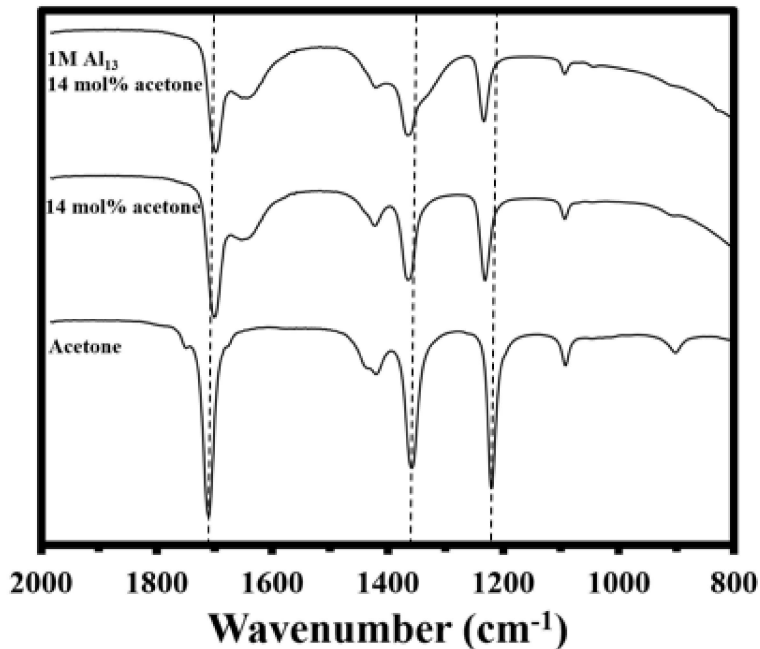


Figure 5.5. Stacked ATR-IR spectra of (top) 1M $f\text{-Al}_{13}$ in 14 mol% acetone in H_2O , (middle) 14% acetone in an H_2O mixture, and (bottom) pure acetone.

V.8. $\text{H}_2\text{O}/\text{DMSO-}d_6$

Two peaks are present for $f\text{-Al}_{13}$ at 7.6 ppm (C) and 3.6 ppm (A) near 5 °C (Figure 5.6).^{†††} This is different in comparison to the $\text{Al}(\text{NO}_3)_3$ spectra in which one peak at 9.5 ppm is observed. The exchange rate for the two peaks are $\log(k_{ex}^{(298)}) = 3.0 \pm 0.6 \text{ s}^{-1}$ and $1.4 \pm 0.5 \text{ s}^{-1}$, respectively. $\log(k_{ex}^{(298)})$ for the two sets of $\mu_2\text{-OH}$ protons of $\kappa\text{-Al}_{13}$ (observed near 3.8 ppm) was determined to be 1.9 s^{-1} and 0.7 s^{-1} . The exchange rate for protons (C) in both $\text{H}_2\text{O}/d_6\text{-Acetone}$ and $\text{H}_2\text{O}/d_6\text{-DMSO}$ solvent mixtures is the same and since the integration for this signal is twice that of (A) and (B), we assign peak (C) to the $\mu_2\text{-OH}'$ protons. Signal (A) has the shortest lifetime (hence, the longest residency time), which indicates it is associated with the least acidic protons – either the $\mu_2\text{-OH}$ or $\mu_3\text{-OH}$

^{†††} The signals are labeled to match the scheme used in the $\text{H}_2\text{O}/\text{acetone-}d_6$ experiment as the proton signals are related to the same proton sites.

protons. Of both sets of protons, the μ_3 -OH are expected to be more acidic due to the strained geometry around the oxygen atom. With increasing temperatures (-20 °C to 75 °C) the μ_3 -OH signal broadens until it is lost in the spectral baseline. From this, the preliminary assignment of μ_3 -OH protons is to peak (B). Therefore peak (A) can be assigned to the μ_2 -OH protons.

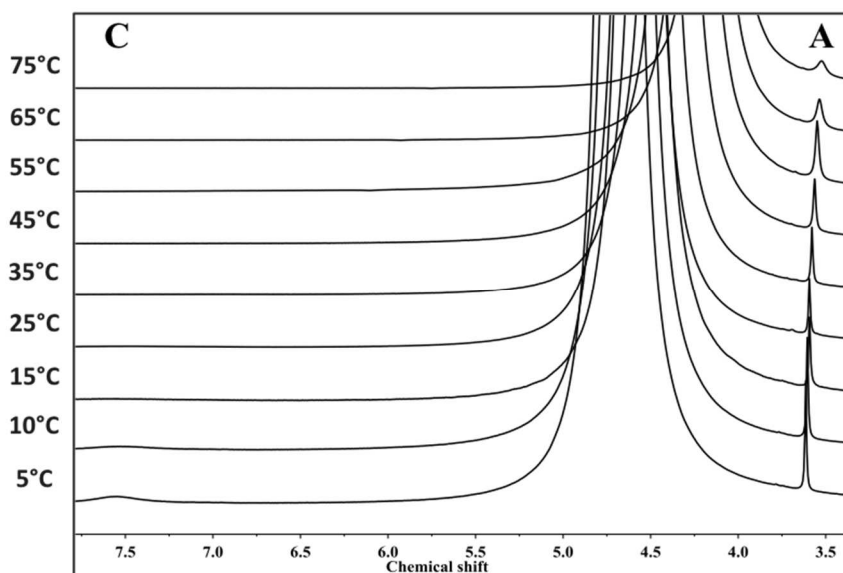


Figure 5.6. ^1H -NMR spectra of variable-temperature experiment for $f\text{-Al}_{13}$ in a 1:2 (v/v) solution of $\text{H}_2\text{O}/\text{DMSO-}d_6$.

A number of ^1H -NMR peaks assigned to bound hydroxyls broaden significantly over an extended temperature range (Table 5.2), suggesting that the bound protons are in dynamic equilibrium with water in the solvent. Proton transfer must be in the slow-exchange regime because the frequency separation is large between the

proton signals corresponding to the *f*-Al₁₃ and the peak centered at 5.2 ppm that is assigned to bulk water in the solvent.^{149,154}

Table 5.2. Full-width half-max (FWHM) values for the proton signal for *f*-Al₁₃ at 3.6 ppm in a 1:2 (v/v) solution of H₂O/ DMSO-*d*₆.

| Temp (°C) | FWHM (Hz) |
|------------------------|-----------|
| 3.61 - 3.52 (C) | |
| 0 | 9.12 |
| 5 | 9.98 |
| 15 | 11.64 |
| 35 | 14.05 |
| 45 | 18.03 |
| 50 | 41.17 |
| 60 | 72.13 |

A closer look at the kinetics for the peak at 3.6 ppm reveals an interesting feature (Figure 5.7). In only one case, the line widths reached a minimum with temperature and began to reverse. This suggests that very low temperatures were causing the tumbling of the molecule to slow appreciably and that this slower tumbling led to line width broadening. For this peak alone (3.6 ppm in the H₂O/DMSO-*d*₆ solution mixture), an Arrhenius-like relation was added to Equation 5.3 to approximate the increased broadening due to increased viscosity:

$$\frac{1}{\tau} = k_{ex} = \frac{k_b \cdot T}{h} e^{\frac{\Delta S^\ddagger}{R}} e^{\frac{-\Delta H^\ddagger}{RT}} + W_{298} e^{\frac{E}{RT}} \quad (5.3)$$

Where E and W are only fitting parameters and not essential to the analysis.

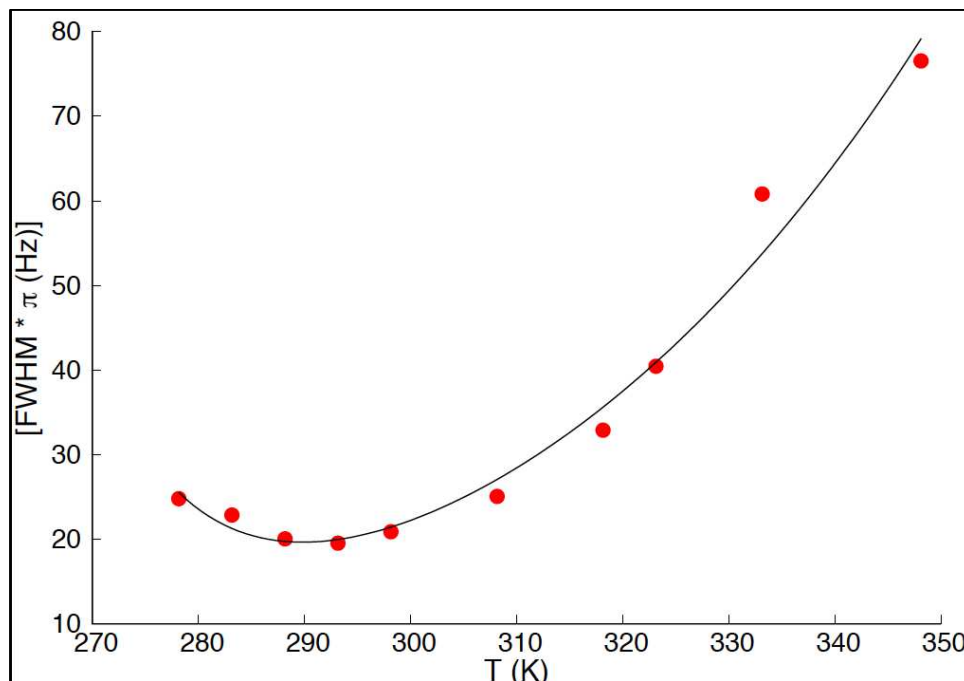


Figure 5.7. Plot of the kinetics data for the μ_2 -OH proton site (at 3.6 ppm) on $f\text{-Al}_{13}$ in a 1:2 (v/v) solution of $\text{H}_2\text{O}/\text{DMSO-}d_6$.

V.9. D₂O

One signal is visible for $f\text{-Al}_{13}$ between 3.45 ppm and 3.75 ppm over the temperature range of 10 °C to 40 °C (Figure 5.8). No signal is observed in the spectrum for $\text{Al}(\text{NO}_3)_3$ other than solvent confirming that the peak in the $f\text{-Al}_{13}$ spectrum is for hydroxyl protons on the tridecamer. Unfortunately, the exchange rate for this proton cannot be determined because the FWHM does not broaden or narrow with changing temperature. Therefore no exchange for this site is observable on the NMR timescale. The limited exchange and presence of this

signal suggests it is associated with a proton that is less acidic than the others on *f*-Al₁₃. Based upon chemical shift and known proton residency times, this peak is most likely for the μ₂-OH protons.

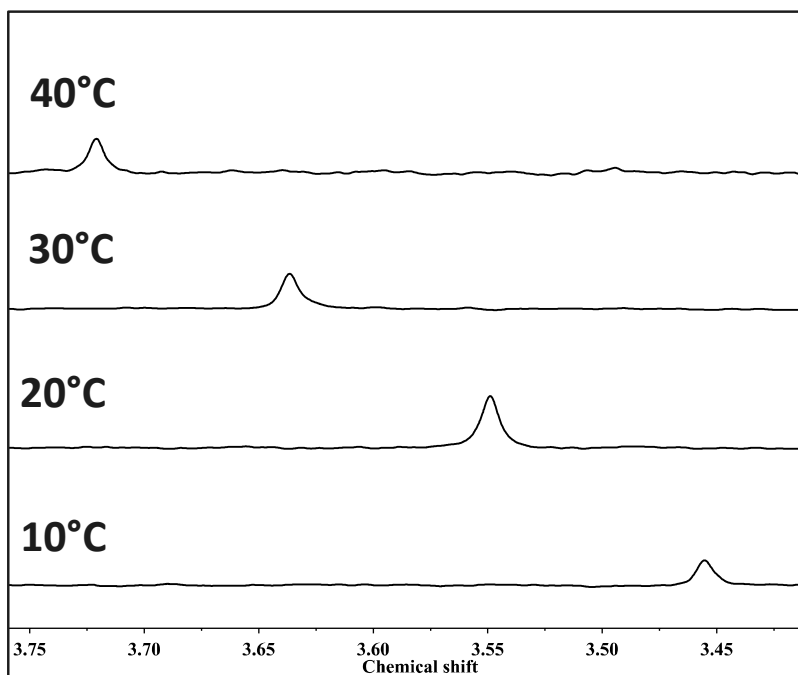


Figure 5.8. ¹H-NMR spectra of the variable-temperature experiment for *f*-Al₁₃ in D₂O.

V.10. Proton exchange rates for *f*-Al₁₃

The results for the three hydroxyl protons on *f*-Al₁₃ are compiled in Table 5.3 where the fitted activation parameters and the logarithms of estimated lifetimes

($\frac{1}{\tau} = k_{ex}$) of protons on various *f*-Al₁₃ bridging oxygen atoms are estimated.

Table 5.3. Exchange rates, residency times, and activation parameters for proton sites on *f*-Al₁₃. Standard errors are in parentheses.

| Proton site | $\log(k_{ex}^{(298)}/s^{-1})$ | Proton lifetimes (s) | ΔH^\ddagger (kJ·mol ⁻¹) | ΔS^\ddagger (J·mol ⁻¹ ·K ⁻¹) |
|--|-------------------------------|----------------------|---|---|
| H₂O/acetone-<i>d</i>₆ | | | | |
| μ ₃ -OH | 4(1) | 0.0001 | 44 (8) | -30(30) |
| μ ₂ -OH' | 3.0(0.2) | 0.001 | 32.8(0.7) | -78(3) |
| H₂O/DMSO-<i>d</i>₆ | | | | |
| μ ₂ -OH' | 3.0(0.6) | 0.001 | 39(3) | -60(10) |
| μ ₂ -OH | 1.4(0.5) | 0.040 | 22(3) | -146(8) |

The logarithms of the exchange coefficients are compiled because the uncertainties are large and derive largely from the ~10% standard errors assigned to the ΔH^\ddagger values, which are exponentiated to get k_{ex} . As mentioned previously uncertainties are normally distributed in $\log(k_{ex})$, not k_{ex} . The key point to derive from Table 5.3 is that the lifetimes are on the order of milliseconds ($k_{ex} \approx 10^3 s^{-1}$), which compares well with previous work on κ -Al₁₃ (Table 5.4).¹⁴⁹

Table 5.4. Exchange rates, residency times, and activation parameters for proton sites on κ -Al₁₃. Available standard errors are in parentheses.

| Proton site | $\log(k_{298}/s^{-1})$ | Proton lifetimes (s) | ΔH^\ddagger (kJ·mol ⁻¹) | ΔS^\ddagger (J·mol ⁻¹ ·K ⁻¹) |
|--|------------------------|----------------------|---|---|
| H₂O/acetone-<i>d</i>₆ | | | | |
| η-OH ₂ | 3.7 | 0.0002 | 33(2) | 65(7) |
| H₂O/DMSO-<i>d</i>₆ | | | | |
| μ ₂ -OH ^{fast} | 1.9 | 0.013 | 20(1) | 140(2) |
| μ ₂ -OH ^{slow} | 0.7 | 0.201 | 23 | 153 |
| D₂O | | | | |
| μ ₂ -OH ^{slow} | 1.9 | 0.013 | 31(1) | 106(3) |

The average lifetimes at 298 K for protons on the two sets of $\kappa\text{-Al}_{13}$ $\mu_2\text{-OH}$ bridges in a 2:1 H₂O : DMSO solution were estimated at: 0.013 and 0.2 s⁻¹, within uncertainties to the values estimated here for $f\text{-Al}_{13}$. What we cannot evaluate in this study is whether or not there are proton-enhanced pathways for exchange of the protons on $\mu_2\text{-OH}$ bridges, as was detected for one site in the $\kappa\text{-Al}_{13}$.

V.11. Conclusions

Variable temperature ¹H-NMR was used to determine the exchange rates and residency times of bridging hydroxyl protons on $f\text{-Al}_{13}$. Three types of protons ($\mu_3\text{-OH}$, $\mu_2\text{-OH}$, and $\mu_2\text{-OH}'$) have been identified and preliminary spectral assignments have been made. This information will be useful as geochemical reactions become important in the development of functional materials for electronics applications.¹⁴

V.12. Bridge to Chapter VI

The next chapter begins the discussion of new structures composed of new elements including transition metals. Although the example presented forthwith was not synthesized using the aforementioned procedures, Chapter VI shows that inorganic molecules with applications that extend beyond semiconductors can be synthesized through simple methods.

CHAPTER VI

AN ANIONIC $\{\text{Cu}(\mu\text{-OH})_2\text{Cu}\}$ RHOMB-CENTERED TETRANUCLEAR COPPER (II) SULFATE CLUSTER FORMS A 1-D HYDROGEN BONDED NETWORK IN THE CRYSTALLINE STATE

Dr. Lev N. Zakharov performed single-crystal XRD and Milton N. Jackson, Jr. performed Raman spectroscopy. I synthesized of the Copper (II) sulphate cluster and wrote the manuscript from which this chapter is adapted. Professor Dr. Darren W. Johnson was the principle investigator and edited the manuscript that resulted from this work, which was submitted to *Acta Cryst C*.

VI.1. Introduction

Simple copper salts have garnered interest for a variety of applications including the use of copper(II) sulfate pentahydrate as an herbicide and copper(II) arsenate as a wood preservative. More complex structures that incorporate copper into molecules containing multi-dentate oxygen and nitrogen-donating ligands have been developed and studied for a variety of applications such as molecular magnetism and gas adsorption.¹⁵⁵⁻¹⁵⁸ Notable studies of polynuclear copper structures have focused on compounds that function as

catalysts and mimics for biological processes.^{159–161} An interesting feature of a number of these species is the rhomb, or “diamond core” structure that is proposed to play a role in many metalloenzymatic processes. Several discrete high valent oxo compounds (composed of Ni^{III}, Co^{III}, and Cu^{III} metal ions) have been reported in the literature that contain a {M-(μ-O)₂-M} rhomb core.^{162–165} However, these complexes typically experience thermal instability at room temperature. The metal-oxo rhomb core is also found in transition metal coordination polymers with greater thermal stability, but the discrete {M-(μ-OH)₂-M} core is rarely observed.^{166,167}

The preparation and crystal structure of a new inorganic coordination cluster linked together in the crystalline state through hydrogen bonds, $\{(\text{C}_5\text{H}_5\text{NH})_2[\text{Cu}_4(\text{OH})_2(\text{SO}_4)_4(\text{H}_2\text{O})_4]\}_n$ (1) is reported herein. This anionic species is composed of tetranuclear divalent Cu ion subunits that each contain a {M-(μ-OH)₂-M} rhomboid core. The subunits are connected in a 1-D array through hydrogen bonds between the pyridinium counteranions and the sulfato ligands. Surprisingly, in the presence of a huge excess of pyridine, the tetramer prefers hydrogen-bonding to the pyridinium ion over direct coordination to this organic molecule as is seen with related structures crystallized from other solvents.¹⁶⁷ This structure also represents a new contribution to the small but growing class of all-inorganic Cu-based cluster compounds.

VI.2. Synthesis of $\{(\text{C}_5\text{H}_5\text{NH})_2[\text{Cu}_4(\text{OH})_2(\text{SO}_4)_4(\text{H}_2\text{O})_4]\}_n$

A solution of 0.05 M CuSO₄ and 0.05 M Ni(NO₃)₂ (50:50 v/v mix, 1 mL total, both in DMF) was placed into a test tube. A 0.05 M solution of pyridine in MeOH (1 mL) was

slowly added to this test tube using a syringe. The pyridine solution formed a layer above the metal salt solution - after a few days the pyridine solution diffused into the metal salt solution. Ethyl acetate (EtOAc) was added to the contents of the test tube via vapor diffusion and after several weeks light green crystals formed (9% isolated yield).

VI.3. Crystal structure determination

Single-crystal x-ray diffraction was performed on a Bruker Smart Apex diffractometer 173(2) K using Mo K α radiation ($\lambda = 0.71073 \text{ \AA}$). Adsorption corrections were applied by SADABS. The structure was solved by direct methods completed by subsequent difference Fourier syntheses, and refined by full-matrix least-squares procedures on F^2 . All non-hydrogen atoms were refined with anisotropic thermal parameters. All calculations were performed by the Bruker SHELXTL package. Selected bond lengths and angles are summarized in Table 6.1.

Table 6.1. Selected bond lengths and angles for (1).

| | Bond length (\AA) | | Bond angle ($^\circ$) |
|------------------|--|--------------------|---|
| Cu(1)-O(10) | 1.9588(16) | O(10)-Cu(1)-O(2) | 88.34(6) |
| Cu(1)-O(2) | 1.9830(15) | O(2)-Cu(1)-O(1) | 97.17(6) |
| Cu(1)-O(1) | 2.0028(15) | O(10)-Cu(1)-O(1A) | 90.80(6) |
| Cu(1)-O(1A) | 2.0321(15) | O(1)-Cu(1)-O(1A) | 84.08(6) |
| Cu(1)-O(6) | 2.2692(16) | O(10)-Cu(1)-O(6) | 94.64(6) |
| Cu(1)-Cu(1A) | 2.9967(6) | O(10)-Cu(1)-Cu(1A) | 132.20(5) |
| Cu(2)-O(7) | 1.9173(16) | O(7)-Cu(2)-O(1) | 95.02(7) |
| Cu(2)-O(11) | 1.9621(15) | O(7)-Cu(2)-O(3) | 108.32(8) |
| Cu(2)-O(1) | 1.9690(15) | O(11)-Cu(2)-O(3) | 88.51(6) |
| Cu(2)-O(3) | 2.2141(17) | Cu(2)-O(1)-Cu(1) | 121.58(7) |
| O(2)-Cu(1)-O(6) | 91.19(6) | Cu(2)-O(1)-Cu(1A) | 122.72(7) |
| O(1)-Cu(1)-O(6) | 90.59(6) | Cu(1)-O(1)-Cu(1A) | 95.92(6) |
| O(1A)-Cu(1)-O(6) | 84.96(6) | O(7)-Cu(2)-O(11) | 85.60(7) |

VI.4. Crystallographic structure analysis

$\{(C_5H_5NH)_2[Cu_4(OH)_2(SO_4)_4(H_2O)_4]\}_n$ is comprised of two distinct Cu centers. The distorted octahedral copper(II) ions (Cu1 in Figure 6.1) are bridged by two μ_3 -OH groups to form a centro-symmetric $\{Cu(\mu-OH)_2-Cu\}$ rhomb core. The Cu-O distances in the equatorial plane, (1.9568(16)-2.0321(15) Å) are significantly shorter than the Cu-O distances in the apical positions (2.2692(16) and 2.523(2) Å). A search of the Cambridge Crystallographic Data Centre (CCDC) identifies several structures with similar octahedral coordination modes, containing four short and two long Cu-O distances in equatorial and apical positions.¹⁶⁸

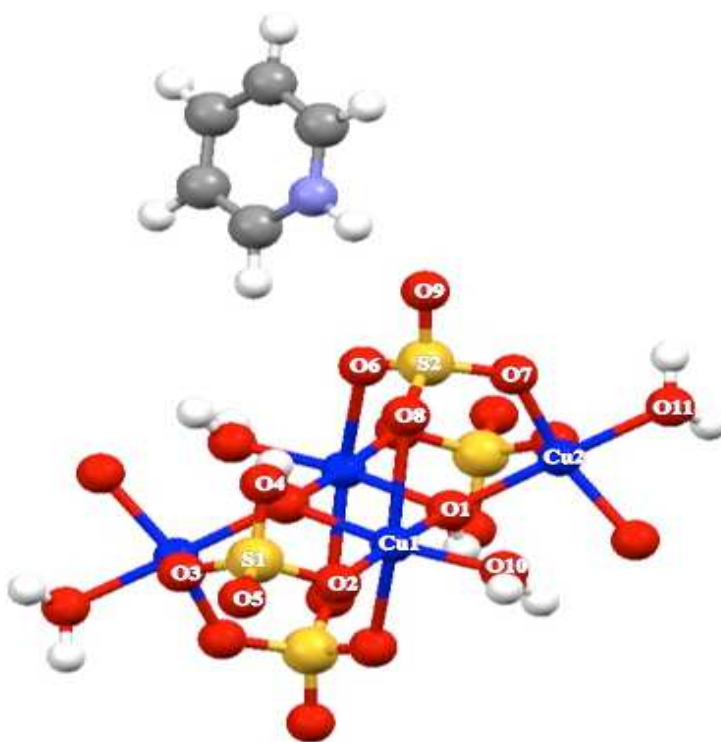


Figure 6.1. Ball and stick representation of the $\{(C_5H_5NH)_2[Cu_4(OH)_2(SO_4)_4(H_2O)_4]\}_n$ tetramer. The pyridinium cation hydrogen bonds to the μ_3 -sulfato ligand and water ligand of two adjacent Cu_4 subunits. Oxygen and sulfur atoms neighboring Cu1 and Cu2 are labeled (hydrogen labels omitted for clarity).

The core is connected to the trigonal bipyramidal copper(II) ions (Cu2) by four μ_3 -sulfato ligands; water fills the remaining coordination sites of each CuO_6 site. Each sulfato ligand bridges three Cu ions creating two $\text{Cu}_3(\mu_3\text{-OH})$ edge-shared tetrahedra. One of the equatorial Cu-O distances in the trigonal bipyramid is longer compared to two others, 2.2141(17) Å vs. 1.9173(16) and 1.9509(16) Å. The Cu-O(OH) and Cu-O(H_2O) distances for the apical positions are close to each other at 1.9690(15) Å and 1.9621(15) Å, respectively.

The inversion center about the central $\text{Cu}_2(\text{OH})_2$ rhomb establishes a symmetry that leads to two dimeric units bridged by the rhomb core. The chemical formula of this structure is closely related to that of the natrochalite-type mineral $[\text{NaCu}_2(\text{SO}_4)_2(\text{OH})\cdot\text{H}_2\text{O}]$ although natrochalite only has octahedral Cu ions and no $\{\text{M}(\mu\text{-OH})_2\text{-M}\}$ bridging sites.

(1) is linked to form an anionic 1-D chain that propagates along the a axis (Figure 6.2a) in a similar manner to $\{((\text{NH}_2)\text{C}_5\text{H}_4\text{NH})[\text{Cu}_2(\text{OH})(\text{SO}_4)(\text{H}_2\text{O})]\}_n$, which was reported by Lah and coworkers.¹⁶⁹ In the crystal structure these 1-D chains are joined into a 3-D network by hydrogen bonds forming between the terminal water molecules and SO_4 units (Figure 6.2b). The extended 3-D network is charge balanced by pyridinium ions held within the network channels by N-H...O and C-H...O hydrogen bonding to the 1-D chains. The cations are stacked inside the network channels with distances between their average planes of 3.707 Å indicating a weak π - π stacking interactions between them as well.

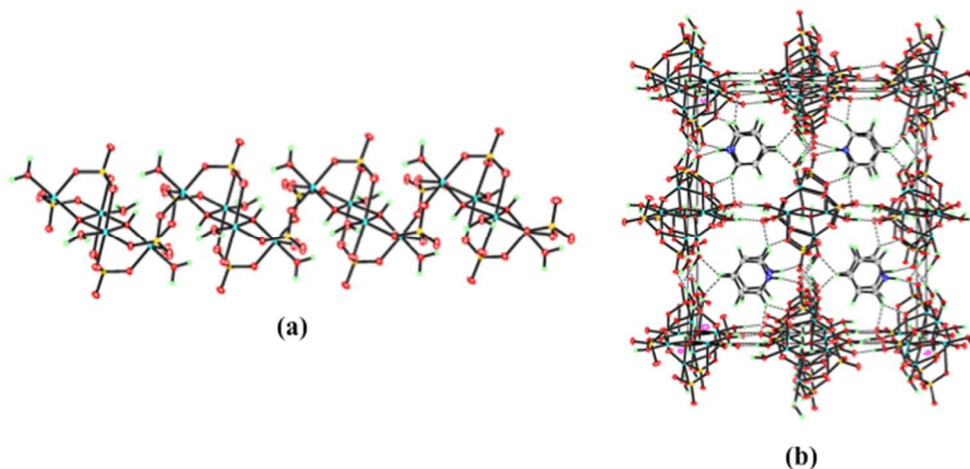


Figure 6.2. A fragment of $\{[\text{Cu}_4(\text{OH})_2(\text{SO}_4)_4(\text{H}_2\text{O})_4]\}_n$ 1-D chain (a) and the view of the packing of $\{(\text{C}_5\text{H}_5\text{NH})_2[\text{Cu}_4(\text{OH})_2(\text{SO}_4)_4(\text{H}_2\text{O})_4]\}_n$ along the a axis. H-bonds are drawn by dash lines. Ellipsoids are presented at the 30% probability level.

The role of $\text{Ni}(\text{NO}_3)_2$ in the reaction is not clear; however, when it is not included as a synthetic reagent, the resulting product is the previously published $\{[\text{H}_2\text{N}(\text{CH}_3)_2][\text{Cu}_2(\text{OH})(\text{SO}_4)_2(\text{H}_2\text{O})_2]\}_n$ coordination polymer.¹⁷⁰ In that structure dimethylammonium cations form hydrogen bonds within the polymer network, linking the dimeric chains into 2-D sheets. The variations observed between these two extended structures are proposed to be due to the presence of dimethylamine, a product of DMF hydrolysis. In addition, several related Cu polynuclear compounds with similar structural features to $\{(\text{C}_5\text{H}_5\text{NH})_2[\text{Cu}_4(\text{OH})_2(\text{SO}_4)_4(\text{H}_2\text{O})_4]\}_n$ have been reported in the literature that contain organic ligands such as tetrazole, pyridine, and other N-donating ligands that directly coordinate to the Cu cluster core.^{170–173} This all inorganic Cu tetramer is a new structure type in that regard, and given the interest in purely inorganic clusters as precursors for metal oxide and related functional films, this cluster type provides a new addition to the field.^{1,47,53,174} The bond lengths and angles of the $\{\text{M}-(\mu\text{-OH})_2\text{-M}\}$ motif

for $\{(C_5H_5NH)_2[Cu_4(OH)_2(SO_4)_4(H_2O)_4]\}_n$ fall within the range observed for other complexes featuring the $\{M-(\mu-O)_2-M\}$ rhomb core (Figures 6.3 and 6.4).¹⁷⁵

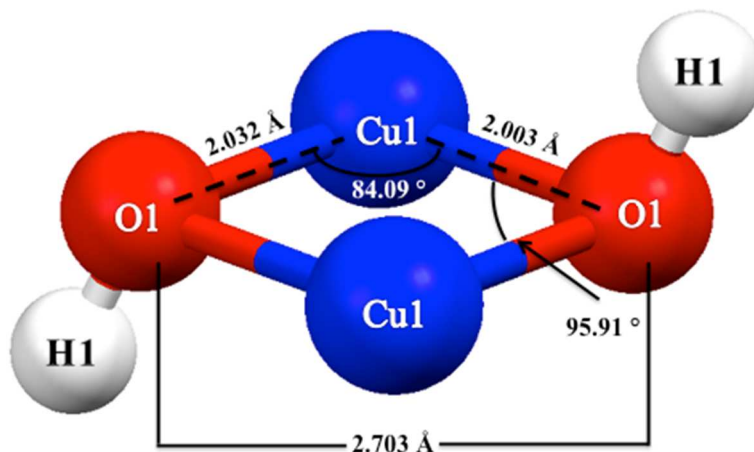


Figure 6.3. Selected bond lengths and angles for the rhomboid $\{M-(\mu-OH)_2-M\}$ core of $\{(C_5H_5NH)_2[Cu_4(OH)_2(SO_4)_4(H_2O)_4]\}_n$. Atoms are not to scale.

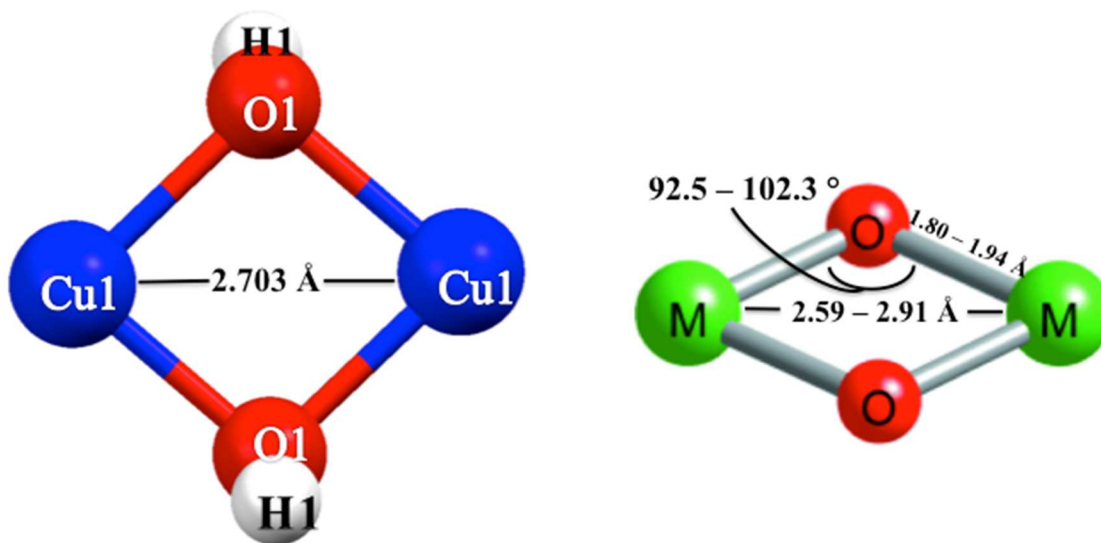


Figure 6.4. Bond lengths and angles for $\{(C_5H_5NH)_2[Cu_4(OH)_2(SO_4)_4(H_2O)_4]\}_n$ (left) and ranges observed for the rhomboid core in related $\{M(\mu-O)_2-M\}$ sites (right). Image on the right from Que, *et. al.* Atoms are not shown to scale.

VI.5. Raman spectroscopy analysis

Raman spectra of a single crystal of $\{(C_5H_5NH)_2[Cu_4(OH)_2(SO_4)_4(H_2O)_4]\}_n$ were collected using an Alpha 300S SNOM confocal Raman microscope in a 180° backscattering configuration. A continuous wave pump laser provided ~ 60 mW of power with an excitation wavelength of 532 nm. A 0.3 m spectrometer equipped with 600 grooves/mm grating was used to detect Raman scattering with a spectral resolution of 2.5 cm^{-1} . The spectra from the copper cluster were averaged over 500 accumulations at 0.75 s exposure time per scan. The intense Si signature at 520.5 cm^{-1} was used as an internal reference.

Raman spectroscopy provides additional information about the coordination and bonding environment of the Cu cluster. A spectral comparison between liquid pyridine, cupric sulfate, and single crystalline $\{(C_5H_5NH)_2[Cu_4(OH)_2(SO_4)_4(H_2O)_4]\}_n$ is shown in Figure 6.5. An expanded inset of the Raman spectrum for the copper tetramer (Figure 6.5c) reveals several weak modes between 2800 cm^{-1} and 3700 cm^{-1} , most notably the weak, narrow O-H stretching vibration of the bridging metal center $\{M-(\mu-OH)_2-M\}$ at 3572 cm^{-1} . In addition, the intense C-H symmetric stretching band at 3052 cm^{-1} for pyridine (Figure 6.5b) is not present in the copper tetramer spectrum, signifying an overall lowering in the C_{2v} symmetry of pyridine due to interactions with the tetramer. This loss of symmetry is further suggested by the disappearance of the ring bending modes at 978 cm^{-1} and 1022 cm^{-1} (Figure 6.5a).¹⁷⁶

The doubly degenerate sulfato symmetry stretching modes of cupric sulfate at 1016 cm^{-1} and 1045 cm^{-1} are not present in the copper cluster. This symmetric stretching mode of

sulfate is observed as a sharp intense peak at 979 cm^{-1} , a very common feature among many similar copper-based minerals with sulfate as a counterion.^{176,177} Several weak features present from $100\text{ cm}^{-1} - 600\text{ cm}^{-1}$ can be assigned to various Cu-O and sulfato bending and anti-symmetric stretching modes. Three weaker modes also appear at 832 cm^{-1} , 866 cm^{-1} , and 883 cm^{-1} for the copper tetramer that are related to the $\{\text{M}-(\mu\text{-OH})_2\text{-M}\}$ anti-symmetric stretching vibrations.

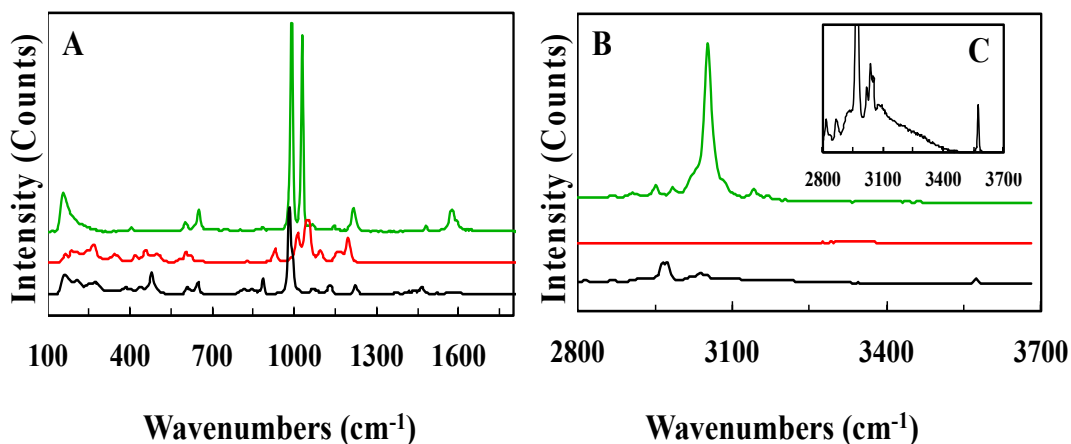


Figure 6.5. Stacked Raman spectra of pyridine (green), cupric sulfate (red), and $\{(\text{C}_5\text{H}_5\text{NH})_2[\text{Cu}_4(\text{OH})_2(\text{SO}_4)_4(\text{H}_2\text{O})_4]\}_n$ (black). A) $100\text{ cm}^{-1} - 1700\text{ cm}^{-1}$ B) $2800\text{ cm}^{-1} - 3700\text{ cm}^{-1}$. C) inset of the copper cluster from 2800 cm^{-1} to 3700 cm^{-1} .

VI.6. Conclusions

The 1-D structure $\{(\text{C}_5\text{H}_5\text{NH})_2[\text{Cu}_4(\text{OH})_2(\text{SO}_4)_4(\text{H}_2\text{O})_4]\}_n$ was synthesized and characterized using single crystal X-ray diffraction and Raman spectroscopy. The $\{\text{Cu}-(\mu\text{-OH})_2\text{-Cu}\}$ rhomboid core of each tetramer is coordinated to an adjacent tetramer to form connected 1D strands that are linked to planar pyridinium

countercations arranged in π - π stacking motifs hydrogen bonded to the sulfato ligands of the tetramers. The unique anionic nature and rhomboid features of this structure add a new compound in a small class of all inorganic copper structures.

VI.7. Bridge to Chapter VII

Chapter VI is the final chapter to focus on comprehensive studies. Chapter VII begins with a summary of the research presented in this dissertation then concludes potential projects that can be further developed and continued on by future graduate students.

CHAPTER VII

CONCLUSIONS AND FUTURE OUTLOOKS

VII.1. Introduction

For the duration of a Ph.D. career, research is performed and papers are written to detail scientific discoveries from that time. Usually new ideas and research directions arise that cannot be undertaken within five or six years. This chapter is here to share thoughts (a glimpse) toward the future for Group 13 tridecamer analysis and inorganic cluster development. First up is a summary of the research presented throughout the pages of this dissertation. Then descriptions of studies and experiments that are currently in their infancy will follow; continuing the work from Chapters II through VI and highlighting new opportunities that can help to further our understanding of these Group 13 tridecamers and unlock alternative synthetic approaches for a variety of structures with a myriad of applications in future technology development.

VII. 2. Research summary

The research presented in this dissertation falls into the category of either characterization or synthesis. The full complement of single crystal data was given in Chapter II showing how one synthetic method can produce different structures in the $f\text{-Ga}_{13-x}\text{In}_x$ cluster family by only varying the ratios of starting material. These ratios also dictate the types of metal oxides that form when these clusters are heated in a manner comparable to the annealing process of thin films. Chapter III took characterization a step further and showed the efficacy of SSNMR in identifying the local environments of gallium ions within the $f\text{-Ga}_{13}$ tridecamer. Although this structure is rather symmetric, SSNMR was used to verify different metal ion environments due to distortions in the octahedral geometry around the gallium ions in each ring of the cluster. Chapter IV introduced a new method of synthesis that expands the library of Group 13 tridecamers to include heterometallic $f\text{-Al}_{13-x}\text{In}_x$ clusters that are otherwise difficult to produce. Now comparisons can be made between all heterometallic analogues in both the solid and solution states. Chapter V delves in to the solution characterization of aluminum compounds, focusing on the $f\text{-Al}_{13}$ tridecamer, which is similar to the well-studied $\kappa\text{-Al}_{13}$. Here we begin to investigate the geological relevance of $f\text{-Al}_{13}$ and try to start piecing together some of the questions about the reactivity (i.e., transmetalation and aggregation) we observe. Synthesis is again discussed in Chapter VI, but this time it is to introduce a new copper-based cluster.

VII. 3. Future outlooks

VII.3.1. Computational peak assignments for *f*-Al₁₃

The solution ¹H-NMR of *f*-Al₁₃ varies depending on the solvent medium (Table 7.1). Protic solvents act as a source of H⁺ leading to a significant amount of exchange between water molecules bound to the tridecamer and the deuterated solvent. In deuterated methanol (CD₃OD, *d*₄-MeOH) for example, residual protons from trace MeOH are observed. Exchange between solvent deuterium atoms (²D) and the protons on the bound water molecules lead to a single HOD peak. No other protons are visible, which makes it difficult to analyze these tridecamers. Aprotic solvents do not have an acidic proton, therefore exchange between the water ligands and solvent involves a ligand-exchange event in which the tridecamer can be observed in various stages of ligand substitution.

Table 7.1. Protic and aprotic solvents in which the *f*-Al₁₃ tridecamer is soluble.

| Solvent | Dielectric constant (ε) | Dipole moment (D) |
|--------------------------|-------------------------|-------------------|
| Protic solvents | | |
| MeOH | 33 | 1.70 |
| H₂O | 80 | 1.85 |
| Aprotic solvents | | |
| THF^{***} | 7.5 | 1.75 |
| Acetone | 21 | 2.88 |
| DMF | 38 | 3.82 |
| MeCN | 37 | 3.92 |
| DMSO | 47 | 3.96 |

^{***} Tetrahydrofuran (THF) is classified as a borderline polar aprotic solvent.

VII.3.2. Precursor ecological toxicity studies

A concern regarding the manufacture and use of semiconductors is the toxicity associated with the waste streams generated from processing and recycling. In collaboration with Dr. Stacey Harper (Oregon State University), we have begun to test the toxicity of the Group 13 tridecamers along with other CSMC functional film precursors. The results show that no significant mortality of Zebrafish occurred with $f\text{-Al}_{13}$ over a 5-day test period, even at the highest dose tested (250mg/L). Yolk sac edema (swelling around the yolk sac) was noted at the highest test concentration in 100% of the embryos (n=21) surviving to 120 hours post fertilization (Figure 7.1).

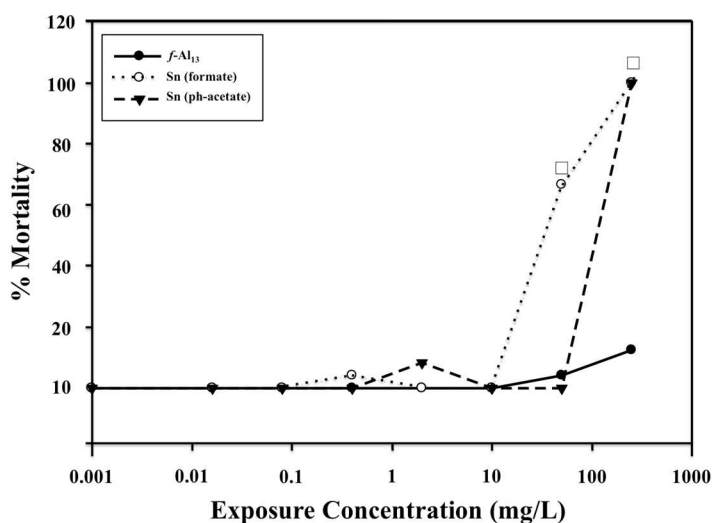


Figure 7.1. A comparison of Zebrafish mortality for $f\text{-Al}_{13}$ and organotin complexes. $f\text{-Al}_{13}$ has low mortality in comparison to Sn (formate) and Sn (phenylacetate) complexes for which significant mortality occurred at 50 mg/L and 250 mg/L, respectively.

$f\text{-Ga}_{13-x}\text{In}_x$ compounds are orders of magnitude less toxic than $f\text{-Ga}_{13}$ (Figure 7.2). Interestingly, both $f\text{-Ga}_7\text{In}_6$ and $f\text{-Ga}_{10}\text{In}_3$ show nearly identical mortality

concentrations. Making comparisons between these and the remaining $f\text{-Ga}_{13-x}\text{In}_x$ tridecamers, as well as $f\text{-Ga}_{13}$, will be important when considering the how composition affects the performance of these materials as precursors for functional thin film semiconductors.

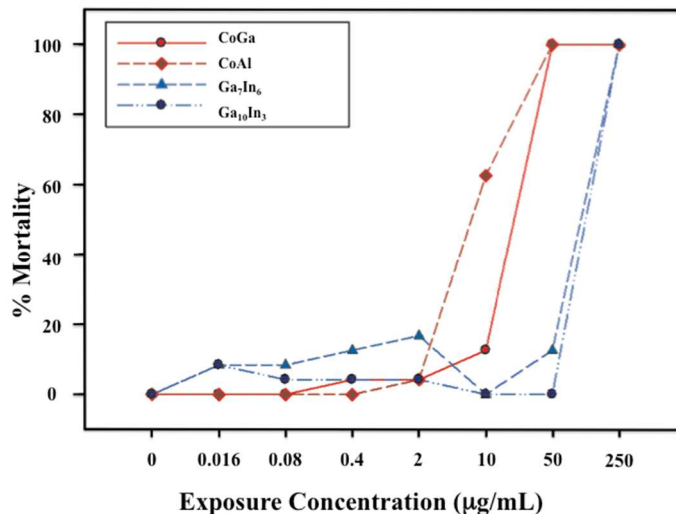


Figure 7.2. A comparison of Zebrafish mortality for $f\text{-Ga}_7\text{In}_6$, $f\text{-Ga}_{10}\text{In}_3$, and CoM (M = Al and Ga) complexes. Higher toxicity (and higher variance in the amount of toxicity) was observed for the Co samples with CoGa being most toxic.

VII.3.3. DLS and SAXS studies on $f\text{-Al}_7\text{In}_6$

Chapter IV discussed preliminary size and structural solution phase analysis for $f\text{-Al}_{13}$ and $f\text{-Al}_7\text{In}_6$ using $^1\text{H-NMR}$, $^1\text{H-DOSY}$, and DLS. The next step is to start probing the mechanism for oligomer growth, which will be easiest to study by following the transmetalation reaction. Previous experiments and knowledge about how these structures aggregate suggest that the metal ions of the central and

middle rings of $f\text{-M}_{13}$ are bound together and form a stable unit that remains unperturbed in solution. The association and dissociation of indium and aluminium, respectively, can be tracked by monitoring changes in the size, conductivity, and potential of a reaction solution throughout the transmetalation process.

VII.3.3.1. Dynamic light scattering experiments

When $\text{In}(\text{NO}_3)_3$ is added to a solution of $f\text{-Al}_{13}$, a heterometallic $f\text{-Al}_x\text{In}_{13-x}$ cluster will form. Interest in the formation mechanism of the heterometallic cluster led to *in-situ* monitoring of the transmetalation reaction with Dynamic Light Scattering (DLS). The transmetalation reaction was first performed in MeOH (see IV.3.1), but the initial DLS observations were made in H_2O ; so to start, *in-situ* transmetalation studies were run in H_2O . The ratio $f\text{-Al}_{13}$ to $\text{In}(\text{NO}_3)_3$ was calculated for $f\text{-Al}_7\text{In}_6$. The size of $f\text{-Al}_{13}$ in H_2O ($R_h = 1$ nm) did not change after several days of monitoring. Upon addition of $\text{In}(\text{NO}_3)_3$ (also, $R_h = 1$ nm) to the aqueous $f\text{-Al}_{13}$ solution, a larger species of ~ 6.5 nm formed and persisted over time. This is the first experiment that shows oligomerization at the on-set of transmetalation. Further it confirms that the dynamic solution behavior of transforming $f\text{-Al}_{13}$ into $f\text{-Al}_7\text{In}_6$ is not a simple substitution phenomenon, as bulk solid analysis suggests.

VII.3.3.2. Small-angle X-ray scattering experiments

SAXS measurements at different concentrations reveal that $f\text{-Al}_{13}$ ($R_g = 0.5$ nm) may not be as stable in water as $f\text{-Ga}_{13}$ ($R_g = 0.6$ nm), with some degree of dissociation (Table 7.2) occurring. Over several days though, there is no change in the radius of gyration (R_g) or Pair Distance Distribution Function (PDDF). To mirror the *in-situ* DLS study for $f\text{-Al}_7\text{In}_6$, $\text{In}(\text{NO}_3)_3$ is added to a solution of $f\text{-Al}_{13}$. Over a two-day period the R_g gradually decreased as the PDDF increased.

Table 7.2 Radius of gyration (R_g) of $f\text{-Al}_{13}$ and the transmetalation product from the addition of $\text{In}(\text{NO}_3)_3$ to $f\text{-Al}_{13}$, expected to be $f\text{-Al}_7\text{In}_6$. Both experiments were performed in H_2O at two different concentrations, 1M and 100mM.

| Sample | Conc. (M) | Time (hr) | R_g (nm) | PDDF (nm) |
|----------------------------|-----------|-----------|--------------|-----------|
| $f\text{-Al}_{13}$ | 1 | 14 | 0.458 | 1.345 |
| $f\text{-Al}_7\text{In}_6$ | 1 | 10 min. | 0.495 | 1.414 |
| | | 3 | 0.493 | 1.651 |
| | | 6 | 0.492 | 1.791 |
| | | 22 | 0.465 | 3.213 |
| | | 45 | 0.468 | 4.093 |
| <i>Average</i> | | | 0.483 | |
| $f\text{-Al}_7\text{In}_6$ | 0.1 | 10 min. | 0.471 | 0.839 |
| | | 3 | 0.476 | 0.906 |
| | | 6 | 0.510 | 1.023 |
| | | 22 | 0.467 | 2.652 |
| | | 45 | 0.451 | 3.031 |
| <i>Average</i> | | | 0.475 | |

Based upon the SAXS scatter plot, it appears there are distinct populations of different sizes rather than a monomeric unit polymerizing into different chain lengths (Figure 7.3). However, multiphase modelling is necessary for more concrete evidence. Drs. May Nyman and Rose Ruther (Oregon State University) helped to set up these preliminary experiments.

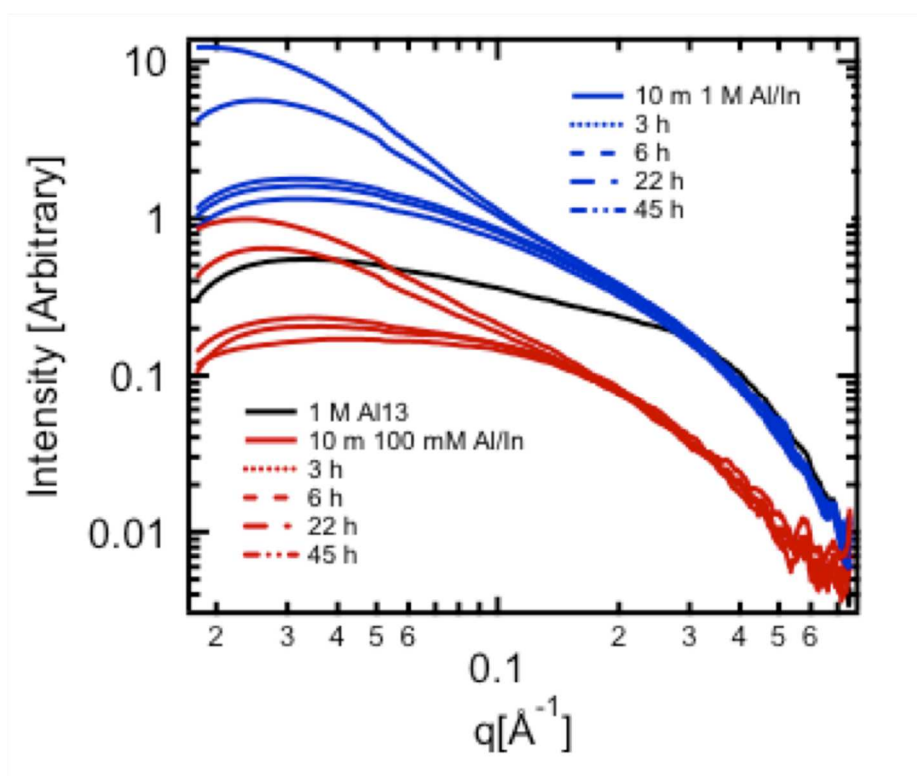


Figure 7.3. SAXS scatter curves for $f\text{-Al}_{13}$ and the expected $f\text{-Al}_7\text{In}_6$ tridecamers at 1M and 100 mM concentrations.

VII.3.4. Group 13 cluster speciation – Mass spectrometry

Mass spectrometry is a very useful technique for identifying compounds in solution, but in our case it is extremely complicated due to extensive fragmentation of a highly charged (+15) species. However, on the path towards proposing

monomer to tridecamer intermediates, mass spectrometry is an ideal characterization tool. The goal would then be to synthesize n-mers ($n < 13$ metal ions) with reduced charge that could potentially exist in solution once the cluster is dissolved. For greater stability, these polynuclear species can be supported by organic ligands.³⁵ This way it might be possible to tease out the as-yet unidentified species that are present in solution. By doing so we can find stable intermediate molecules and develop a mechanism to show how the $f\text{-Al}_{13}$ and $f\text{-Ga}_{13}$ clusters form. Initial work in this area began with the help of Dr. J. Scott McIndoe (University of Victoria) and more recently was continued with the help of Dr. William H. Casey (UC Davis).

VII.3.5. *New bridging ligands*

Use of alternative bridging ligands is an easy way to design clusters known to be difficult to prepare as well as incorporate ligands with versatile capabilities into molecular structures. Several oxo-containing ligands, together with azides, have been used to build polynuclear clusters.¹⁷⁸ Metal phosphates have potential applications as adsorbents, catalysts, and fuel cell membranes.¹⁷⁹ Incorporating phosphates/phosphites into molecular structures can be an interesting new method for composing tunable molecules with a diverse set of applications.

Small, volatile organic compounds such as formic acid can be utilized as supporting ligands for polynuclear compounds. Once the clusters form, the ligands can be removed either under vacuum or with moderate heating. If oligomers exist in solution prior to volatilization, the reaction might drive the formation of the high

nuclearity molecules that crystallize from solution. This could be a new approach to many molecular clusters otherwise unseen due to long-standing synthetic barriers.

VII.3.6. Transition metal cluster synthesis

Another goal has been to utilize the synthetic procedures used to prepare Group 13 tridecamers for new structures that incorporate high abundance/low toxicity elements. To date that has proved difficult with the traditional synthetic routes previously discussed in Chapters II and IV (Table 7.3).

Table 7.3. Results of selected metal exchange experiments. Transmetalation occurred only in the instance where $\text{In}(\text{NO}_3)_3$ was mixed in solution with *f*-Ga₁₃.

| Metal I (mg) | Metal II (mg) | M(I): M(II) Ratio | MeOH (mL) | DBNA (mg) | Pred. St. | Result |
|---------------------------------------|------------------|----------------------|--------------|--------------|---------------------------------|---|
| <i>f</i> -Ga ₁₃ (24.2) | Al (35.5) | 1:10 | 3.0 | 50.0 | Ga _x Al _y | <i>f</i> -Ga ₁₃ |
| <i>f</i> -Ga ₁₃ (23.5) | Cu (11.9) | 1:5 | 3.0 | 41.0 | Ga _x Cu _y | <i>f</i> -Ga ₁₃ |
| <i>f</i> -Ga ₁₃ (243.8) | Al (17.9) | 1:5 | 3.0 | 52.0 | Ga _x Al _y | <i>f</i> -Ga ₁₃ |
| <i>f</i> -Ga ₁₃ (20.7) | In (49.1) | 1:20 | 3.0 | 37.0 | Ga _x In _y | <i>f</i> -Ga ₇ In ₆ |

New procedures are currently being used to produce new compounds and one that has proved successful resulted in the synthesis of $[\text{Fe}(\mu_3\text{-O})(\text{H}_2\text{O})_3(\text{CH}_3\text{-CO}_2)_6][(\text{NO}_3)](\text{CH}_3\text{C}(\text{O})\text{OH})$ (Figure 7.4).^{180,181} Here 0.5 mL of 30% H_2O_2 was added to a 0.005 M solution of $\text{Fe}(\text{NO}_3)_3$ in MeOH. Ethyl acetate (EtOAc) was diffused into the solution and after ~ 6 weeks red crystals of Fe_3 formed. Glacial acetic acid (4 mL) can be added directly to a solution of $\text{Fe}(\text{NO}_3)_3$ (5 mmol) in MeOH (4 mL) to create the same structure. Most other examples of trinuclear oxo-centered iron clusters have interesting features such as supporting ligands, polyoxometalate donor ligands, and/or mixed valency.^{182,183,184} As of now Fe_3 is the first example of a fully oxidized trinuclear cluster. More importantly the solubility of Fe_3 in MeOH and H_2O opens the door for future transmetalation experiments that might overcome prior synthetic challenges.

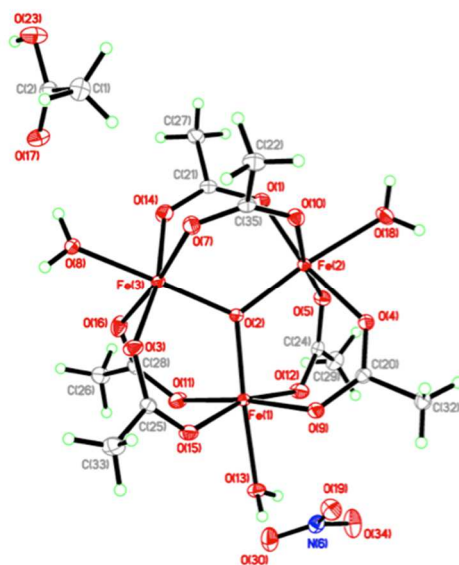


Figure 7.4. Crystal structure of $[\text{Fe}(\mu_3\text{-O})(\text{H}_2\text{O})_3(\text{CH}_3\text{-CO}_2)_6](\text{NO}_3)(\text{CH}_3\text{C}(\text{O})\text{OH})$ (Fe_3).

VII.3.7. Main group cluster synthesis

Another step in the progress of cluster synthesis is the incorporation of main group elements into similar structure types. In the same manner that transition metals can provide benefits in the development of new technologies, so too can main group elements. Bismuth telluride (Bi_2Te_3), for example, is a well-known thermoelectric material utilized in mobile refrigeration and CPU cooling.¹⁸⁵ Solution-processed alternatives for these application-driven materials can prove useful in the realm of scalability and sustainability. Initial attempts to synthesize bismuth-hydroxo polynuclear compounds have been successful.^{186–191} However, solubility is limited in water and other polar solvents. Current efforts are underway to incorporate water-soluble sulfur-based ligands into said compounds, but to date characterization of the final products has been difficult.^{192–195} Nevertheless, once these compounds can become water-soluble, work can begin to start developing heterometallic structures.

VII.4. Conclusions

Although it is difficult to predict what kind of topologies and structures will lead to a high nuclearity cluster in advance, many synthetic approaches have been used to obtain isolated clusters. What this work shows is that there are many options for the manner in which to approach new syntheses and designs.³⁴ What is also apparent is that there is no limit to the number of molecular clusters that can be made or the applications they can fulfil. This possibility makes the field of cluster synthesis broad and full of opportunities to discover.

APPENDIX A

SOLUTION-STATE ANALYSIS OF THE *f*-AL₁₃ TRIDECAMER

This appendix contains unpublished experiments used in an attempt to assign ¹H-NMR signals to specific protons on the *f*-Al₁₃ tridecamer. I am responsible for all syntheses and ¹H-NMR experiments in all cases presented herein.

A.1. Variable-temperature ¹H-NMR studies

The NMR timescale is often referred to when considering the chemical dynamics of compounds in solution. The exchange rate of water ligands on [Al(H₂O)₆]³⁺ is orders of magnitude slower than on [Ga(H₂O)₆]³⁺ and even slower compared to [In(H₂O)₆]³⁺.¹⁹⁶ §§§ *f*-Al₁₃ and the related Group 13 oligomers are species that exhibit dynamic behavior. They exist in an equilibrium that is influenced by factors such as pH and concentration. The complexity associated with the slow exchange process for [Al(H₂O)₆]³⁺ has made peak analysis challenging for *f*-Al₁₃ in comparison to its *f*-Ga₁₃ and heterometallic *f*-Ga_{13-x}In_x counterparts because ligand exchange with aprotic solvents leads to spectra with complex splitting motifs.¹⁰³ After complete solvation in *d*₆-DMSO, the ¹H-NMR spectra for *f*-Ga₁₃ and *f*-Ga_{13-x}In_x species simplify, leading to easy assignment of the μ₃-OH and μ₂-OH protons.

§§§ $k_{\text{ex}}([\text{Al}(\text{H}_2\text{O})_6]^{3+}) = 6 \text{ s}^{-1}$; $k_{\text{ex}}([\text{Ga}(\text{H}_2\text{O})_6]^{3+}) = 5 \times 10^{-4} \text{ s}^{-1}$; $k_{\text{ex}}([\text{In}(\text{H}_2\text{O})_6]^{3+}) = 5 \times 10^{-5} \text{ s}^{-1}$.

The proton chemical shift is related to the conformation of molecule in solution and the number of structural configurations is dictated by the potential energy profile of the molecule in question.⁵⁶ Changing the solution temperature can alter the observable number of conformations so that overlapping resonances separate and peaks coalesce, or previously unobserved resonances become visible. In the case of exchangeable protons, chemical shifts are dependent upon the degree of both inter- and intra-molecular hydrogen bonding. Changes in temperature can also affect the degree of hydrogen bonding which is related to the aforementioned chemical shifts. Variable-temperature (VT) NMR and mixed-solvent experiments are currently being employed to help parse through the complexity of the $f\text{-Al}_{13}$ spectrum in two ways: 1) signals will begin to coalesce and move with increasing temperatures, which indicates chemical exchange between nearby atomic sites, and 2) solvent effects (e.g. dipole moment, electronegativity, etc.) will help to track signals associated with nuclei in similar chemical environments. The combination of both NMR experiments can help assemble a clearer picture of this molecular structure by overcoming this dynamic exchange.

A.2.1. *f*-Al₁₃ in *d*₆-DMSO

The VT-NMR spectra for *f*-Al₁₃ show both signal coalescence and peak shifting in *d*₆-DMSO (Figure A.1). From our previous experience with NMR analysis of *f*-Al₁₃ in *d*₆-DMSO, we know definitively that the peaks between 3.5 ppm and 4.3 ppm are signals for the protons on the bridging hydroxide ligands of the cation. The resonances at 3.64 ppm and 3.83 ppm begin to converge with increasing temperature and can indicate a degree of exchange between these two sites. Since there is no peak broadening in the direction of the upfield water peak (not shown at 3.31 ppm) the chemical exchange is likely only between these two sites, suggesting that they are near to one another. These two peaks also shift away from the peak at 4.18 ppm so no exchange is likely occurring with this site. It does however appear that exchange is happening amongst the protons at this chemical shift as indicated by line broadening.

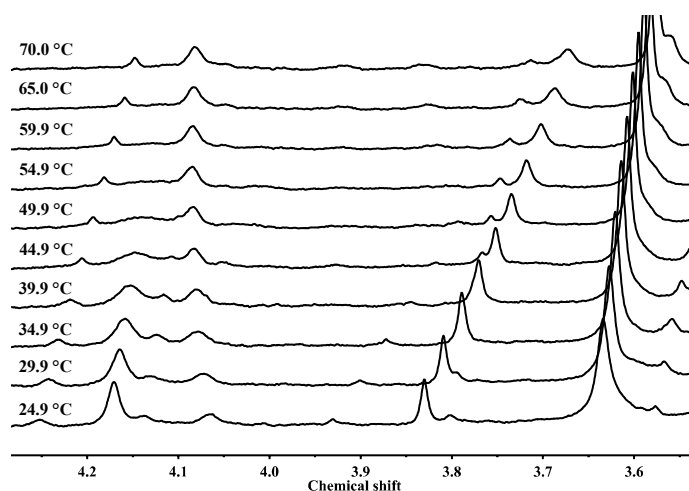


Figure A.1. VT-NMR spectra for *f*-Al₁₃ in *d*₆-DMSO from 25 °C to 70 °C. All spectra were normalized based upon the largest peak (water) and references for *d*₆-DMSO (2.50 ppm).

A.2.2. $f\text{-Al}_{13}$ in $d_7\text{-DMF}$

A similar shifting pattern for the two peaks at 4.33 ppm and 4.81 ppm (at $-10\text{ }^\circ\text{C}$) is observed in $d_7\text{-DMF}$ suggesting that they might be chemically equivalent (Figure A.2). These signals have near-identical movement to the peaks between 3.6 and 3.8 ppm in $d_6\text{-DMSO}$, therefore these peaks could be representative of the same sites in different solvents, but additional experiments are necessary to make a connection between solvent systems. Room temperature mixed solvent experiments were then conducted to see if there was a correlation between peak shifts and solvent environment.

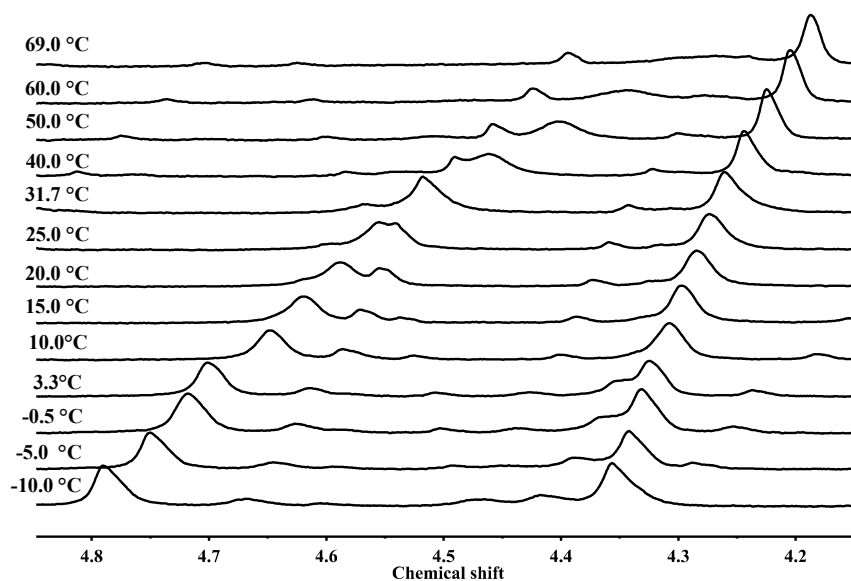


Figure A.2. VT-NMR spectra for $f\text{-Al}_{13}$ in $d_7\text{-DMF}$ from $-10\text{ }^\circ\text{C}$ to $69\text{ }^\circ\text{C}$. All spectra were normalized based upon the largest peak (water) and referenced to $d_7\text{-DMF}$ (8.03 ppm).

A.3. Mixed-solvent Experiments

d_7 -DMF (B) was added to an NMR tube containing $f\text{-Al}_{13}$ and d_6 -DMSO (A) until a 1:1 (v/v) of both solvents was achieved. The reverse experiment was run to rule out preferential coordination of one solvent over another and observe the movement protons at different sites on the cluster due to the change in solvent polarity. The distance of the μ_3 -OH protons from the water ligands where solvent exchange occurs would lead to a minimal ppm shift in the peak related to these six protons (Figure A.3.). Protons closer to the water ligands (μ_2 -OH') should experience the largest shift and the μ_2 -OH protons would fall somewhere in between. The degree of shifting will only be able to confirm the relationship between peaks and structure.

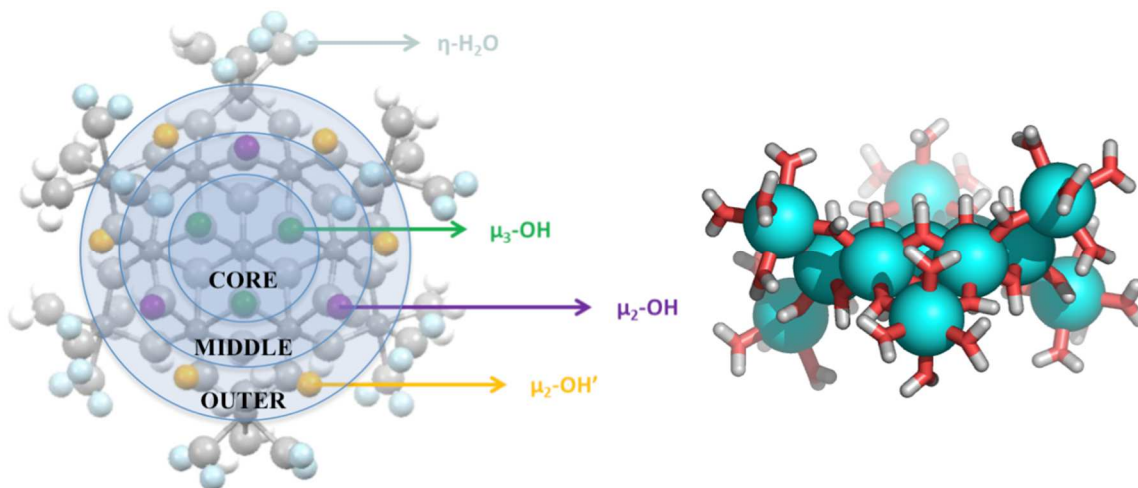


Figure A.3. (Left): Diagram of $f\text{-Al}_{13}$ with various proton sites labeled. (Right): Side view of $f\text{-Al}_{13}$.

For DMSO/DMF, two peaks at 4.49 ppm and 4.25 ppm shift upfield begin to shift towards a peak at 3.78 ppm as the ratio of DMSO- d_6 /DMF- d_7 increases (Figure A.4). A at 5.3 ppm (not shown) does not move significantly while another at 3.5 ppm shifts upfield.

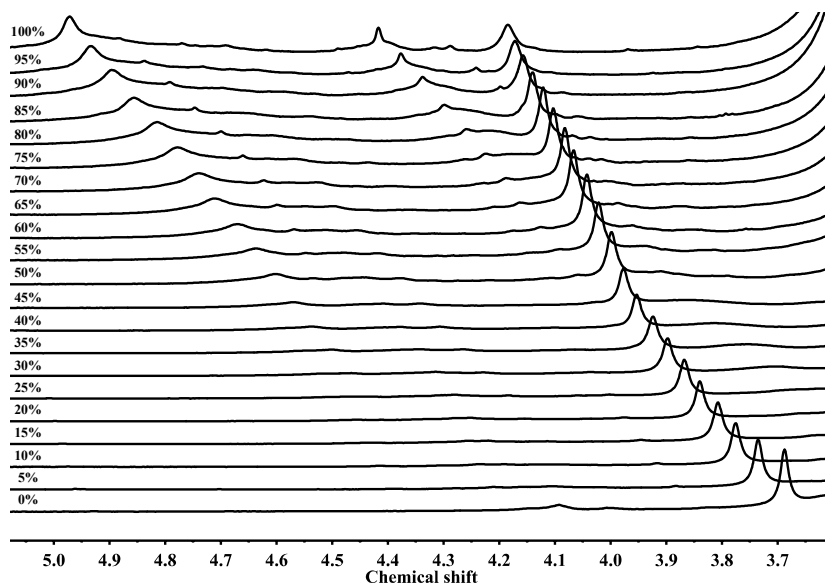


Figure A.4. Mixed solvent analysis of $f\text{-Al}_{13}$ in d_7 -DMF and DMSO- d_6 at 25 °C. Spectra are labelled with increasing amounts of d_6 -DMSO (0%-100%).

Presently, it is difficult to accurately assign these signals because the temperature ranges for these experiments are not large enough to truly describe the extent of peak coalescence and shifting. Other solvent systems including DMSO/MeCN, DMSO/DMF, and DMSO/Acetone will be used to help abate temperature issues and in tandem with computational analysis, these experiments will help to solve the complex mystery that is the ^1H NMR spectrum of $f\text{-Al}_{13}$.

APPENDIX B

SUPPLEMENTAL INFORMATION FOR CHAPTER II

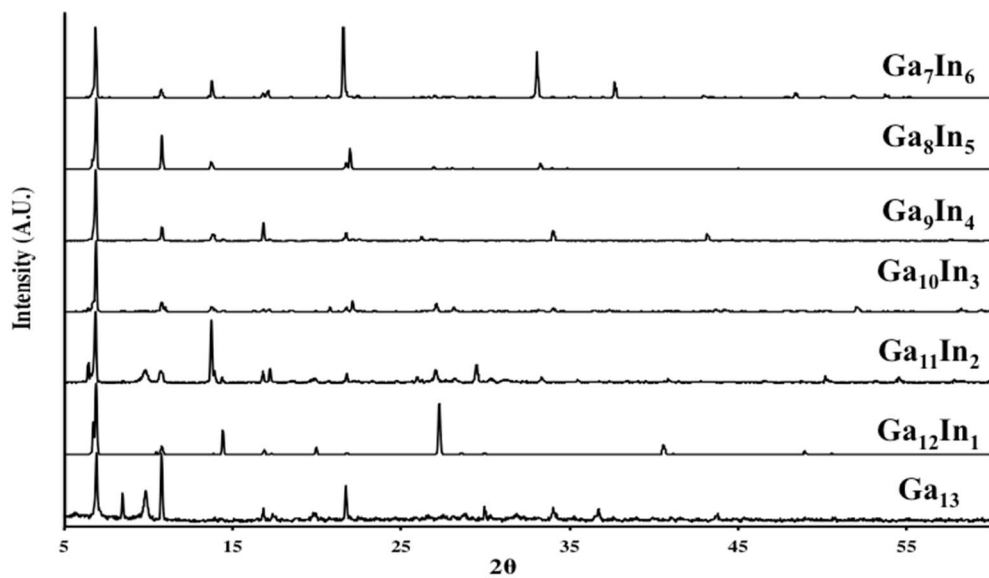


Figure B.1. Powder XRD traces of bulk $f\text{-Ga}_{13}$ and 1-6 at 25 °C. °C.

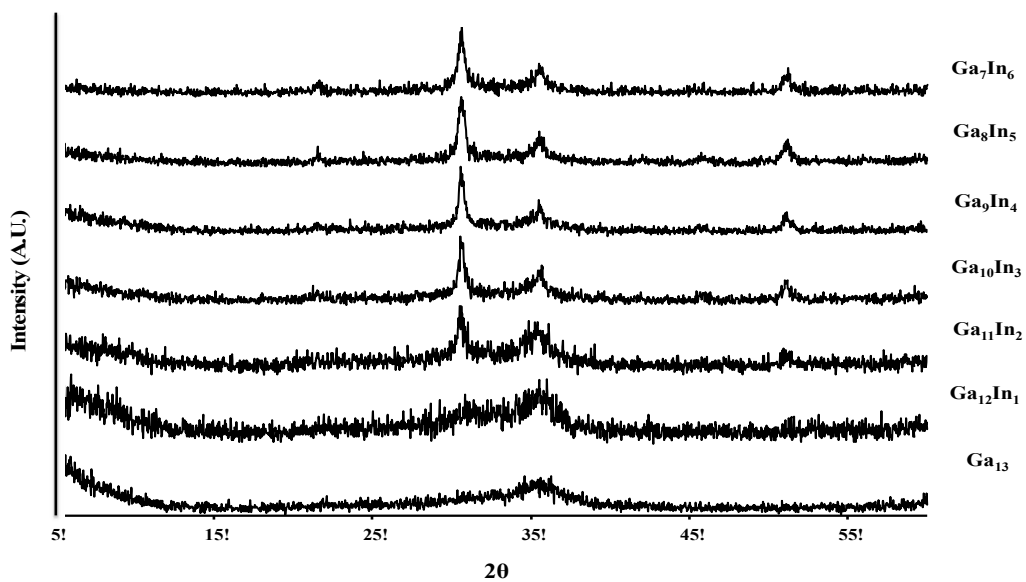


Figure B.2. Powder XRD traces of bulk $f\text{-Ga}_{13}$ and 1-6 at 250 °C.

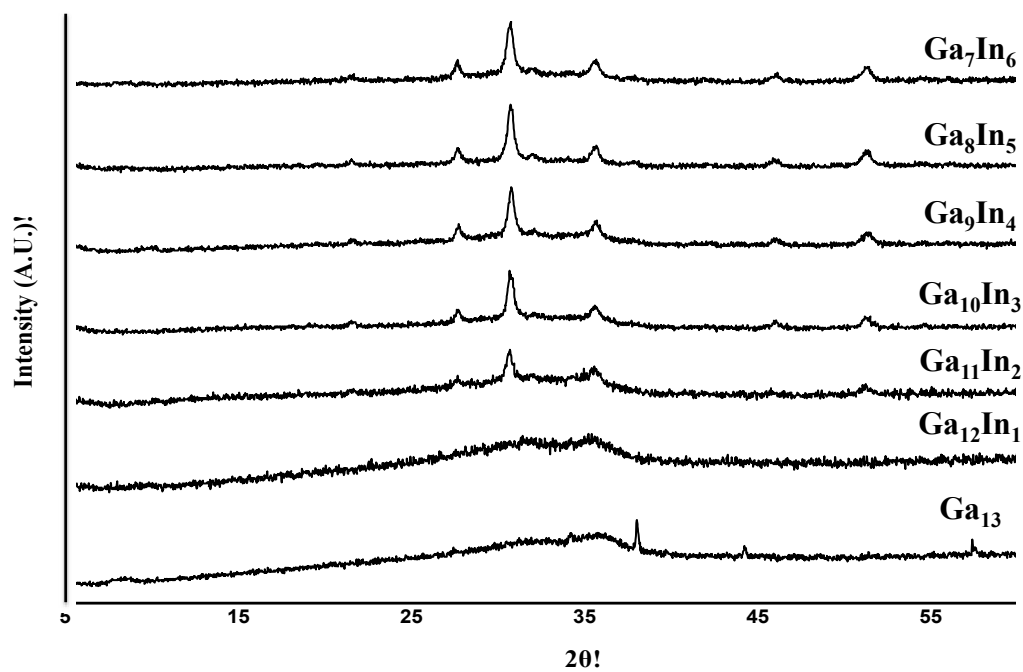


Figure B.3. Powder XRD traces of bulk *f*-Ga₁₃ and 1-6 at 600 °C.

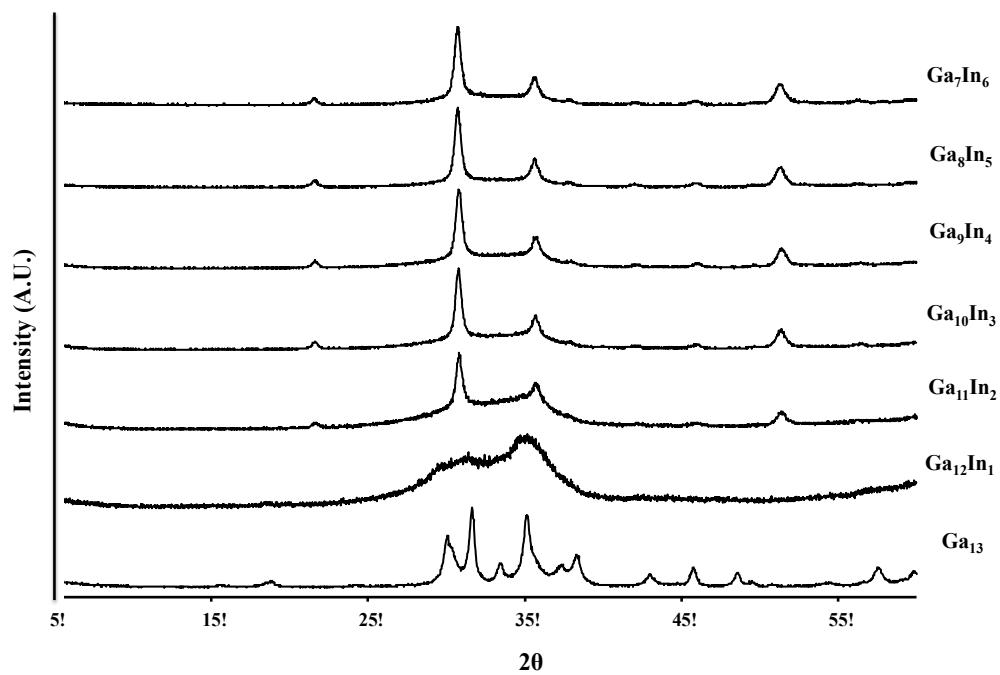


Figure B.4. Powder XRD traces of bulk *f*-Ga₁₃ and 1-6 at 800 °C.

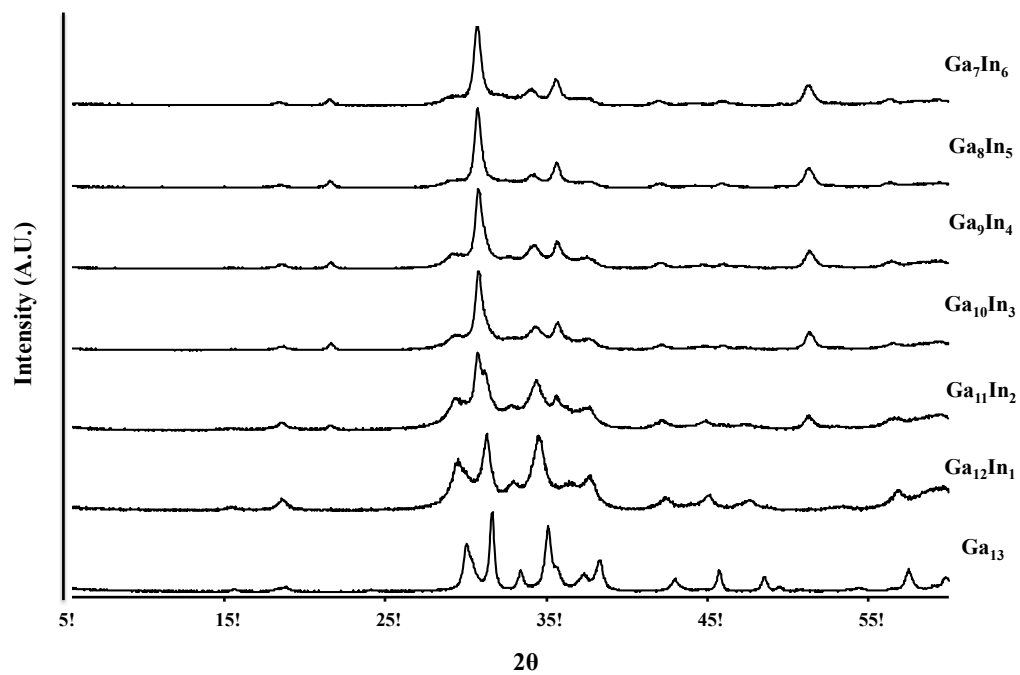


Figure B.5. Powder XRD traces of bulk *f*-Ga₁₃ and 1-6 at 900 °C.

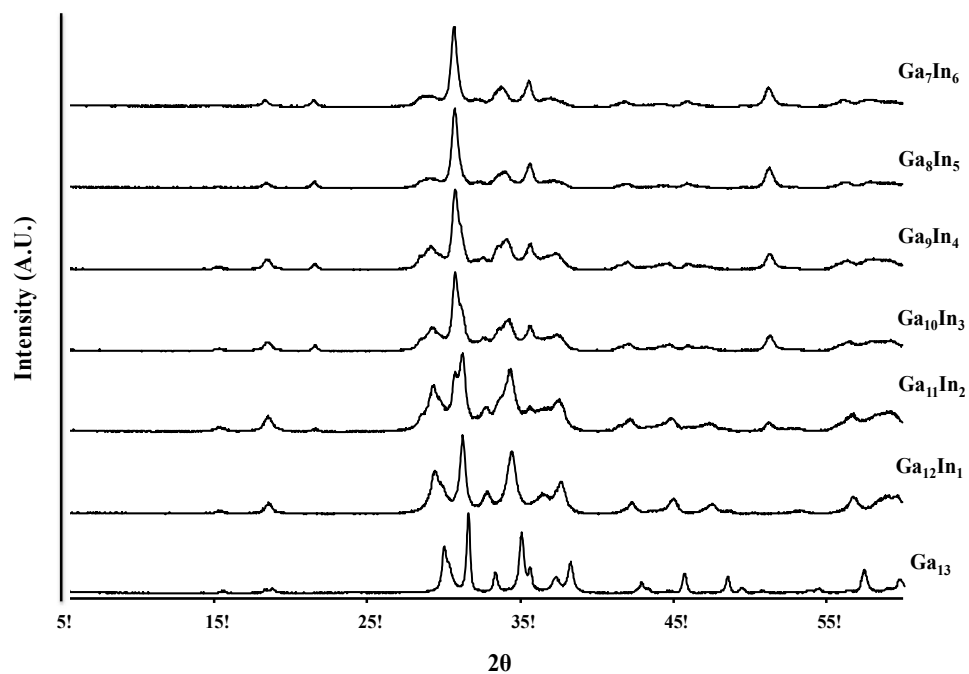


Figure B.6. Powder XRD traces of bulk *f*-Ga₁₃ and 1-6 at 1000 °C.

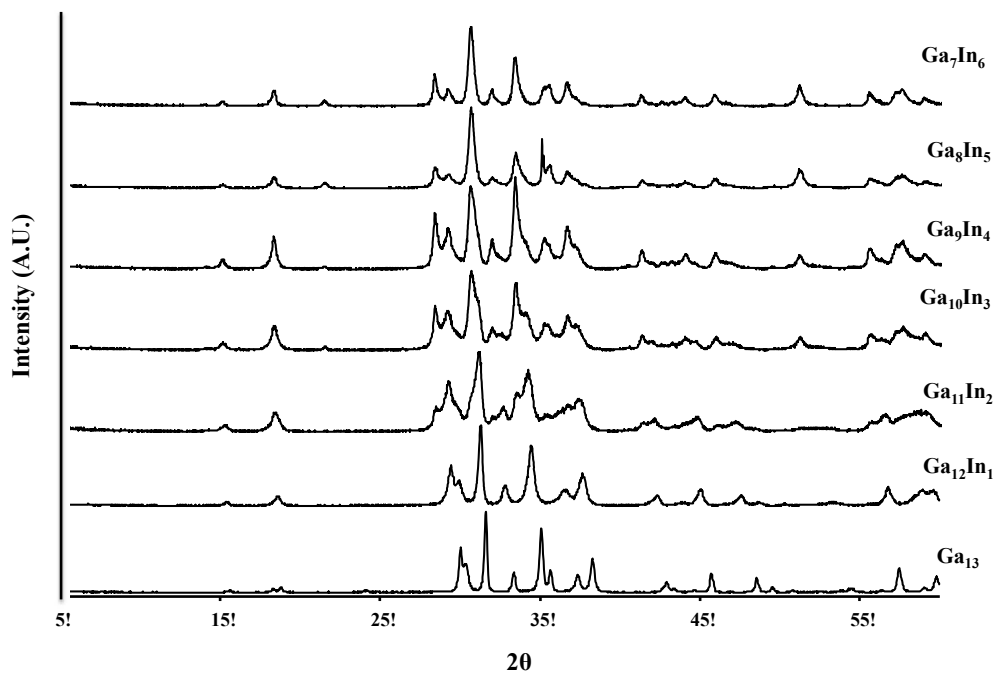


Figure B.7. Powder XRD traces of bulk *f*-Ga₁₃ and 1-6 at 1100 °C.

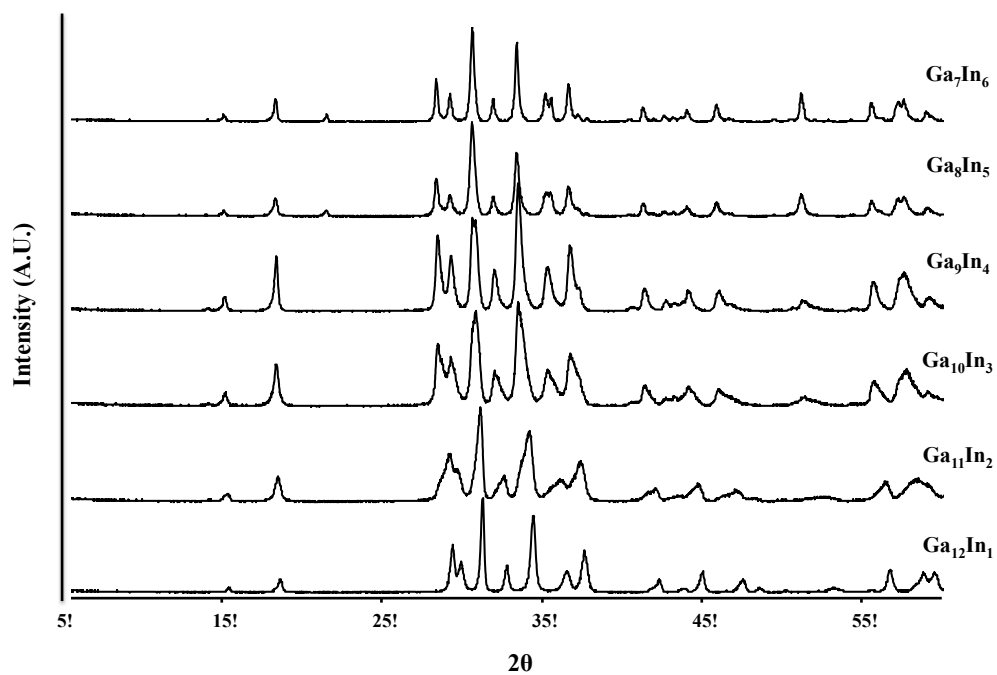


Figure B.8. Powder XRD traces of bulk *f*-Ga₁₃ and 1-6 at 1200 °C.

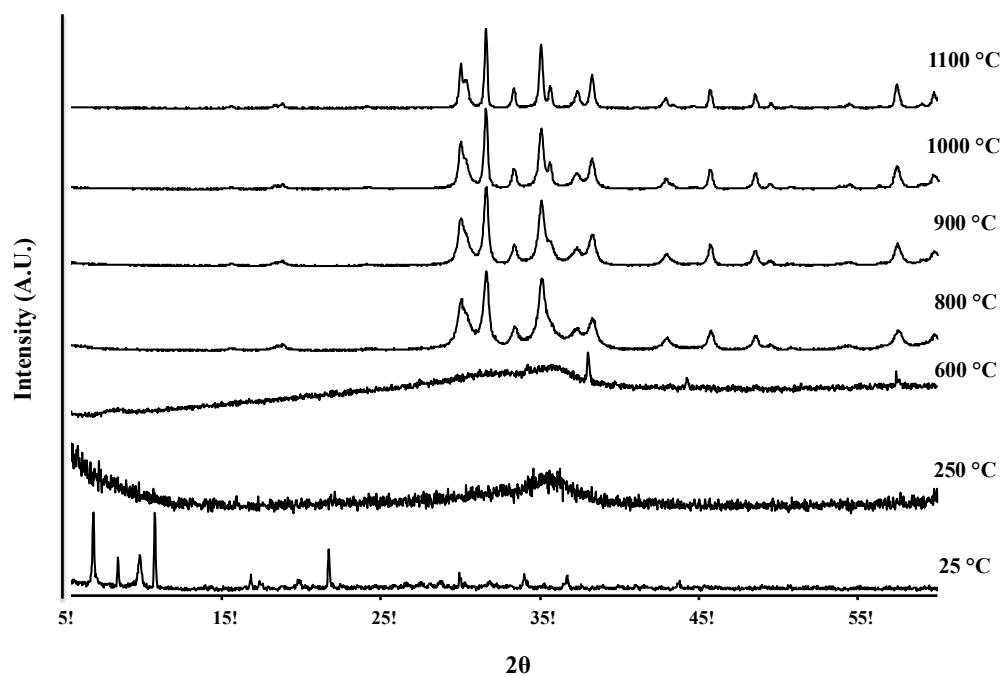


Figure B.9. Powder XRD traces of bulk $f\text{-Ga}_{13}$ heated to specific temperatures.

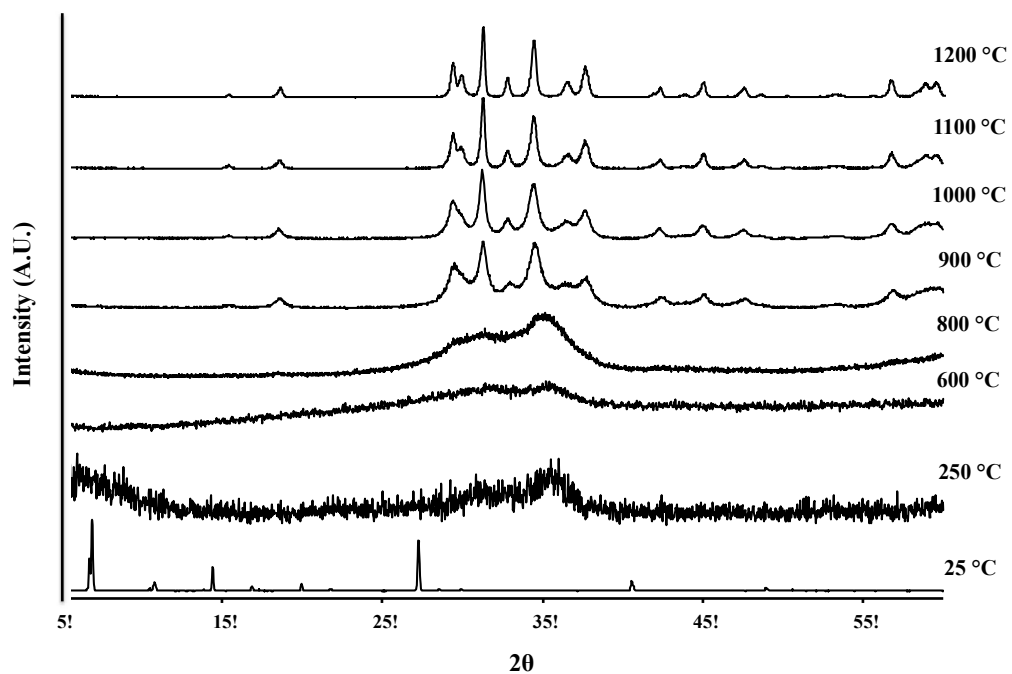


Figure B.10. Powder XRD traces of bulk $f\text{-Ga}_{12}\text{In}_1$ heated to specific temperatures.

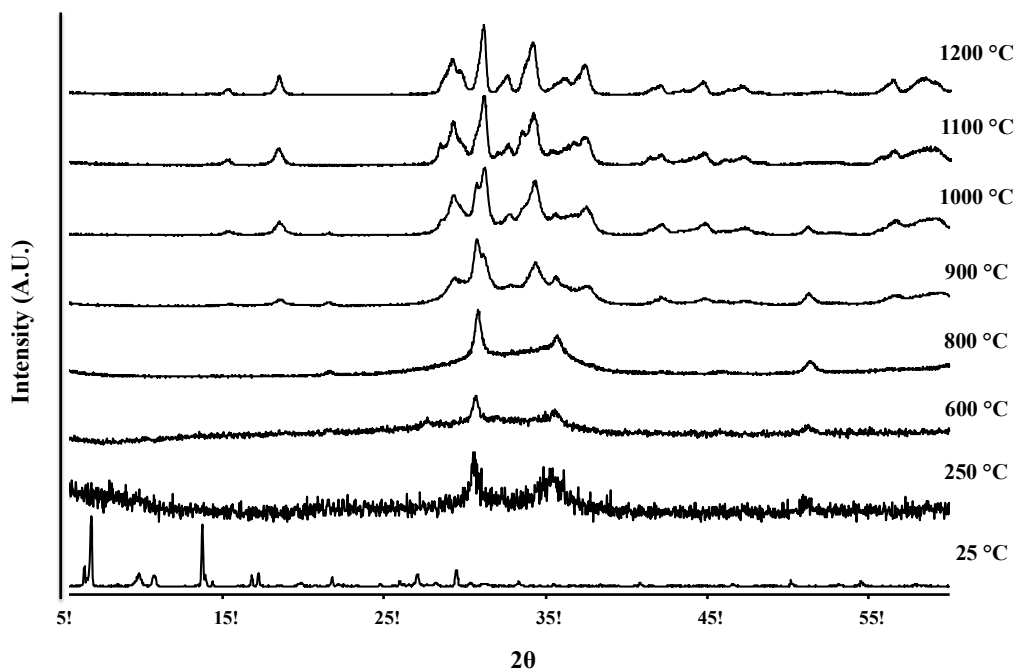


Figure B.11. Powder XRD traces of bulk $f\text{-Ga}_{11}\text{In}_2$ heated to specific temperatures.

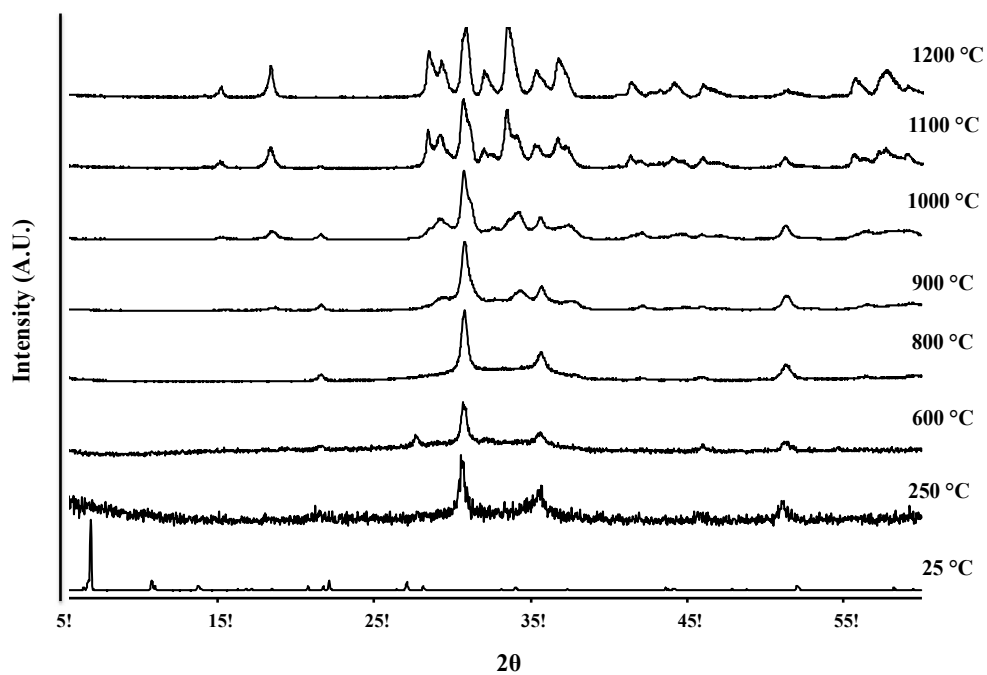


Figure B.12. Powder XRD traces of bulk $f\text{-Ga}_{10}\text{In}_3$ heated to specific temperatures.

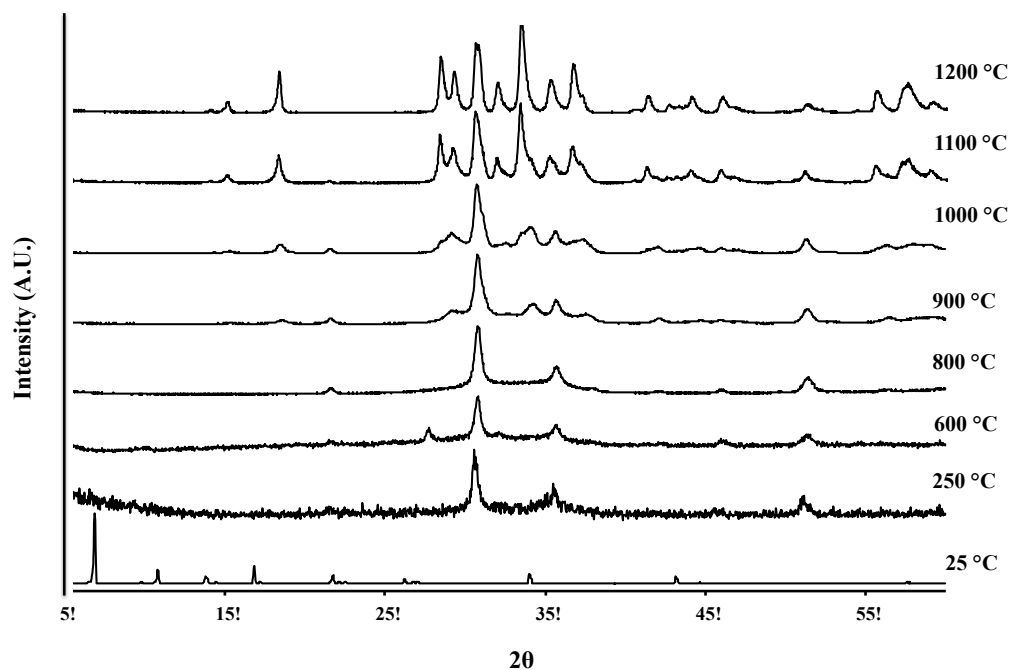


Figure B.13. Powder XRD traces of bulk $f\text{-Ga}_9\text{In}_4$ heated to specific temperatures.

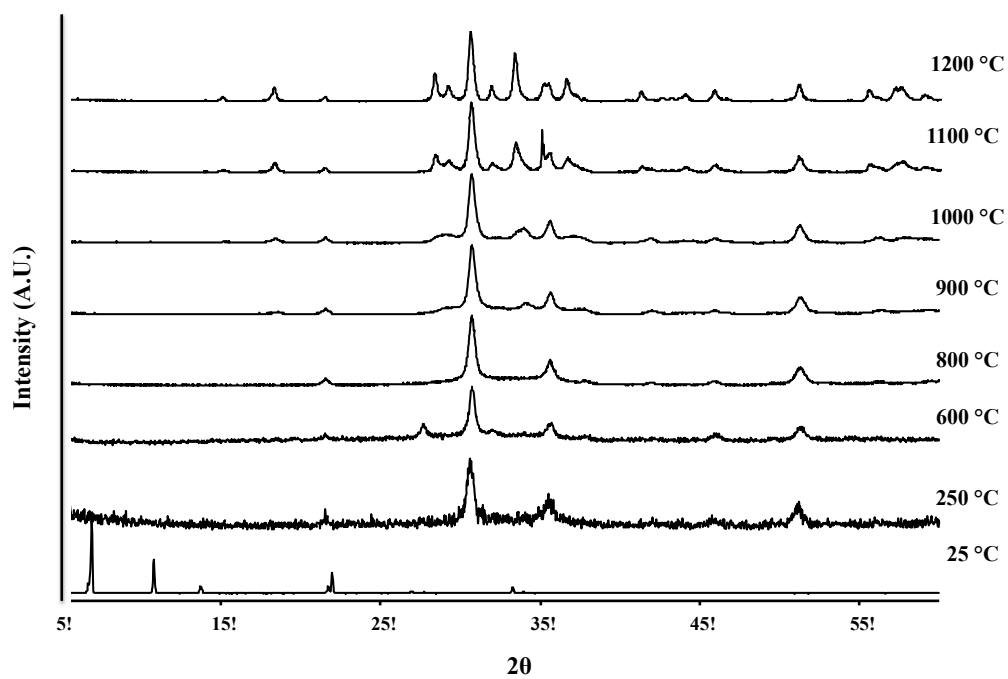


Figure B.14. Powder XRD traces of bulk $f\text{-Ga}_8\text{In}_5$ heated to specific temperatures.

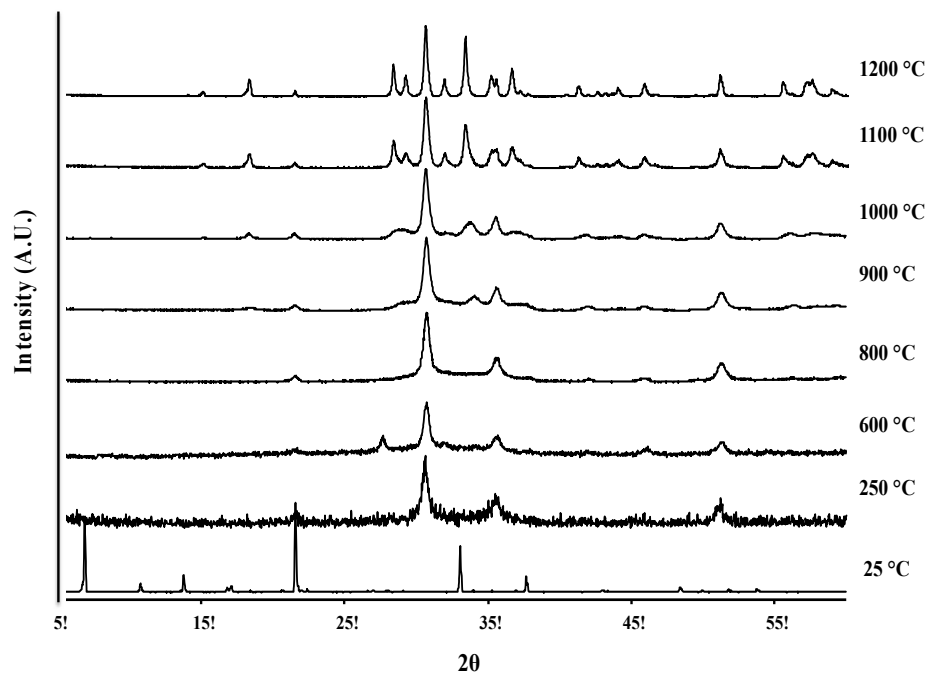


Figure B.15. Powder XRD traces of bulk $f\text{-Ga}_7\text{In}_6$ heated to specific temperatures.

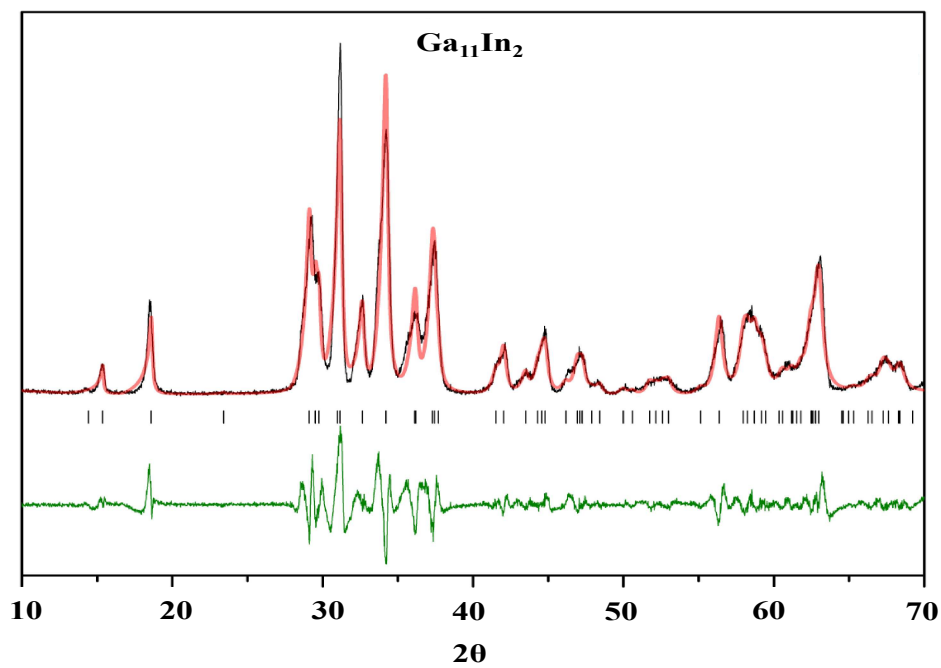


Figure B.16. Pawley fit for $f\text{-Ga}_{11}\text{In}_2$.

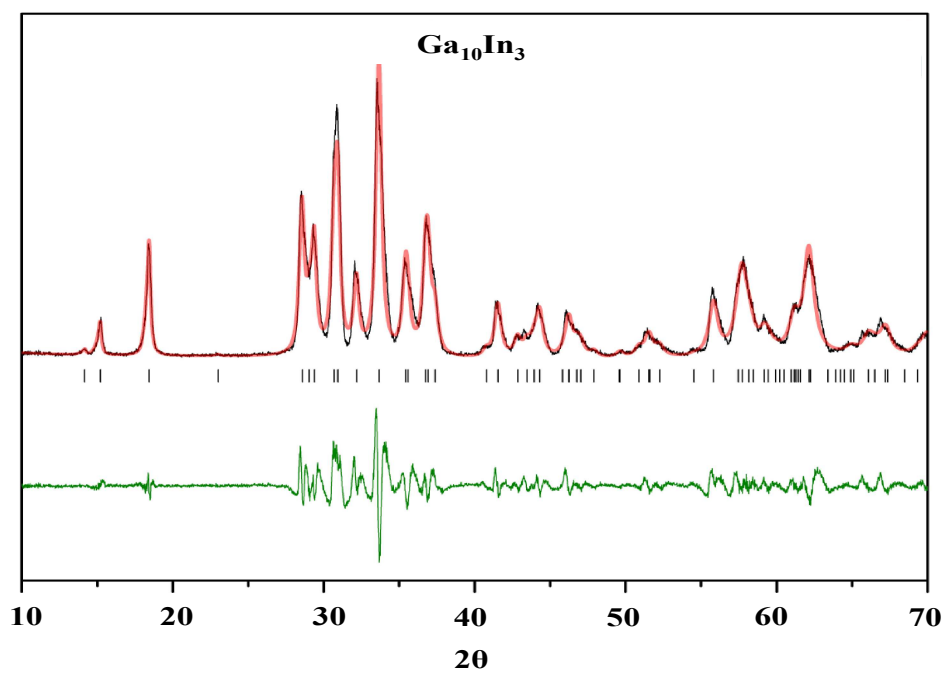


Figure B.17. Pawley fit for f -Ga₁₀In₃.

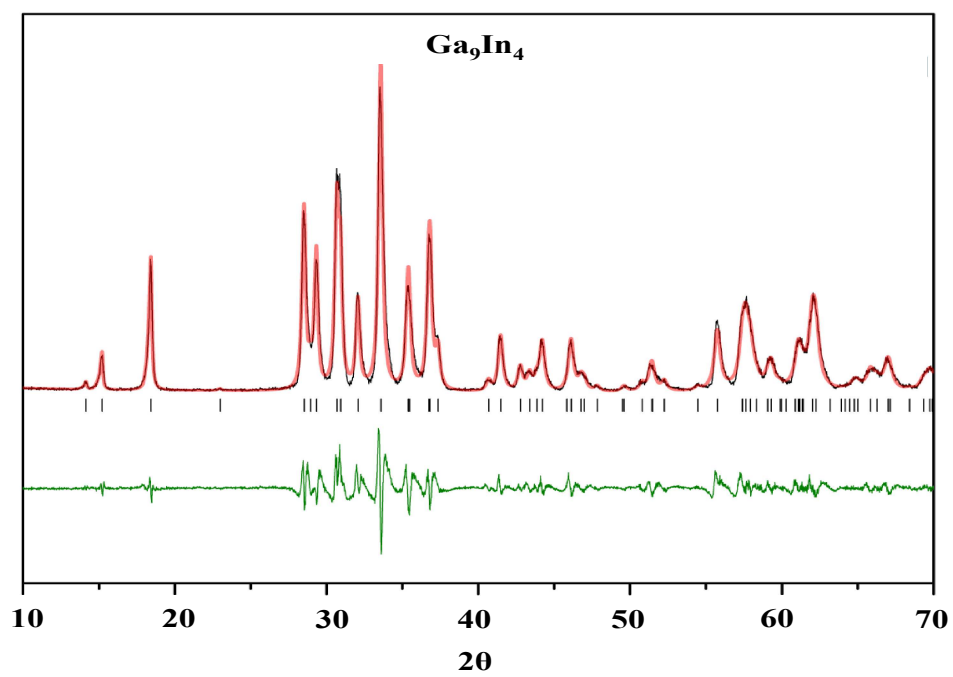


Figure B.18. Pawley fit for f -Ga₉In₄.

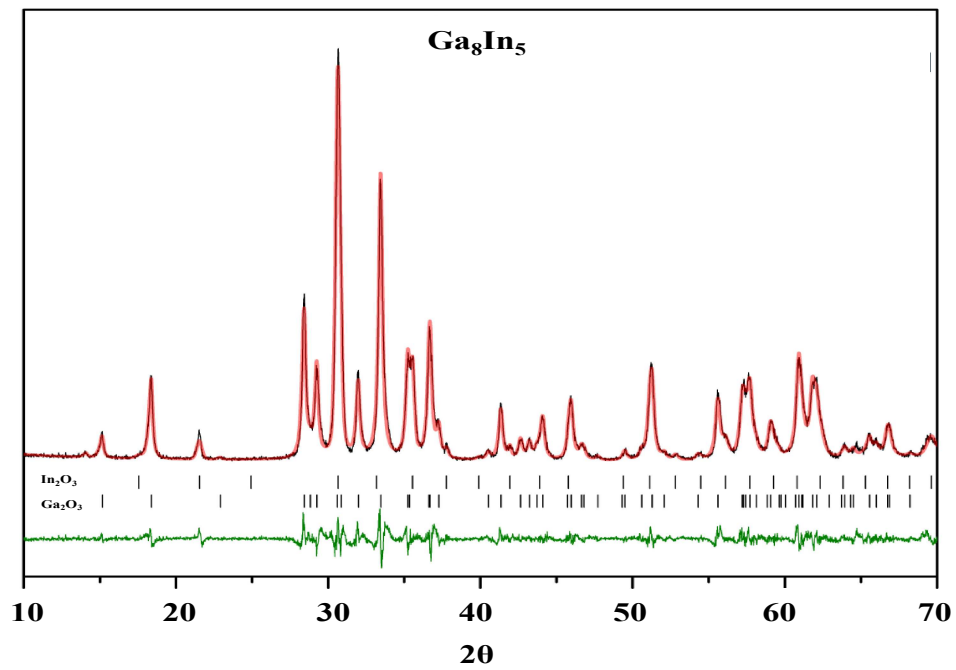


Figure B.19. Pawley fit for $f\text{-Ga}_8\text{In}_5$.

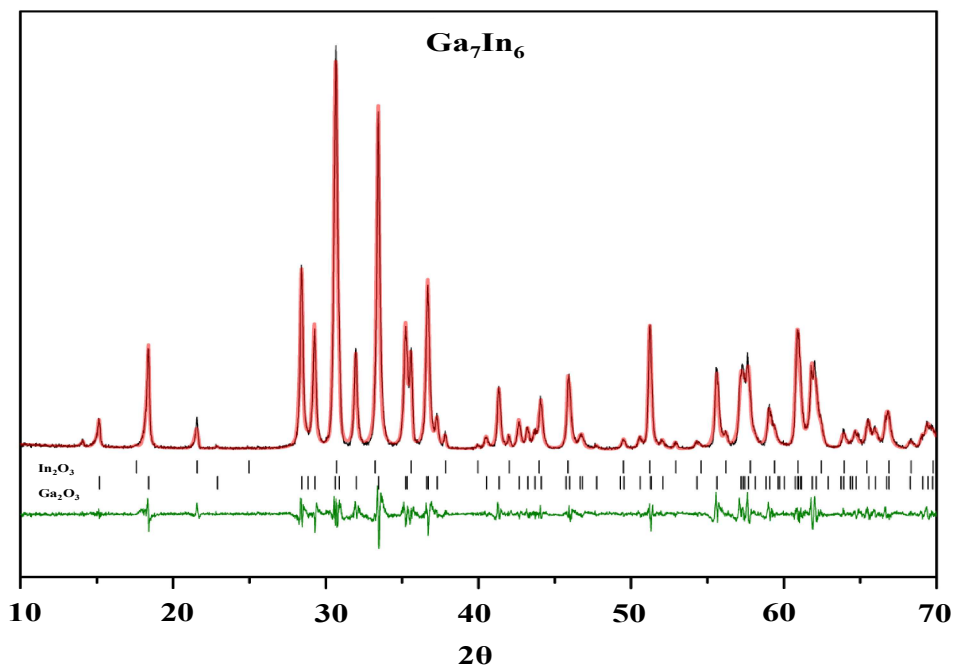


Figure B.20. Pawley fit for $f\text{-Ga}_7\text{In}_6$.

APPENDIX C

SUPPLEMENTAL INFORMATION FOR CHAPTER III

Table C.1. Values used in DMFit to produce the modeled spectra. All models were generated with "int2QUAD" and all values associated with the CSA set to zero.

| | Core | Middle ring | Outer ring |
|---|------|-------------|------------|
| δ_{iso} ($^{69,71}\text{Ga}$), ppm | 60.7 | 45.6 | -0.6 |
| C_Q (^{71}Ga), MHz | 5.0 | 13.9 | 6.7 |
| C_Q (^{69}Ga), MHz | 9.0 | 21.5 | 11.1 |
| η_Q | 0.0 | 0.8 | 0.9 |
| EM ^{71}Ga 21.1 T, Hz | 542 | 300 | 630 |
| Amp ^{71}Ga 21.1 T | 1.78 | 0.38 | 1.32 |
| EM ^{71}Ga 13.9 T, Hz | 500 | 500 | 500 |
| Amp ^{71}Ga 13.9 T | 2.30 | 0.14 | 1.39 |
| EM ^{69}Ga 21.1 T, Hz | 2766 | 5956 | 2860 |
| Amp ^{69}Ga 21.1 T | 2.55 | 0.19 | 1.57 |
| EM ^{69}Ga 13.9 T, Hz | 2766 | 5956 | 2860 |
| Amp ^{69}Ga 13.9 T | 4.06 | 0.11 | 0.64 |

Table C.2. Experiment parameters for GaSe 3QMAS NMR experiments at 21.1 T. Superscripts (a,b,...) correspond to spectra shown in Figures 3.1 and 3.2.

| Experiment | Excitation | | Conversion | | Mixing | | F1 SW (kHz) | Points | | Recycle Delay (s) | NS | Exp. Time (hr) |
|-----------------------------|--------------------|-------------------------|--------------------|-------------------------|--------------------|-------------------------|----------------|--------|------|-------------------------|-------|----------------------|
| | Dur. (μ s) | B ₁ (kHz) | Dur. (μ s) | B ₁ (kHz) | Dur. (μ s) | B ₁ (kHz) | | F1 | F2 | | | |
| 3QMAS ^a | 2.50 | 140 | 1.20 | 140 | 10.00 | 12 | 31.25 | 32 | 2048 | 0.5 | 6000 | 27 |
| 3QMAS ^b | 2.50 | 140 | 1.20 | 140 | 10.00 | 12 | 125 | 32 | 2048 | 0.5 | 14280 | 64 |
| 3QMAS- SPAM ^c | 2.50 | 140 | 1.20 | 140 | 10.00 | 12 | 31.25 | 32 | 2048 | 0.5 | 6000 | 27 |
| 3QMAS- SPAM ^d | 2.50 | 140 | 1.20 | 140 | 10.00 | 12 | 125 | 32 | 2048 | 0.5 | 19200 | 84 |

^{71}Ga 3QMAS NMR experiments were performed at 21.1 T using a 2.5 mm H/X MAS Bruker probe at 31.25 kHz MAS. The choice of NMR probe for 3QMAS experiments, 2.5 mm MAS vs. 1.3 mm MAS, was due to insufficient sensitivity of the latter. ^{71}Ga 3QMAS NMR acquisition parameters are summarized in Table C.2. The maximum rf field achieved for excitation and conversion pulses was 140 kHz, corresponding to a 1.8 μs non-selective 90 pulse calibrated using a 1.0 M $\text{Ga}(\text{NO}_3)_3$ solution reference sample. High-power 100 kHz rf proton decoupling was attempted during 3QMAS, however it resulted in noticeable line-broadening and to overall lower signal to noise, this is due to proton recoupling under MAS caused by large ^1H CSA. Two types of 3QMAS experiments were performed, employing a traditional three-pulse 3QMAS sequence with Z-filter¹⁹⁷, and a soft-pulse-added-mixing (SPAM) modification of the three-pulse

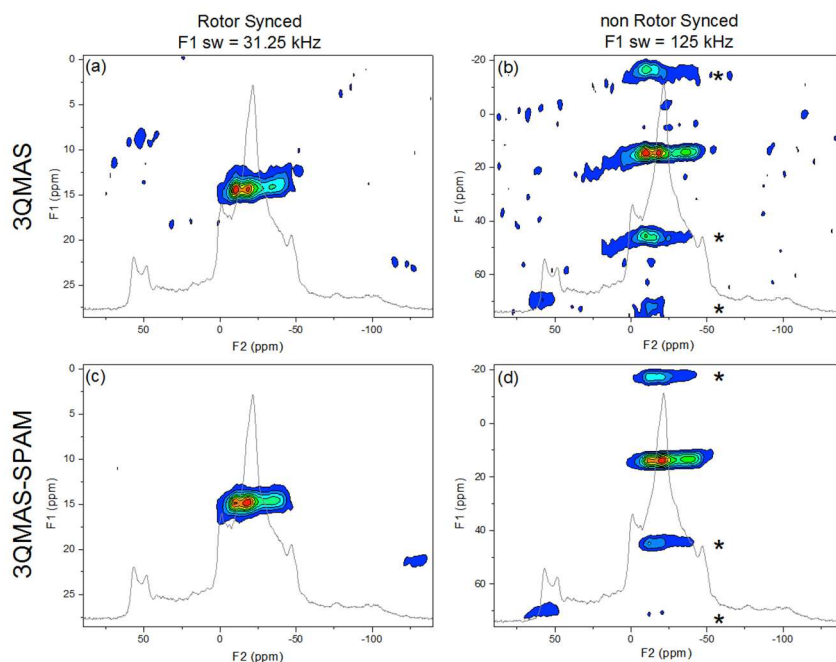


Figure C.1. ^{71}Ga MQMAS NMR spectra $f\text{-Ga}_{13}$ recorded at 21.1 T. * indicate spinning side bands. The 1D MAS spectrum is overlaid to indicate correlation between 3QMAS resonances and the 1D data. sequence (Figure C.1).¹⁹⁸

Because of the large range of observed ^{71}Ga NMR chemical shifts and the high GaSe resonance frequency it was impossible to fit simultaneously all the signals of interest at their correct ppm positions using a single rotor-synchronized F1 window, $\text{SWH1}=31.25$ kHz. Non-rotor synchronized experiments were performed using SWH1 at four times of the MAS spinning speed, 125 kHz, however these experiments resulted in lower signal to noise (Figure C.2).

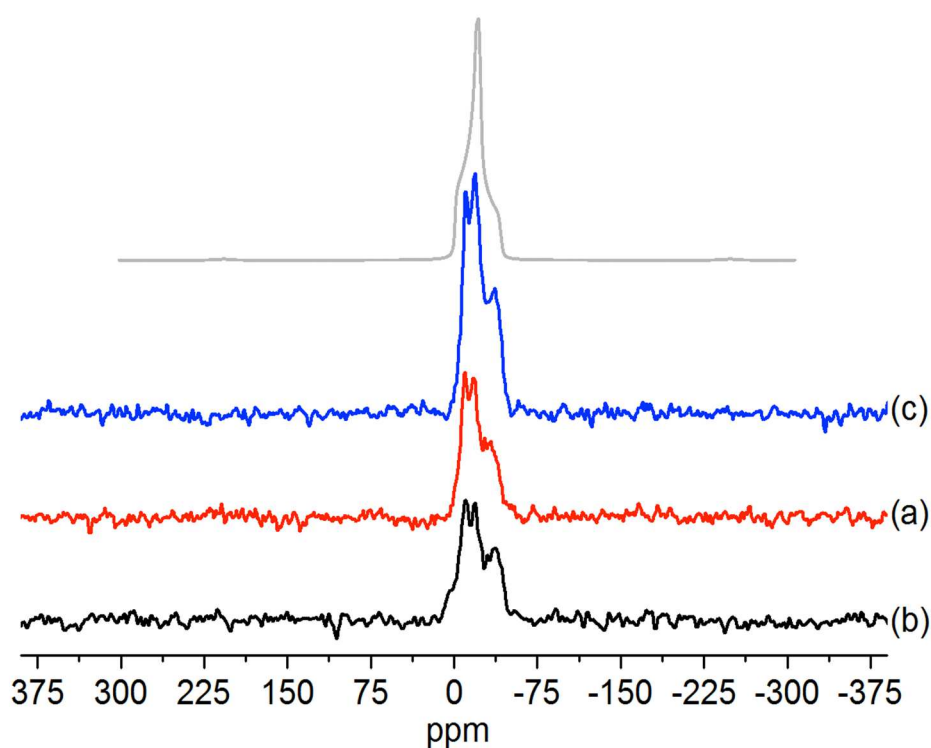


Figure C.2. Effects of experimental conditions on signal to noise in ^{71}Ga 3QMAS NMR spectra. Compared here are the slices corresponding to the outer ring gallium sites extracted from ^{71}Ga 3QMAS NMR spectra shown in Figure reffig:MQMASCompare. The vertical intensities were scaled to reproduce the same noise level. (a) rotor-synchronized 3QMAS, total experimental time 27 hrs. (b) non-synchronized 3QMAS, experimental time 64 hrs to achieve the same signal to noise as in (a). (c) rotor-synchronized SPAM 3QMAS, experimental time 27 hrs, resulting in about twice the signal intensity comparing with (a) in the same amount of time. Note some distortions in the line shape are obvious when comparing 3QMAS slices with a computed model MAS spectrum shown above (gray).

While the core Ga signal can be clearly observed at about 60 ppm in the non-synchronized 3QMAS spectra, in the rotor-synchronized 3QMAS spectra the corresponding resonance is displaced due to narrow F1 sweep width limited by the MAS spinning speed of 31.25 kHz. Due to inefficient conversion between 3Q and 1Q quantum coherences for very large quadrupole coupling constants the middle ring gallium ions never appear in any of the 3QMAS spectra, even after three days of acquisition.

=====

The ground-state geometry of **f-Ga₁₃**

Ga13p

Using: TURBOMOLE V6.3

=====

Method: b3-lyp

Basis: def2-SVP

Atoms: 133; Charge: 15; Spin: 1; Basis Functions: 1448

Energy = -28660.37243573595

| Item | Max Val. | Criteria | Pass? | RMS Val. | Criteria | Pass? |
|--------|-----------|-----------|-------|-----------|-----------|-------|
| Energy | 0.0000002 | 0.0000010 | yes | | | |
| Step | 0.0008758 | 0.0010000 | yes | 0.0001415 | 0.0005000 | yes |
| Grad | 0.0001369 | 0.0010000 | yes | 0.0000157 | 0.0005000 | yes |

=====

Atomic Coordinates (Angstroms)

Type X Y Z

Ga -0.00005 -0.00001 -0.00012

Ga -3.16908 -1.05931 0.02024
Ga -0.66689 -3.27114 -0.01998
Ga 2.50170 -2.21494 0.01606
Ga 3.16905 1.05928 -0.02031
Ga 0.66683 3.27104 0.01994
Ga -2.50189 2.21493 -0.01657
Ga -3.87834 -4.43740 1.90578
Ga 1.90525 -5.57758 -1.90573
Ga 5.78166 -1.13534 1.90725
Ga 3.87873 4.43778 -1.90486
Ga -1.90552 5.57768 1.90514
Ga -5.78189 1.13498 -1.90772
O -1.75708 0.35512 -0.95736
O -1.18248 -1.34659 0.95825
O 0.57028 -1.69899 -0.95802
O 1.75698 -0.35537 0.95711
O 1.18240 1.34656 -0.95840
O -0.57046 1.69893 0.95777
O -2.23675 -2.49844 -0.98259
O 1.05120 -3.18872 0.98019
O 3.28041 -0.68313 -0.98557
O 2.23662 2.49821 0.98266
O -1.05113 3.18854 -0.98051
O -3.28060 0.68326 0.98523
O -4.01281 -2.43294 1.26605
O -1.93985 -4.35759 1.15753
O 0.10196 -4.69137 -1.26287
O 2.80629 -3.85526 -1.16849
O 4.11706 -2.25719 1.25492
O 4.74643 0.50325 1.15841
O 4.01298 2.43306 -1.26569

O 1.94003 4.35770 -1.15708
O -0.10222 4.69149 1.26252
O -2.80650 3.85530 1.16793
O -4.11710 2.25696 -1.25549
O -4.74641 -0.50351 -1.15866
O -4.77443 -5.22778 0.25336
O -3.45765 -3.92075 3.83274
O -5.82294 -4.56938 2.67970
O -3.60720 -6.38297 2.53913
O 1.64728 -4.96808 -3.83463
O 2.16739 -6.72920 -0.24406
O 1.04338 -7.33541 -2.65375
O 3.72041 -6.31672 -2.55738
O 6.92725 -1.49396 0.26053
O 5.10277 -1.03889 3.82893
O 7.32874 0.06488 2.56271
O 6.85786 -2.75796 2.67756
O 3.45851 3.92196 -3.83210
O 4.77444 5.22723 -0.25177
O 5.82357 4.56997 -2.67805
O 3.60796 6.38370 -2.53713
O -2.16758 6.72907 0.24337
O -1.64779 4.96844 3.83424
O -1.04382 7.33563 2.65312
O -3.72077 6.31676 2.55659
O -5.10273 1.03857 -3.82923
O -6.92745 1.49424 -0.26105
O -6.85828 2.75719 -2.67841
O -7.32934 -0.06455 -2.56349
H -1.78613 0.35285 -1.92907
H -1.19479 -1.37424 1.92986

H 0.58718 -1.72116 -1.92962
H 1.78605 -0.35321 1.92882
H 1.19480 1.37426 -1.93001
H -0.58747 1.72106 1.92937
H -2.72506 -3.02063 -1.64096
H 1.26435 -3.88159 1.62779
H 3.97220 -0.84271 -1.64940
H 2.72503 3.02048 1.64090
H -1.26407 3.88111 -1.62849
H -3.97294 0.84302 1.64844
H -4.67421 -2.00539 1.83777
H -1.53367 -5.20657 1.41463
H -0.59656 -5.04403 -1.84166
H 3.74222 -3.92047 -1.43570
H 4.08295 -3.04766 1.82158
H 5.27829 1.28066 1.41243
H 4.67426 2.00556 -1.83759
H 1.53388 5.20672 -1.41409
H 0.59629 5.04445 1.84115
H -3.74243 3.92049 1.43516
H -4.08287 3.04722 -1.82243
H -5.27806 -1.28101 -1.41277
H -4.46139 -5.96446 -0.31303
H -5.75302 -5.33734 0.28867
H -2.63592 -4.05086 4.34984
H -4.18804 -3.93842 4.49454
H -6.14943 -5.41183 3.08246
H -6.58311 -3.95516 2.78460
H -3.96298 -7.20006 2.11656
H -3.42640 -6.65873 3.46859
H 2.16539 -4.32583 -4.36263

H 1.28880 -5.61349 -4.48788
H 2.97946 -6.83016 0.29631
H 1.76381 -7.62788 -0.25800
H 1.60704 -8.03867 -3.06120
H 0.13164 -7.69225 -2.73886
H 4.04229 -6.29410 -3.48942
H 4.25590 -7.03348 -2.14196
H 7.38483 -0.84578 -0.31510
H 7.53343 -2.26984 0.29711
H 4.84523 -0.25494 4.35730
H 5.44740 -1.69057 4.48343
H 8.21853 0.15515 2.14658
H 7.47131 0.36800 3.49040
H 7.72528 -2.61633 3.13152
H 6.74011 -3.73328 2.70497
H 2.63694 4.05264 -4.34930
H 4.18905 3.94019 -4.49372
H 4.46137 5.96360 0.31502
H 5.75307 5.33649 -0.28665
H 6.15028 5.41257 -3.08032
H 6.58371 3.95572 -2.78298
H 3.96375 7.20048 -2.11395
H 3.42744 6.66010 -3.46646
H -2.97968 6.82991 -0.29697
H -1.76410 7.62779 0.25723
H -2.16590 4.32622 4.36228
H -1.28948 5.61398 4.48746
H -1.60756 8.03884 3.06056
H -0.13213 7.69262 2.73816
H -4.25636 7.03344 2.14117
H -4.04262 6.29408 3.48863

H -4.84422 0.25487 -4.35750
H -5.44783 1.68993 -4.48383
H -7.38463 0.84652 0.31540
H -7.53390 2.26988 -0.29834
H -7.72573 2.61493 -3.13211
H -6.74074 3.73252 -2.70649
H -8.21808 -0.15742 -2.14532
H -7.47041 -0.37009 -3.49080

=====

Thermodynamic Analysis

Temperature = 298.15 Kelvin

Pressure = 101325 Pa

SCF Energy = -28660.37243573595

Zero-point correction (ZPE) = -28659.41223 .96019819648

Internal Energy (U) = -28660.10399 .26844178461

Enthalpy (H) = -28659.29137 1.08105860509517

Gibbs Free Energy (G) = -28659.55981 .81261866646

Frequencies -- 18.88 20.62 27.73 35.41 37.09 39.61

APPENDIX D

SUPPLEMENTAL INFORMATION FOR CHAPTER IV

Table D.1. Crystal data and structure refinement for
 $[\text{Al}_7\text{In}_6(\mu_3\text{-OH})_6(\mu\text{-OH})_{18}(\text{H}_2\text{O})_{24}](\text{NO}_3)_{15}$

| | | |
|--|--|------------------------|
| Identification code | mai52 | |
| Empirical formula | C3 H90 Al7 In6 N15 O96 | |
| Formula weight | 2750.68 | |
| Temperature | 193(2) K | |
| Wavelength | 0.71073 \approx | |
| Crystal system | Rhombohedral | |
| Space group | R-3 | |
| Unit cell dimensions | a = 20.3816(10) \approx | $\alpha = 90^\circ$. |
| | b = 20.3816(10) \approx | $\alpha = 90^\circ$. |
| | c = 18.5110(17) \approx | $\alpha = 120^\circ$. |
| Volume | 6659.4(8) \approx^3 | |
| Z | 3 | |
| Density (calculated) | 2.058 Mg/m ³ | |
| Absorption coefficient | 1.752 mm ⁻¹ | |
| F(000) | 4098 | |
| Crystal size | 0.22 x 0.21 x 0.10 mm ³ | |
| Theta range for data collection | 1.59 to 26.97 $^\circ$. | |
| Index ranges | -26 \leq h \leq 25, -26 \leq k \leq 26, -23 \leq l \leq 23 | |
| Reflections collected | 24903 | |
| Independent reflections | 3218 [R(int) = 0.0230] | |
| Completeness to theta = 26.97 $^\circ$ | 100.0 % | |
| Absorption correction | Semi-empirical from equivalents | |
| Max. and min. transmission | 0.8443 and 0.6992 | |

Table D.1., continued

| | |
|-----------------------------------|---|
| Refinement method | Full-matrix least-squares on F ² |
| Data / restraints / parameters | 3218 / 12 / 213 |
| Goodness-of-fit on F ² | 1.107 |
| Final R indices [I>2sigma(I)] | R1 = 0.0163, wR2 = 0.0435 |
| R indices (all data) | R1 = 0.0171, wR2 = 0.0439 |
| Largest diff. peak and hole | 0.365 and -0.305 e. ^{≈-3} |

Table D.2. Atomic coordinates (x 10⁴) and equivalent isotropic displacement parameters (≈²x 10³) for [Al₇In₆(μ₃-OH)₆(μ-OH)₁₈(H₂O)₂₄](NO₃)₁₅. U(eq) is defined as one third of the trace of the orthogonalized U^{ij} tensor.

| | x | y | z | U(eq) |
|-------|---------|---------|---------|-------|
| In(1) | 8212(1) | 1215(1) | 4073(1) | 20(1) |
| Al(1) | 10000 | 0 | 5000 | 16(1) |
| Al(2) | 9811(1) | 1373(1) | 5023(1) | 16(1) |
| O(1) | 9444(1) | 364(1) | 4485(1) | 17(1) |
| O(2) | 8905(1) | 720(1) | 5464(1) | 18(1) |
| O(3) | 9343(1) | 1697(1) | 4384(1) | 21(1) |
| O(4) | 7995(1) | 119(1) | 4289(1) | 21(1) |
| O(5) | 7087(1) | 803(1) | 3636(1) | 29(1) |
| O(6) | 8430(1) | 2349(1) | 3864(1) | 36(1) |
| O(7) | 7677(1) | 1280(1) | 5059(1) | 34(1) |
| O(8) | 8490(1) | 1182(1) | 2950(1) | 35(1) |
| N(1S) | 7968(1) | 755(1) | 6971(1) | 29(1) |
| O(1S) | 7806(1) | 1024(1) | 7496(1) | 53(1) |
| O(2S) | 8632(1) | 918(1) | 6882(1) | 59(1) |
| O(3S) | 7461(1) | 330(1) | 6543(1) | 42(1) |
| N(2S) | 9648(1) | 3822(1) | 4961(1) | 43(1) |

Table D.2., continued

| | | | | |
|-------|----------|---------|---------|-------|
| O(4S) | 9028(1) | 3744(2) | 4845(1) | 80(1) |
| O(5S) | 9901(1) | 3504(1) | 4561(1) | 51(1) |
| O(6S) | 10050(1) | 4227(1) | 5479(1) | 51(1) |

Table D.3. Bond lengths [\approx] and angles [∞] for $[\text{Al}_7\text{In}_6(\mu_3\text{-OH})_6(\mu\text{-OH})_{18}(\text{H}_2\text{O})_{24}](\text{NO}_3)_{15}$.

| | |
|--------------|------------|
| In(1)-O(3) | 2.0845(11) |
| In(1)-O(4) | 2.0880(11) |
| In(1)-O(6) | 2.1596(14) |
| In(1)-O(7) | 2.1634(14) |
| In(1)-O(8) | 2.1651(14) |
| In(1)-O(5) | 2.1657(12) |
| Al(1)-O(1)#1 | 1.8922(11) |
| Al(1)-O(1)#2 | 1.8922(11) |
| Al(1)-O(1)#3 | 1.8922(11) |
| Al(1)-O(1)#4 | 1.8922(11) |
| Al(1)-O(1) | 1.8922(11) |
| Al(1)-O(1)#5 | 1.8922(11) |
| Al(2)-O(3) | 1.8355(12) |
| Al(2)-O(2) | 1.8406(12) |
| Al(2)-O(2)#1 | 1.8411(12) |
| Al(2)-O(4)#1 | 1.8430(12) |
| Al(2)-O(1)#1 | 1.9998(12) |
| Al(2)-O(1) | 2.0605(12) |
| O(1)-Al(2)#4 | 1.9998(12) |
| O(1)-H(1O) | 0.902(17) |
| O(2)-Al(2)#4 | 1.8411(12) |
| O(2)-H(2O) | 0.928(17) |

Table D.3., continued

| | |
|-----------------|------------|
| O(3)-H(3O) | 0.916(16) |
| O(4)-Al(2)#4 | 1.8430(12) |
| O(4)-H(4O) | 0.888(16) |
| O(5)-H(5OA) | 0.934(18) |
| O(5)-H(5OB) | 0.956(19) |
| O(6)-H(6OA) | 0.932(19) |
| O(6)-H(6OB) | 0.98(2) |
| O(7)-H(7OA) | 0.914(18) |
| O(7)-H(7OB) | 0.935(19) |
| O(8)-H(8OA) | 0.934(19) |
| O(8)-H(8OB) | 0.921(18) |
| N(1S)-O(2S) | 1.233(2) |
| N(1S)-O(1S) | 1.239(2) |
| N(1S)-O(3S) | 1.245(2) |
| N(2S)-O(4S) | 1.211(3) |
| N(2S)-O(5S) | 1.254(2) |
| N(2S)-O(6S) | 1.262(2) |
| O(3)-In(1)-O(4) | 92.50(4) |
| O(3)-In(1)-O(6) | 87.64(5) |
| O(4)-In(1)-O(6) | 179.15(5) |
| O(3)-In(1)-O(7) | 102.17(5) |
| O(4)-In(1)-O(7) | 93.41(5) |
| O(6)-In(1)-O(7) | 85.73(6) |
| O(3)-In(1)-O(8) | 92.00(5) |
| O(4)-In(1)-O(8) | 93.98(5) |
| O(6)-In(1)-O(8) | 86.86(6) |
| O(7)-In(1)-O(8) | 163.70(6) |
| O(3)-In(1)-O(5) | 173.08(5) |
| O(4)-In(1)-O(5) | 92.27(5) |

Table D.3., continued

| | |
|---------------------|-----------|
| O(6)-In(1)-O(5) | 87.66(5) |
| O(7)-In(1)-O(5) | 82.54(5) |
| O(8)-In(1)-O(5) | 82.67(6) |
| O(1)#1-Al(1)-O(1)#2 | 180.00(5) |
| O(1)#1-Al(1)-O(1)#3 | 96.85(4) |
| O(1)#2-Al(1)-O(1)#3 | 83.15(4) |
| O(1)#1-Al(1)-O(1)#4 | 96.85(4) |
| O(1)#2-Al(1)-O(1)#4 | 83.15(4) |
| O(1)#3-Al(1)-O(1)#4 | 96.85(4) |
| O(1)#1-Al(1)-O(1) | 83.15(4) |
| O(1)#2-Al(1)-O(1) | 96.85(4) |
| O(1)#3-Al(1)-O(1) | 180.00(6) |
| O(1)#4-Al(1)-O(1) | 83.15(4) |
| O(1)#1-Al(1)-O(1)#5 | 83.15(4) |
| O(1)#2-Al(1)-O(1)#5 | 96.85(4) |
| O(1)#3-Al(1)-O(1)#5 | 83.15(4) |
| O(1)#4-Al(1)-O(1)#5 | 180.00(5) |
| O(1)-Al(1)-O(1)#5 | 96.85(4) |
| O(3)-Al(2)-O(2) | 91.92(5) |
| O(3)-Al(2)-O(2)#1 | 94.88(5) |
| O(2)-Al(2)-O(2)#1 | 166.15(7) |
| O(3)-Al(2)-O(4)#1 | 99.78(6) |
| O(2)-Al(2)-O(4)#1 | 95.54(5) |
| O(2)#1-Al(2)-O(4)#1 | 95.17(5) |
| O(3)-Al(2)-O(1)#1 | 166.78(6) |
| O(2)-Al(2)-O(1)#1 | 93.23(5) |
| O(2)#1-Al(2)-O(1)#1 | 77.68(5) |
| O(4)#1-Al(2)-O(1)#1 | 91.84(5) |
| O(3)-Al(2)-O(1) | 93.06(5) |

Table D.3., continued

| | |
|--------------------|-----------|
| O(2)-Al(2)-O(1) | 76.15(5) |
| O(2)#1-Al(2)-O(1) | 91.44(5) |
| O(4)#1-Al(2)-O(1) | 164.98(5) |
| O(1)#1-Al(2)-O(1) | 76.40(6) |
| Al(1)-O(1)-Al(2)#4 | 101.31(5) |
| Al(1)-O(1)-Al(2) | 99.14(5) |
| Al(2)#4-O(1)-Al(2) | 95.74(5) |
| Al(1)-O(1)-H(1O) | 122.6(16) |
| Al(2)#4-O(1)-H(1O) | 115.4(16) |
| Al(2)-O(1)-H(1O) | 118.0(16) |
| Al(2)-O(2)-Al(2)#4 | 109.77(6) |
| Al(2)-O(2)-H(2O) | 125.0(17) |
| Al(2)#4-O(2)-H(2O) | 122.2(16) |
| Al(2)-O(3)-In(1) | 131.22(6) |
| Al(2)-O(3)-H(3O) | 115.2(15) |
| In(1)-O(3)-H(3O) | 112.8(15) |
| Al(2)#4-O(4)-In(1) | 128.29(6) |
| Al(2)#4-O(4)-H(4O) | 113.8(16) |
| In(1)-O(4)-H(4O) | 113.0(16) |
| In(1)-O(5)-H(5OA) | 115(2) |
| In(1)-O(5)-H(5OB) | 123(3) |
| H(5OA)-O(5)-H(5OB) | 110(3) |
| In(1)-O(6)-H(6OA) | 118(2) |
| In(1)-O(6)-H(6OB) | 125(3) |
| H(6OA)-O(6)-H(6OB) | 109(3) |
| In(1)-O(7)-H(7OA) | 115.3(19) |
| In(1)-O(7)-H(7OB) | 122(2) |
| H(7OA)-O(7)-H(7OB) | 107(3) |
| In(1)-O(8)-H(8OA) | 117(2) |

Table D.3., continued

| | |
|--------------------|------------|
| In(1)-O(8)-H(8OB) | 122.6(19) |
| H(8OA)-O(8)-H(8OB) | 107(3) |
| O(2S)-N(1S)-O(1S) | 119.01(17) |
| O(2S)-N(1S)-O(3S) | 121.27(16) |
| O(1S)-N(1S)-O(3S) | 119.72(16) |
| O(4S)-N(2S)-O(5S) | 120.0(2) |
| O(4S)-N(2S)-O(6S) | 120.9(2) |
| O(5S)-N(2S)-O(6S) | 119.13(19) |

Symmetry transformations used to generate equivalent atoms:

#1 $y+1, -x+y+1, -z+1$ #2 $-y+1, x-y-1, z$ #3 $-x+2, -y, -z+1$

#4 $x-y, x-1, -z+1$ #5 $-x+y+2, -x+1, z$

Table D.4. Anisotropic displacement parameters ($\approx 2 \times 10^3$) for $[\text{Al}_7\text{In}_6(\mu_3\text{-OH})_6(\mu\text{-OH})_{18}(\text{H}_2\text{O})_{24}](\text{NO}_3)_{15}$. The anisotropic displacement factor exponent takes the form: $-2 \sum^2 [h^2 a^* 2 U^{11} + \dots + 2 h k a^* b^* U^{12}]$

| | U ¹¹ | U ²² | U ³³ | U ²³ | U ¹³ | U ¹² |
|-------|-----------------|-----------------|-----------------|-----------------|-----------------|-----------------|
| In(1) | 17(1) | 17(1) | 24(1) | 2(1) | -2(1) | 8(1) |
| Al(1) | 15(1) | 15(1) | 19(1) | 0 | 0 | 7(1) |
| Al(2) | 14(1) | 15(1) | 19(1) | -1(1) | -1(1) | 7(1) |
| O(1) | 16(1) | 18(1) | 17(1) | 0(1) | 0(1) | 9(1) |
| O(2) | 17(1) | 16(1) | 21(1) | -2(1) | 1(1) | 8(1) |
| O(3) | 17(1) | 18(1) | 26(1) | 4(1) | -1(1) | 7(1) |
| O(4) | 17(1) | 18(1) | 26(1) | 2(1) | -4(1) | 7(1) |
| O(5) | 24(1) | 32(1) | 32(1) | -3(1) | -7(1) | 14(1) |
| O(6) | 38(1) | 20(1) | 47(1) | 2(1) | 1(1) | 13(1) |
| O(7) | 34(1) | 38(1) | 29(1) | -4(1) | 0(1) | 18(1) |

Table D.4., continued

| | | | | | | |
|-------|-------|--------|-------|--------|--------|-------|
| O(8) | 38(1) | 35(1) | 28(1) | 0(1) | 4(1) | 15(1) |
| N(1S) | 31(1) | 34(1) | 26(1) | -2(1) | 2(1) | 19(1) |
| O(1S) | 46(1) | 83(1) | 46(1) | -35(1) | -14(1) | 45(1) |
| O(2S) | 30(1) | 98(2) | 42(1) | -21(1) | 3(1) | 27(1) |
| O(3S) | 35(1) | 49(1) | 42(1) | -19(1) | -2(1) | 20(1) |
| N(2S) | 47(1) | 45(1) | 41(1) | -2(1) | 0(1) | 28(1) |
| O(4S) | 62(1) | 118(2) | 82(2) | -6(1) | -7(1) | 61(2) |
| O(5S) | 64(1) | 57(1) | 46(1) | -21(1) | -13(1) | 41(1) |
| O(6S) | 72(1) | 57(1) | 37(1) | -14(1) | -5(1) | 40(1) |

Table D.5. Hydrogen coordinates ($\times 10^4$) and isotropic displacement parameters ($\approx 2 \times 10^3$) for $[\text{Al}_7\text{In}_6(\mu_3\text{-OH})_6(\mu\text{-OH})_{18}(\text{H}_2\text{O})_{24}](\text{NO}_3)_{15}$.

| | x | y | z | U(eq) |
|--------|----------|----------|----------|---------|
| H(1O) | 9429(14) | 368(14) | 3998(9) | 46(7) |
| H(2O) | 8778(15) | 767(15) | 5935(10) | 52(7) |
| H(3O) | 9664(12) | 2098(11) | 4099(11) | 37(6) |
| H(4O) | 7529(10) | -235(12) | 4169(13) | 41(6) |
| H(5OA) | 6693(16) | 554(19) | 3969(16) | 88(11) |
| H(5OB) | 6940(30) | 560(30) | 3175(15) | 137(17) |
| H(6OA) | 8677(18) | 2713(17) | 4222(15) | 88(11) |
| H(6OB) | 8090(20) | 2470(30) | 3590(20) | 148(19) |
| H(7OA) | 8002(14) | 1574(15) | 5415(13) | 62(9) |
| H(7OB) | 7293(16) | 849(15) | 5285(18) | 90(12) |
| H(8OA) | 8700(20) | 880(20) | 2840(20) | 108(14) |

Table D.5., continued

| | | | | |
|--------|----------|----------|----------|-------|
| H(8OB) | 8730(16) | 1610(13) | 2667(15) | 66(9) |
|--------|----------|----------|----------|-------|

Table D.6. Torsion angles [$^{\circ}$] for $[\text{Al}_7\text{In}_6(\mu_3\text{-OH})_6(\mu\text{-OH})_{18}(\text{H}_2\text{O})_{24}](\text{NO}_3)_{15}$.

| | |
|---------------------------|------------|
| O(1)#1-Al(1)-O(1)-Al(2)#4 | -98.00(7) |
| O(1)#2-Al(1)-O(1)-Al(2)#4 | 82.00(7) |
| O(1)#3-Al(1)-O(1)-Al(2)#4 | 155(100) |
| O(1)#4-Al(1)-O(1)-Al(2)#4 | -0.22(5) |
| O(1)#5-Al(1)-O(1)-Al(2)#4 | 179.78(5) |
| O(1)#1-Al(1)-O(1)-Al(2) | -0.21(4) |
| O(1)#2-Al(1)-O(1)-Al(2) | 179.79(4) |
| O(1)#3-Al(1)-O(1)-Al(2) | -108(100) |
| O(1)#4-Al(1)-O(1)-Al(2) | 97.57(7) |
| O(1)#5-Al(1)-O(1)-Al(2) | -82.43(7) |
| O(3)-Al(2)-O(1)-Al(1) | 172.13(5) |
| O(2)-Al(2)-O(1)-Al(1) | -96.65(5) |
| O(2)#1-Al(2)-O(1)-Al(1) | 77.16(5) |
| O(4)#1-Al(2)-O(1)-Al(1) | -39.0(2) |
| O(1)#1-Al(2)-O(1)-Al(1) | 0.21(4) |
| O(3)-Al(2)-O(1)-Al(2)#4 | -85.40(5) |
| O(2)-Al(2)-O(1)-Al(2)#4 | 5.82(5) |
| O(2)#1-Al(2)-O(1)-Al(2)#4 | 179.63(5) |
| O(4)#1-Al(2)-O(1)-Al(2)#4 | 63.4(2) |
| O(1)#1-Al(2)-O(1)-Al(2)#4 | 102.67(6) |
| O(3)-Al(2)-O(2)-Al(2)#4 | 86.00(7) |
| O(2)#1-Al(2)-O(2)-Al(2)#4 | -33.47(18) |
| O(4)#1-Al(2)-O(2)-Al(2)#4 | -173.99(6) |
| O(1)#1-Al(2)-O(2)-Al(2)#4 | -81.82(6) |
| O(1)-Al(2)-O(2)-Al(2)#4 | -6.69(5) |

Table D.6., continued

| | |
|-------------------------|------------|
| O(2)-Al(2)-O(3)-In(1) | -18.56(9) |
| O(2)#1-Al(2)-O(3)-In(1) | 149.36(8) |
| O(4)#1-Al(2)-O(3)-In(1) | -114.52(8) |
| O(1)#1-Al(2)-O(3)-In(1) | 94.3(2) |
| O(1)-Al(2)-O(3)-In(1) | 57.66(9) |
| O(4)-In(1)-O(3)-Al(2) | -27.51(9) |
| O(6)-In(1)-O(3)-Al(2) | 151.64(9) |
| O(7)-In(1)-O(3)-Al(2) | 66.52(9) |
| O(8)-In(1)-O(3)-Al(2) | -121.58(9) |
| O(5)-In(1)-O(3)-Al(2) | -161.1(4) |
| O(3)-In(1)-O(4)-Al(2)#4 | 31.08(8) |
| O(6)-In(1)-O(4)-Al(2)#4 | -68(4) |
| O(7)-In(1)-O(4)-Al(2)#4 | -71.28(8) |
| O(8)-In(1)-O(4)-Al(2)#4 | 123.26(8) |
| O(5)-In(1)-O(4)-Al(2)#4 | -153.93(8) |

Symmetry transformations used to generate equivalent atoms:

#1 $y+1, -x+y+1, -z+1$ #2 $-y+1, x-y-1, z$ #3 $-x+2, -y, -z+1$

#4 $x-y, x-1, -z+1$ #5 $-x+y+2, -x+1, z$

Table D.7. Hydrogen bonds for $[\text{Al}_7\text{In}_6(\mu_3\text{-OH})_6(\mu\text{-OH})_{18}(\text{H}_2\text{O})_{24}](\text{NO}_3)_{15}$ [\approx and ∞].

| D-H...A | d(D-H) | d(H...A) | d(D...A) | $\angle(\text{DHA})$ |
|------------------------|-----------|-----------|------------|----------------------|
| O(2)-H(2O)...O(2S) | 0.928(17) | 1.830(17) | 2.755(2) | 174(3) |
| O(2)-H(2O)...O(3S) | 0.928(17) | 2.62(2) | 3.3076(18) | 131(2) |
| O(3)-H(3O)...O(3S)#10 | 0.916(16) | 1.894(16) | 2.8081(18) | 175(2) |
| O(4)-H(4O)...O(1S)#60 | 0.888(16) | 1.921(18) | 2.7824(19) | 163(2) |
| O(5)-H(5OA)...O(6S)#40 | 0.934(18) | 1.852(19) | 2.780(2) | 172(3) |

Table D.7., continued

| | | | |
|--------------------------------|---------|----------|--------|
| O(5)-H(5OB)...O(5S)#70.956(19) | 2.05(2) | 2.986(2) | 167(4) |
| O(5)-H(5OB)...O(3S)#60.956(19) | 2.40(4) | 2.934(2) | 115(3) |
| O(6)-H(6OA)...O(4S)0.932(19) | 2.18(2) | 3.065(3) | 158(3) |
| O(6)-H(6OA)...O(5S)0.932(19) | 2.28(3) | 3.022(2) | 136(3) |
| O(6)-H(6OA)...N(2S)0.932(19) | 2.53(2) | 3.442(2) | 164(3) |
| O(7)-H(7OA)...O(1S)#80.914(18) | 1.82(2) | 2.690(2) | 159(3) |
| O(7)-H(7OA)...O(2S)#80.914(18) | 2.55(2) | 3.293(2) | 139(2) |
| O(7)-H(7OB)...O(5S)#40.935(19) | 1.90(2) | 2.805(2) | 162(3) |
| O(7)-H(7OB)...O(3S)0.935(19) | 2.65(3) | 3.262(2) | 124(3) |

Symmetry transformations used to generate equivalent atoms:

#1 $y+1, -x+y+1, -z+1$ #2 $-y+1, x-y-1, z$ #3 $-x+2, -y, -z+1$

#4 $x-y, x-1, -z+1$ #5 $-x+y+2, -x+1, z$ #6 $-x+y+4/3, -x+2/3, z-1/3$

#7 $y+1/3, -x+y+2/3, -z+2/3$ #8 $-x+5/3, -y+1/3, -z+4/3$

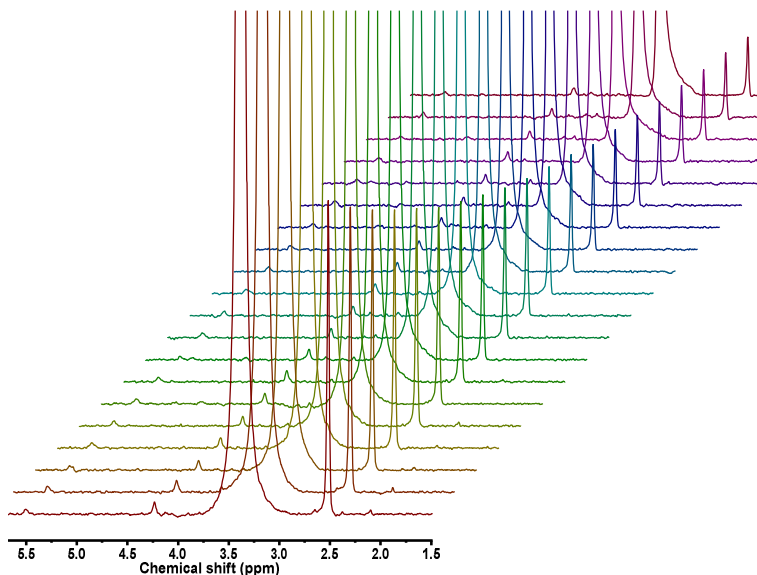


Figure D.1. Stacked plot of $[\text{Al}_7\text{In}_6(\mu_3\text{-OH})_6(\mu\text{-OH})_{18}(\text{H}_2\text{O})_{24}](\text{NO}_3)_{15}$ DOSY in d_6 -DMSO.

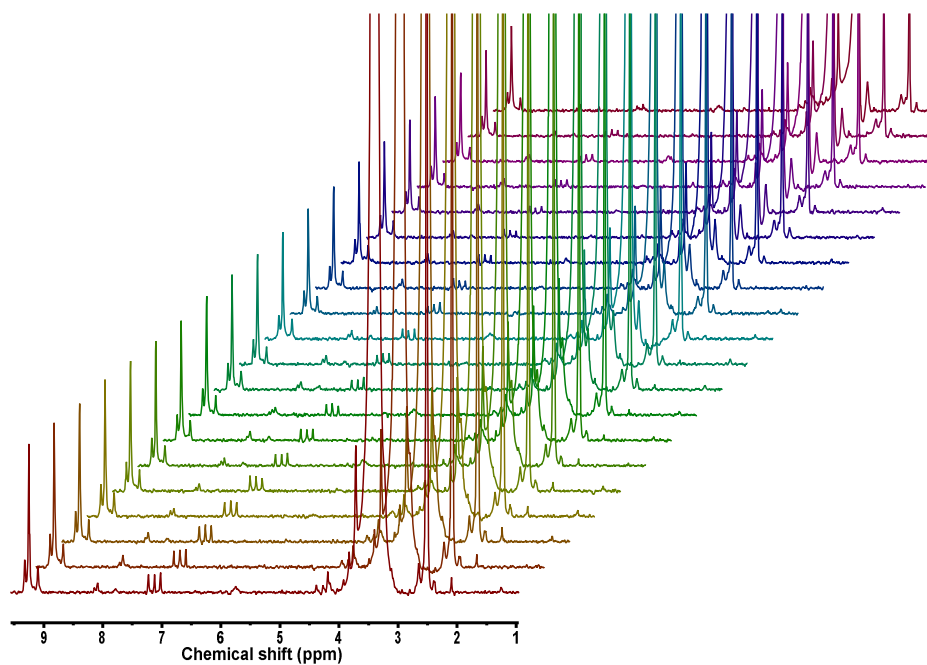


Figure D.2. Stacked plot of $[\text{Al}_{13}(\mu_3\text{-OH})_6(\mu\text{-OH})_{18}(\text{H}_2\text{O})_{24}](\text{NO}_3)_{15}$ DOSY in d_6 -DMSO.

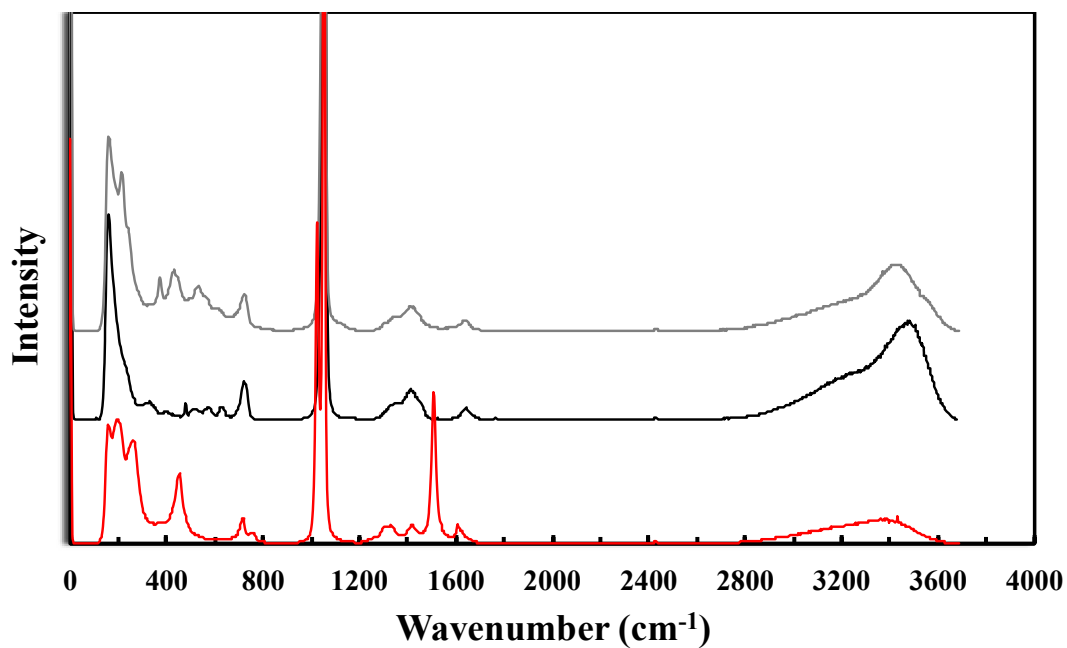


Figure D.3. Stacked plot of solid state Raman spectra for $f\text{-Al}_7\text{In}_6$ (grey), $f\text{-Al}_{13}$ (black), and $\text{In}(\text{NO}_3)_3$ (red).

Table D.8. Diffusion coefficient (**D**) and hydrodynamic radius (**R_h**) values for **f-Al₇In₆** in *d*₆-DMSO. The values for each peak associated with the clusters are averaged together (**in bold**) to give the overall **D** and **R_h** for each cluster. Values not corrected for DOSY software error.

| Freq. (ppm) | Diffusion Coefficient (m ² /s) | Standard error | Temp (K) | η (Pa·s) | r (Å) | r STDV |
|-------------|---|-----------------|------------|-----------------|--------------|-------------|
| | 8.83E-11 | 2.31E-11 | 298 | 2.03E-03 | 12.18 | 3.18 |
| 4.239 | 8.58E-11 | 1.75E-11 | 298 | 2.03E-03 | 12.53 | 2.56 |
| 4.235 | 9.26E-11 | 1.98E-11 | 298 | 2.03E-03 | 11.61 | 2.48 |
| 4.234 | 8.15E-11 | 2.49E-11 | 298 | 2.03E-03 | 13.19 | 4.03 |
| 4.231 | 9.43E-11 | 1.66E-11 | 298 | 2.03E-03 | 11.40 | 2.01 |
| 3.237 | 9.84E-11 | 2.10E-11 | 298 | 2.03E-03 | 10.92 | 2.33 |
| 3.228 | 9.06E-11 | 2.50E-11 | 298 | 2.03E-03 | 11.86 | 3.27 |
| 3.226 | 9.83E-11 | 2.49E-11 | 298 | 2.03E-03 | 10.93 | 2.77 |
| 3.220 | 9.43E-11 | 2.42E-11 | 298 | 2.03E-03 | 11.40 | 2.92 |
| 3.210 | 8.29E-11 | 2.47E-11 | 298 | 2.03E-03 | 12.96 | 3.86 |
| 3.207 | 9.13E-11 | 2.63E-11 | 298 | 2.03E-03 | 11.77 | 3.39 |
| 3.205 | 8.88E-11 | 2.84E-11 | 298 | 2.03E-03 | 12.10 | 3.87 |
| 3.182 | 8.61E-11 | 2.55E-11 | 298 | 2.03E-03 | 12.48 | 3.70 |
| 3.177 | 7.47E-11 | 2.50E-11 | 298 | 2.03E-03 | 14.39 | 4.82 |
| 3.171 | 7.62E-11 | 1.92E-11 | 298 | 2.03E-03 | 14.10 | 3.55 |

Table D.9. Diffusion coefficient (**D**) and hydrodynamic radius (**R_h**) values for **f-Al₁₃In** in *d*₆-DMSO. The values for each peak associated with the clusters are averaged together (**in bold**) to give the overall **D** and **R_h** for each cluster. Values not corrected for DOSY software error.

| Freq. (ppm) | Diffusion Coefficient (m ² /s) | Standard error | Temp (K) | η (Pa·s) | r (Å) | r STDV |
|-------------|---|-----------------|------------|-----------------|--------------|-------------|
| | 8.06E-11 | 2.10E-11 | 298 | 2.03E-03 | 13.33 | 3.48 |
| 8.0849 | 7.69E-11 | 2.92E-11 | 298 | 2.00E-03 | 14.223 | 5.407 |
| 4.2745 | 6.47E-11 | 2.53E-11 | 298 | 2.00E-03 | 16.9 | 6.612 |
| 4.2725 | 6.99E-11 | 1.75E-11 | 298 | 2.00E-03 | 15.643 | 3.911 |
| 4.2686 | 9.78E-11 | 3.10E-11 | 298 | 2.00E-03 | 11.178 | 3.547 |
| 4.1905 | 6.43E-11 | 9.72E-12 | 298 | 2.00E-03 | 17.013 | 2.572 |
| 4.1876 | 6.89E-11 | 8.84E-12 | 298 | 2.00E-03 | 15.863 | 2.035 |
| 4.1739 | 8.82E-11 | 2.36E-11 | 298 | 2.00E-03 | 12.393 | 3.321 |
| 4.169 | 6.75E-11 | 2.53E-11 | 298 | 2.00E-03 | 16.192 | 6.055 |
| 4.1602 | 6.44E-11 | 2.95E-11 | 298 | 2.00E-03 | 16.976 | 7.768 |
| 4.1505 | 1.17E-10 | 2.05E-11 | 298 | 2.00E-03 | 9.3829 | 1.651 |
| 4.1466 | 1.07E-10 | 3.17E-11 | 298 | 2.00E-03 | 10.233 | 3.039 |
| 3.8292 | 7.24E-11 | 1.36E-11 | 298 | 2.00E-03 | 15.111 | 2.833 |
| 3.7159 | 7.53E-11 | 6.35E-12 | 298 | 2.00E-03 | 14.521 | 1.226 |
| 3.6963 | 9.47E-11 | 2.25E-11 | 298 | 2.00E-03 | 11.55 | 2.747 |

Table D.10. Solid state Raman vibrational frequencies for $[\text{Al}_7\text{In}_6(\mu_3\text{-OH})_6(\mu\text{-OH})_{18}(\text{H}_2\text{O})_{24}](\text{NO}_3)_{15}$ at 25°C. Data for $f\text{-Al}_{13}$ was previously published.⁷²

| Peak Position (cm ⁻¹) | Peak Assignment |
|-----------------------------------|--|
| 212 | In-O, b |
| 369 | Al-O, str. |
| 428 524 | In-OH-Al, str, In-OH-Al, str. |
| 594 | Al-O, str |
| 720 | NO ₃ ⁻ , asym. str. |
| 1048 | NO ₃ ⁻ sym. str. |
| 1334 | NO ₃ ⁻¹ |
| 1401 | NO ₃ ⁻¹ |
| 1627 | H ₂ O•••NO ₃ ⁻¹ , d |
| 3273 | O-H, str. |
| 3411 | O-H, str. |
| 3540 | “Free” H ₂ O |

s=strong, m=medium, w=weak, v=very, br=broad, sh=shoulder, asy = asymmetric, sym = symmetric, b = bend, d = deformation, str = stretch; The numbers in table are in wavenumbers (cm⁻¹)

Table D.11. DLS data for the hydrodynamic radius of a 2mM solution of *f*-Al₇In₆ in DMSO.

| Acquisition | Peak 1 Radius (0.1-10nm) | Peak %Pd | Peak 1 %Intensity | Peak 1 %Mass | Peak 2 Radius (10-100nm) | Peak 2 %Pd | Peak 2 %Intensity | Peak 2 %Mass |
|-------------|-----------------------------|-------------|----------------------|-----------------|-----------------------------|---------------|----------------------|-----------------|
| 1 | 0.68 | 10.43 | 0.02 | 50.71 | 72.17 | 48.74 | 97.23 | 28.94 |
| 2 | 1.3 | 25.35 | 0.4 | 88.78 | 72.31 | 51.31 | 99.24 | 10.4 |
| 3 | 9.04 | 10.19 | 4.48 | 17.25 | 62.81 | 17.44 | 95.52 | 82.75 |
| 4 | 0.59 | 13.25 | 0.35 | 98.31 | 10.37 | 20.57 | 2.26 | 0.14 |
| 5 | 0.62 | 10.52 | 0.24 | 95.99 | 66.69 | 41.29 | 94.49 | 2.52 |
| 6 | 4.89 | 11.91 | 1.48 | 27.26 | 65.55 | 40.47 | 94.99 | 52.4 |
| 7 | 1.26 | 14.58 | 0.52 | 85.94 | 71.34 | 57.04 | 98.99 | 8.88 |
| 8 | 0.68 | 11 | 0.25 | 96.53 | 10.98 | 18.11 | 3.46 | 0.38 |
| 9 | -- | -- | -- | -- | 12.01 | 8.12 | 5.96 | 10.99 |
| 10 | 1.83 | 9.92 | 0.64 | 74.75 | 75.84 | 67.28 | 99.16 | 20.46 |
| Mean | 2.32 | 13.02 | 0.93 | 70.61 | 52.01 | 37.04 | 69.13 | 21.79 |
| SD | 2.86 | 4.88 | 1.39 | 31.2 | 28.47 | 19.82 | 45.06 | 26.7 |
| SD% | 8.18 | 23.8 | 1.94 | 973.49 | 810.31 | 392.68 | 2030.24 | 713.08 |
| Min | 0.59 | 9.92 | 0.02 | 17.25 | 10.37 | 8.12 | 2.26 | 0.14 |
| Max | 9.04 | 25.35 | 4.48 | 98.31 | 75.84 | 67.28 | 99.24 | 82.75 |

Table D.12. DLS data for the hydrodynamic radius of a 2mM solution of *f*-Al₁₃ in DMSO.

| Acquisition | Peak 1 Radius (0.1-10nm) | Peak %Pd | Peak 1 %Intensity | Peak 1 %Mass | Peak 2 Radius (10-100nm) | Peak 2 %Pd | Peak 2 %Intensity | Peak 2 %Mass |
|-------------|--------------------------|----------|-------------------|--------------|--------------------------|------------|-------------------|--------------|
| 1 | 1.44 | 18.78 | 1.9 | 87.6 | 21.88 | 42.24 | 27.48 | 0.99 |
| 2 | 1.69 | 19.56 | 2.15 | 82.52 | 24.28 | 45.48 | 29.32 | 1.15 |
| 3 | 1.06 | 23.58 | 1.05 | 90.54 | 18.9 | 41.11 | 21.56 | 0.77 |
| 4 | 1.38 | 20.54 | 1.38 | 83.7 | 22.04 | 44.75 | 25.18 | 1.16 |
| 5 | 1.88 | 25.02 | 1.66 | 72.65 | -- | -- | -- | -- |
| 6 | 2.51 | 22.55 | 0.89 | 31.53 | -- | -- | -- | -- |
| 7 | 1.31 | 23.43 | 1.21 | 85.51 | 19.42 | 41.35 | 24.92 | 1.42 |
| 8 | 1.33 | 22.75 | 1.78 | 89.52 | 22.34 | 44.43 | 28.49 | 0.9 |
| 9 | 1.05 | 23.62 | 1.59 | 93.59 | 21.05 | 46.57 | 26.89 | 0.58 |
| 10 | 1.39 | 19.55 | 1.79 | 86.86 | 21.87 | 42.39 | 27.72 | 0.96 |
| 11 | 2.75 | 28.43 | 1.41 | 47.11 | 19.46 | 42.12 | 23.9 | 6.17 |
| 12 | 1.54 | 14.91 | 1.77 | 83.29 | 21.67 | 42.34 | 28.23 | 1.36 |
| 13 | 1.87 | 15.28 | 2.58 | 80.3 | 25.41 | 41.29 | 31.26 | 1.14 |
| 14 | 1.27 | 23.17 | 1.99 | 91.61 | 23.2 | 41.85 | 28.94 | 0.6 |
| 15 | 1.03 | 21.21 | 1.25 | 91.89 | 24.69 | 47.87 | 34.32 | 0.63 |
| Mean | 1.57 | 21.49 | 1.63 | 79.88 | 22.02 | 43.37 | 27.55 | 1.37 |
| SD | 0.51 | 3.55 | 0.44 | 17.55 | 2.03 | 2.21 | 3.27 | 1.47 |
| SD% | 32.37 | 16.52 | 27.26 | 21.97 | 9.21 | 5.1 | 11.86 | 106.97 |
| Min | 1.03 | 14.91 | 0.89 | 31.53 | 18.9 | 41.11 | 21.56 | 0.58 |
| Max | 2.75 | 28.43 | 2.58 | 93.59 | 25.41 | 47.87 | 34.32 | 6.17 |

Table D.13. DLS data for the hydrodynamic radii of *f*-Al₇In₆ in H₂O.

| Acquisition | Peak 1 Radius (0.1-10nm) | Peak 1 %Pd | Peak 1 %Intensity | Peak 1 %Mass | Peak 2 Radius (10-100nm) | Peak 2 %Pd | Peak 2 %Intensity | Peak 2 %Mass |
|-------------|-----------------------------|---------------|----------------------|-----------------|-----------------------------|---------------|----------------------|-----------------|
| 1 | -- | -- | -- | -- | 13.69 | 59.93 | 98.75 | 99.36 |
| 2 | -- | -- | -- | -- | 13.87 | 53.57 | 99.95 | 99.49 |
| 3 | 1.45 | 37.14 | 1.85 | 87.74 | 12.9 | 43.46 | 97.73 | 11.54 |
| 4 | 0.74 | 23.61 | 0.88 | 92.95 | 12.45 | 48.18 | 98.59 | 6.61 |
| 5 | 1.3 | 24.73 | 1.11 | 75.03 | 14.05 | 52.64 | 98.89 | 24.97 |
| 6 | 1.89 | 24.86 | 2.06 | 71.31 | 13.97 | 49.19 | 97.94 | 28.69 |
| 7 | 1.39 | 27.5 | 1.54 | 82.17 | 14 | 49.58 | 98.46 | 17.83 |
| 8 | -- | -- | -- | -- | 14.33 | 57.24 | 100 | 100 |
| 9 | -- | -- | -- | -- | 14.76 | 59.46 | 100 | 100 |
| 10 | 1.45 | 14.45 | 2.3 | 85.87 | 13.7 | 49.91 | 97.61 | 13.86 |
| 11 | 2.13 | 24.96 | 4.54 | 84.75 | 14.24 | 43.75 | 95.46 | 15.25 |
| 12 | 0.68 | 18.92 | 0.63 | 91.58 | 14.52 | 59.41 | 99.37 | 8.42 |
| 13 | 1.1 | 29.96 | 1.09 | 85.61 | 14.03 | 53.24 | 98.91 | 14.39 |
| 14 | 1.99 | 30.21 | 2.8 | 81.73 | 13.97 | 43.74 | 97.2 | 18.27 |
| 15 | -- | -- | -- | -- | 13.89 | 50.86 | 100 | 100 |
| 16 | 0.96 | 15.15 | 1.26 | 91.72 | 12.35 | 43.68 | 95.05 | 8.16 |
| 17 | 1.34 | 20.97 | 0.39 | 46.57 | 14 | 53.15 | 99.61 | 53.43 |
| 18 | 1.48 | 29.79 | 1.46 | 78.13 | 14.16 | 52.87 | 98.48 | 21.68 |
| 19 | -- | -- | -- | -- | 14.55 | 56.05 | 100 | 100 |
| 20 | 1.81 | 27.94 | 3.18 | 85.68 | 14.45 | 46.07 | 96.82 | 14.32 |
| Mean | 1.41 | 25.01 | 1.79 | 81.49 | 13.89 | 51.3 | 98.44 | 42.83 |
| SD | 0.44 | 6.21 | 1.12 | 11.82 | 0.64 | 5.44 | 1.46 | 39.53 |
| SD% | 31.49 | 24.81 | 62.67 | 14.51 | 4.64 | 10.6 | 1.49 | 92.32 |
| Min | 0.68 | 14.45 | 0.39 | 46.57 | 12.35 | 43.46 | 95.02 | 6.61 |
| Max | 2.13 | 37.14 | 4.54 | 92.95 | 14.76 | 59.93 | 100 | 100 |

Table D.14. DLS data for the hydrodynamic radius of *f*-Al₁₃ in H₂O.

| Acquisition | Radius (nm) | Polydispersity (nm) | %PD | PD Index |
|--------------------|--------------------|----------------------------|------------|-----------------|
| 1 | 1 | 0.3 | 32.7 | 0.327 |
| 2 | 1 | 0.4 | 37.8 | 0.378 |
| 3 | 1 | 0.4 | 41.3 | 0.413 |
| 4 | 1 | 0.4 | 42.6 | 0.426 |
| 5 | 1 | 0.5 | 46.7 | 0.467 |
| 6 | 1 | 0.4 | 36.6 | 0.366 |
| 7 | 1 | 0.4 | 37.1 | 0.371 |
| 8 | 1 | 0.5 | 45 | 0.45 |
| 9 | 1.1 | 0.6 | 57.1 | 0.571 |
| 10 | 0.9 | 0.5 | 57.1 | 0.571 |
| 11 | 1.1 | 0.4 | 34.1 | 0.341 |
| 12 | 1 | 0.4 | 44.2 | 0.442 |
| 13 | 1 | 0.4 | 43.1 | 0.431 |
| 14 | 1 | 0.5 | 52.8 | 0.528 |
| 15 | 1.1 | 0.6 | 54.4 | 0.544 |
| 16 | 1 | 0.6 | 54.7 | 0.547 |
| 17 | 1 | 0.4 | 40.6 | 0.406 |
| 18 | 1 | 0.4 | 41.1 | 0.411 |
| 19 | 1 | 0.5 | 50.6 | 0.506 |
| 20 | 1.1 | 0.6 | 55.2 | 0.552 |
| Mean | 1 | 0.5 | 45.2 | 0.452 |
| SD | 0.04 | 0.1 | 7.9 | 0.079 |
| SD% | 3.8 | 18.9 | 15.7 | 17.489 |
| Min | 0.9 | 0.3 | 32.7 | 0.327 |
| Max | 1.1 | 0.6 | 57.1 | 0.571 |

APPENDIX E

SUPPLEMENTAL INFORMATION FOR CHAPTER V

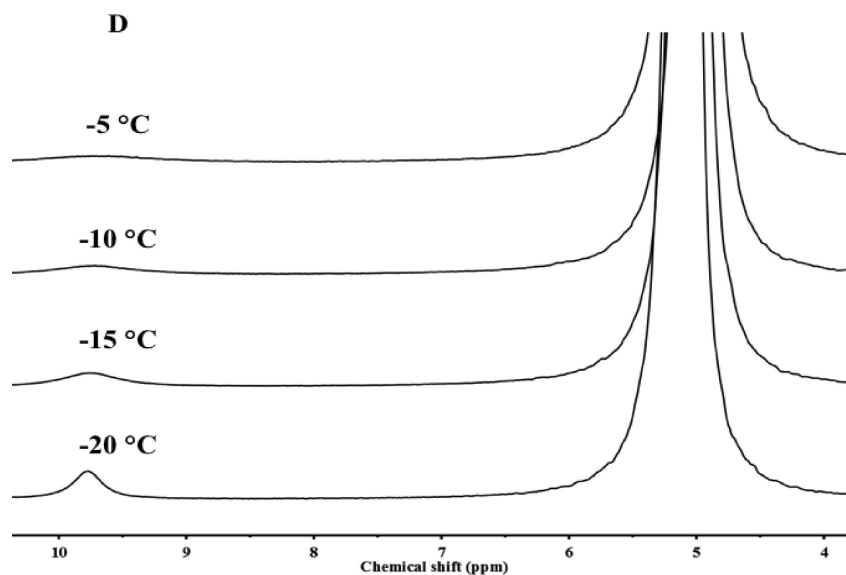


Figure E.1. ^1H -NMR spectra of $\text{Al}(\text{NO}_3)_3$ in a 2.5:1 (v/v) mix of $\text{H}_2\text{O}/\text{acetone-}d_6$.

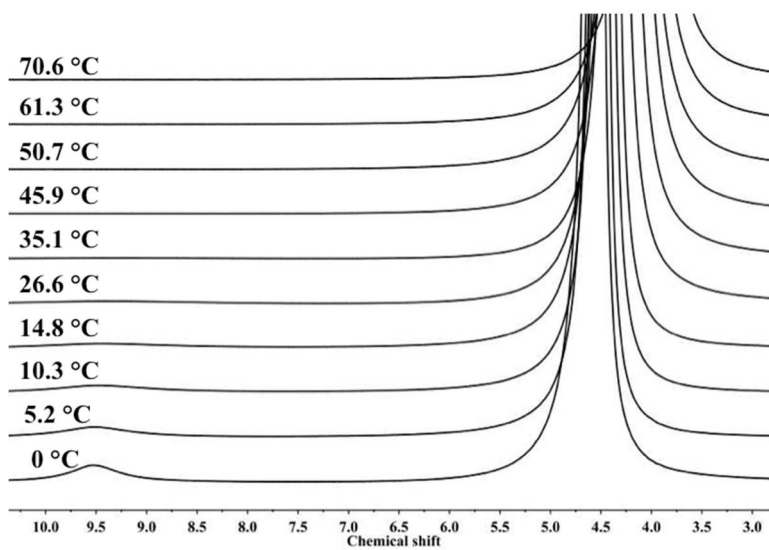


Figure E.2. ^1H -NMR spectra of $\text{Al}(\text{NO}_3)_3$ in a 2:1 (v/v) mix of $\text{H}_2\text{O}/\text{DMSO-}d_6$.

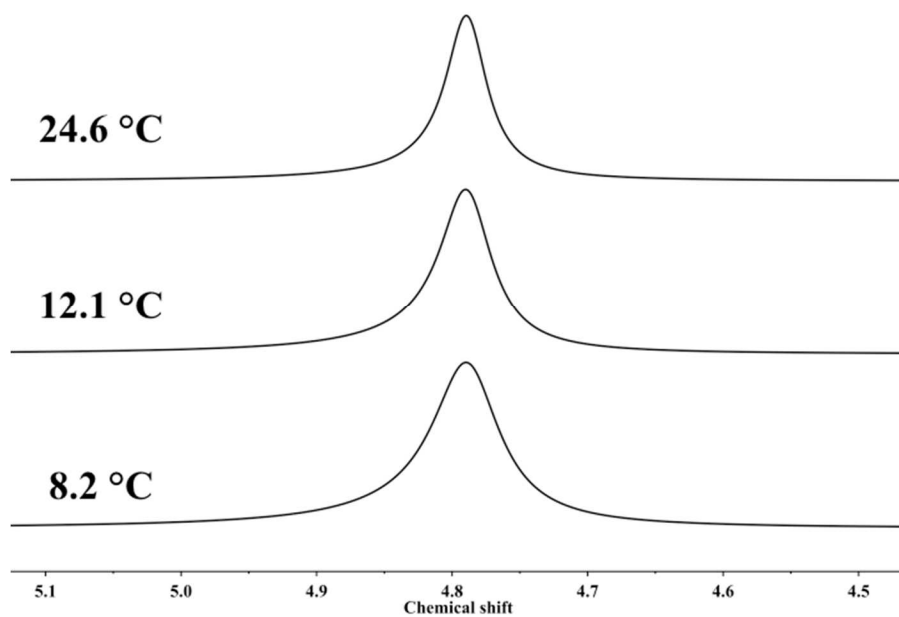


Figure E.3. $^1\text{H-NMR}$ spectra of $\text{Al}(\text{NO}_3)_3$ in D_2O .

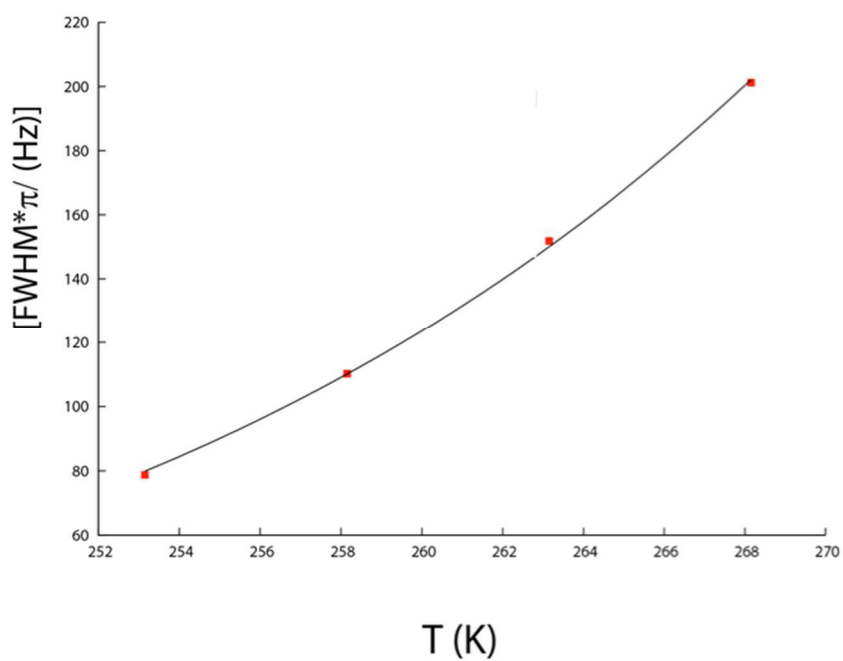


Figure E.4. For 7.8 ppm peak in acetone mix

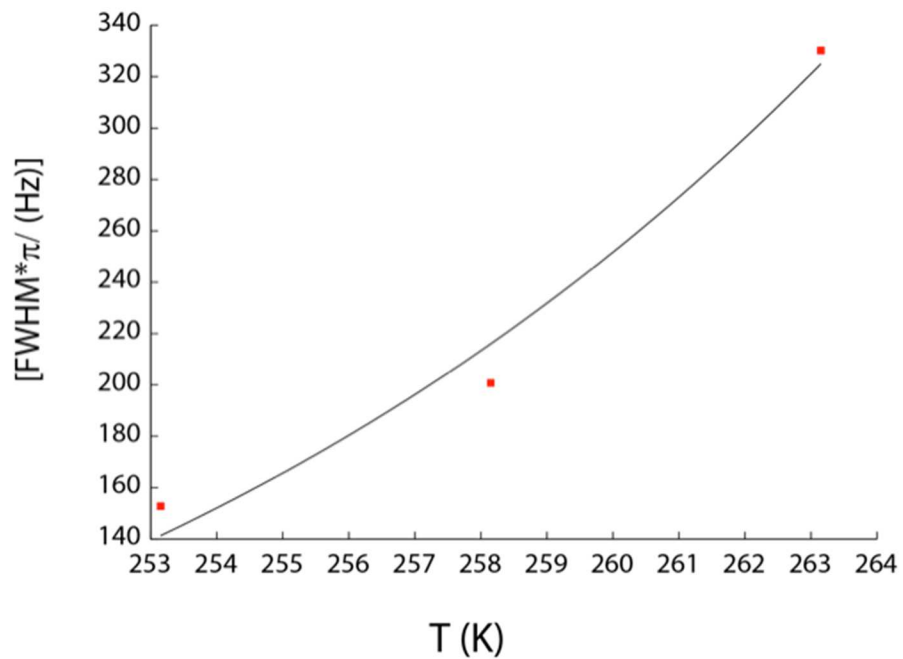


Figure E.5. For 4.5 ppm peak in acetone mix

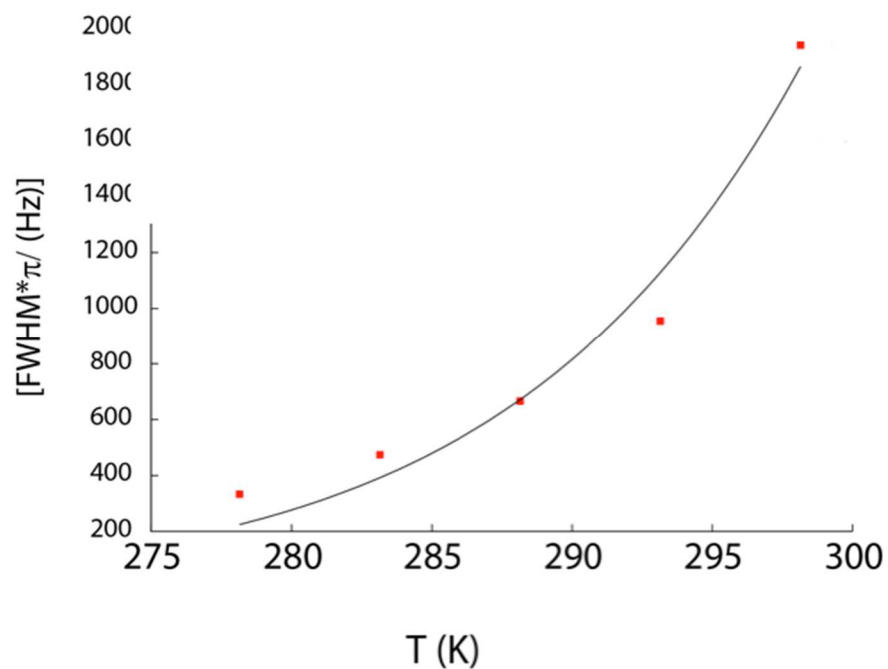


Figure E.6. For 7.5 ppm peak in DMSO mix

APPENDIX F

SUPPLEMENTAL INFORMATION FOR CHAPTER VI

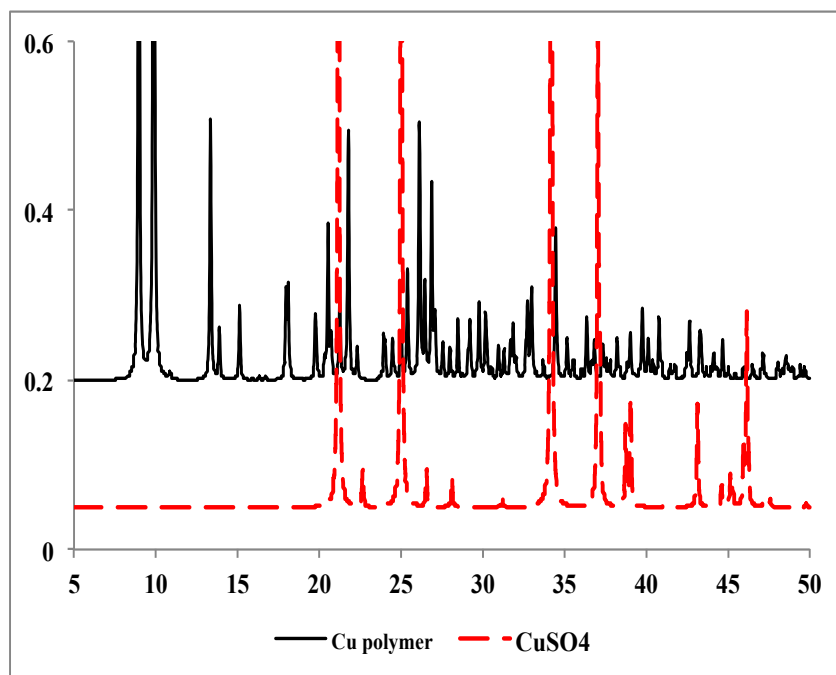


Figure F.1. Calculated powder patterns for $\{(\text{C}_5\text{H}_6\text{N})_2[\text{Cu}_4(\text{OH})_2(\text{SO}_4)_4(\text{H}_2\text{O})_4]\}_n$ (black) and CuSO_4 (red, dotted).

Table F.1. Crystallographic data and structure refinement for $\{(\text{C}_5\text{H}_6\text{N})_2[\text{Cu}_4(\text{OH})_2(\text{SO}_4)_4(\text{H}_2\text{O})_4]\}_n$.

| | | |
|----------------------|---|------------------|
| Empirical formula | $\text{C}_{10} \text{H}_{22} \text{Cu}_4 \text{N}_2 \text{O}_{22} \text{S}_4$ | |
| Formula weight | 904.70 | |
| Temperature | 173(2) K | |
| Wavelength | 0.71073 Å | |
| Crystal system | Orthorhombic | |
| Space group | Pbca | |
| Unit cell dimensions | $a = 7.2662(6) \text{ \AA}$ | $a = 90^\circ$. |

Table F.1., continued

| | | |
|---------------------------------------|--|------------------|
| | $b = 17.9007(16) \text{ \AA}$ | $b = 90^\circ$. |
| | $c = 19.7340(17) \text{ \AA}$ | $g = 90^\circ$. |
| Volume | $2566.8(4) \text{ \AA}^3$ | |
| Z | 4 | |
| Density (calculated) | 2.341 Mg/m^3 | |
| Absorption coefficient | 3.698 mm^{-1} | |
| F(000) | 1808 | |
| Crystal size | $0.26 \times 0.22 \times 0.13 \text{ mm}^3$ | |
| Theta range for data collection | $2.06 \text{ to } 27.00^\circ$. | |
| Index ranges | $-9 \leq h \leq 6, -20 \leq k \leq 22, -23 \leq l \leq 25$ | |
| Reflections collected | 15521 | |
| Independent reflections | 2802 [R(int) = 0.0238] | |
| Completeness to theta = 27.00° | 100.0 % | |
| Absorption correction | Semi-empirical from equivalents | |
| Max. and min. transmission | 0.6449 and 0.4464 | |
| Refinement method | Full-matrix least-squares on F^2 | |
| Data / restraints / parameters | 2802 / 11 / 234 | |
| Goodness-of-fit on F^2 | 1.056 | |
| Final R indices [$I > 2\sigma(I)$] | $R1 = 0.0221, wR2 = 0.0577$ | |
| R indices (all data) | $R1 = 0.0235, wR2 = 0.0587$ | |
| Largest diff. peak and hole | $0.919 \text{ and } -0.397 \text{ e.\AA}^{-3}$ | |

Table F.2. Atomic coordinates ($\times 10^4$) and equivalent isotropic displacement parameters ($\text{\AA}^2 \times 10^3$) for $\{(\text{C}_5\text{H}_6\text{N})_2[\text{Cu}_4(\text{OH})_2(\text{SO}_4)_4(\text{H}_2\text{O})_4]\}_n$. $U(\text{eq})$ is defined as one third of the trace of the orthogonalized U^{ij} tensor.

| | x | y | z | U(eq) |
|-------|---------|---------|---------|-------|
| Cu(1) | 5481(1) | 9186(1) | 4996(1) | 11(1) |

Table F.2., continued

| | | | | |
|-------|----------|----------|---------|-------|
| Cu(2) | 8422(1) | 10309(1) | 4060(1) | 11(1) |
| S(1) | 9569(1) | 8721(1) | 4808(1) | 11(1) |
| S(2) | 4665(1) | 9841(1) | 3486(1) | 13(1) |
| O(1) | 6762(2) | 10161(1) | 4837(1) | 11(1) |
| O(2) | 7588(2) | 8527(1) | 4772(1) | 16(1) |
| O(3) | 10058(2) | 9306(1) | 4322(1) | 25(1) |
| O(4) | 9953(3) | 8969(1) | 5504(1) | 30(1) |
| O(5) | 10668(2) | 8052(1) | 4669(1) | 21(1) |
| O(6) | 4503(2) | 9167(1) | 3904(1) | 19(1) |
| O(7) | 6636(2) | 10032(1) | 3390(1) | 27(1) |
| O(8) | 3691(2) | 10470(1) | 3803(1) | 19(1) |
| O(9) | 3904(2) | 9700(1) | 2803(1) | 19(1) |
| O(10) | 4097(2) | 8294(1) | 5261(1) | 16(1) |
| O(11) | 10084(2) | 10477(1) | 3291(1) | 15(1) |
| N(1S) | 2458(3) | 8339(1) | 2563(1) | 30(1) |
| C(1S) | 2273(4) | 8026(2) | 1949(2) | 39(1) |
| C(2S) | 1871(5) | 7279(2) | 1906(2) | 48(1) |
| C(3S) | 1697(5) | 6864(2) | 2493(2) | 48(1) |
| C(4S) | 1857(5) | 7206(2) | 3111(2) | 44(1) |
| C(5S) | 2245(4) | 7953(2) | 3135(2) | 37(1) |

Table F.3. Bond lengths [\AA] and angles [$^\circ$] for $\{(\text{C}_5\text{H}_6\text{N})_2[\text{Cu}_4(\text{OH})_2(\text{SO}_4)_4(\text{H}_2\text{O})_4]\}_n$.

| | |
|---------------|------------|
| Cu(1)-O(10) | 1.9588(16) |
| Cu(1)-O(2) | 1.9830(15) |
| Cu(1)-O(1) | 2.0028(15) |
| Cu(1)-O(1)#1 | 2.0321(15) |
| Cu(1)-O(6) | 2.2692(16) |
| Cu(1)-Cu(1)#1 | 2.9967(6) |

Table F.3., continued

| | |
|--------------------|------------|
| Cu(2)-O(7) | 1.9173(16) |
| Cu(2)-O(4)#2 | 1.9509(17) |
| Cu(2)-O(11) | 1.9621(15) |
| Cu(2)-O(1) | 1.9690(15) |
| Cu(2)-O(3) | 2.2141(17) |
| S(1)-O(3) | 1.4645(17) |
| S(1)-O(5) | 1.4645(16) |
| S(1)-O(4) | 1.4716(17) |
| S(1)-O(2) | 1.4825(16) |
| S(2)-O(6) | 1.4671(16) |
| S(2)-O(8) | 1.4702(17) |
| S(2)-O(9) | 1.4786(16) |
| S(2)-O(7) | 1.4845(16) |
| O(1)-Cu(1)#1 | 2.0321(14) |
| O(4)-Cu(2)#2 | 1.9509(17) |
| N(1S)-C(5S) | 1.332(4) |
| N(1S)-C(1S) | 1.341(4) |
| C(1S)-C(2S) | 1.372(5) |
| C(2S)-C(3S) | 1.381(5) |
| C(3S)-C(4S) | 1.370(5) |
| C(4S)-C(5S) | 1.366(4) |
| O(10)-Cu(1)-O(2) | 88.34(6) |
| O(10)-Cu(1)-O(1) | 172.33(6) |
| O(2)-Cu(1)-O(1) | 97.17(6) |
| O(10)-Cu(1)-O(1)#1 | 90.80(6) |
| O(2)-Cu(1)-O(1)#1 | 175.98(6) |
| O(1)-Cu(1)-O(1)#1 | 84.08(6) |
| O(10)-Cu(1)-O(6) | 94.64(6) |
| O(2)-Cu(1)-O(6) | 91.19(6) |

Table F.3., continued

| | |
|----------------------|------------|
| O(1)-Cu(1)-O(6) | 90.59(6) |
| O(1)#1-Cu(1)-O(6) | 84.96(6) |
| O(10)-Cu(1)-Cu(1)#1 | 132.20(5) |
| O(2)-Cu(1)-Cu(1)#1 | 139.45(5) |
| O(1)-Cu(1)-Cu(1)#1 | 42.41(4) |
| O(1)#1-Cu(1)-Cu(1)#1 | 41.66(4) |
| O(6)-Cu(1)-Cu(1)#1 | 86.98(4) |
| O(7)-Cu(2)-O(4)#2 | 152.26(9) |
| O(7)-Cu(2)-O(11) | 85.60(7) |
| O(4)#2-Cu(2)-O(11) | 82.33(7) |
| O(7)-Cu(2)-O(1) | 95.02(7) |
| O(4)#2-Cu(2)-O(1) | 96.69(7) |
| O(11)-Cu(2)-O(1) | 178.86(6) |
| O(7)-Cu(2)-O(3) | 108.32(8) |
| O(4)#2-Cu(2)-O(3) | 96.27(8) |
| O(11)-Cu(2)-O(3) | 88.51(6) |
| O(1)-Cu(2)-O(3) | 92.20(6) |
| O(3)-S(1)-O(5) | 109.24(10) |
| O(3)-S(1)-O(4) | 110.48(11) |
| O(5)-S(1)-O(4) | 108.57(11) |
| O(3)-S(1)-O(2) | 111.82(10) |
| O(5)-S(1)-O(2) | 109.22(9) |
| O(4)-S(1)-O(2) | 107.44(10) |
| O(6)-S(2)-O(8) | 110.59(10) |
| O(6)-S(2)-O(9) | 110.01(9) |
| O(8)-S(2)-O(9) | 109.81(10) |
| O(6)-S(2)-O(7) | 109.76(11) |
| O(8)-S(2)-O(7) | 110.03(11) |
| O(9)-S(2)-O(7) | 106.55(10) |

Table F.3., continued

| | |
|--------------------|------------|
| Cu(2)-O(1)-Cu(1) | 121.58(7) |
| Cu(2)-O(1)-Cu(1)#1 | 122.72(7) |
| Cu(1)-O(1)-Cu(1)#1 | 95.92(6) |
| S(1)-O(2)-Cu(1) | 126.85(9) |
| S(1)-O(3)-Cu(2) | 127.05(10) |
| S(1)-O(4)-Cu(2)#2 | 136.61(11) |
| S(2)-O(6)-Cu(1) | 119.76(9) |
| S(2)-O(7)-Cu(2) | 128.68(10) |
| C(5S)-N(1S)-C(1S) | 122.4(2) |
| N(1S)-C(1S)-C(2S) | 119.0(3) |
| C(1S)-C(2S)-C(3S) | 119.4(3) |
| C(4S)-C(3S)-C(2S) | 120.0(3) |
| C(5S)-C(4S)-C(3S) | 119.0(3) |
| N(1S)-C(5S)-C(4S) | 120.2(3) |

Symmetry transformations used to generate equivalent atoms:

#1 -x+1,-y+2,-z+1 #2 -x+2,-y+2,-z+1

Table F.4. Anisotropic displacement parameters ($\text{\AA}^2 \times 10^3$) for $\{(\text{C}_5\text{H}_6\text{N})_2[\text{Cu}_4(\text{OH})_2(\text{SO}_4)_4(\text{H}_2\text{O})_4]\}_n$. The anisotropic displacement factor exponent takes the form: $-2p^2[h^2 a^* 2U^{11} + \dots + 2 h k a^* b^* U^{12}]$

| | U11 | U22 | U33 | U23 | U13 | U12 |
|-------|-------|-------|-------|------|-------|-------|
| Cu(1) | 9(1) | 10(1) | 14(1) | 1(1) | 1(1) | 1(1) |
| Cu(2) | 9(1) | 14(1) | 10(1) | 0(1) | 0(1) | -1(1) |
| S(1) | 10(1) | 9(1) | 14(1) | 0(1) | 0(1) | -1(1) |
| S(2) | 10(1) | 19(1) | 10(1) | 0(1) | -1(1) | -1(1) |
| O(1) | 10(1) | 12(1) | 10(1) | 0(1) | -1(1) | 0(1) |

Table F.4., continued

| | | | | | | |
|-------|-------|-------|-------|--------|--------|--------|
| O(2) | 9(1) | 14(1) | 25(1) | -4(1) | -2(1) | 2(1) |
| O(3) | 20(1) | 24(1) | 31(1) | 14(1) | 9(1) | 8(1) |
| O(4) | 24(1) | 46(1) | 20(1) | -12(1) | 5(1) | -17(1) |
| O(5) | 12(1) | 12(1) | 39(1) | 1(1) | 1(1) | 2(1) |
| O(6) | 25(1) | 16(1) | 15(1) | 0(1) | -4(1) | 0(1) |
| O(7) | 12(1) | 57(1) | 12(1) | -5(1) | 2(1) | -11(1) |
| O(8) | 19(1) | 18(1) | 20(1) | 0(1) | -2(1) | 4(1) |
| O(9) | 19(1) | 29(1) | 11(1) | 3(1) | -5(1) | -8(1) |
| O(10) | 12(1) | 12(1) | 25(1) | 3(1) | 0(1) | 1(1) |
| O(11) | 12(1) | 21(1) | 12(1) | 0(1) | 0(1) | -1(1) |
| N(1S) | 25(1) | 24(1) | 42(1) | -5(1) | 5(1) | -3(1) |
| C(1S) | 39(2) | 44(2) | 34(2) | 2(1) | 2(1) | 9(1) |
| C(2S) | 60(2) | 45(2) | 39(2) | -20(2) | -12(2) | 7(2) |
| C(3S) | 59(2) | 29(2) | 56(2) | -9(2) | -7(2) | -13(2) |
| C(4S) | 53(2) | 38(2) | 42(2) | 2(1) | 4(2) | -15(2) |
| C(5S) | 38(2) | 41(2) | 32(1) | -11(1) | 4(1) | -13(1) |

Table F.5. Hydrogen coordinates ($\times 10^4$) and isotropic displacement parameters ($\text{\AA}^2 \times 10^3$) for $\{(\text{C}_5\text{H}_6\text{N})_2[\text{Cu}_4(\text{OH})_2(\text{SO}_4)_4(\text{H}_2\text{O})_4]\}_n$.

| | x | y | z | U(eq) |
|-------|----------|-----------|----------|--------|
| H(1) | 7510(40) | 10206(16) | 5202(11) | 25(7) |
| H(1S) | 2860(50) | 8855(12) | 2592(17) | 51(10) |
| H(2S) | 2400(60) | 8385(19) | 1529(15) | 70(12) |
| H(3S) | 1670(50) | 7090(20) | 1409(11) | 52(10) |
| H(4S) | 1480(60) | 6291(12) | 2480(20) | 82(14) |

Table F.5., continued

| | | | | |
|--------|-----------|-----------|----------|--------|
| H(5S) | 1610(50) | 6960(20) | 3585(13) | 66(12) |
| H(6S) | 2430(50) | 8239(19) | 3597(13) | 63(12) |
| H(10B) | 4740(40) | 7832(13) | 5269(18) | 43(9) |
| H(10A) | 2950(30) | 8202(18) | 5048(13) | 31(8) |
| H(11B) | 11330(30) | 10460(20) | 3418(18) | 52(10) |
| H(11A) | 9930(50) | 10190(18) | 2897(13) | 46(10) |

Table F.6. Torsion angles [°] for $\{(C_5H_6N)_2[Cu_4(OH)_2(SO_4)_4(H_2O)_4]\}_n$.

| | |
|---------------------------|-------------|
| O(7)-Cu(2)-O(1)-Cu(1) | 55.71(10) |
| O(4)#2-Cu(2)-O(1)-Cu(1) | -149.48(10) |
| O(11)-Cu(2)-O(1)-Cu(1) | 179(100) |
| O(3)-Cu(2)-O(1)-Cu(1) | -52.91(9) |
| O(7)-Cu(2)-O(1)-Cu(1)#1 | -66.90(10) |
| O(4)#2-Cu(2)-O(1)-Cu(1)#1 | 87.91(10) |
| O(11)-Cu(2)-O(1)-Cu(1)#1 | 56(3) |
| O(3)-Cu(2)-O(1)-Cu(1)#1 | -175.52(9) |
| O(10)-Cu(1)-O(1)-Cu(2) | 177.2(4) |
| O(2)-Cu(1)-O(1)-Cu(2) | 41.59(9) |
| O(1)#1-Cu(1)-O(1)-Cu(2) | -134.56(11) |
| O(6)-Cu(1)-O(1)-Cu(2) | -49.69(8) |
| Cu(1)#1-Cu(1)-O(1)-Cu(2) | -134.56(11) |
| O(10)-Cu(1)-O(1)-Cu(1)#1 | -48.2(5) |
| O(2)-Cu(1)-O(1)-Cu(1)#1 | 176.15(6) |
| O(1)#1-Cu(1)-O(1)-Cu(1)#1 | 0.0 |
| O(6)-Cu(1)-O(1)-Cu(1)#1 | 84.87(6) |
| O(3)-S(1)-O(2)-Cu(1) | -64.90(14) |
| O(5)-S(1)-O(2)-Cu(1) | 174.08(11) |

Table F.6., continued

| | |
|-------------------------|-------------|
| O(4)-S(1)-O(2)-Cu(1) | 56.50(15) |
| O(10)-Cu(1)-O(2)-S(1) | -150.17(13) |
| O(1)-Cu(1)-O(2)-S(1) | 24.47(13) |
| O(1)#1-Cu(1)-O(2)-S(1) | 132.2(8) |
| O(6)-Cu(1)-O(2)-S(1) | 115.22(12) |
| Cu(1)#1-Cu(1)-O(2)-S(1) | 28.47(16) |
| O(5)-S(1)-O(3)-Cu(2) | 161.09(12) |
| O(4)-S(1)-O(3)-Cu(2) | -79.55(16) |
| O(2)-S(1)-O(3)-Cu(2) | 40.07(17) |
| O(7)-Cu(2)-O(3)-S(1) | -83.37(15) |
| O(4)#2-Cu(2)-O(3)-S(1) | 109.64(15) |
| O(11)-Cu(2)-O(3)-S(1) | -168.24(15) |
| O(1)-Cu(2)-O(3)-S(1) | 12.66(15) |
| O(3)-S(1)-O(4)-Cu(2)#2 | -24.3(2) |
| O(5)-S(1)-O(4)-Cu(2)#2 | 95.51(19) |
| O(2)-S(1)-O(4)-Cu(2)#2 | -146.48(17) |
| O(8)-S(2)-O(6)-Cu(1) | -57.20(13) |
| O(9)-S(2)-O(6)-Cu(1) | -178.67(10) |
| O(7)-S(2)-O(6)-Cu(1) | 64.39(13) |
| O(10)-Cu(1)-O(6)-S(2) | 161.94(11) |
| O(2)-Cu(1)-O(6)-S(2) | -109.63(11) |
| O(1)-Cu(1)-O(6)-S(2) | -12.45(11) |
| O(1)#1-Cu(1)-O(6)-S(2) | 71.55(11) |
| Cu(1)#1-Cu(1)-O(6)-S(2) | 29.82(10) |
| O(6)-S(2)-O(7)-Cu(2) | -63.16(18) |
| O(8)-S(2)-O(7)-Cu(2) | 58.77(18) |
| O(9)-S(2)-O(7)-Cu(2) | 177.75(14) |
| O(4)#2-Cu(2)-O(7)-S(2) | -110.54(19) |
| O(11)-Cu(2)-O(7)-S(2) | -174.83(17) |

Table F.6., continued

| | |
|-------------------------|-----------|
| O(1)-Cu(2)-O(7)-S(2) | 4.21(17) |
| O(3)-Cu(2)-O(7)-S(2) | 98.21(16) |
| C(5S)-N(1S)-C(1S)-C(2S) | -0.8(5) |
| N(1S)-C(1S)-C(2S)-C(3S) | -1.1(5) |
| C(1S)-C(2S)-C(3S)-C(4S) | 2.5(6) |
| C(2S)-C(3S)-C(4S)-C(5S) | -2.1(6) |
| C(1S)-N(1S)-C(5S)-C(4S) | 1.2(5) |
| C(3S)-C(4S)-C(5S)-N(1S) | 0.2(5) |

Symmetry transformations used to generate equivalent atoms:

#1 -x+1,-y+2,-z+1 #2 -x+2,-y+2,-z+1

Table F.7. Hydrogen bonds for $\{(C_5H_6N)_2[Cu_4(OH)_2(SO_4)_4(H_2O)_4]\}_n$ [\AA and $^\circ$].

| D-H...A | d(D-H) | d(H...A) | d(D...A) | $\angle(DHA)$ |
|--------------------------------|-----------|------------|------------|---------------|
| O(10)-H(10B)...O(5)#30.951(18) | 1.724(19) | 2.670(2) | 173(3) | |
| O(10)-H(10B)...S(1)#30.951(18) | 2.79(2) | 3.6251(16) | 148(3) | |
| O(10)-H(10A)...O(5)#40.948(18) | 1.839(18) | 2.786(2) | 177(3) | |
| O(10)-H(10A)...S(1)#40.948(18) | 2.67(2) | 3.4943(17) | 146(2) | |
| O(11)-H(11B)...O(8)#50.941(19) | 1.874(19) | 2.809(2) | 171(3) | |
| O(11)-H(11B)...S(2)#50.941(19) | 2.67(2) | 3.5387(16) | 154(3) | |
| O(11)-H(11A)...O(9)#60.939(19) | 1.80(2) | 2.707(2) | 162(3) | |
| N(1S)-H(1S)...O(9) | 0.969(19) | 1.74(2) | 2.695(3) | 166(3) |
| O(1)-H(1)...O(3)#2 | 0.908(17) | 2.18(2) | 3.001(2) | 150(3) |
| O(1)-H(1)...O(8)#1 | 0.908(17) | 2.47(3) | 2.931(2) | 112(2) |
| O(1)-H(1)...S(1)#2 | 0.908(17) | 2.86(3) | 3.4069(15) | 120(2) |

Symmetry transformations used to generate equivalent atoms:

Table F.7., continued

#1 -x+1,-y+2,-z+1 #2 -x+2,-y+2,-z+1 #3 x-1/2,-y+3/2,-z+1
#4 x-1,y,z #5 x+1,y,z #6 x+1/2,y,-z+1/2

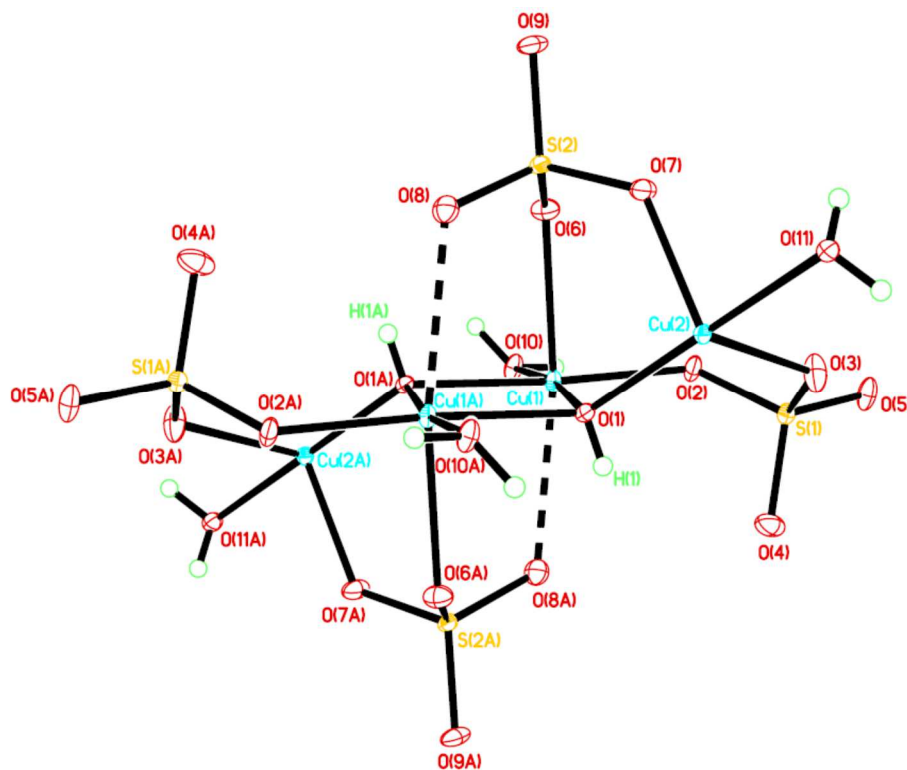


Figure F.2. Crystal structure of $[\text{Cu}_4(\text{SO}_4)_4(\mu_3\text{-OH})_2(\text{H}_2\text{O})_2]_2[\text{C}_5\text{NH}_6]$. Pyridinium counterion is not shown.

APPENDIX G

SUPPLEMENTAL INFORMATION FOR CHAPTER VII

Methodology for *f*-Al₁₃ toxicity studies

Zebrafish (*Danio rerio*) embryos were collected from group spawns of wild-type D5 fish housed at the Sinnhuber Aquatic Research Laboratory (Oregon State University, Corvallis Oregon) and staged such that the chorion surrounding the embryo could be removed enzymatically at 6 hours post fertilization (hpf) to ensure that nanomaterials were in direct contact with the developing embryos.

Exposures consisted of 5-fold serial dilutions of nanomaterials ranging from 250 parts per million (ppm) down to 16 parts per billion (ppb) prepared in fishwater. Control exposures were comprised of fishwater alone (without NPs). Fishwater was prepared by diluting 0.26 g/L Instant Ocean salts (Aquatic Ecosystems, Apopka, FL) into reverse osmosis (RO) water and adjusting the pH to 7.2 ± 0.2 with sodium bicarbonate. Embryos at 8 hpf were exposed in clear, 96-well exposure plates, one animal per well, to various concentrations of test materials. A total of 24 embryos were exposed to each material at each concentration.

Embryos were incubated at 26 °C in covered clear 96-well plates under 14/10 light-cycle until evaluations. Embryos were evaluated at 24 hpf for viability, developmental progression and spontaneous movement (earliest behavior in zebrafish). At 120 hpf, behavioral endpoints (motility, tactile response) were thoroughly evaluated *in vivo* and larval morphology (body axis, eye, snout, jaw, otic vesicle, notochord, heart, brain,

somite, fin, yolk sac, trunk, circulation, pigment, swim bladder) were evaluated and scored in a binary fashion (present or absent).

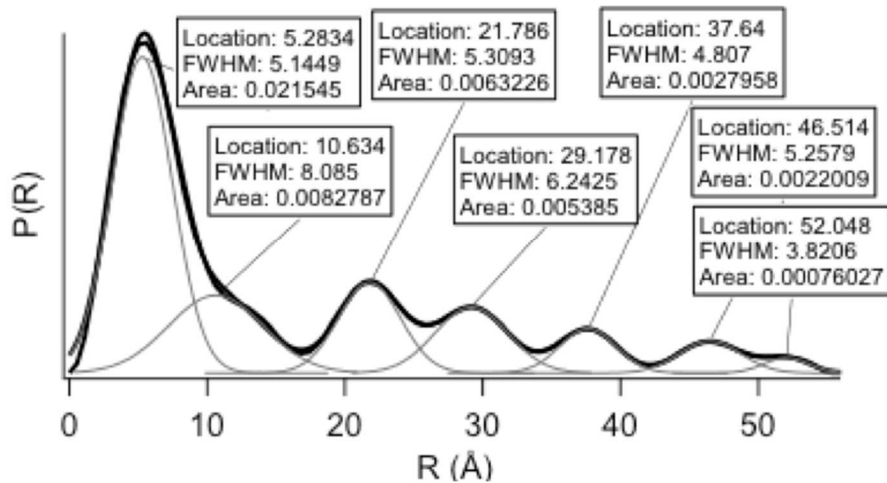


Figure G.1. PDDF analysis of 1M $f\text{-Al}_{13}$ in H_2O .

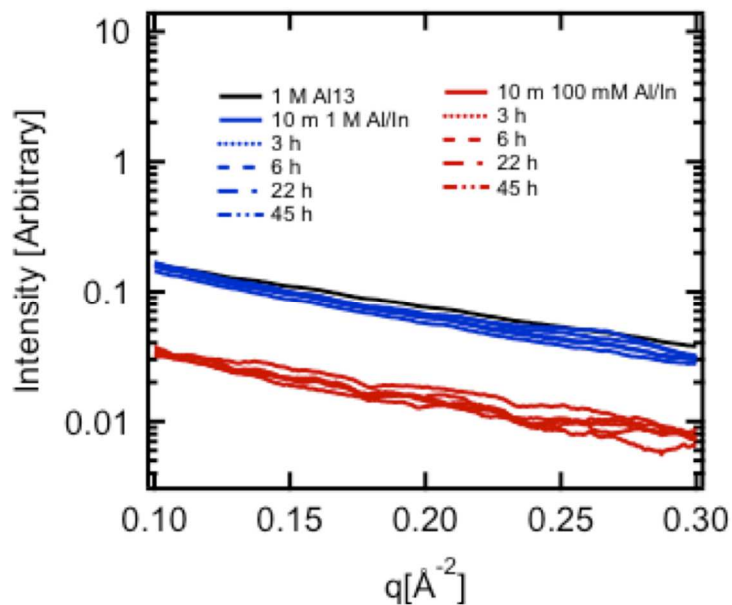


Figure G.2. Q-space plot of $f\text{-Al}_{13}$ (1M) and $f\text{-Al}_{13} + \text{In}(\text{NO}_3)_3$ (1M and 100 mM) in MeOH.

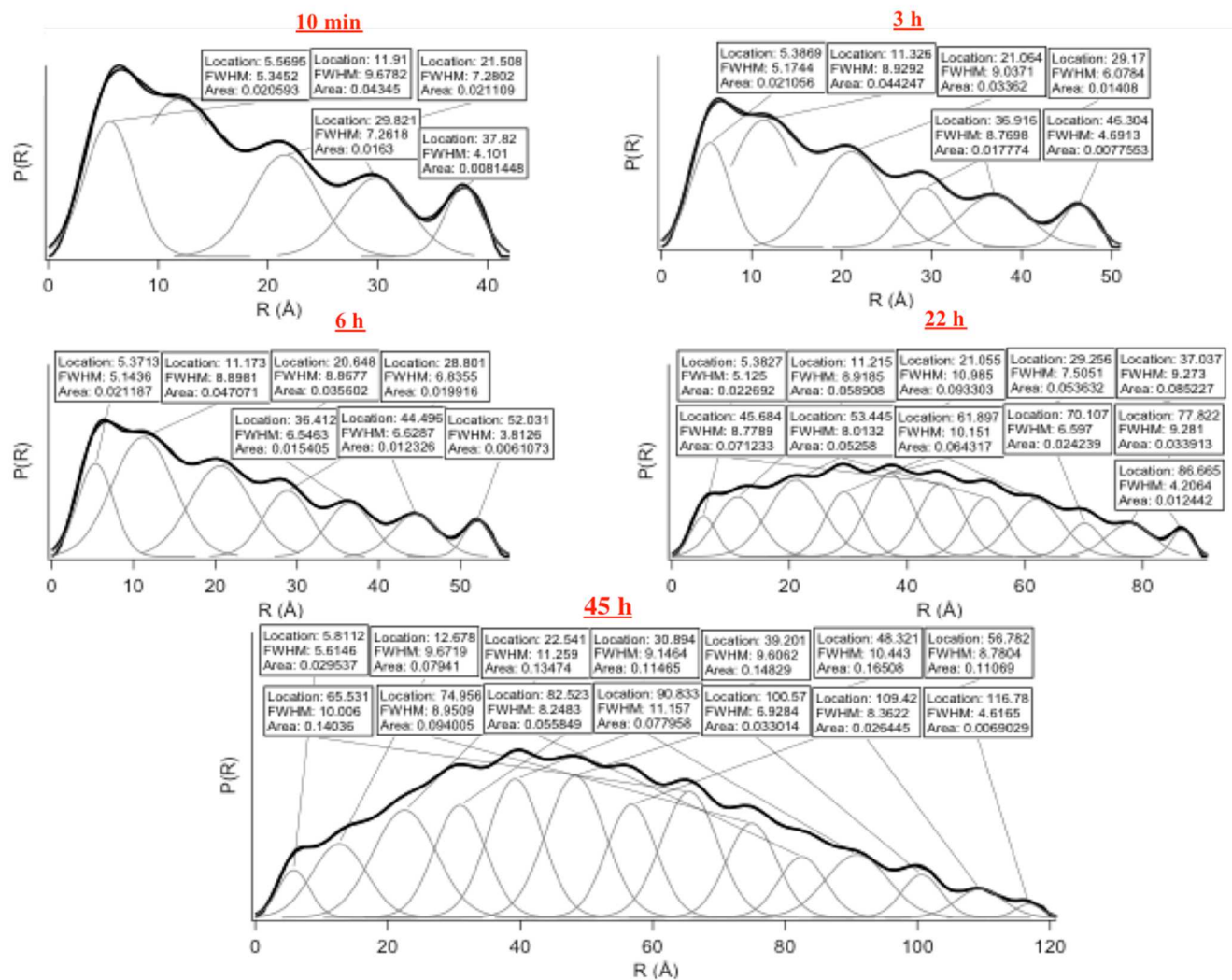


Figure G.3. PDDF analysis of 1M $f\text{-Al}_3 + \text{In}(\text{NO}_3)_3$ in H_2O over time.

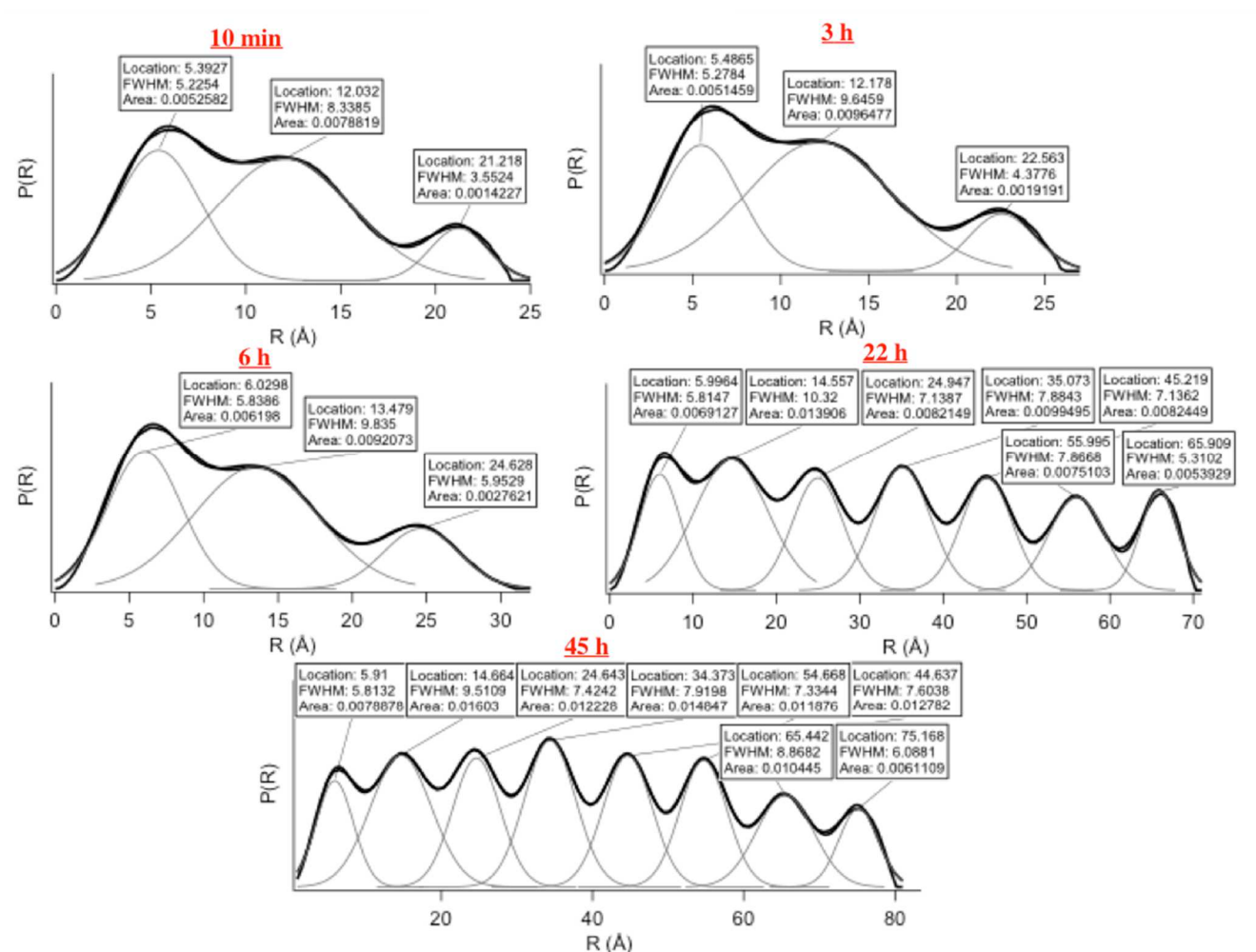


Figure G.4. PDDF analysis of 100 mM $f\text{-Al}_3$ + $\text{In}(\text{NO}_3)_3$ in H_2O over time.

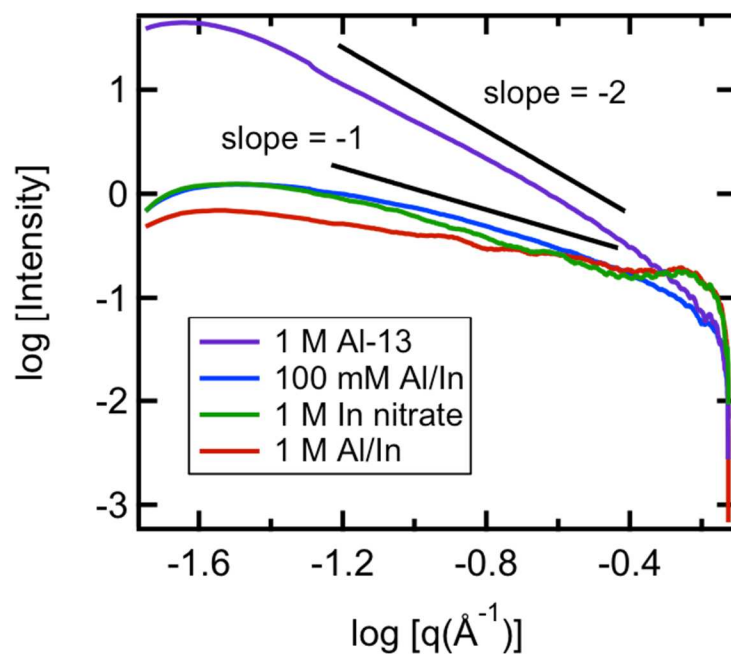


Figure G.5. Log SAXS scatter plot of $f\text{-Al}_{13}$ (1M) and $f\text{-Al}_{13} + \text{In}(\text{NO}_3)_3$ (1M and 100 mM) in MeOH.

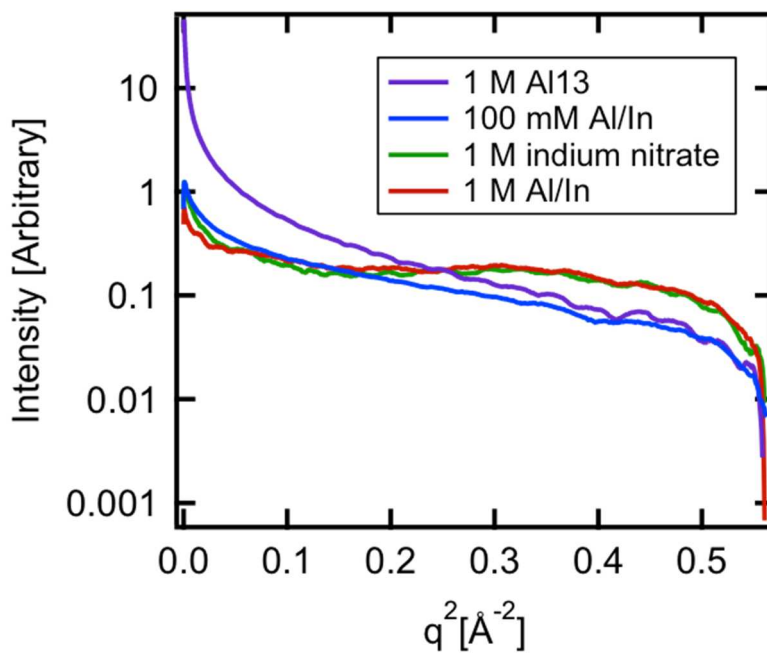


Figure G.6. Log-log SAXS scatter plot of $f\text{-Al}_{13}$ (1M) and $f\text{-Al}_{13} + \text{In}(\text{NO}_3)_3$ (1M and 100 mM) in MeOH.

REFERENCES CITED

- (1) Rather, E.; Gatlin, J. T.; Nixon, P. G.; Tsukamoto, T.; Kravtsov, V.; Johnson, D. *W. J. Am. Chem. Soc.* **2005**, *127*, 3242.
- (2) Greenwood, N. N.; Earnshaw, A. *Chemistry of the Elements (2nd Edition)*; Elsevier: Oxford, 1997.
- (3) Exley, C. *Environ. Sci. Process. Impacts* **2013**, *15*, 1807.
- (4) Sorenson, J. R. J.; Campbell, I. R.; Tepper, L. B.; Lingg, R. D. *Environ. Health Perspect.* **1974**, *8*, 3.
- (5) Kawahara, M.; Kato-Negishi, M. *Int. J. Alzheimers. Dis.* **2011**, *1*.
- (6) Aldridge, S.; Downs, A. J. *The Group 13 Metals Aluminium, Gallium, Indium and Thallium: Chemical Patterns and Peculiarities*; Wiley, 2011.
- (7) Wood, S. A.; Samson, I. M. *Ore Geol. Rev.* **2006**, *28*, 57.
- (8) Marezio, M. *Acta Crystallogr.* **1966**, *20*, 723.
- (9) Furrer, G.; Phillips, B. L.; Ulrich, K.-U.; Pöthig, R. *Science (80-)*. **2002**, *297*, 2245.
- (10) Johansson, G.; Lundgren, G.; Sillén, L. G.; Söderquist, R. *Acta Chem. Scand.* **1960**, *14*, 769.
- (11) Johansson, G.; Lundgren, G.; Sillén, L. G.; Söderquist, R. *Acta Chem. Scand.* **1960**, *14*, 771.
- (12) Barron, A. R. *Dalt. Trans.* **2014**, *43*, 8127.
- (13) Casey, W. H.; Rustad, J. R.; Spiccia, L. *Chem. – A Eur. J.* **2009**, *15*, 4496.
- (14) Putnis, A. *Sci.* **2014**, *343*, 1441.
- (15) Nomura, K.; Ohta, H.; Takagi, A.; Kamiya, T.; Hirano, M.; Hosono, H. *Nature* **2004**, *432*, 3383.
- (16) Takamoto, T.; Kaneiwa, M.; Imaizumi, M.; Yamaguchi, M. *Prog. Photovoltaics Res. Appl.* **2005**, *13*, 495.

- (17) Ringel, S. A.; Carlin, J. A.; Andre, C. L.; Hudait, M. K.; Gonzalez, M.; Wilt, D. M.; Clark, E. B.; Jenkins, P.; Scheiman, D.; Allerman, A.; Fitzgerald, E. A.; Leitz, C. W. *Prog. Photovoltaics Res. Appl.* **2002**, *10*, 417.
- (18) Tomasulo, S.; Yaung, K. N.; Lee, M. L. *IEEE J. Photovoltaics* **2012**, *2*, 56.
- (19) Mauk, M. G.; Tata, A. N.; Feyock, B. W. *J. Cryst. Growth* **2001**, *225*, 359.
- (20) Tsintzos, S. I.; Pelekanos, N. T.; Konstantinidis, G.; Hatzopoulos, Z.; Savvidis, P. G. *Nature* **2008**, *453*, 372.
- (21) Kim, H.-M.; Cho, Y.-H.; Lee, H.; Kim, S. Il; Ryu, S. R.; Kim, D. Y.; Kang, T. W.; Chung, K. S. *Nano Lett.* **2004**, *4*, 1059.
- (22) Ming-Jiunn, J.; Biing-Jye, L.; Tarn, J. C.; Chuan-Ming, C.; Chia-Cheng, L. Transparent conductive layer such as of indium tin oxide is deposited between the electrode and the semiconductor diode to spread the current evenly to the diode and reduce series resistance, 2000.
- (23) Goldberger, J.; He, R.; Zhang, Y.; Lee, S.; Yan, H.; Choi, H.-J.; Yang, P. *Nature* **2003**, *422*, 599.
- (24) Huang, Y.; Duan, X.; Cui, Y.; Lieber, C. M. *Nano Lett.* **2002**, *2*, 101.
- (25) Johnson, J. C.; Choi, H.-J.; Knutsen, K. P.; Schaller, R. D.; Yang, P.; Saykally, R. *J. Nat Mater* **2002**, *1*, 106.
- (26) Sheka Chaus, I. S., Mitiureva, T. T., I. A. *The chemistry of gallium*,; Elsevier Pub. Co.: Amsterdam; New York, 1966.
- (27) Presley, R. E.; Hong, D.; Chiang, H. Q.; Hung, C. M.; Hoffman, R. L.; Wager, J. F. *Solid. State. Electron.* **2006**, *50*, 500.
- (28) Lim, H.; Yin, H.; Park, J.-S.; Song, I.; Kim, C.; Park, J.; Kim, S.; Kim, S.-W.; Lee, C. B.; Kim, Y. C.; Park, Y. S.; Kang, D. *Appl. Phys. Lett.* **2008**, *93*.
- (29) Jeong, S.; Ha, Y.-G.; Moon, J.; Facchetti, A.; Marks, T. J. *Adv. Mater.* **2010**, *22*, 1346.
- (30) Chiang, H. Q.; McFarlane, B. R.; Hong, D.; Presley, R. E.; Wager, J. F. *J. Non. Cryst. Solids* **2008**, *354*, 2826.
- (31) Han, S.-Y.; Herman, G. S.; Chang, C. *J. Am. Chem. Soc.* **2011**, *133*, 5166.
- (32) Park, S.; Clark, B. L.; Keszler, D. A.; Bender, J. P.; Wager, J. F.; Reynolds, T. A.; Herman, G. S. *Sci.* **2002**, *297*, 65.

- (33) Mensinger, Z. L.; Gatlin, J. T.; Meyers, S. T.; Zakharov, L. N.; Keszler, D. A.; Johnson, D. W. *Angew. Chemie Int. Ed.* **2008**, *47*, 9484.
- (34) Winpenny, R. E. P. *J. Chem. Soc. Dalton Trans.* **2002**, 1.
- (35) Mensinger, Z. L.; Wang, W.; Keszler, D. A.; Johnson, D. W. *Chem. Soc. Rev.* **2012**, *41*, 1019.
- (36) Bradley, S. M.; Kydd, R. A.; Yamdagni, R. *J. Chem. Soc. Dalton Trans.* **1990**, 413.
- (37) Goodwin, J. C.; Teat, S. J.; Heath, S. L. *Angew. Chemie* **2004**, *116*, 4129.
- (38) Johansson, G. *Acta Chem. Scand.* **1962**, *16*, 403.
- (39) Casey, W. H.; Phillips, B. L.; Furrer, G. *Rev. Mineral. Geochemistry* **2001**, *44*, 167.
- (40) Sun, Z.; Wang, H.; Feng, H.; Zhang, Y.; Du, S. *Inorg. Chem.* **2011**, *50*, 9238.
- (41) Casey, W. H.; Olmstead, M. M.; Phillips, B. L. *Inorg. Chem.* **2005**, *44*, 4888.
- (42) Seichter, W.; Mögel, H.-J.; Brand, P.; Salah, D. *Eur. J. Inorg. Chem.* **1998**, *1998*, 795.
- (43) Gatlin, J. T.; Mensinger, Z. L.; Zakharov, L. N.; MacInnes, D.; Johnson, D. W. *Inorg. Chem.* **2008**, *47*, 1267.
- (44) Rowsell, J.; Nazar, L. F. *J. Am. Chem. Soc.* **2000**, *122*, 3777.
- (45) Abeysinghe, S.; Unruh, D. K.; Forbes, T. Z. *Inorg. Chem.* **2013**, *52*, 5991.
- (46) Gerasko, O. A.; Mainicheva, E. A.; Naumov, D. Y.; Kuratieva, N. V.; Sokolov, M. N.; Fedin, V. P. *Inorg. Chem.* **2005**, *44*, 4133.
- (47) Kamunde-Devonish, M. K.; Jackson Jr., M. N.; Mensinger, Z. L.; Zakharov, L. N.; Johnson, D. W.; Jackson, M. N. *Inorg. Chem.* **2014**, *53*, 7101.
- (48) Kamunde-Devonish, M. K.; Mensinger, Z. L.; Fast, D. B.; Gatlin, J. T.; Zakharov, L. N.; Dolgos, M. R.; Johnson, D. W. *Synthesis and Structural Characterization of a Series of Aqueous Heterometallic Tridecameric Group 13 Hydroxide Clusters*; 2014.
- (49) Mainicheva, E. A.; Gerasko, O. A.; Sheludyakova, L. A.; Naumov, D. Y.; Naumova, M. I.; Fedin, V. P. *Russ. Chem. Bull.* **2006**, *55*, 267.

- (50) Schmitt, W.; Baissa, E.; Mandel, A.; Anson, C. E.; Powell, A. K. *Angew. Chemie Int. Ed.* **2001**, *40*, 3577.
- (51) King, P.; Stamatatos, T. C.; Abboud, K. A.; Christou, G. *Angew. Chemie Int. Ed.* **2006**, *45*, 7379.
- (52) Wang, W.; Liu, W.; Chang, I.-Y.; Wills, L. A.; Zakharov, L. N.; Boettcher, S. W.; Cheong, P. H.-Y.; Fang, C.; Keszler, D. A. *Proc. Natl. Acad. Sci.* **2013**, *110*, 18397.
- (53) Wang, W.; Wentz, K. M.; Hayes, S. E.; Johnson, D. W.; Keszler, D. A. *Inorg. Chem.* **2011**, *50*, 4683.
- (54) Michot, L. J.; Montarges-Pelletier, E.; Lartiges, B. S.; d'Espinose de la Caillerie, J.-B.; Briois, V. *J. Am. Chem. Soc.* **2000**, *122*, 6048.
- (55) Oliveri, A. F.; Elliott, E. W.; Carnes, M. E.; Hutchison, J. E.; Johnson, D. W. *ChemPhysChem* **2013**, *14*, 2655.
- (56) Jacobsen, N. E. *NMR Spectroscopy Explained: Simplified Theory, Applications and Examples for Organic Chemistry and Structural Biology*; John Wiley & Sons, Inc., 2007; pp. 1–668.
- (57) Ronconi, L.; Sadler, P. J. *Coord. Chem. Rev.* **2008**, *252*, 2239.
- (58) Parish, R. V. *NMR, NQR, EPR, and Mossbauer Spectroscopy in Inorganic Chemistry*; Burgess, J., Ed.; Ellis Horwood Limited: Chichester, West Sussex, 1990.
- (59) Allouche, L.; Gerardin, C.; Loiseau, T.; Ferey, G.; Taulelle, F. *Angew. Chemie Int. Ed.* **2000**, *39*, 511.
- (60) Allouche, L.; Taulelle, F. *Inorg. Chem. Commun.* **2003**, *6*, 1167.
- (61) Fu, G.; Nazar, L. F.; Bain, A. D. *Chem. Mater.* **1991**, *3*, 602.
- (62) Phillips, B. L.; Casey, W. H.; Karlsson, M. *Nature* **2000**, 379.
- (63) Casey, W. H. *Chem. Rev.* **2006**, *106*, 1.
- (64) Allouche, L.; Huguenard, C.; Taulelle, F. *J. Phys. Chem. Solids* **2001**, *62*, 1525.
- (65) Parker Wallace O'Neil; Millini, R.; Kiricsi, I.; Parker, W. O. N. *Inorg. Chem.* **1997**, *36*, 571.

- (66) Lee, S. K.; Stebbins, J. F.; Weiss, C. A.; Kirkpatrick, R. J. *Chem. Mater.* **2003**, *15*, 2605.
- (67) Akitt, J. W. In *Multinuclear NMR*; Mason, J., Ed.; Springer US, 1987; pp. 259–292.
- (68) Akitt, J. W. *Nuclear Magnetic Resonance Spectroscopy in Liquids containing Compounds of Aluminium and Gallium*; Annual Reports on NMR Spectroscopy; Elsevier, 1972; Vol. 5, pp. 465–556.
- (69) Wehrli, F. W. In *Annual Reports on NMR Spectroscopy*; Webb, G. A., Ed.; Annual Reports on {NMR} Spectroscopy; Academic Press, 1979; Vol. 9, pp. 125–219.
- (70) Ma, Z. L.; Wentz, K. M.; Hammann, B. A.; Chang, I.; Kamunde-Devonish, M. K.; Cheong, P. H.; Johnson, D. W.; Terskikh, V. V.; Hayes, S. E. *Chem. Mater.* **2014**, *13*, 4978.
- (71) Cohen, Y.; Avram, L.; Frish, L. *Angew. Chemie Int. Ed.* **2005**, *44*, 520.
- (72) Jackson, M. N.; Wills, L. A.; Chang, I.; Carnes, M. E.; Scatena, L. F.; Cheong, P. H.; Johnson, D. W. *Inorg. Chem.* **2013**, *52*, 6187.
- (73) Li, J.; Cookson, D. J.; Gerson, A. R. *Cryst. Growth Des.* **2008**, *8*, 1730.
- (74) Baes, C. F.; Mesmer, R. E. *The hydrolysis of cations*; Wiley, 1976.
- (75) Zhong, S. U. N.; Hai-Dong, Z.; Hong-Ge-Er, T.; Rui-Fen, W.; Fan-Zhu, Z. H. U. *Chinese J. Struct. Chem.* **2006**, *25*, 1217.
- (76) Schmitt, W.; Jordan, P. a; Henderson, R. K.; Moore, G. R.; Anson, C. E.; Powell, A. K. *Coord. Chem. Rev.* **2002**, *228*, 115.
- (77) Mensinger, Z. L.; Zakharov, L. N.; Johnson, D. W. *Inorg. Chem.* **2009**, *48*, 3505.
- (78) Swaddle, T. W.; Rosenqvist, J.; Yu, P.; Bylaska, E.; Phillips, B. L.; Casey, W. H. *Science (80-.)*. **2005**, *308*, 1450.
- (79) Lindquist, A. *Konsten att rena vatten*; Kemira Kemwater, 2003.
- (80) Duan, J.; Gregory, J. *Adv. Colloid Interface Sci.* **2003**, *100-102*, 475.
- (81) Williams, R. J. P. *Coord. Chem. Rev.* **1996**, *149*, 1.
- (82) Dietrich, D.; Schlatter, C. *Aquat. Toxicol.* **1989**, *15*, 197.
- (83) Powell, a. K.; Heath, S. L. *Coord. Chem. Rev.* **1996**, *149*, 59.

- (84) Lee, A. P.; Furrer, G.; Casey, W. H. *J. Colloid Interface Sci.* **2002**, *250*, 269.
- (85) Smart, S. E.; Vaughn, J.; Pappas, I.; Pan, L. *Chem. Commun.* **2013**, *49*, 11352.
- (86) Jordan, P. A.; Clayden, N. J.; Heath, S. L.; Moore, G. R.; Powell, A. K.; Tapparo, A. **1996**, *149*, 281.
- (87) Malone, S. A.; Cooper, P.; Heath, S. L. *Dalt. Trans.* **2003**, 4572.
- (88) Heath, S. L.; Jordan, P. A.; Johnson, I. D.; Moore, G. R.; Powell, A. K.; Helliwell, M. *794*, 785.
- (89) Espinose, J.; Caillerie, D.; Man, P. P.; Vicente, M. A. **2002**, 4133.
- (90) Johnson, D. W.; Healey, E. R.; Gatlin, J. T.; Mensinger, Z. L. Methods for producing gallium and other oxo/hydroxo-bridged metal aquo clusters, April 19, 2011.
- (91) Sheldrick, G. M. SADABS. *SADABS, Empirical Absorption corrections program*, University of Göttingen, 1995.
- (92) Van der Sluis, P.; Spek, a. L. *Acta Crystallogr. Sect. A Found. Crystallogr.* **1990**, *46*, 194.
- (93) Bruker (2000). SMART, SAINT and SHELXTL. Bruker AXS Inc., Madison, Wisconsin, USA.
- (94) Coelho, A. Topas-Academic, Coelho Software, 2012.
- (95) Cooper, G. J. T.; Newton, G. N.; Long, D.-L.; Kögerler, P.; Rosnes, M. H.; Keller, M.; Cronin, L. *Inorg. Chem.* **2009**, *48*, 1097.
- (96) Downs, A. J. *Chemistry of Aluminium, Gallium, Indium, and Thallium*; Springer Netherlands, 1993.
- (97) Oliveri, A. F.; Wills, L. A.; Hazlett, C. R.; Carnes, M. E.; Cheong, P. H.-Y.; Johnson, D. W. *No Title*; 2014.
- (98) Geller, S. *J. Chem. Phys.* **1960**, *33*.
- (99) Edwards, D. D.; Folkins, P. E.; Mason, T. O. *J. Am. Ceram. Soc.* **1997**, *80*, 253.
- (100) Shannon, R. D.; Prewitt, C. T. *J. Inorg. Nucl. Chem.* **1968**, *30*, 1389.
- (101) Anderson, J. T.; Munsee, C. L.; Hung, C. M.; Phung, T. M.; Herman, G. S.; Johnson, D. C.; Wager, J. F.; Keszler, D. A. *Adv. Funct. Mater.* **2007**, *17*, 2117.

- (102) Meyers, S. T.; Anderson, J. T.; Hong, D.; Hung, C. M.; Wager, J. F.; Keszler, D. *A. Chem. Mater.* **2007**, *19*, 4023.
- (103) Oliveri, A. F.; Carnes, M. E.; Baseman, M. M.; Richman, E. K.; Hutchison, J. E.; Johnson, D. W. *Angew. Chemie Int. Ed.* **2012**, *51*, 10992.
- (104) MacKenzie, K. J. D.; Smith, E. *Multinuclear Solid-State Nuclear Magnetic Resonance of Inorganic Materials*; Pergamon Materials Series; Elsevier Science, 2002; pp. 653–662.
- (105) Larsen, F. H.; Jakobsen, H. J.; Ellis, P. D.; Nielsen, N. C. *J. Magn. Reson.* **1998**, *131*, 144.
- (106) Wu, G.; Rovnyak, D.; Griffin, R. G. *J. Am. Chem. Soc.* **1996**, *118*, 9326.
- (107) Frisch, M. J.; Trucks, G. W.; Schlegel, H. B.; Scuseria, G. E.; Robb, M. A.; Cheeseman, J. R.; Scalmani, G.; Barone, V.; Mennucci, B.; Petersson, G. A. *Gaussian, Inc., Wallingford, CT* **2010**.
- (108) TURBOMOLE V6.3 2011, University of Karlsruhe and Forschungszentrum Karlsruhe GmbH, 1989-2007, TURBOMOLE GmbH, since 2007; available from <http://www.turbomole.com>.ID - 230.
- (109) Becke, A. D. *J. Chem. Phys.* **1993**, *98*.
- (110) Lee, C.; Yang, W.; Parr, R. *Phys. Rev. B* **1988**, *37*, 785.
- (111) Sierka, M.; Hogeckamp, A.; Ahlrichs, R. *J. Chem. Phys.* **2003**, *118*.
- (112) Schäfer, A.; Horn, H.; Ahlrichs, R. *J. Chem. Phys.* **1992**, *97*.
- (113) Weigend, F.; Häser, M.; Patzelt, H.; Ahlrichs, R. *Chem. Phys. Lett.* **1998**, *294*, 143.
- (114) Freude, D.; Haase, J. In *Special Applications SE - I*; Pfeifer, H.; Barker, P., Eds.; NMR Basic Principles and Progress; Springer Berlin Heidelberg, 1993; Vol. 29, pp. 1–90.
- (115) Massiot, D.; Fayon, F.; Capron, M.; King, I.; Le Calvé, S.; Alonso, B.; Durand, J.-O.; Bujoli, B.; Gan, Z.; Hoatson, G. *Magn. Reson. Chem.* **2002**, *40*, 70.
- (116) Middlemiss, D. S.; Blanc, F.; Pickard, C. J.; Grey, C. P. *J. Magn. Reson.* **2010**, *204*, 1.
- (117) Wasylishen, R. E.; Ashbrook, S. E.; Wimperis, S. *NMR of Quadrupolar Nuclei in Solid Materials*; eMagRes Books; Wiley: Chichester, West Sussex, 2012.

- (118) Bradley, S.; Kydd, R.; Yamdagni, R.; Fyfe, C. In *Expanded Clays and Other Microporous Solids SE - 2*; Occelli, M.; Robson, H., Eds.; Springer US, 1992; pp. 13–31.
- (119) Bradley, S. M.; Kydd, R. A. *J. Chem. Soc. Dalton Trans.* **1993**, 2407.
- (120) Pyykkö, P. *Mol. Phys.* **2008**, *106*, 1965.
- (121) Loiseau, T.; Lecroq, L.; Volkringer, C.; Marrot, J.; Férey, G.; Haouas, M.; Taulelle, F.; Bourrelly, S.; Llewellyn, P. L.; Latroche, M. *J. Am. Chem. Soc.* **2006**, *128*, 10223.
- (122) Keszler, D. *Nat Mater* **2011**, *10*, 9.
- (123) Wager, J. F.; Yeh, B.; Hoffman, R. L.; Keszler, D. A. *Curr. Opin. Solid State Mater. Sci.* **2014**, *18*, 53.
- (124) Mitzi, D. *Solution Processing of Inorganic Materials*; Wiley, 2008.
- (125) Bloor, L. G.; Carmalt, C. J.; Pugh, D. *Coord. Chem. Rev.* **2011**, *255*, 1293.
- (126) Hwang, Y. H.; Jeon, J. H.; Seo, S.-J.; Bae, B.-S. *Electrochem. Solid-State Lett.* **2009**, *12*, H336.
- (127) Hwang, Y. H.; Bae, B. *Journal Disp. Technol.* **2013**, *9*, 704.
- (128) Kim, H. J.; No, S. Y.; Eom, D.; Hwang, C. S. *J. Korean Phys. Soc.* **2006**, *9*, 1271.
- (129) Silva, R. F.; Zaniquelli, M. E. D. *Thin Solid Films* **2004**, *449*, 86.
- (130) Fan, G.; Sun, W.; Wang, H.; Li, F. *Chem. Eng. J.* **2011**, *174*, 467.
- (131) Socol, G.; Socol, M.; Stefan, N.; Axente, E.; Popescu-Pelin, G.; Craciun, D.; Duta, L.; Mihailescu, C. N.; Mihailescu, I. N.; Stanculescu, A.; Visan, D.; Sava, V.; Galca, A. C.; Luculescu, C. R.; Craciun, V. *Appl. Surf. Sci.* **2012**, *260*, 42.
- (132) J. Deery, M.; W. Howarth, O.; R. Jennings, K. *J. Chem. Soc. Dalton Trans.* **1997**, 4783.
- (133) Spyratou, A.; Clifford, S.; Melich, X.; Deville, C.; Tissot, M.; Bonvin, G.; Perrottet, P.; Williams, A. *Aust. J. Chem.* **2009**, *62*, 1291.
- (134) Sahureka, F.; Burns, R. C.; von Nagy-Felsobuki, E. I. *Inorganica Chim. Acta* **2003**, *351*, 69.

- (135) Corella-Ochoa, M. N.; Miras, H. N.; Long, D.-L.; Cronin, L. *Chem. – A Eur. J.* **2012**, *18*, 13743.
- (136) Lee, A. P.; Phillips, B. L.; Olmstead, M. M.; Casey, W. H. *Inorg. Chem.* **2001**, *40*, 4485.
- (137) Keggin, J. F. *Proc. R. Soc. London A Math. Phys. Eng. Sci.* **1934**, *144*, 75.
- (138) Mensinger, Z. L.; Zakharov, L. N.; Johnson, D. W. *Acta Crystallogr. Sect. E. Struct. Rep. Online* **2008**, *64*, i8.
- (139) Gili, P.; Núñez, P.; Martín-Zarza, P.; Lorenzo-Luis, P. A. *Acta Crystallogr. Sect. C* **2000**, *56*, e441.
- (140) Vorotyntsev, M. A.; Zinovyeva, V. A.; Picquet, M. *Electrochim. Acta* **2010**, *55*, 5063.
- (141) Tsierkezos, N. *J. Solution Chem.* **2007**, *36*, 289.
- (142) Cheng, I. F.; Muftikian, R.; Fernando, Q.; Korte, N. *Chemosphere* **1997**, *35*, 2689.
- (143) Rudolph, W. W.; Fischer, D.; Tomney, M. R.; Pye, C. C. *Phys. Chem. Chem. Phys.* **2004**, *6*, 5145.
- (144) Olander, D. P.; Marianelli, R. S.; Larson, R. C. *Anal. Chem.* **1969**, *41*, 1097.
- (145) Bottero, J. Y.; Cases, J. M.; Flessinger, F.; Poirier, J. E. *J. Phys. Chem.* **1980**, *84*, 2933.
- (146) Schuster, R. E.; Fratiello, A. *J. Chem. Phys.* **1967**, *47*, 1554.
- (147) Fratiello, A.; Lee, R. E.; Nishida, V. M.; Schuster, R. E. *J. Chem. Phys.* **1968**, *48*, 3705.
- (148) Connick, R. E.; Fiat, D. N. *J. Chem. Phys.* **1963**, *39*, 1349.
- (149) Houston, J. R.; Phillips, B. L.; Casey, W. H. *Geochim. Cosmochim. Acta* **2006**, *70*, 1636.
- (150) Smith, D. S. Density and viscosity measurements of acetone water solutions under high pressure and controlled temperatures ., 1972.
- (151) Al-tamer, M. Y. *Tikrit J. Pure Sci.* **2006**, *11*, 1.
- (152) Seo, D. M.; Borodin, O.; Balogh, D.; O'Connell, M.; Ly, Q.; Han, S.-D.; Passerini, S.; Henderson, W. a. *J. Electrochem. Soc.* **2013**, *160*, A1061.

- (153) Max, J.-J.; Chapados, C. *J. Chem. Phys.* **2003**, *119*, 5632.
- (154) Sandström, J. *Dynamic Nmr Spectroscopy*; Academic Press, 1982.
- (155) Aronica, C.; Pilet, G.; Chastanet, G.; Wernsdorfer, W.; Jacquot, J.-F.; Luneau, D. *Angew. Chem. Int. Ed. Engl.* **2006**, *45*, 4659.
- (156) Bu, X.-H.; Tong, M.-L.; Chang, H.-C.; Kitagawa, S.; Batten, S. R. *Angew. Chem. Int. Ed. Engl.* **2004**, *43*, 192.
- (157) Procopio, E. Q.; Fukushima, T.; Barea, E.; Navarro, J. A. R.; Horike, S.; Kitagawa, S. *Chemistry* **2012**, *18*, 13117.
- (158) Tangoulis, V.; Raptopoulou, C. P.; Paschalidou, S.; Tsohos, A. E.; Bakalbassis, E. G.; Terzis, A.; Perlepes, S. P. *Inorg. Chem.* **1997**, *36*, 5270.
- (159) Johnston, E. M.; Dell'Acqua, S.; Ramos, S.; Pauleta, S. R.; Moura, I.; Solomon, E. I. *J. Am. Chem. Soc.* **2014**, *136*, 614.
- (160) Li, D.-D.; Huang, F.-P.; Chen, G.-J.; Gao, C.-Y.; Tian, J. L.; Gu, W.; Liu, X.; Yan, S.-P. *J. Inorg. Biochem.* **2010**, *104*, 431.
- (161) Li, D.-D.; Tian, J. L.; Gu, W.; Liu, X.; Yan, S.-P. *J. Inorg. Biochem.* **2010**, *104*, 171.
- (162) Brunold, T. C. *Proc. Natl. Acad. Sci.* **2007**, *104*, 20641.
- (163) Hikichi, S.; Yoshizawa, M.; Sasakura, Y.; Akita, M.; Moro-oka, Y. *J. Am. Chem. Soc.* **1998**, *120*, 10567.
- (164) Kundu, S.; Pfaff, F. F.; Miceli, E.; Zaharieva, I.; Herwig, C.; Yao, S.; Farquhar, E. R.; Kuhlmann, U.; Bill, E.; Hildebrandt, P.; Dau, H.; Driess, M.; Limberg, C.; Ray, K. *Angew. Chem. Int. Ed. Engl.* **2013**, *52*, 5622.
- (165) Larsen, P. L.; Parolin, T. J.; Powell, D. R.; Hendrich, M. P.; Borovik, A. S. *Angew. Chemie Int. Ed.* **2003**, *42*, 85.
- (166) Jia, T.; Zhu, S.; Shao, M.; Zhao, Y.; Li, M. *Inorg. Chem. Commun.* **2008**, *11*, 1221.
- (167) Zheng, Y.-Q.; Cheng, D.-Y.; Liu, B.-B.; Huang, W.-X. *Dalt. Trans.* **2011**, *40*, 277.
- (168) Zheng, Y.-Q.; Lin, J.-L. *J. Coord. Chem.* **2008**, *61*, 3420.
- (169) Lah, N.; Leban, I.; Giester, G. *Acta Crystallogr. Sect. C* **2007**, *C63*, m222.

- (170) Burrows, A. D.; Mahon, M. F.; Sebestyen, V. M.; Lan, Y.; Powell, A. K. *Inorg. Chem.* **2012**, *51*, 10983.
- (171) Li, G.; Song, S.; Xu, N.; Liu, X.; Su, Z. *J. Solid State Chem.* **2008**, *181*, 2406.
- (172) Darling, K.; Ouellette, W.; Prosvirin, A.; Freund, S.; Dunbar, K. R.; Zubieta, J. *Cryst. Growth Des.* **2012**, *12*, 2662.
- (173) Chen, J.; Wang, T.-W.; Zhang, Z.; Song, Y.; Zhao, Q.; Ni, J.; Wang, Z.-L. *J. Mol. Struct.* **2006**, *794*, 154.
- (174) Telecky, A.; Xie, P.; Stowers, J.; Grenville, A.; Smith, B.; Keszler, D. A. *J. Vac. Sci. Technol. B* **2010**, *28*, C6S19.
- (175) Que Jr., L.; Tolman, W. B. *Angew. Chem. Int. Ed. Engl.* **2002**, *41*, 1114.
- (176) Frost, R. L.; Williams, P. A.; Martens, W.; Leverett, P.; Klopogge, J. T. *Am. Mineral.* **2004**, *89*, 1130.
- (177) Martens, W.; Frost, R. L.; Klopogge, J. T.; Williams, P. A. *J. Raman Spectrosc.* **2003**, *34*, 145.
- (178) Wang, X.-T.; Wang, B.-W.; Wang, Z.-M.; Zhang, W.; Gao, S. *Inorganica Chim. Acta* **2008**, *361*, 3895.
- (179) Fan, J.; Slebodnick, C.; Hanson, B. E. *Inorg. Chem. Commun.* **2006**, *9*, 103.
- (180) Sato, T.; Ambe, F.; Endo, K.; Katada, M.; Maeda, H.; Nakamoto, T.; Sano, H. *J. Am. Chem. Soc.* **1996**, *118*, 3450.
- (181) Sato, T.; Ambe, F. *Acta Crystallogr. Sect. C Cryst. Struct. Commun.* **1996**, *52*, 3005.
- (182) Poganiuch, P.; Liu, S.; Papaefthymiou, G. C.; Lippard, S. J. *J. Am. Chem. Soc.* **1991**, *113*, 4645.
- (183) Shi, Q.; Zhang, Z.-M.; Li, Y.-G.; Wu, Q.; Yao, S.; Wang, E.-B. *Inorg. Chem. Commun.* **2009**, *12*, 293.
- (184) Saalfrank, R. W.; Scheurer, A.; Pokorny, K.; Maid, H.; Reimann, U.; Hampel, F.; Heinemann, F. W.; Schünemann, V.; Trautwein, A. X. Trinuclear Oxo-Centered Iron and Iron/Nickel Clusters – Ligand-Controlled Homo/Hetero Valency. *European Journal of Inorganic Chemistry*, 2005, *2005*, 1383–1387.
- (185) Mehring, M. *Coord. Chem. Rev.* **2007**, *251*, 974.

- (186) Lazarini, F. *Acta Cryst* **1979**, 448.
- (187) Lazarini, F. *Acta. Cryst.* **1978**, 3169.
- (188) Christensen, A. N.; Chevallier, M.-A.; Skibsted, J.; Iversen, B. B. *J. Chem. Soc. Dalt. Trans.* **2000**, 265.
- (189) Norlund Christensen, A.; Lebech, B. *Dalt. Trans.* **2012**, 41, 1971.
- (190) Miersch, L.; Ruffer, T.; Schlesinger, M.; Lang, H.; Mehring, M. *Inorg. Chem.* **2012**, 51, 9376.
- (191) Liu, B.; Zhou, W.-W.; Zhou, Z.-Q.; Zhang, X.-Y. *Inorg. Chem. Commun.* **2007**, 10, 1145.
- (192) Miersch, L.; Schlesinger, M.; Troff, R. W.; Schalley, C. A.; Ruffer, T.; Lang, H.; Zahn, D.; Mehring, M. *Chem. – A Eur. J.* **2011**, 17, 6985.
- (193) Miersch, L.; Ruffer, T.; Schaarschmidt, D.; Lang, H.; Troff, R. W.; Schalley, C. A.; Mehring, M. *Eur. J. Inorg. Chem.* **2013**, 2013, 1427.
- (194) Miersch, L.; Ruffer, T.; Lang, H.; Schulze, S.; Hietschold, M.; Zahn, D.; Mehring, M. *Eur. J. Inorg. Chem.* **2010**, 2010, 4763.
- (195) Andrews, P. C.; Busse, M.; Junk, P. C.; Forsyth, C. M.; Peiris, R. *Chem. Commun.* **2012**, 48, 7583.
- (196) Helm, L.; Merbach, A. E. *Chem. Rev.* **2005**, 105, 1923.
- (197) Amoureux, J.-P.; Fernandez, C.; Steuernagel, S. *J. Magn. Reson. Ser. A* **1996**, 123, 116.
- (198) Gan, Z.; Kwak, H.-T. *J. Magn. Reson.* **2004**, 168, 346.